

Investigating the Relationship Between Open Magnetic Flux and the Substorm Cycle

**Thesis submitted for the degree of
Doctor of Philosophy
at the University of Leicester**

by

Peter D. Boakes

**Radio and Space Plasma Physics Group
University of Leicester**

December 2009

Abstract

Investigating the Relationship Between Open Magnetic Flux and the Substorm Cycle

Peter D. Boakes

This thesis is concerned with the open magnetic flux content of the magnetosphere during the substorm cycle.

We develop an automated technique of identifying the global location of the open/closed magnetic field line boundary (OCB) from auroral images of the ionospheric northern polar cap made by the IMAGE FUV detector, and hence of estimating the open magnetic flux content of any one hemisphere (F_{pc}). Systematic offsets are found between the location of the OCB as estimated from the auroral images and from in-situ measurements of precipitating particles consistent with previous studies. These offsets are used to provide a more accurate global estimation of the location of the OCB.

This method is used to estimate the average F_{pc} content of the magnetosphere from 12,731 auroral images from December and January of 2000-2002, 173 of which occur at the time of substorm onset. From these distributions we are able, for the first time, to determine the probability of substorm onset as a function of F_{pc} . The probability of substorm onset is found to be negligible below ~ 0.3 GWb, increases linearly until ~ 0.9 GWb, and is undefined above this. These results are discussed in terms of various models for substorm onset and place important constraints on any future models.

We also find that substorms showing a clear particle injection signature, as seen at geosynchronous orbit, occur, on average, at higher values of open magnetic flux than those showing varied or no injection activity. In the final part of this thesis we investigate these three distinct categories of substorms further by carrying out a superposed epoch analysis of F_{pc} , maximum nightside auroral brightness, solar wind and IMF conditions, geomagnetic activity and auroral oval boundary motions. We find that the level and form of solar wind driving appears to characterise the injection signature seen.

Declaration

I, Peter D. Boakes, confirm that the work presented in this thesis is my own. Information derived from other sources has been suitably referenced.

The following scientific papers have been published during the time of these doctoral studies, the first two of which make up the bulk of chapters 4 and 5 of this thesis:

Boakes, P. D., Milan, S. E., Abel, G. A., Freeman, M. P., Chisham, G., and Hubert, B., A statistical study of the open magnetic flux content of the magnetosphere at the time of substorm onset, *Geophys. Res. Lett.*, *36*, L04105, doi:10.1029/2008GL037059, 2009.

Boakes, P. D., Milan, S. E., Abel, G. A., Freeman, M. P., Chisham, G., Hubert, B., and Sotirelis, T., On the use of IMAGE FUV for estimating the latitude of the open/closed magnetic field line boundary in the ionosphere, *Annales Geophysicae*, *26*, 2759-2769, 2008.

Milan, S. E., Grocott, A., Forsyth, C., Imber, S. M., **Boakes, P. D.**, and Hubert, B., A superposed epoch analysis of auroral evolution during substorm growth, onset and recovery: open magnetic flux control of substorm intensity, *Annales Geophysicae*, *27*, 659-668, 2009a.

Milan, S. E., Hutchinson, J., **Boakes, P. D.**, and Hubert, B., Influences on the radius of the auroral oval, *Annales Geophysicae*, *27*, 2913-2924, 2009b.

Milan, S. E., **Boakes, P. D.**, and Hubert, B., Response of the expanding/contracting polar cap to weak and strong solar wind driving: Implications for substorm onset, *J. Geophys. Res.*, *113*, A09215, doi:10.1029/2008JA0133402008a.

Milan, S., Grocott, A., Forsyth, C., Imber, S. M., **Boakes, P. D.**, and Hubert, B., Looking through the oval window, *Astron. Geophys.*, *49*, 16-18, 2008b.

Acknowledgements

I would like to thank the Radio and Space Plasma Physics (RSPP) Group at the University of Leicester and the British Antarctic Survey (BAS) for giving me the opportunity to carry out my PhD in their fine institutions. I would also like to thank the Science Technologies and Facilities Council (STFC) and BAS for supporting me financially throughout my studies.

Many people have provided advice and support without which the completion of this thesis would not have been possible. In particular I would like thank my supervisor, Steve Milan, for always having his door open and never complaining, even when he had to read my thesis drafts late into the night. I would also like to thank my supervisor at BAS, Gary Abel, and colleagues Mervyn Freeman and Gareth Chisham for providing much valued input and encouragement over the last three years. I am also indebted to all those scientists who have been involved in the multitude of missions and instruments whose data has been employed in this thesis, particularly those who have provided advice and support on the use of this data.

Finally, I would like to thank all those members of RSPP who have contributed to the completion of this thesis in some manner. From those who have helped with useful comments and advice or by sharing their knowledge of programming, to all those who have been involved in providing light relief through activities such as film nights, poker nights, provision of fantastic cakes, days at the cricket/football/rugby, trips to the pub (you know which one), curries (you know where), and to others for being good friends, many thanks to you all!

Table of Contents

Chapter 1: Introduction	1
1.1 The Solar Wind and IMF	1
1.2 The Magnetosphere	2
1.2.1 Magnetospheric regions	2
1.2.2 Magnetic Reconnection and the Dungey Cycle	5
1.2.3 The Expanding Contracting Polar Cap	8
1.3 The Ionosphere and Auroral Precipitation	10
1.3.1 The Ionosphere	10
1.3.2 Ionospheric Currents	11
1.3.3 Auroral Generation	12
1.3.4 The Dayside Auroral Precipitation	13
1.3.5 Nightside Auroral Precipitation	13
1.4 Summary	14
Chapter 2: Review of Relevant Substorm Research	15
2.1 Introduction to Substorms	15
2.1.1 The Growth Phase	15
2.1.2 The Expansion Phase and Onset Signatures	16
2.1.3 The Recovery Phase	18
2.1.4 Sawtooth Events	19
2.1.5 Steady Magnetospheric Convection	19
2.1.6 Pseudo-Breakup	20
2.1.7 Poleward Boundary Intensification	20
2.2 Onset Models	21
2.2.1 The near-Earth Neutral Line Model	21
2.2.2 The Current Disruption Model	22
2.2.3 A Critical Threshold for Substorm Onset and Solar Wind Triggering	23
2.3 Identifying the Location of the Open/Closed Magnetic	27

Field Line Boundary in the Ionosphere	
2.3.1 Particle Precipitation Measurements	27
2.3.2 All-sky Cameras, Meridian Scanning Photometers, Coherent and Incoherent Scatter Radar and Ground-based Magnetometers	28
2.3.3 Satellite Images	29
2.4 Summary of Previous Studies on the Polar Cap Flux, Solar Wind and IMF conditions, Geomagnetic Activity and Motion of Auroral Boundaries during the Substorm Cycle	31
2.4.1 Variations in Open Magnetic Flux	31
2.4.2 Variations in the Solar Wind, IMF, Auroral Intensity and Geomagnetic Activity During Substorms and Correlation with F_{pc}	34
2.4.3 Auroral Boundary Motions	40
2.5 Summary	42
Chapter 3: Instrumentation	44
3.1 IMAGE FUV	44
3.1.1 The Wideband Imaging Camera	44
3.1.2 The Spectrographic Imager	45
3.1.3 Image Processing	47
3.2 DMSP	47
3.3 LANL	48
3.4 Measurement of Magnetic Fields	49
3.4.1 The Fluxgate Magnetometer	49
3.4.2 Search Coil Magnetometers	50
3.5 Solar Wind Monitoring Spacecraft	50
3.5.1 ACE	50
3.5.2 Wind	51
3.5.3 Geotail	51
3.6 Ground Based Magnetometers and Geomagnetic Indices	52

Chapter 4: Estimating the Latitude of the Open/Closed Magnetic Field Line Boundary in the Ionosphere	54
4.1 A Method for Identifying the Location of the Open/Closed Magnetic Field Line Boundary in the Ionosphere from IMAGE FUV Auroral Images	56
4.1.1 Instrumentation and Data Set	56
4.1.2 Methodology	56
4.2 Statistical Comparison of IMAGE FUV OCB proxies	59
4.3 Comparison with DMSP Auroral Boundaries	61
4.4 Boundary Optimization	64
4.5 Discussion	66
4.6 Summary	68
Chapter 5: A Statistical Study of the Open Magnetic Flux Content of the Magnetosphere at the time of Substorm Onset	70
5.1 Methodology	70
5.1.1 Estimating the Open Magnetic Flux Content of the Magnetosphere	70
5.1.2 Selection of Parent and Substorm Distributions	74
5.1.3 LANL Substorm Classification	74
5.2 Results	73
5.2.1 The Open Magnetic Flux at the Time of Substorm Onset	76
5.2.2 Probability of Substorm Onset as a Function of Open Magnetic Flux	76
5.3 Discussion & Conclusions	77
5.3.1 Are All Frey Events Substorms?	77
5.3.2 What do the Distributions Tell Us About Substorm Onset?	78
5.4 Summary	80

Chapter 6: A Superposed Epoch Analysis of Substorm Dynamics	82
6.1 Open Magnetic Flux, Auroral Intensity, IMF and Solar Wind conditions and Geomagnetic Indices	82
6.1.1 Methodology	82
6.1.2 Observations and Discussion	85
6.1.2.1 Overview of Category 1 and 2 Events	85
6.1.2.2 Summary and Discussion of Category 3 events	93
6.2 Auroral Boundaries	95
6.2.1 Methodology	98
6.2.2 Superposed Study of All Substorms	99
6.2.3 Superposed Boundary Movements of LANL Categories	102
6.2.3.1 Motion of the OCB	103
6.2.3.2 Motion of the Equatorward Boundary	104
6.2.3.3 Oval Width Variation	105
6.3 Discussion	105
6.4 Summary and Conclusions	113
6.4.1 Auroral Boundary Motions	113
6.4.2 Study of LANL Categories	114
 Chapter 7: Summary and Future Work	 115
7.1 Summary	115
7.2 Future Work	118
 References	 120

Chapter 1. Introduction

The subject of this thesis is the magnetospheric substorm. The substorm process results from the coupling between the Earth's magnetic field and the interplanetary magnetic field originating in the Sun. The purpose of this chapter is to introduce the solar wind, interplanetary magnetic field and the Earth's magnetosphere-ionosphere system, and the coupling between them.

1.1 The Solar Wind and IMF

In the early twentieth century it was postulated that a stream of electrons emitted from the Sun could penetrate the Earth's atmosphere (Birkeland, 1909), thus causing the northern lights. It was later realised (Birkeland, 1916) that in order to remain neutral the stream of particles must also contain an equal number of positively charged ions. It was first thought that the solar wind consisted of bursts of these electrically neutral streams of electrons and ions until Hoffmeister (1943) noted that the tail of a comet was not strictly radial but lagged the radial direction by approximately 5 degrees. Biermann (1951) postulated that the observations that comet tails always have a component directed away from the Sun must be caused by a constant solar wind stream emitted by the Sun in all directions, interacting with the comet tail and pushing it away. Parker (1958) demonstrated, through simple gas dynamics, that the high temperature and huge pressure difference between the solar corona and surrounding interstellar medium allows the plasma to stream away from the Sun, overcoming the force of gravity. The existence of the solar wind was soon confirmed by the first satellite observations made by Gringauz *et al.* (1960).

Satellite observations have now confirmed that the solar wind mainly consists of equal numbers of ions and electrons with the ion component made up of ~95% protons, 5% helium ions and trace amounts of heavier ions (Kivelson and Russell, 1995). Parker (1958) also showed that the solar wind speed increases with radial distance from the Sun, reaching supersonic speeds by the time it reaches Mercury's orbit. Typical solar wind properties at a distance of 1 AU from the Sun (1.5×10^{11} m, the distance from the Sun to the Earth) are shown in Table 1.1. The solar wind flow is not isotropic

Typical Properties of the Solar Wind at near Earth Orbit

Proton Density	6.0 cm⁻³
Electron Density	6.0 cm⁻³
Flow Speed	470 km/s
Dynamic Pressure	2.5 nPa
Magnetic Field	7 nT

Table 1.1: Typical properties of the solar wind and IMF at 1 AU (Prölss, 2004).

but consists of three components of differing speeds, ‘slow’ flows of typically 300-450 km s⁻¹ originating from active regions on the solar surface, ‘fast’ flows of 600-900 km s⁻¹ thought to originate from coronal holes, and finally very high speed transient flows possibly related to coronal mass ejections (Kivelson and Russell, 1995).

Due to the high conductivity of the solar wind plasma, the Sun’s magnetic field is ‘frozen-in’ to the solar wind (Baumjohann and Treumann, 1997) and carried with it into interplanetary space. This magnetic field is known as the interplanetary magnetic field (IMF), varying in strength at the Earth from ~1 to greater than 40 nT. The Sun rotates with an average periodicity of 27 days (slightly longer at the poles and slightly less at the equator). This rotation causes the IMF to propagate outward from the surface of the Sun in a spiral-like pattern known as the Parker spiral (see Figure 1.1a). During the low-activity minimum of the 11 year solar cycle the radial component of the solar magnetic field lines are directed into the southern hemisphere and out of the northern hemisphere. In the next solar cycle this asymmetry reverses. By Ampère’s law, when there is a curl in a magnetic field a current must flow (see Baumjohann and Treumann, 1997). Ampère’s law thus requires a current sheet to form in the out-flowing IMF at the boundary between magnetic field lines of opposite polarity. This is illustrated in Figure 1.1b and is known as the heliospheric current sheet. The Sun’s magnetic field is not a simple dipole field and contains many higher order terms. This complex nature results in complex ‘ripples’ in the heliospheric current sheet which are often likened to the folds in a ballerina’s skirt. As the Earth moves above and below the current sheet it will experience periods when the IMF is directed away and towards the Earth, as well a large range of IMF clock angles (see Figure 1.2).

1.2 The Magnetosphere

1.2.1 Magnetospheric Regions

The magnetosphere is the region of near-Earth space governed by the Earth’s magnetic field. In the absence of any external influences, the Earth’s magnetic field can be approximated to be dipolar, with its magnetic pole offset from the geographic pole by approximately 11°. Chapman and Ferraro (1930) used a simple application of the frozen-in condition (Baumjohann and Treumann, 1997) to postulate that the Earth’s

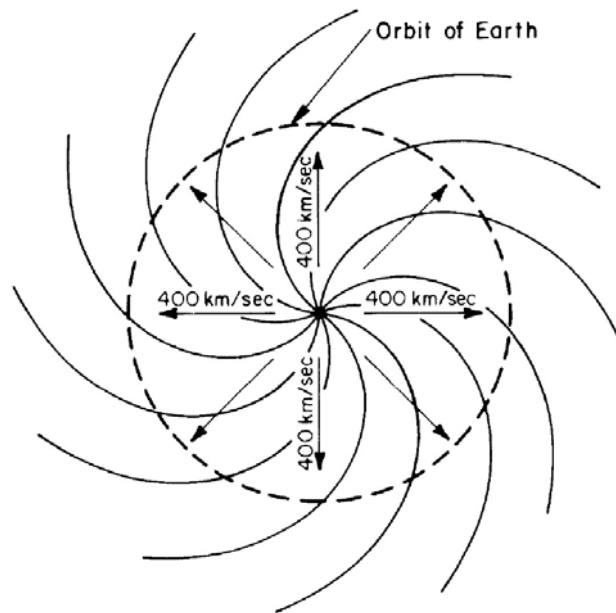


Figure 1.1a: Representation of the Parker spiral assuming a constant radial speed of 400 km s^{-1} and radial solar magnetic field (from Kivelson and Russell, 1995). The IMF is carried radially outwards from the Sun with the solar wind and forms a spiral pattern due to the Sun's rotation.

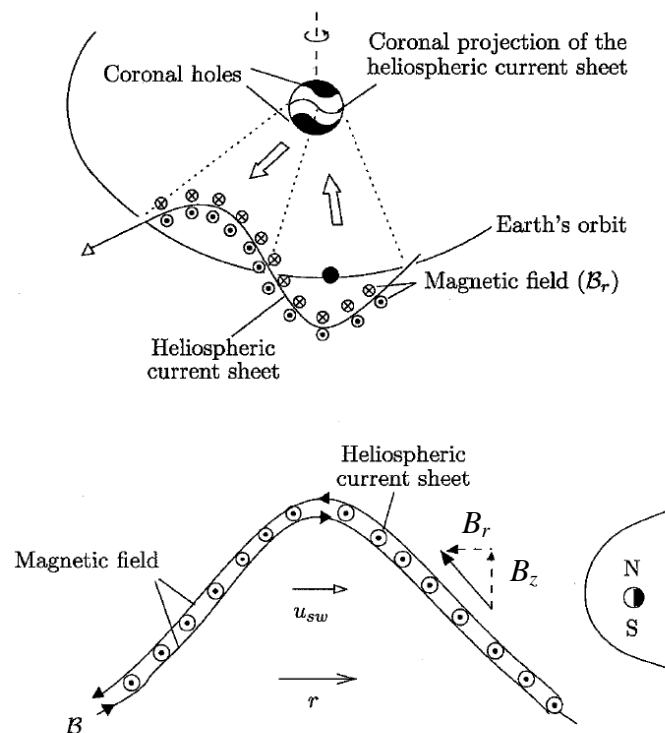
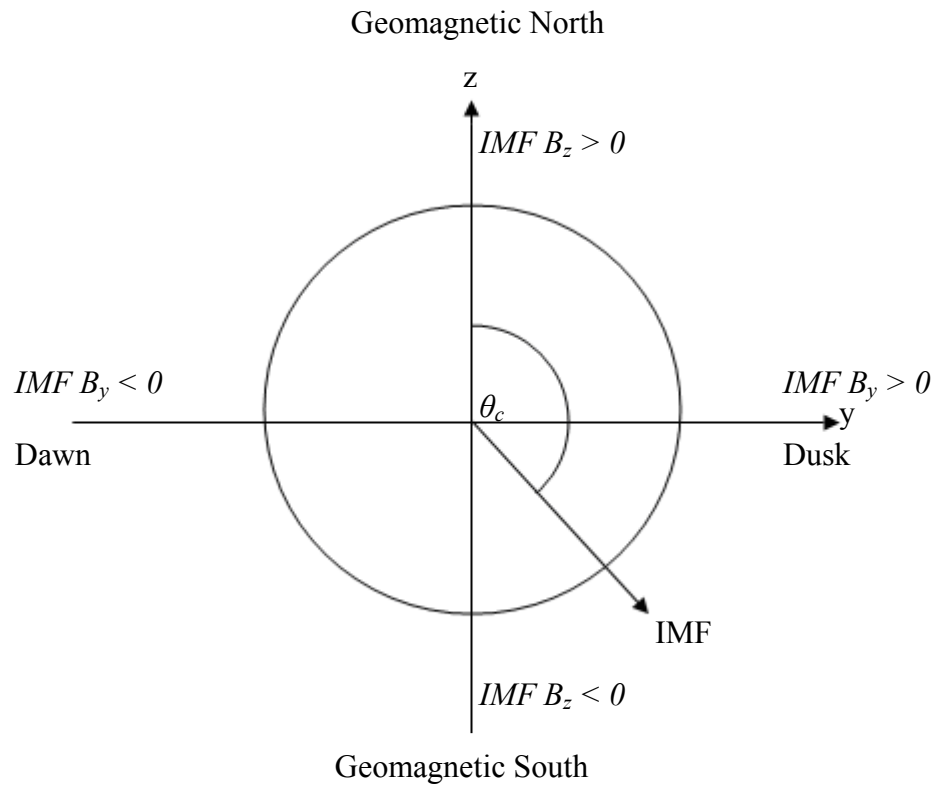


Figure 1.1b: Schematic representations of the warp in the heliospheric current sheet and how the Earth will experience different orientations of IMF as it moves through it (adapted from Pröss, 2004), where u_{sw} is in the direction of radial solar wind flow and B_z and B_r are the north-south and radial components of the IMF in the frame of reference of the Earth's magnetic axis.



$$\theta_c = \arctan(|B_y| / B_z) \quad 0 \leq \theta_c \leq \pi$$

Figure 1.2: Definition of the IMF clock angle and GSM coordinate system. Here we are looking from the Sun toward the Earth along the Sun-Earth line. In the geocentric solar magnetic (GSM) coordinate system zero X, Y and Z is located at the center of the Earth. The X component is directed along the Sun-Earth line in and out of the plane of the page. Positive X is toward the Sun with negative X behind the Earth. The Z component is perpendicular to X and is in the plane of the Earth's dipole. Hence $IMF B_z < 0$ is oppositely directed to the northward magnetic field of the Earth. The Y component is directed along the dawn-dusk line, with positive Y in the direction of dusk. The IMF clock angle (θ_c) is defined as the angle made by the IMF with geomagnetic north in the GSM Y-Z plane.

magnetic field must create a cavity in the solar wind, whose outer boundary separates plasma of terrestrial and solar origin. This cavity is called the magnetosphere. Figure 1.3 shows a schematic of the main regions of the magnetosphere, where the Sun is located to the left of the figure.

The first feature to be encountered on the far left hand side of Figure 1.3 is the bow shock, first postulated by Axford (1962) and Kellogg (1962). The information needed to deflect the solar wind flow around the magnetosphere travels at a velocity less than the solar wind flow speed. This results in the bow shock located at approximately $14 R_E$ from the center of the Earth where the supersonic solar wind flow brakes to subsonic speeds.

As the solar wind plasma is slowed through the bow shock region it is also heated and compressed such that a region of hot, compressed solar wind plasma forms between the bow shock and magnetopause. This region of ‘shocked’ solar wind has a density and magnetic field strength approximately four times that in the un-shocked solar wind and is known as the magnetosheath. The plasma of the magnetosheath can gain direct entry to the magnetosphere and ionosphere (section 1.3) through the cusp, mantle and dayside entry layer regions (see below).

The boundary between the magnetosphere and solar wind is known as the magnetopause, and was first postulated by Chapman and Ferraro (1931). Typically the nose of the magnetopause is located at $\sim 10 R_E$, its exact location depending on the balance between the ram pressure of the solar wind and magnetic pressure of the dayside magnetosphere. There is a large gradient between the strength of the shocked IMF and terrestrial magnetic field at the magnetopause and thus by Ampère’s law a current must flow. On the dayside magnetopause this current flows in the dawn-dusk direction and closes over the tail lobes and in the magnetotail (Prölss, 2004).

The cusp region exists at the neutral point between dayside magnetic field lines and the nightside field lines of the lobes and is often defined as the region of direct entry of solar wind plasma into the magnetosphere (Heikkila and Winningham, 1971). Extending equatorward from the cusp is the dayside entry layer. Here the plasma density is nearly as high as in the magnetosheath (Haerendel and Paschmann, 1975;

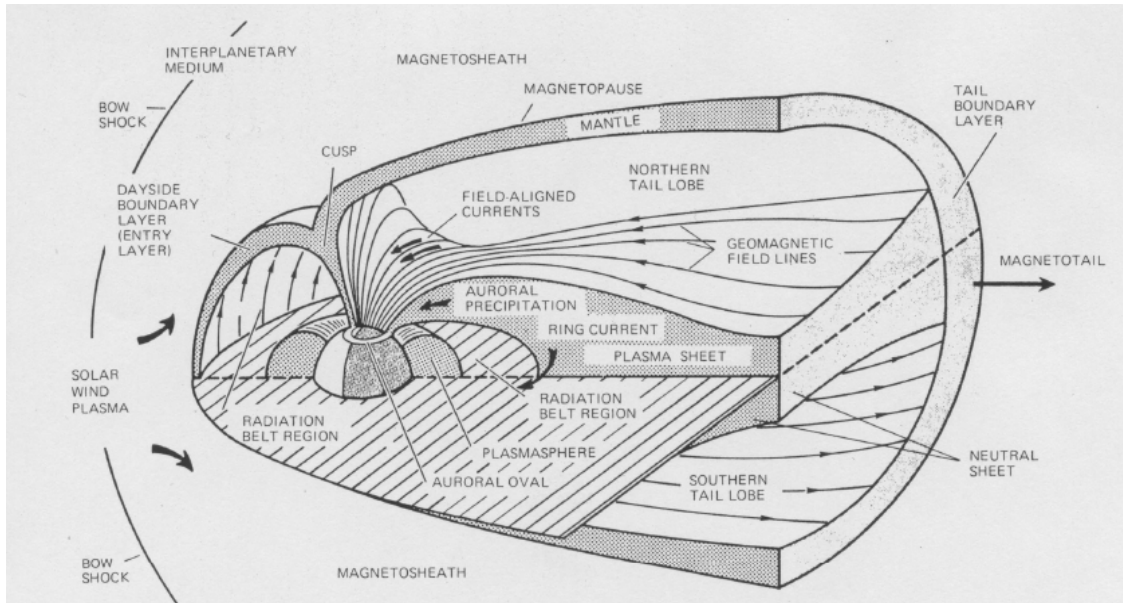


Figure 1.3: Schematic of the regions of the magnetosphere (from Kelley, 1989).

Paschmann *et al.*, 1976). At the equator, the entry layer extends around the magnetosphere in the plane of the equator into a layer known as the low-latitude boundary layer (LLBL, not shown in Figure 1.3). The LLBL (e.g. Eastman *et al.*, 1976; Fujimoto *et al.*, 1998) consists of particles from a mixture of both magnetosheath and magnetospheric origins. The high latitude extension of the cusp is termed the mantle (Rosenbauer *et al.*, 1975). Particles from these regions can gain direct entry to the Earth's upper atmosphere and thus play an important role in the creation of the dayside auroral emission (see section 1.3.4).

While the dayside magnetosphere is compressed by the solar wind flow, the tail of the magnetosphere is stretched several hundred R_E downtail. The northern and southern lobes of the tail are open. That is, they have one magnetic footprint connected to the surface of the Earth and the other ultimately connected to the solar surface. The closed magnetic field line region at the center of the tail is known as the plasma sheet, which can be broken down into two regions. The boundary plasma sheet is a thin hot layer of mostly field-aligned plasma which surrounds the thicker and denser central plasma sheet (CPS). The large gradient between the oppositely directed field lines of the northern and southern lobes requires a current by Ampère's law. This results in a dawn-dusk current flowing near the center of the plasma sheet, known as the cross-tail current or neutral sheet.

Within the closed field line region of the plasma sheet, and extending round to the dayside, lies the radiation belt region. The radiation belts consist of two separate regions of hot, trapped particles, mirroring (see Figure 1.4 and section 1.2.2) between the northern and southern poles as well as gradient and curvature drifting (see below and Figure 1.4) around the Earth. Between ~ 1.1 and $3.3 R_E$, in the equatorial plane, lies the inner radiation belt region where the maximum flux of the most energetic protons (~ 4 -50 MeV) in the magnetosphere resides. The inner radiation belt region has a fairly stable population which may vary due to geomagnetic storms and with the 11 year solar cycle. The outer radiation belt lies at ~ 3 -9 R_E , covering geosynchronous orbit (6.6 R_E), and is much more dynamic than the inner belt. The outer belt is the region of maximum flux for energetic electrons within the magnetosphere (Prölss, 2004). Typical electron energies are between 20-200 keV but can be as high as 10 MeV (e.g. Krimigis *et al.*, 1985). The outer radiation belt is thought to be highly modulated

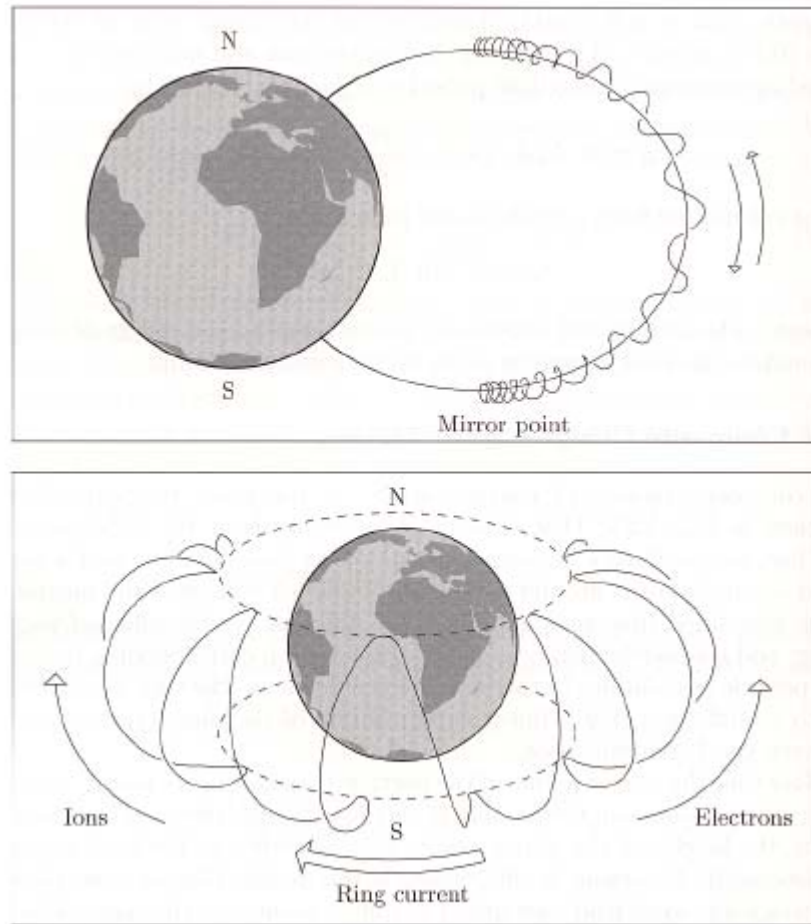


Figure 1.4: Motion of particles trapped on closed magnetic field lines (from Prölss, 2004). Top: Magnetic mirroring. Particles travelling along magnetic field lines into a converging magnetic field will feel a force perpendicular to the magnetic field direction which has a component pointing away from direction of increasing field. Hence the velocity of the particle in the direction of converging field decreases until it is reversed such that the particle changes direction along the field lines. The point at which the particles direction reverses is called the mirror point. If the particles mirror point is within the upper atmosphere, the particles may interact with atmospheric neutrals, the source of auroral emission (Baumjohann and Treumann, 1997).

Bottom: Particle motion due to mirroring and gradient and curvature drift. When there is a gradient in the magnetic field strength (the Earth's magnetic field strength decreases away from the Earth) such that the length scales of the gradient is comparable to the gyro-radius of particles traversing the magnetic field lines, as well mirroring between the hemispheres of the Earth, the particles will also feel a force perpendicular to both the direction and gradient in magnetic field. This is called the gradient drift. A related drift is the curvature drift which occurs due to the curvature of field lines such that the magnetic field direction changes along it (see Prölss, 2004). Both gradient and curvature drift are charge dependent such that electrons drift eastwards and protons drift westwards around the Earth (Prölss, 2004).

by the injection of energetic particles during substorms (see chapter 2) and storms (see McPherron *et al.*, 2008) and plays a major role in modulating the strength of the ring current (see below).

As well as mirroring between the two hemispheres of the Earth, particles trapped on closed magnetic field lines also feel a gradient and curvature drift (Baumjohann and Trumann, 1997 and Figure 1.4) such that electrons drift eastward around the Earth and ions drift westwards. The energetic particles of the outer radiation belts can complete an entire orbit of the Earth in only a few minutes (e.g. Liemohn and Chan, 2007). The relative motion of trapped ions and electrons creates a current flowing in the westwards direction between $\sim 2-7 R_E$, overlapping the radiation belt region, known as the ring current (see Figures 1.3 and 1.4). The strength of the ring current, as measured by ground-based instrumentation (see section 3.6) is a good indicator of the level of geomagnetic/storm activity of the magnetosphere (e.g. Frank, 1967).

Inside of and overlapping the radiation belt region lies the region known as the plasmasphere. The plasmasphere lies Earthward of the inner edge of the plasma sheet. This is a region of cold, dense plasma that has escaped from the ionosphere, and which co-rotates with the Earth. The outer edge of the plasmasphere is known as the plasmopause and has been shown to often lie between $3-5 R_E$ (Kivelson and Russell, 1995).

1.2.2 Magnetic Reconnection and the Dungey Cycle

In the Chapman-Ferraro magnetosphere, the magnetosphere is considered to be completely closed to the solar wind due to the frozen-in condition, which states that an infinitely conducting plasma in a magnetic field is frozen-in to the magnetic field such that plasmas travelling in two different magnetic field line regions cannot mix. However, Dungey (1961) proposed that when the IMF is strongly southward, that is, oppositely directed to the northward terrestrial field lines near the nose of the dayside magnetosphere, a process known as magnetic reconnection can occur at the dayside magnetopause, allowing the two different magnetic field and plasma regions to conjoin. A schematic representation of the reconnection process is shown in Figure 1.5. When two oppositely directed magnetic field lines come together they enter the region known

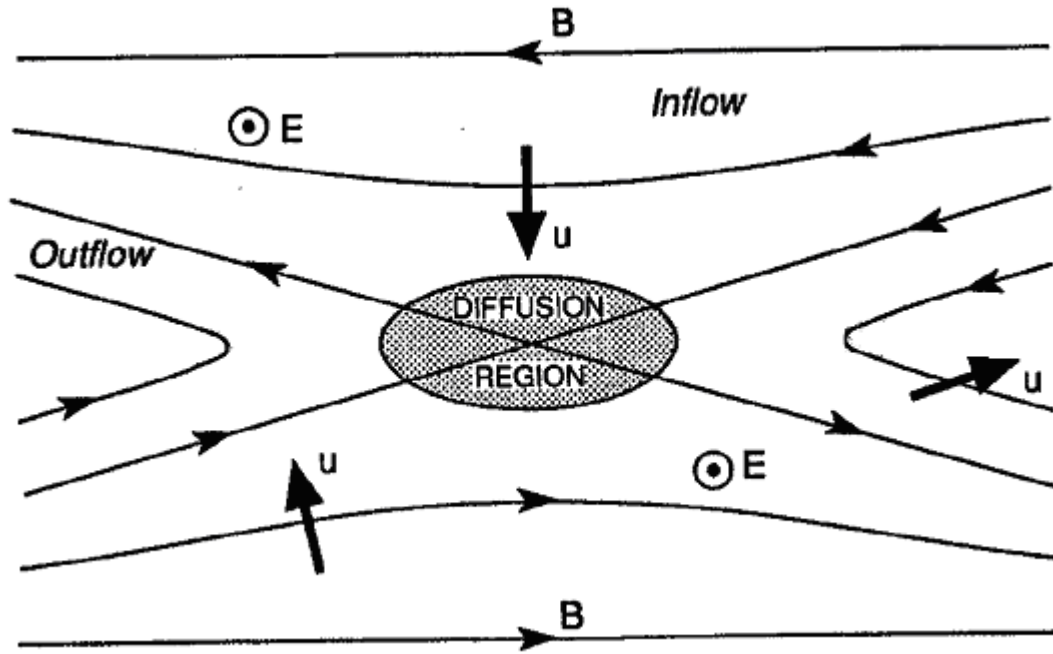


Figure 1.5: Schematic representation of magnetic reconnection (adapted from Kivelson and Russell, 1995). Oppositely directed magnetic field lines travel into the diffusion region from above and below, join at the reconnection x-line where they split into two separate field lines which subsequently travel away from the diffusion region in the perpendicular direction.

as the diffusion region. Here, the characteristic length scale of the plasma becomes short enough that diffusion becomes important such that the magnetic field can become decoupled from the plasma. In the diffusion region the frozen-in approximation no longer holds and reconnection occurs along what is known as a reconnection x-line, or neutral line (where the total magnetic field strength is zero). Magnetic field lines flow into the diffusion region, from the top and bottom of the figure, where they join at the neutral line and split perpendicular to the neutral line such that two new field lines are formed. The highly kinked nature of these new field lines imposes a large magnetic tension upon them such that the field lines are accelerated away from the reconnection site in the perpendicular direction (Kivelson and Russell, 1995). Plasma travelling along the magnetic field lines of the two separate regions now finds itself on field lines which are continuous across the two previously separate field line regions such that plasma of the two different regimes can mix.

In the proposed model by Dungey (1961), reconnection can occur at both the dayside magnetopause and within the magnetotail, completing what is known as the Dungey cycle. The proposed model explained many of the observation features of the magnetosphere, including the twin cell convection pattern (see below), the stretched tail of the magnetotail (e.g. Wolfe *et al.*, 1967), the erosion of dayside closed magnetic flux during extended periods of southward IMF (e.g. Aubry *et al.*, 1970; Holzer and Slavin, 1979) and the increased magnetospheric activity during southward IMF (e.g. Fairfield and Cahill 1966; Fairfield, 1967). The Dungey cycle is represented schematically in Figure 1.6a and summarised below.

When the IMF is oppositely directed to the northward terrestrial field lines at the sub-solar point, the first closed terrestrial magnetic field line (having both footprints connected to the surface of the Earth) at the dayside magnetopause is split in two by reconnection (point a, Figure 1.6a), creating two new field lines each with one magnetic footprint connected to either the northern or southern pole of the Earth, and the other ultimately to the surface of the Sun (field line b, Figure 1.6a). These field lines are called open magnetic field lines and contribute to the amount of open magnetic flux threading the magnetosphere. These open magnetic field lines are quickly swept back over the northern and southern poles by the solar wind flow (b-d), and form the long tail of the magnetosphere known as the magnetotail. Dungey (1965) estimated that field

lines remain open for approximately 4 hours before they become close enough in the tail to be reclosed through reconnection at what is known as the distant neutral line (DNL), point e. Reconnection at the distant neutral line recloses open magnetic field lines, forming both Earthward and tailward moving loops of closed magnetic flux which have both footprints connected to the surface of the Earth and solar corona respectively. Spacecraft observations of the plasma outflow from the DNL reconnection site place the DNL at a distance of approximately 100-150 R_E downtail (e.g. Slavin *et al.*, 1985). Closed field lines ejected tailward continue to move away from the Earth while the Earthward moving flux tubes convect around the Earth at low latitudes in both dawnward and duskward directions (f-g) to replenish the flux opened on the dayside.

The open magnetospheric magnetic field lines map to the high latitude region over the poles in a region known as the polar cap (see Figure 1.6b). Particles on open magnetic field lines will mirror only once near one of the poles of the Earth before continuing their long journey down their open magnetic field lines. Equatorward of the polar cap lies the closed magnetic field region. Since the Earth's magnetic field converges at the poles, particles travelling along these field lines will mirror (change direction) as they reach the poles (Prölss, 2004, see Figure 1.4), bouncing between the two hemispheres of the Earth. When the mirror point is at a low enough altitude to penetrate the upper atmosphere of the Earth they can interact with atmospheric particles, creating the bright ring of auroral emission known as the auroral oval (Figure 1.3). The boundary between open and closed magnetic field lines is known as the open/closed magnetic field line boundary, or OCB. Figure 1.6b shows the motion of magnetic field lines across the northern polar cap during the Dungey cycle, as viewed from above. The motion of the field lines is shown by the dashed lines, the magnetic field is directed into the page and the induced electric field (see Baumjohann and Treumann, 1997) direction is shown by the arrows. In the upper layers of the Earth's atmosphere/ionosphere (see below) plasma is coupled to the magnetic field and moves with it. The pattern formed by the motion of field lines and plasma is known as the ionospheric convection pattern (e.g. Cowley and Lockwood, 1992).

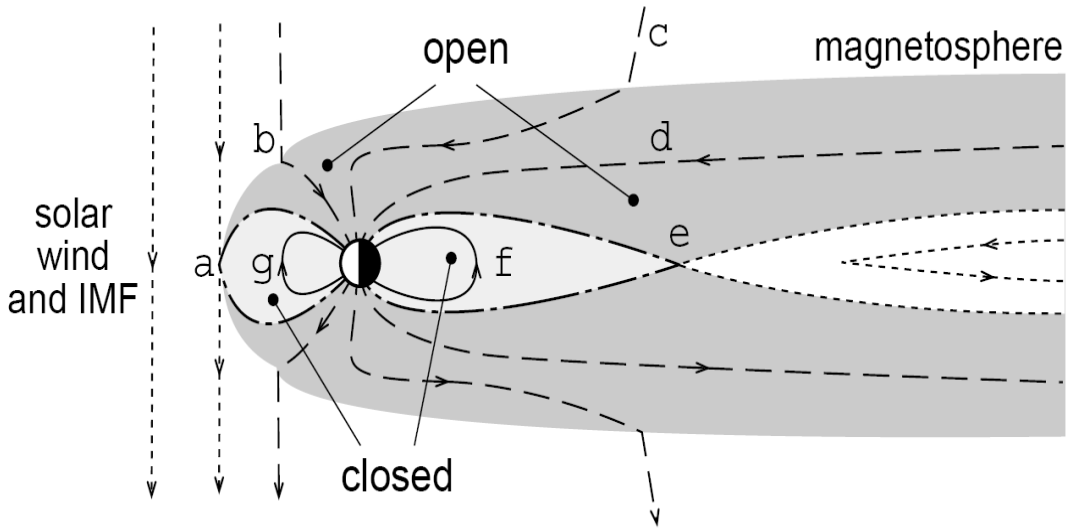


Figure 1.6a: Schematic of the Dungey cycle (from Milan *et al.*, 2003).

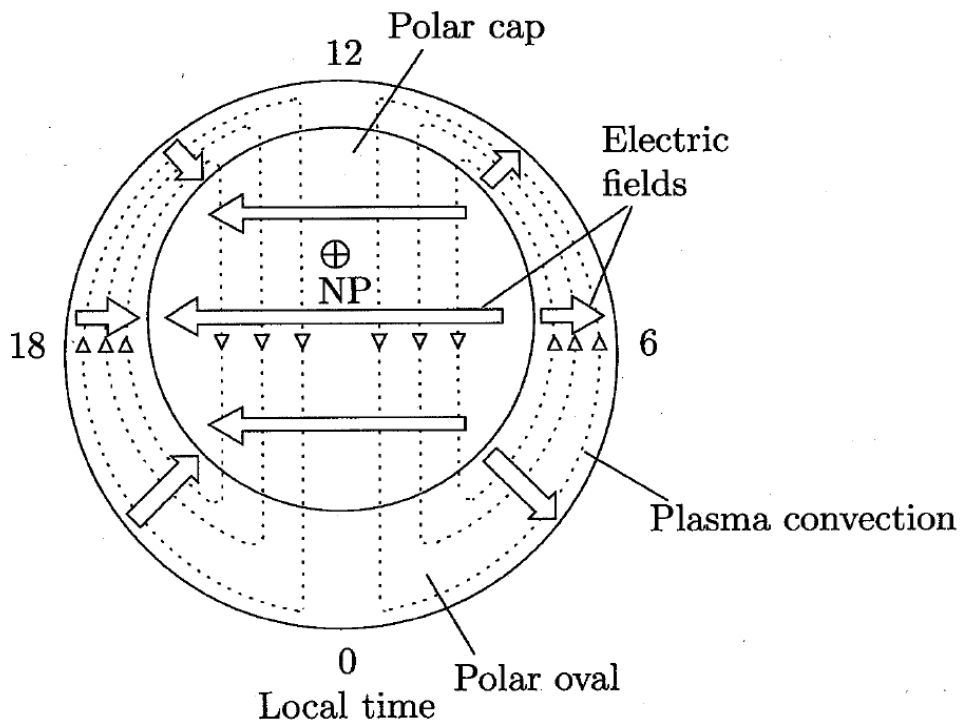


Figure 1.6b: Schematic of the Dungey cycle as seen from above the northern polar cap (from Prölss, 2004). Dashed lines show the motion of magnetic field lines across the polar cap, known as the ionospheric convection pattern. The magnetic field is directed into the page and the arrows show the direction of the electric field in the ionosphere.

1.2.3 The Expanding-Contracting Polar Cap

The polar cap in any one hemisphere is defined as the area threaded by open magnetic flux. Magnetic reconnection at the dayside magnetopause adds open magnetic flux to the magnetospheric system, thus acting to increase the size of the polar cap. Conversely, tail reconnection closes open magnetic flux and works to decrease the size of the polar cap. The rate of change in polar cap size can thus be expressed in terms of the day and nightside reconnection rates as follows:

$$B\left(\frac{dA_{pc}}{dt}\right) = dF_{pc} / dt = \phi_D - \phi_N, \quad (1.1)$$

where B is the magnetic field strength of the Earth (assumed to be constant everywhere across the polar region, which is only an approximation), A_{pc} is the area of the polar cap, F_{pc} is the amount of open magnetic flux threading the polar cap, ϕ_D and ϕ_N are rates of day and nightside reconnection respectively. This is a simple formulation of Faraday's law, magnetic flux inside a closed loop must be equal to the electric field integrated around the loop, applied to the ionosphere where the closed loop is the OCB. ϕ_D and ϕ_N are voltages associated with the opening and closing of flux on the dayside and nightside. The electric field is associated with convective flow in the ionosphere (Siscoe and Huang, 1985; Lockwood and Cowley, 1992).

In the original definition of the Dungey cycle the dayside and nightside reconnection rates were considered to be equal. However, many studies have since shown that the polar cap size is highly variable (see section 2.4). This result is easily explained by a Dungey cycle in which the dayside reconnection is not a steady process but responds to changes in the orientation of the IMF. Indeed, it is known that the IMF is highly variable and can switch between northward (no dayside reconnection) and southward (dayside reconnection proceeds) orientations over time scales of a few minutes (e.g. see Figures 3, 4 and 5 of Milan *et al.*, 2009b). While the rate of dayside reconnection will depend on the orientation and strength of the IMF, the rate of nightside reconnection will be dependent on the conditions within the magnetotail, which are in turn controlled by the level of dayside reconnection. However, it takes at least 30 minutes for

information on dayside reconnection to be transported to the tail (Cowley and Lockwood, 1992). Nightside reconnection thus cannot respond to changes at the dayside instantaneously and it is expected that day and nightside reconnection rates will rarely be in balance. This leads to an expansion and contraction of the polar cap area as discussed by Russell (1972), Siscoe and Huang (1985), Cowley and Lockwood (1992), Lockwood and Cowley (1992), Taylor *et al.* (1996), Milan *et al.* (2003, 2006, 2007) and Lockwood *et al.* (2005).

Figure 1.7 shows a schematic representation of the response of the polar cap and ionospheric convection pattern to different rates of day and nightside reconnection, assuming that the equilibrium position of the OCB is circular. Panel a shows the response for a burst of dayside reconnection only. The solid part of the elongated circle represents the location of the OCB at the start of a period of enhanced dayside reconnection. The low-latitude reconnection site at the dayside magnetopause maps to the dot-dashed line around 12 noon, known as the merging gap, co-located with the OCB. As the dayside reconnection proceeds the merging gap portion of the OCB quickly moves to lower latitudes to encompass the region of newly opened magnetic flux around 12 noon. As the newly-opened field lines are subsequently dragged across the polar cap (their motion shown by the arrowed lines), plasma flows are induced in the ionosphere which redistribute the newly opened flux around the polar cap as the polar cap tries to relax back to its circular configuration. This results in a poleward motion of the merging gap portion of the OCB and an equatorward motion of the OCB at all other MLTs. If the dayside reconnection were to be turned off (and there is no nightside reconnection such that open flux is neither added nor removed from the polar cap) the OCB would relax to the location shown by the dot-dashed circle and the flow would die away as this happens.

Panel b represents the equivalent pattern for an entirely nightside burst of reconnection. In this scenario nightside reconnection eats into the open flux of the polar cap near midnight, resulting in the poleward motion of the nightside merging gap. The OCB at other local times slowly moves to higher latitudes as the flux is redistributed throughout the polar cap. The dot-dashed circle again represents the location of the OCB if reconnection were to be subsequently turned off.

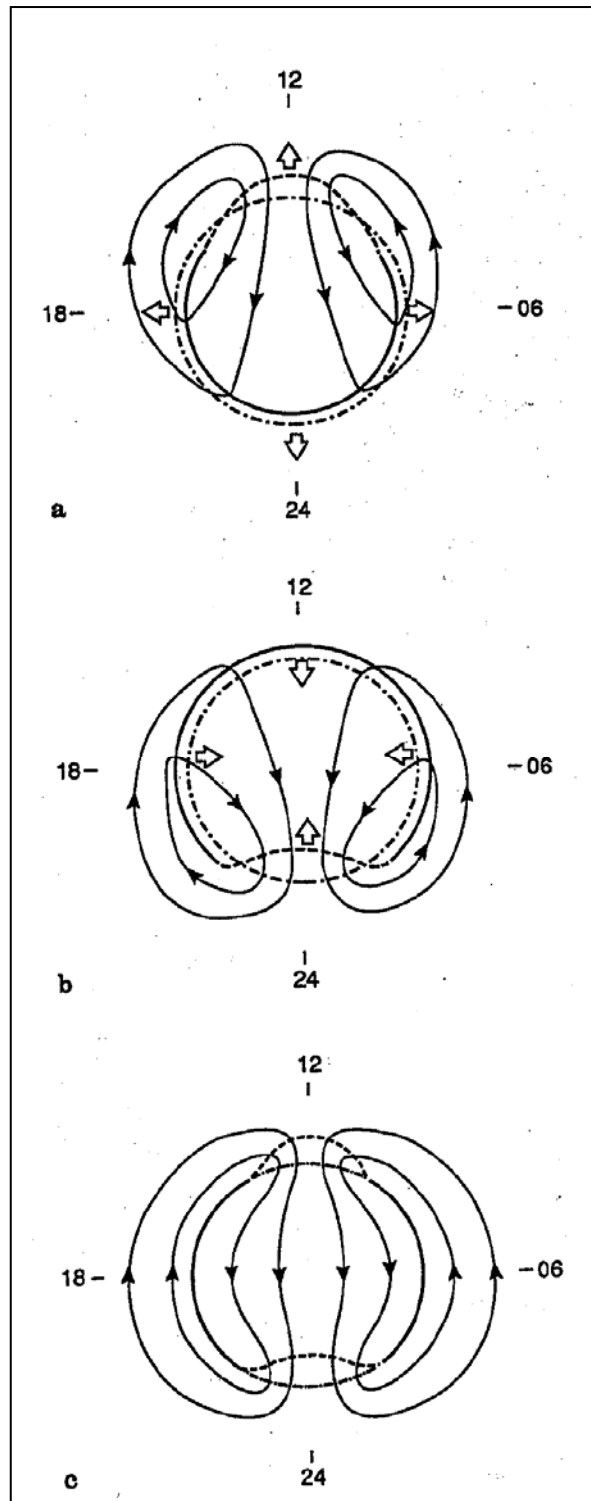


Figure 1.7: Schematic of the expanding and contracting nature of the polar cap for a burst of dayside reconnection (panel a), a burst of nightside reconnection (panel b) and balanced dayside and nightside reconnection (panel c) (from Cowley and Lockwood, 1992). The dashed line shows the location of the ionospheric merging gap and the solid circle represents the location of the OCB at all other local times. The dashed-dot line represents the final location of the OCB if reconnection were to be turned-off after a period of dayside (panel a) or nightside (panel b) reconnection. The arrowed lines show the ionospheric convection pattern.

In reality both day and nightside reconnection proceed in tandem. This scenario is represented in panel c of Figure 1.7 for completely balanced day and nightside reconnection. Here the OCB remains at a fixed location as the convection of open magnetic flux into the polar cap at the dayside equals the convection of open magnetic flux out of the polar cap on the nightside. However, as discussed above, day and nightside reconnection rates are rarely in balance resulting in an expansion or contraction of the polar cap, depending on which process is dominant.

Under northward IMF magnetic reconnection can also occur in one or both magnetospheric lobes under certain conditions. Dual lobe reconnection, reconnection occurring between the IMF and open lobe field lines in both tail lobes simultaneously such that the same IMF field line is reconnected in both hemispheres, can occur when the IMF is strongly northward and the B_y component is close to zero such that the IMF is oppositely directed to the terrestrial field in both lobes at high latitudes (e.g. Dungey, 1963, Imber *et al.* 2006, 2007). This type of reconnection results in the closure of open magnetic flux. When the IMF B_z component is strongly northward but the IMF B_y component is not close to zero the IMF can drape around the magnetosphere such that reconnection occurs in one lobe only. This type of reconnection is called single lobe reconnection (e.g. Dungey, 1963; Russell, 1972; Reiff, 1985; Milan *et al.*, 2000). Since reconnection occurs on already open magnetic field lines, no new open flux is created. Instead the open flux within the polar cap is ‘stirred’.

1.3 The Ionosphere and Auroral Precipitation

1.3.1 The Ionosphere

Due to solar UV radiation, the upper part of the Earth’s atmosphere is partially ionized. This region is known as the ionosphere. The ionosphere can be broken down into several different regions illustrated in Figure 1.8. The lowermost region, between 50 and 90 km above the Earth’s surface, is known as the D region and is only present during the day. The E region exists between ~90 and 130 km and is more highly ionized than the D region. The uppermost region, the F region, extends from ~ 170 km to ~250 km and can be split into two separate region, F1 and F2 (Kivelson and Russell, 1995). The upper ionosphere is highly coupled to the magnetosphere and convects with

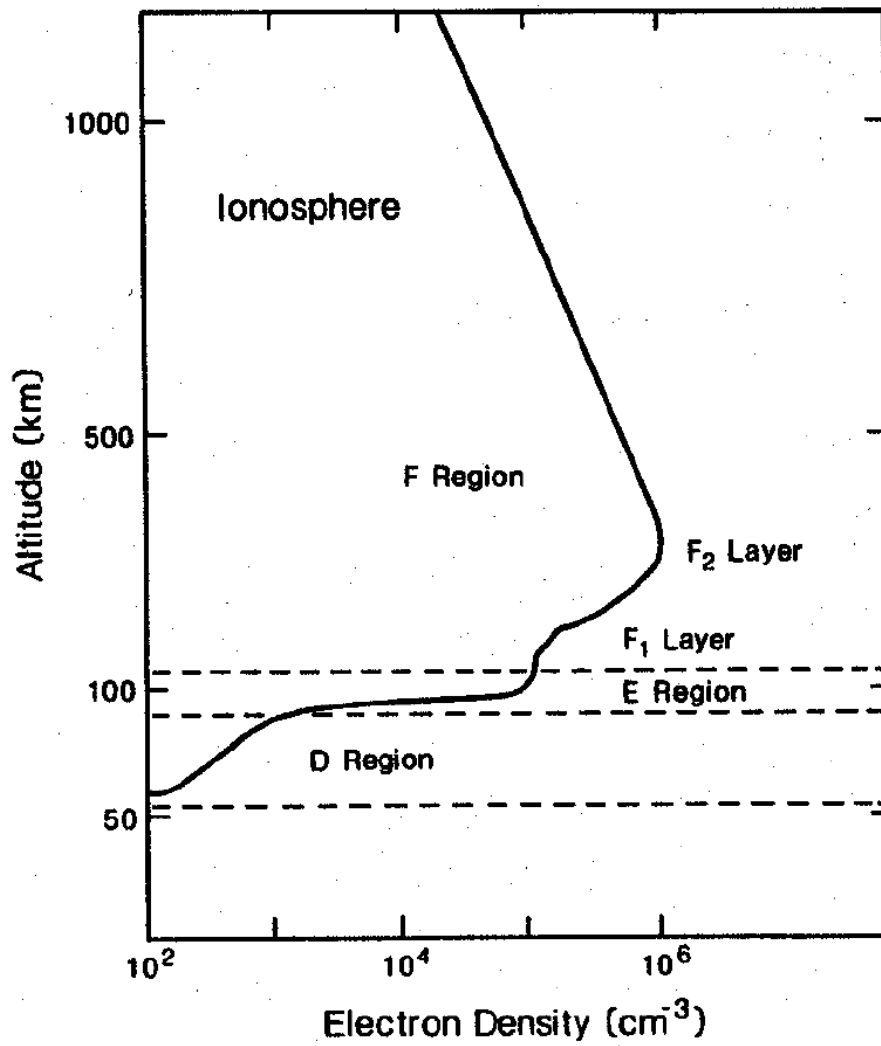


Figure 1.8: Regions of the ionosphere (from Kivelson and Russell, 1995).

the motion of magnetic fields (see below). The lower part of the ionosphere becomes decoupled from the magnetic field due to collisions with atmospheric particles and moves with the atmospheric winds, as well as co-rotating with the Earth.

1.3.2 Ionospheric Currents

Several currents flow within the ionosphere and have importance for the work carried out in this thesis. These currents are summarised below and for the northern polar cap in Figure 1.9.

When particles are frozen-in to magnetic field lines it can be shown that in the presence of an electric field the particles will move in the direction given by $\underline{E} \times \underline{B}$, where \underline{E} and \underline{B} are the electric and magnetic field vectors respectively (see Baumjohann and Trumann, 1997). However, particles in the atmosphere will also be affected by collisions with other atmospheric particles. The height at which collisions become important depends on the ratio between the collisional frequency and the gyro-frequency of the particles (the frequency at which the particles gyrate around the magnetic field, see Baumjohann and Trumann, 1997). Since ions have a smaller gyro-frequency than electrons, collisions become important for ions at higher altitudes (less dense regions) than for electrons. Collisions start to significantly effect the motion of ions at altitudes of ~150 km and at ~80 km for electrons. Thus between ~80 and 150 km electrons remain ‘frozen’ to the magnetic field and continue to move with the $\underline{E} \times \underline{B}$ drift (in the direction of the ionospheric convection pattern, Figure 1.6b) while $\underline{E} \times \underline{B}$ motion of ions is slowed such that below ~125 km protons move mostly in the direction of \underline{E} (shown in Figure 1.6b). The relative motions of the electrons and protons generate Hall currents, which flow in the opposite direction to the convection pattern, and Pederson currents (flowing in the direction of the electric field). Hall currents are illustrated by dashed lines in Figure 1.9a, and Pederson currents by the solid black lines. As illustrated in Figure 1.9a, Pederson currents diverge on the dawnward side of the auroral oval and converge on the duskward side. Field-aligned currents (FACs; or Birkeland currents) (e.g. Iijima and Potemra, 1978) form at the boundaries of the auroral oval to close the Pederson current system. The average morphology of FACs in the ionosphere is shown in Figure 1.9b. Region 1 FACs exist at the poleward edge of

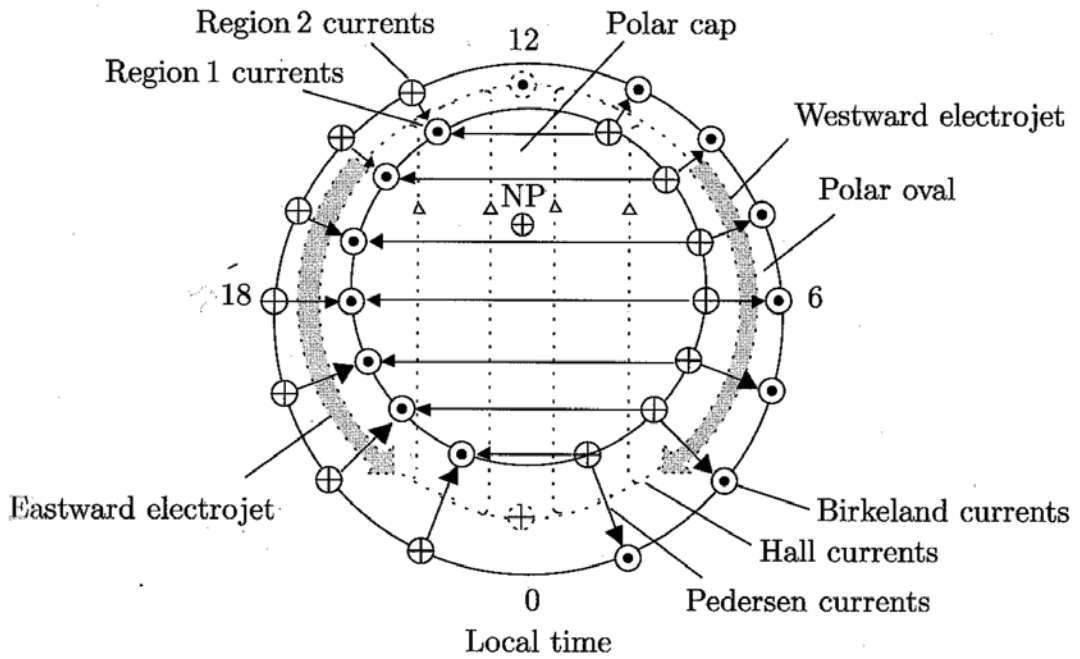


Figure 1.9a: Morphology of ionospheric currents (from Prölss, 2004).

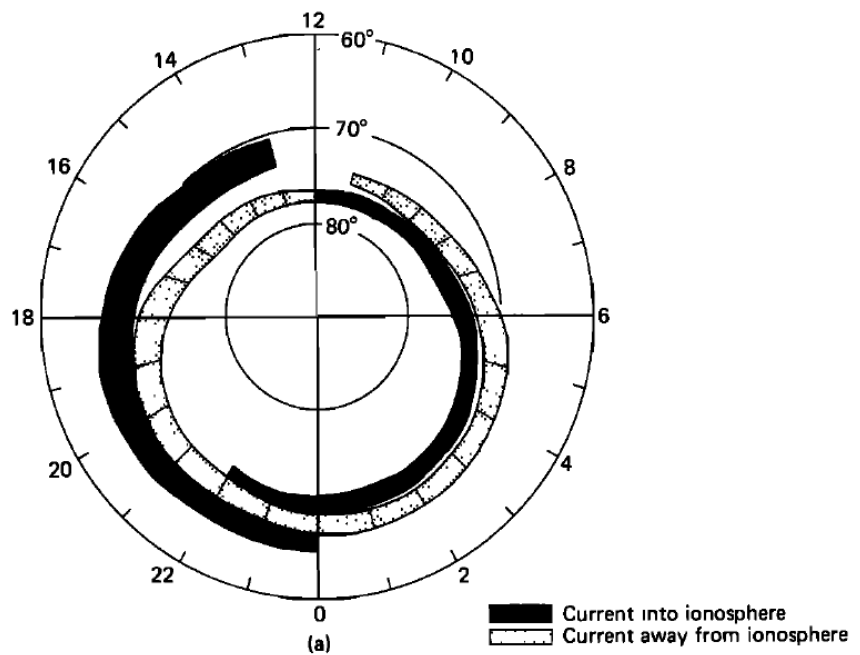


Figure 1.9b: Average morphology of field-aligned currents (from Iijima and Potemra, 1978). Region 1 currents are located at the poleward edge of the auroral oval and are directed into the ionosphere in the dawnward sector and out of the ionosphere in the duskward sector. Region 2 currents are located at the equatorward edge of the auroral oval and are oppositely directed to region 1 currents.

the auroral oval and are directed out of the ionosphere in the duskward sector (18-22 magnetic local time) and into the ionosphere in the dawnward sector (02-06 magnetic local time). Region 2 FACs are located at the equatorward edge of the auroral oval and are oppositely directed to the region 1 currents. The average morphology extends round to the dayside, however, it has been shown that the location at which the FACs switch from down-going to up-going, and vice-versa, varies over a large MLT range depending on the orientation of the IMF B_y component (Weimer, 2001). Region 1 currents are closed on the magnetopause and region 2 currents in the ring current.

Precipitating particles cause significant ionisation in the auroral oval such that the conductivity is much higher than in the polar cap. The Hall currents flowing in the auroral oval are thus much stronger than those within the polar cap and are known as the eastward and westward electrojets (Figure 1.9a) or the auroral electrojets. These currents produce the largest ground magnetic disturbances of all the current systems (Baumjohann and Treumann, 1997).

1.3.3 Auroral Generation

Several processes are involved in the generation of the aurora. For precipitating protons the main mechanism is via charge exchange. The precipitating protons gain an electron via collisions with atmospheric neutrals, becoming an excited H atom which subsequently decays to its ground state emitting Lyman-alpha radiation (see section 3.1.2). The energetic H atom can undergo many subsequent collisions, gaining and losing its electron many times. The auroral Lyman-alpha emission (~121.6 nm) can be distinguished from other Lyman-alpha emission as it is Doppler shifted due to the downward motion of the emitting H atoms.

The electron aurora is produced in a variety of ways by the interaction of the precipitating electrons and atmospheric neutrals. This includes elastic collisions, collisional ionisation (the removal of an electron from an atmospheric particle), collisional dissociation (splitting of a molecule into ions via an electron collision) and collisional excitation (where an incident electron collides with a neutral atom giving it energy which is subsequently released via the emission of a photon) (Prölss, 2004).

1.3.4 The Dayside Auroral Precipitation

There are several source regions of the precipitating particles which create the dayside auroral emission. In-situ particle precipitation measurements from low-latitude spacecraft have been used to characterise the precipitation from these different regions (e.g. Newell *et al.* 1991a), which have been mapped to the ionosphere by Newell and Meng (1992) and is illustrated in Figure 1.10a. The most equatorward precipitation region is a region of high-energy (several keV electrons and tens of keV ions) plasma thought to originate from the dayside extensions of the BPS and CPS (see above). BPS precipitation differs from CPS precipitation in that fewer high-energy ions and more low-energy electrons are present. The BPS precipitation also tends to have more spatial and spectral structure than the CPS (Newell *et al.*, 1991b). Poleward of this is a region of precipitation thought to originate from the LLBL. This region is very difficult to distinguish from cusp precipitation (see below), particularly in electrons, but in general consists of a less dense but thermalized ion population. Poleward of the LLBL is the cusp precipitation region characterised by very high fluxes of < 1 keV electrons and < 10 keV ions. As discussed previously, the cusp and LLBL regions are where the shocked solar wind of the magnetosheath can gain direct entry to the magnetosphere, and the precipitation from these regions is thus of magnetosheath origin. Further poleward is a region of low energy (less than a few eV), low density precipitating ions thought to originate from the mantle region. At very high latitudes a region of polar rain precipitation may be present. This consists of a homogeneous population of very low energy (less than a few hundred eV) electrons, travelling on open magnetic field lines and thought to originate from the solar corona (Fairfield and Scudder *et al.*, 1985). Polar rain is intense poleward of the main dayside auroral oval, gradually declining in intensity as it moves towards the nightside (Newell *et al.*, 1996).

1.3.5 Nightside Auroral Precipitation

On the nightside the auroral precipitation can be classified into two distinct regions, the diffuse auroral precipitation and the discrete auroral precipitation. The average locations of the diffuse and discrete aurora are shown in Figure 1.10b. The equatorward part of the auroral oval is made up of diffuse auroral emission. The diffuse auroral emission is thought to be the result of the relatively steady precipitation of particles from the CPS

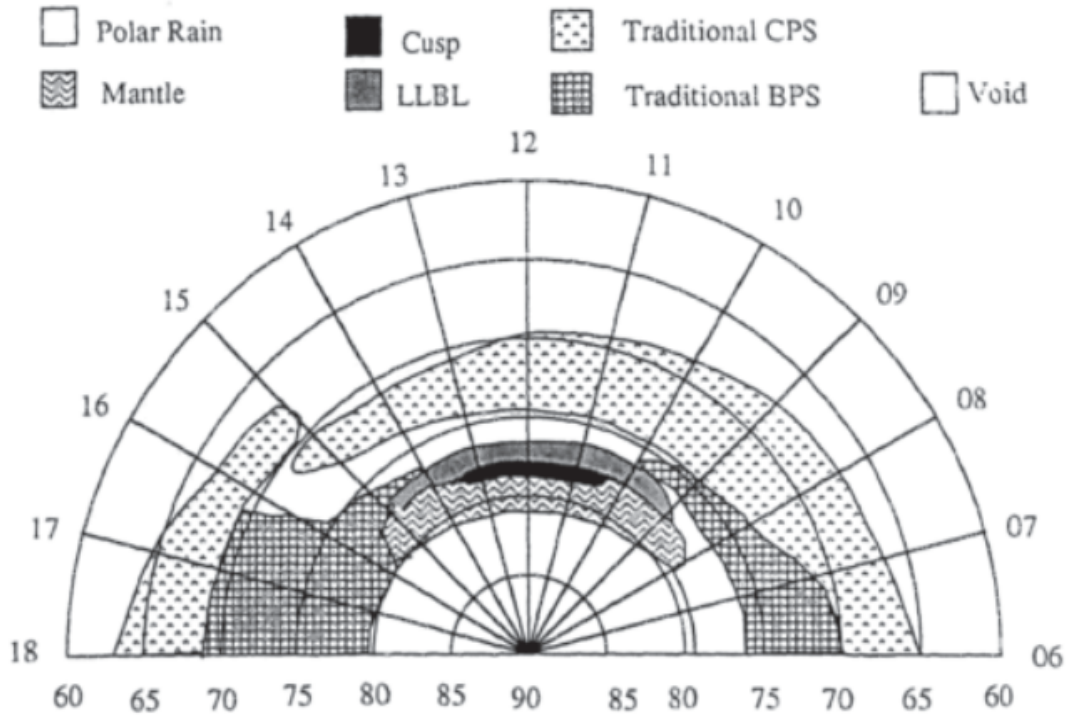


Figure 1.10a: Average locations of the dayside auroral oval precipitation regions (from Newell and Meng, 1992). Radial lines represent hours of MLT and concentric circles MLAT.

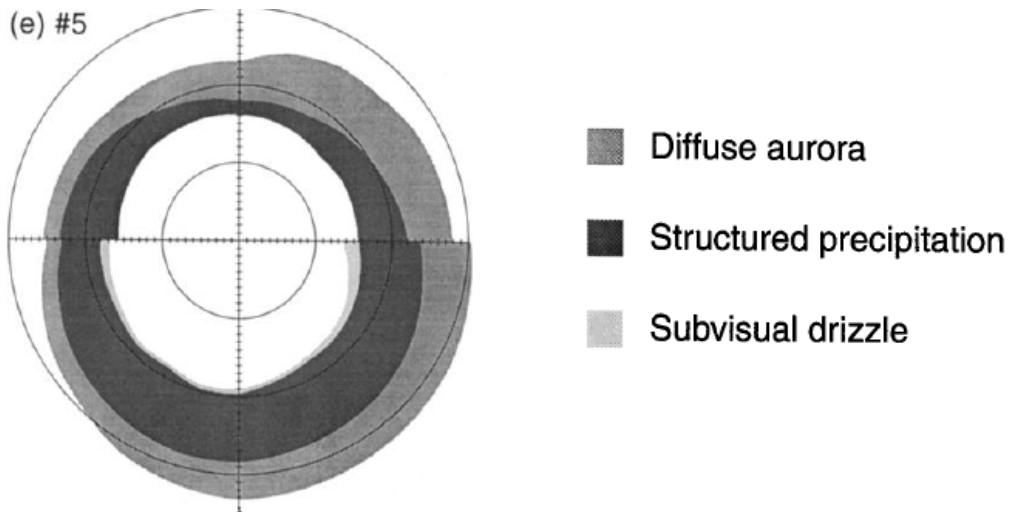


Figure 1.10b: Average location of the diffuse, discrete and sub-visual regions derived from in-situ measurements of precipitating electrons for high activity times (from Sotirelis and Newell, 2000). Concentric circles are drawn at 60°, 70° and 80° MLAT in AACGM.

(Newell *et al.*, 1996). The equatorward edge of the diffuse aurora is thought to map to the inner edge of the plasma sheet or ion isotropy boundary (Mende *et al.*, 2003 and references therein). The energy range of precipitating particles tends to be fairly broad, between a few hundred eV to a few tens of keV.

While the diffuse aurora have a distinct lack of structure, the poleward region of nightside precipitation consists of long east-west bands of luminosity with very small north-south extensions (Kivelson and Russell, 1995). This discrete aurora is thought to originate from particles accelerated down field-aligned currents from the BPS. This precipitation is more energetic than the diffuse aurora, with energies typically in the range 1-10 keV (Newell *et al.*, 1996). At the poleward edge of the BPS precipitation is a region of weak ions and electron precipitation known as the sub-visual drizzle region. This precipitation tends to be more structured than polar rain and is of slightly higher energy. While polar rain is defined as a region of low energy electron precipitation, the sub-visual drizzle region also contains a higher flux low energy ion component. The intensity of the sub-visual drizzle region decreases poleward of the nightside auroral oval (Newell *et al.*, 1996).

1.4 Summary

In this chapter we have introduced the solar wind and IMF and set out the regions of the Earth's magnetosphere and ionosphere. The coupling between these regions has been introduced in terms of the Dungey cycle and the expanding-contracting nature of the polar cap.

The subject of this thesis is the magnetospheric substorm. The substorm process is a natural extension of the coupling processes in the solar wind-magnetosphere-ionosphere system which has been discussed in this chapter. The substorm is introduced to the reader in the following chapter. Firstly, a summary of the observational features of the three distinct phases of the substorm is given, before a more detailed review of the substorm research most relevant to the work in this thesis is carried out.

Chapter 2. Review of Relevant Substorm Research

In the first part of this chapter the subject the magnetospheric substorm is introduced. The three main phases of the substorm are introduced and their observational features discussed. A brief overview of other substorm-like magnetospheric activity is given as well as a summary of the two main onset models for substorm onset.

In the second part of this chapter a more detailed review of the previous work most relevant to the work carried out in this thesis is given. Firstly, a review of the methods used to identify the location of the open/closed magnetic field line boundary (OCB) in the ionosphere is given in section 2.3. Studies of the open magnetic flux content of the magnetosphere, solar wind and IMF conditions, auroral and geomagnetic activity and auroral boundary motions during the substorm cycle are summarised in section 2.4.

2.1 Introduction to Substorms

Based on observations of auroral arcs from a set of ground-based all-sky cameras, Akasofu (1964) was the first to produce a working model of auroral activity during substorms. In this model he defined two distinct phases of the substorm, the substorm expansion and recovery phases. Using a suite of ground-based magnetometers to show how geomagnetic activity slowly increased prior to the explosive onset of the substorm expansion phase (termed the substorm onset), McPherron (1970) introduced the concept of the substorm growth phase. These three main phases of the substorm are summarised below.

2.1.1 The Growth Phase

Figure 2.1 summarises some of the typical features seen during the growth phase of an isolated substorm event. The growth phase is usually defined as a period of 30-60 minutes of southward orientated IMF (negative B_z) prior to substorm onset (Lester and Murdin, 2001). Under southward IMF reconnection occurs at the dayside sub-solar point opening previously closed terrestrial magnetic field lines to the solar wind (see section 1.2.2 and 1.2.3). The newly opened field lines are then swept back over the

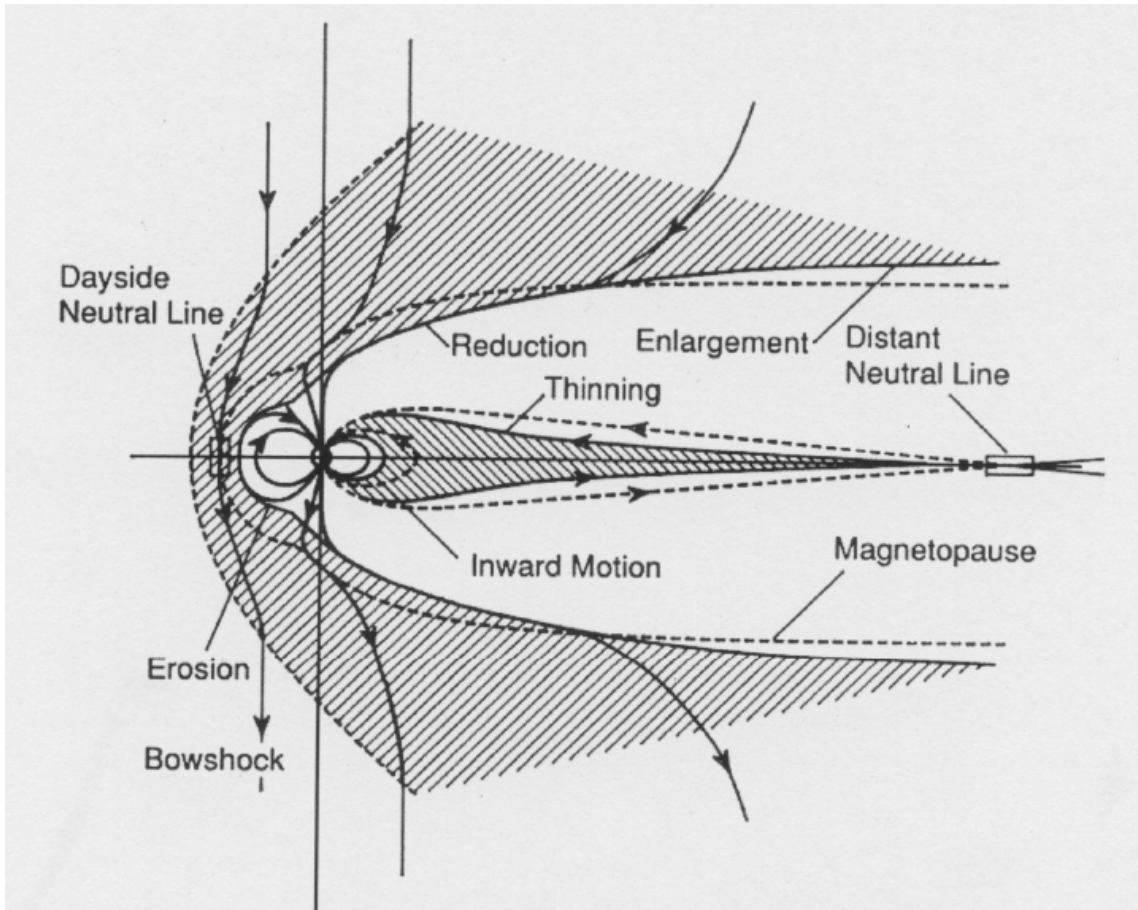


Figure 2.1: Typical features of the substorm growth phase (from Kivelson and Russell, 1995).

polar cap and into the magnetotail by the solar wind flow, leading to the accumulation of open magnetic flux in the tail. As the polar cap size increases the auroral oval moves to lower latitudes (see Figure 2.2, panels a-c). Convection of closed tail magnetic field lines to the dayside is not fast enough to replenish the flux opened on the dayside, leading to the erosion of the dayside magnetopause (Aubry *et al.*, 1970).

The addition of open magnetic flux to the tail lobes increases the flaring angle of the magnetotail such that the solar wind impinges upon the magnetopause at a less grazing angle and thus the total force impinged upon the tail by the solar wind is increased (e.g. Petrinec and Russell, 1996). This increased compressional force and increase in lobe magnetic flux, increases the magnetic field pressure within the lobes and hence the pressure exerted in turn on the plasma sheet. As a consequence, the plasma sheet thins (e.g. Asano *et al.*, 2004). As the plasma sheet thins, the inner edge of the plasma sheet moves earthwards and the cross-tail current increases. The increase in tail lobe flux also causes the lobe field to become less dipolar and more ‘tail-like’.

Enhanced convection of magnetic field lines in the ionosphere causes the enhancement of the auroral electrojets (section 1.3.2), observed as a gradual increase in magnetic activity in ground-based magnetometers (see below). The substorm growth phase is thought to be a necessary condition of the substorm process in which energy is extracted from the solar wind by dayside reconnection and stored in the magnetotail. This increase in energy and pressure in the tail cannot continue indefinitely and must be released. This release of energy is achieved during the substorm expansion phase.

2.1.2 The Expansion Phase and Onset Signatures

In the first model of the expansion phase (Akasofu, 1964) the substorm onset, and the start of the expansion phase, is defined as the time at which the most equatorward auroral arc observed by ground-based all-sky cameras shows a sudden and rapid increase in intensity. The global dynamics of the auroral oval during a substorm event, as viewed in the far ultraviolet (FUV), is shown in Figure 2.2 where local noon is to the top of each panel and local midnight to the bottom. During the growth phase, panels a-c, the auroral oval expands as more open magnetic flux is added to the polar cap; a pseudo-breakup (a short lived substorm-like auroral brightening or failed substorm; see

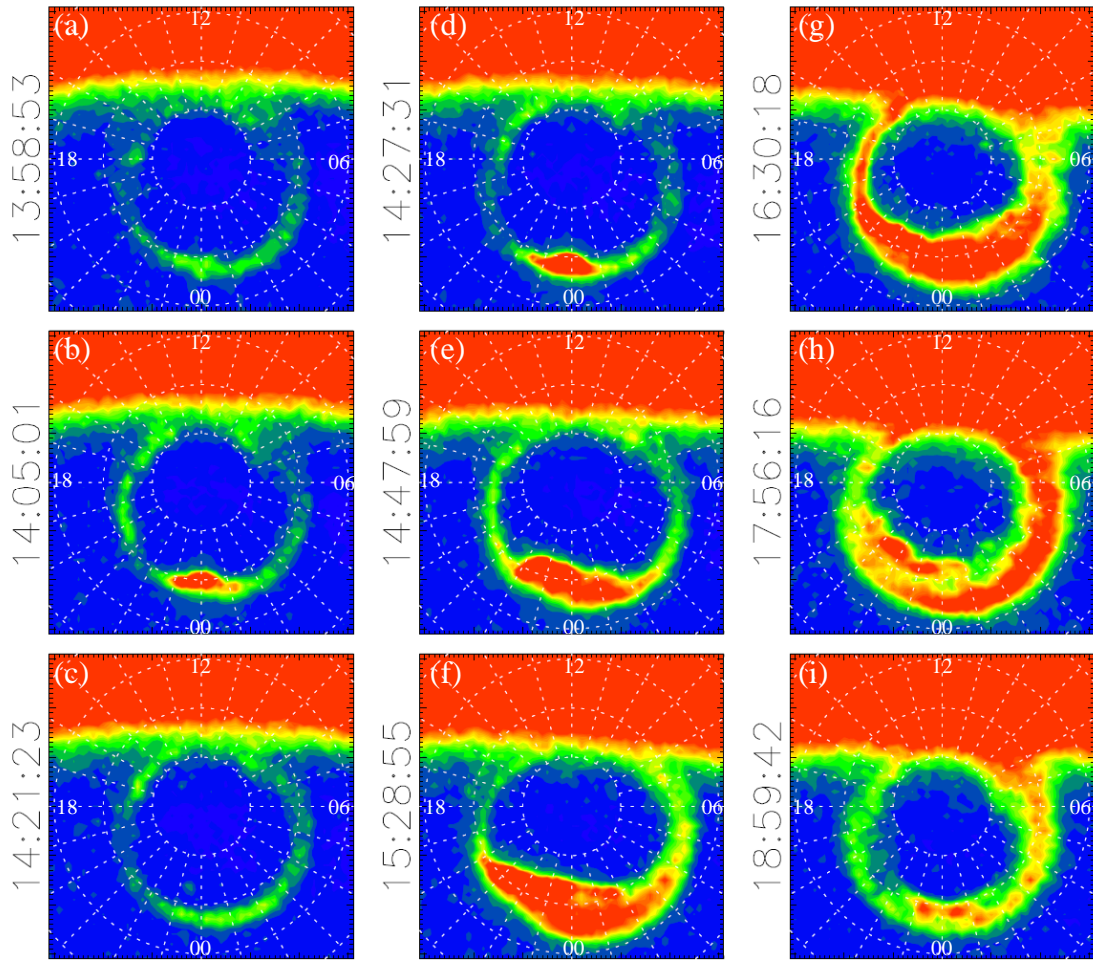


Figure 2.2: IMAGE WIC observations of the northern polar cap during an isolated substorm on the 10th of January 2001. Local noon (12 MLT) is to the top of each panel and local midnight (00 MLT) to the bottom. The bright emission seen at the top of each panel is due to dayglow. During the substorm growth phase, panels a-c, the auroral oval gradually moves to lower latitude, signifying an increase in the open magnetic flux content of the polar cap. Substorm onset is seen at 14:27:31, panel d. During the expansion phase of the substorm the nightside auroral brightening expands in all directions and the polar cap shrinks signifying a closure of open magnetic flux. During the recovery phase, panels h-i, auroral activity returns to quiet time levels and the polar cap begins to increase in size once more. A pseudo-breakup is seen at 14:05:01, panel b.

section 2.1.6) is seen in panel b. At substorm onset, panel d, a sudden brightening in the nightside auroral oval is seen. The brightening expands in all directions, causing a decrease in polar cap size, panels e-h, indicating a rapid closure of open magnetic flux (see also section 1.2.3).

The rapid auroral brightening is the visible manifestation of the onset of the expansion phase. Many phenomenological models have been proposed to explain the observational features of the substorm expansion phase. Currently, the two leading models both agree that the expansion phase begins with the onset of large-scale reconnection in the magnetotail at a newly formed near-Earth neutral line (NENL) and disruption of the near-Earth cross-tail current to form the substorm current wedge (SCW; see section 2.2.2 and Figure 2.3). Both models are discussed in more detail in section 2.2. As the expansion phase progresses, tail reconnection closes large amounts of the previously opened magnetic flux, decreasing the size of the polar cap and dipolarising the tail magnetic field (see section 2.2.1 and Figure 2.4). Energetic electrons and protons are accelerated down these newly closed magnetic field lines into the ionosphere, where their interaction with atmospheric neutral atoms causes the bright auroral displays seen (see section 1.3.3). Observational results place the initial reconnection site and auroral brightening between 20:00 and 02:00 MLT and 55-75° MLAT (e.g. Kamide and Winningham, 1977; Craven and Frank 1991; Gerard *et al.*, 2004).

Other signatures of substorm onset include the injection of energetic particles into near-Earth orbit and large scale geomagnetic field variations as observed by ground-based magnetometers. These are discussed in more detail below.

The injection of energetic electrons and protons into geosynchronous orbit is one of the most common signatures of substorm onset and have been shown to be associated with almost all other substorm onset signatures (e.g. Arnoldy and Chan, 1969; Belian *et al.*, 1981; Yeoman *et al.*, 1994; Abel *et al.*, 2006). Enhancements of energetic electrons and protons are observed at the time of substorm onset by particle analyzers onboard spacecraft located near geosynchronous orbit ($\sim 6.6 R_E$). Injections above 25 keV are particularly dramatic (e.g. Walker *et al.*, 1976; Baker *et al.*, 1978; Belian *et al.*, 1978), though injections are also seen at lower energies (e.g. DeForest and McIlwain, 1971; Parks *et al.*, 1980). The injection region is usually found at pre-

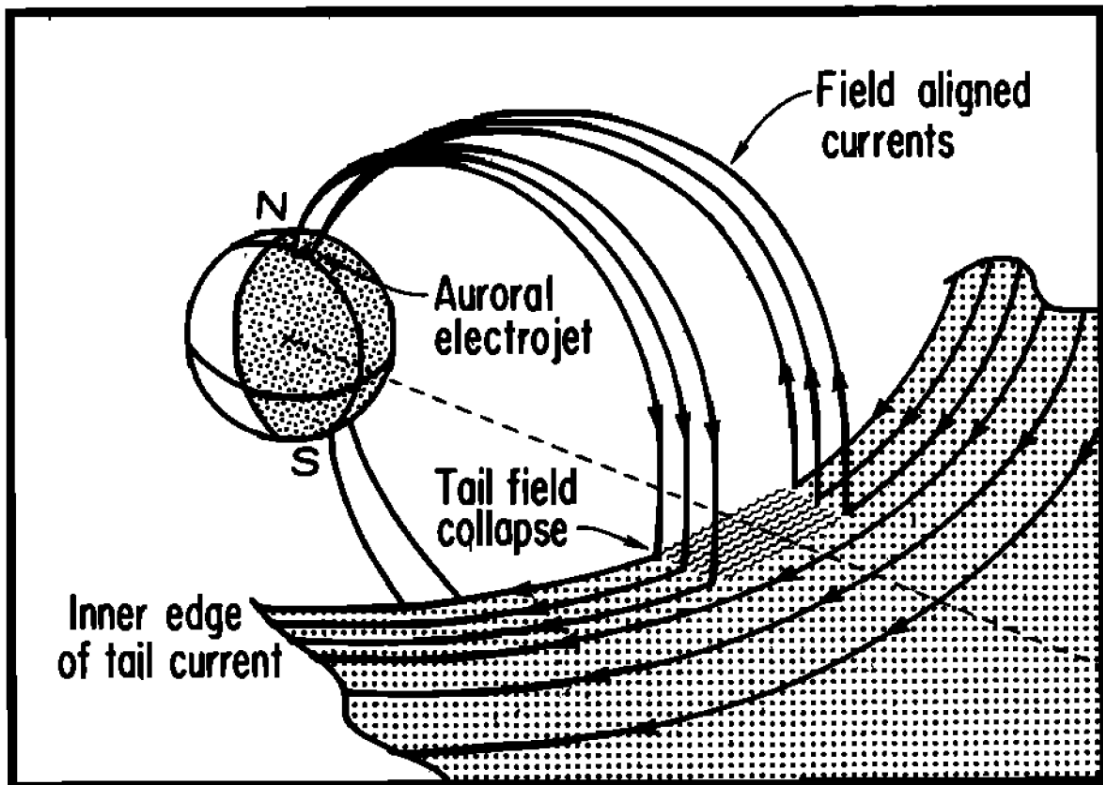


Figure 2.3: Schematic of the substorm current wedge and substorm auroral electrojet (from McPherron *et al.*, 1973).

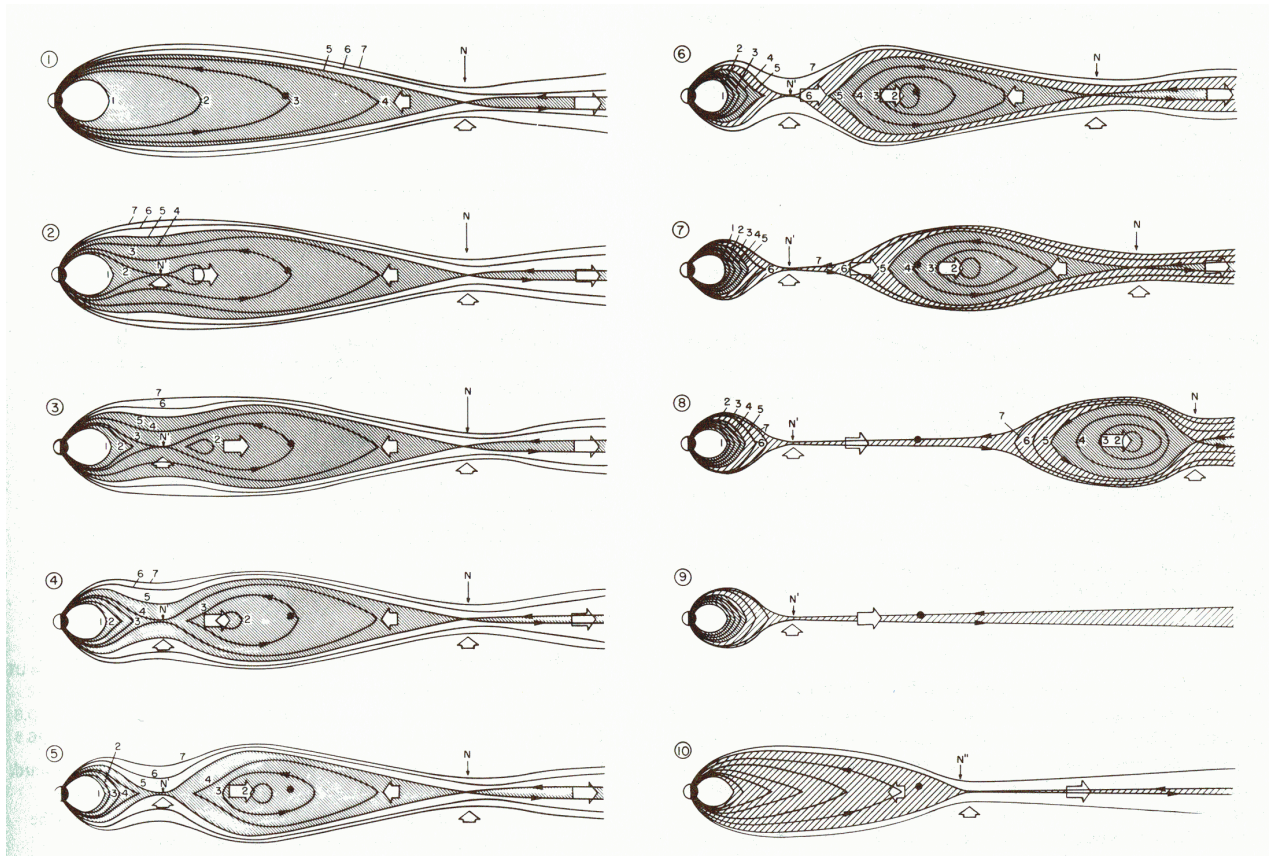


Figure 2.4: Schematic representation of magnetotail reconfiguration during the substorm cycle (from Hones, 1984). Magnetic field lines are represented by black lines, plasma flows by white arrows, the distant neutral line by N and the NENL by N'. The plasma sheet is represented by the shaded region. The substorm growth phase is shown in panel 1. Substorm expansion progresses through panels 2-9, with reconnection moving to open magnetic field lines between panels 5 and 6. The recovery phase progresses through panels 9-10.

midnight MLTs (e.g. Lopez *et al.*, 1990), near the MLT of the initial substorm auroral brightening, and confined by the SCW (e.g. Vagina *et al.*, 1995). An average delay of 1.8-2.5 minutes has been observed between injection and the initial onset of auroral activity (Liou *et al.*, 2001a). Various models and theories have been proposed to explain the simultaneous enhancement of particles of all energies (e.g. McIlwain, 1974; Kivelson *et al.*, 1980; Moore *et al.*, 1981; Mauk and Meng, 1983; Birn *et al.*, 1997; Sergeev *et al.*, 1998; Sarris *et al.*, 2002; Sarris and Li, 2005; Liu *et al.*, 2009) but the mechanism is still not well understood. See also section 5.1.3.

As discussed in section 3.6 of this thesis, the AL and AU indices provide a measure of the strength of the westward and eastward auroral electrojets. Figure 2.5 shows the typical variation of the AL and AU indices through the three phases of an isolated substorm event. During the growth phase of the substorm enhanced convection leads to the enhancement of both the eastward and westward auroral electrojets and a slow increase in the magnitude of AL and AU is seen (1-2, Figure 2.5). At onset (point 2) the cross-tail current is diverted through the SCW (Figure 2.3) and is closed in the ionosphere by the substorm electrojet. This westward travelling current expands as the SCW expands, impinging on the poleward edge of the oppositely directed eastward convection electrojet. The expansion of the substorm electrojet thus acts to increase the magnitude of the AL index and decrease the magnitude of AU during the expansion phase of the substorm (points 2-3, Figure 2.5). Eventually a peak is reached in the AL index and the indices begin to return to quiet time levels as the substorm electrojet fades during the recovery phase (point 3 onwards).

2.1.3 The Recovery Phase

The start of the recovery phase is marked by the halt of the poleward motion of the auroral oval and, if dayside reconnection is ongoing, subsequent retreat to lower latitudes (panels h-i, Figure 2.2). The auroral intensity fades during the recovery phase and auroral dynamics return to quiet time levels. These ionospheric signatures of the recovery phase are the result of the decline of reconnection in the magnetotail at the NENL and the decay of the SCW.

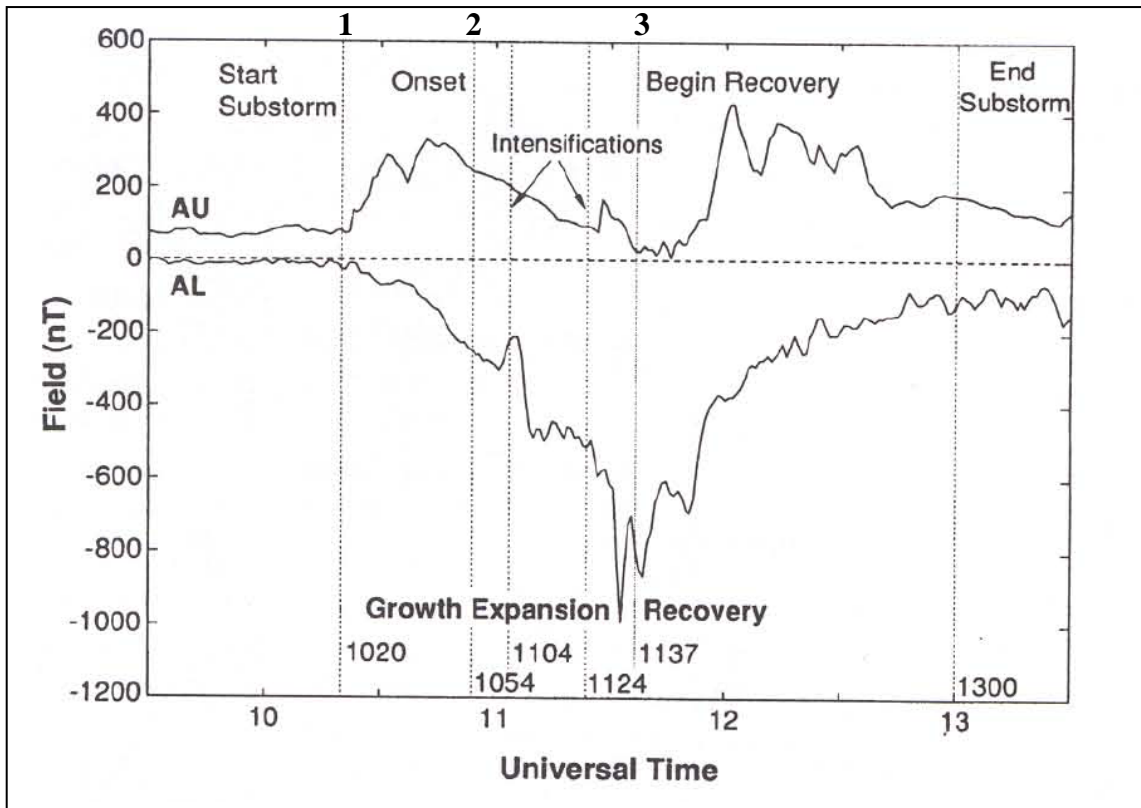


Figure 2.5: Typical features of the substorm process in the AL and AU geomagnetic indices (from Kivelson and Russell, 1995). The AL and AU indices provide a measure of the westward and eastward electrojets respectively. During the substorm growth phase convection increases causing an enhancement of both eastward and westward currents. At substorm onset, the formation of the SCW and westward substorm electrojet enhances the westward current, seen as large negative excursion in AL, and decreases the eastward current (AU). During recovery phase the substorm electrojet decays and the indices return to background levels. Intensifications may be caused by pseudo-breakups.

2.1.4 Sawtooth Events

Sawtooth events are essentially periodic substorms identified by the quasi-periodic enhancement of energetic electron and proton fluxes at near-Earth orbit (Belian *et al.*, 1995; Henderson, 2004; Henderson *et al.*, 2006). Figure 2.6 shows a typical sawtooth period in both energetic electrons (panel a) and protons (panel b) as seen by particle analyzers onboard the LANL spacecraft. Periodic dispersionless injections are seen in both electrons and protons within the injection region. The wave-like pattern of proton injections, similar to the teeth on a saw, gives these events their name. A typical event consists of 3-8 individual teeth which occur quasi-periodically approximately every 2-4 hours. Typically they occur during geomagnetic storms when the solar wind driving is strong and steady (e.g. Pulkkinen *et al.*, 2007). They occur with moderate solar wind density, velocity and dynamic pressure and with steady and strongly southward IMF (e.g. DeJong *et al.*, 2007; Huang *et al.*, 2009b). The tail magnetic field variation during a sawtooth event characteristically shows periodic stretching and relaxation at the periodicity of the teeth (e.g. Pulkkinen *et al.*, 2006). The continued injection of energetic particles into near-Earth orbit leads to the enhancement of the ring current (McPherron *et al.*, 2008). Magnetic field variations suggest that substorm activity during sawtooth events occurs over a larger spread in magnetic local time than for isolated events (Clauer *et al.*, 2006).

2.1.5 Steady Magnetospheric Convection

An SMC event is defined as an extended period of time (>90 minutes and as long as 10 hours) in which the aurora are active as compared to quiet time levels but with an absence of substorm-like activity (e.g. Pytte *et al.*, 1978; Sergeev 1977). SMC events occur during periods of steady solar wind driving, moderate, steady and southward IMF conditions, typically slow solar wind speeds ($<400 \text{ km s}^{-1}$) and should have a fixed polar cap area and steady location of particle precipitation boundaries (e.g. McPherron *et al.*, 2005, 2008; Sergeev *et al.*, 1996; O'Brian *et al.*, 2002). SMCs have been associated with a double auroral oval configuration in which the nightside auroral oval consists of two bright regions separated by a dark band (e.g. Elphinstone *et al.*, 1995; Pulkkinen *et al.*, 1995). SMC events have very similar characteristics to the recovery phase of substorms. A time period which displays the above characteristics is therefore defined

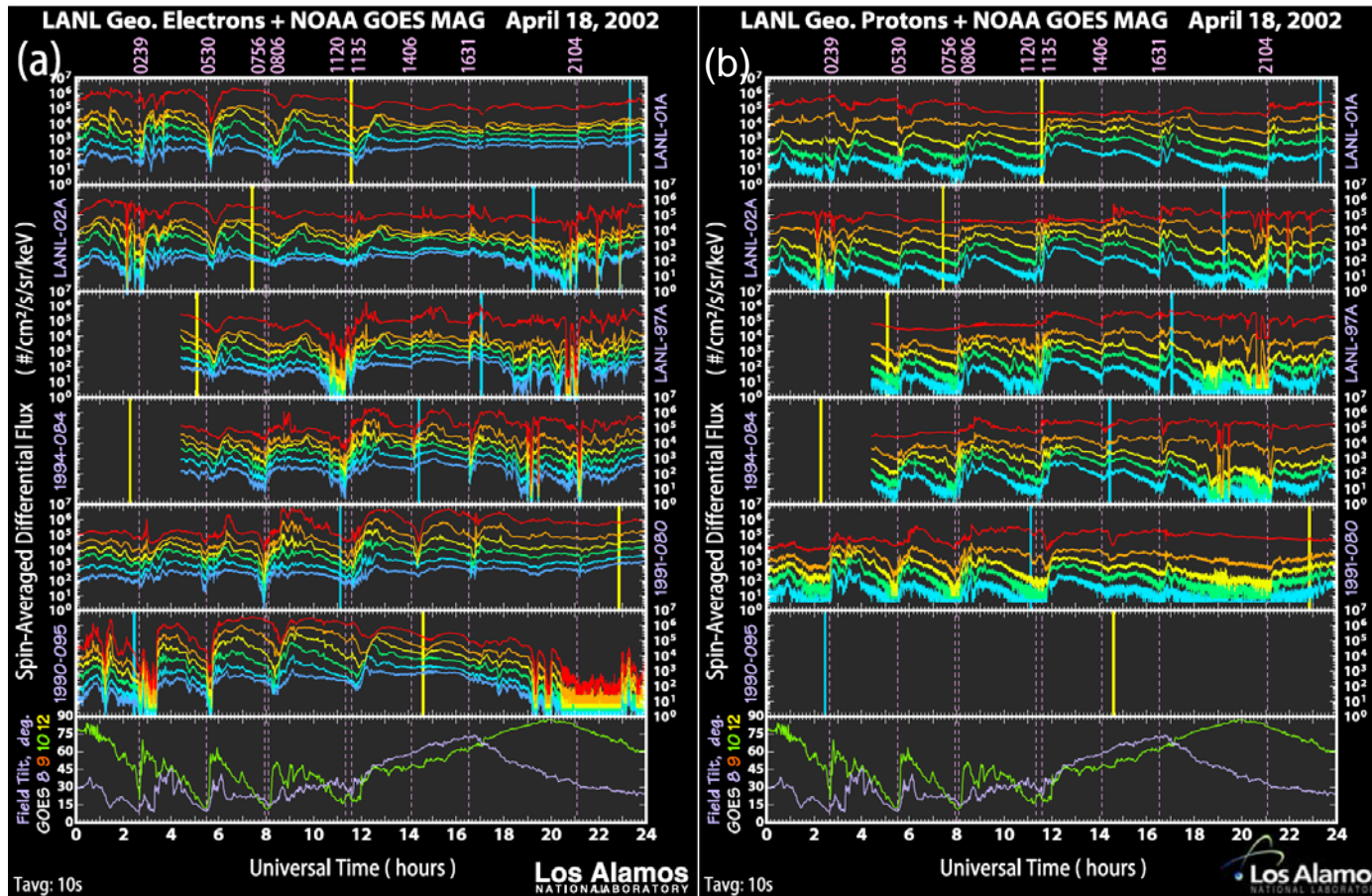


Figure 2.6: Energetic electron (left hand) and proton (right hand) observations from seven of the LANL spacecraft are shown for a typical sawtooth period on the 18th of April 2002 (from Henderson *et al.*, 2006). Vertical yellow and blue lines show the time at which the spacecraft are located at local noon and midnight respectively.

as an SMC if the period lasts longer than the typical length of the substorm recovery phase, approximately 90 minutes. SMC events often occur after the onset of an isolated substorm event (e.g. McPherron *et al.*, 2005), suggesting that substorms play an important role in preconditioning the magnetosphere for SMC events. The steady size of the polar cap during SMC events suggests that dayside and nightside reconnection rates must be in balance. For more information on SMCs see McPherron *et al.* (2008) and references therein.

2.1.6 Pseudo-Breakup

Akasofu (1964) noted that on occasion an auroral arc would intensify, as if marking the start of substorm onset, but a global expansion of the intensification would not occur with auroral activity fading back to quiet time levels after only a few minutes. These events were termed pseudo-breakups. Pseudo-breakups show many of the signatures of substorm onset, including an brightening of the most equatorward auroral arc, Pi2 pulsations (irregular magnetic fluctuations caused by the rapid depolarization of the tail magnetic field, see Olson (1999) and Liou *et al.* (2000) and references therein), enhancement of the westward auroral electrojet, formation of a SCW, field depolarization and energetic particle injection to geosynchronous orbit (see McPherron *et al.*, 2008 and references therein). It is often hard to distinguish between small substorms and pseudo-breakups. The defining feature of pseudo-breakup is the lack of global expansion and very localised nature, weak onset signatures and short duration (<10 minutes). Pseudo-breakups are often described as failed substorms in which reconnection is initiated in the plasma sheet but either does not progress to the open field lines in the lobes or halts for some other reason (McPherron *et al.*, 2008). An example of a pseudo-breakup, as seen by a global auroral imager, is seen in panel b of Figure 2.2.

2.1.7 Poleward Boundary Intensifications

Poleward Boundary Intensifications (PBIs) are transient intensifications of the nightside auroral oval which occur near the poleward edge of the auroral oval. PBIs have been shown to occur with a periodicity of approximately 10 minutes under all geomagnetic conditions (Lyons *et al.*, 1998), but most often occur in the recovery phases of substorm

events (Zesta *et al.*, 2002). The brightening starts at the poleward edge of the auroral oval and may or may not move equatorward and in local time. Zesta *et al.* (2002) suggested that PBIs are caused by localised reconnection occurring at a distant neutral line.

2.2 Onset Models

2.2.1 The Near-Earth Neutral Line Model

In the NENL model (McPherron *et al.*, 1973; Baker *et al.*, 1996) the substorm expansion phase is initiated by the spontaneous start of reconnection in the near-Earth plasma sheet. Figure 2.4 shows a detailed schematic of the evolution of the magnetotail during the substorm process as described by the NENL model (Hones, 1984). During the growth phase of the substorm (panel 1) more open magnetic flux is added to the magnetotail through reconnection at the dayside magnetopause than is closed at the distant neutral line in the tail, leading to the accumulation of open magnetic flux in the tail. This leads to an increase in pressure in the magnetospheric lobes which must be balanced by the plasma sheet and hence results in a thinning of the plasma sheet. The plasma sheet cannot thin indefinitely and once the increase in plasma sheet pressure can no longer be sustained reconnection is initiated at a new NENL within the closed magnetic field line region of the plasma sheet (panel 2). As reconnection continues to eat through the closed magnetic field lines of the plasma sheet, panels 3-4, plasma is fed into the NENL in the vertical direction and ejected on newly formed closed magnetic flux loops both earthward and tailward. Earthward moving field lines having both footprints connected to the surface of the Earth and tailward moving field lines having both footprints connected to the solar corona. Once reconnection reaches the last plasma sheet field line, panel 5, the closed loops of plasma tailward of the neutral line are pinched off from the earthward plasma sheet, forming a plasmoid of hot energetic plasma wrapped in the open magnetic flux of the tail lobes (panel 6). The plasmoid is subsequently dragged downtail by the magnetic tension of the field lines (see section 1.2.2), panels 6-8, leaving a thin plasma sheet in its wake, panel 9. Meanwhile, reconnection at the NENL continues onto the open magnetic field lines of the lobes, creating new closed magnetic flux tubes which will eventually convect back round to

the dayside completing the Dungey cycle (panels 6-9). During the recovery phase of the substorm the NENL retreats to its distant location and the reconnection rate decreases.

In the NENL model, both the injection of energetic particles into near-Earth orbit and the disruption of the cross-tail current and formation of the SCW are caused by the formation of the NENL. Observations made by spacecraft in the magnetotail of the earthward and tailward plasma flows resulting from the NENL place the initial location of the NENL between 20-30 R_E (e.g. Nagai *et al.*, 1998). Other papers suggest that the location is closer to 18 R_E (e.g. Slavin *et al.*, 2005).

2.2.2 The Current Disruption Model

In the current disruption model of substorm onset, current disruption is not a consequence of the formation of the NENL, but rather the cause. In the current disruption onset model (Chao *et al.*, 1977; Lui, 1991, 1996) the growth phase develops as described in section 2.2.1, thinning the plasma sheet and resulting in an increase in the cross-tail current. Eventually the plasma sheet reaches a thickness comparable to the gyroradius of ions, causing ions to become demagnetised from the magnetic field and non-adiabatic in nature. The interaction between the ions and adiabatic electrons flowing in the opposite direction cause plasma instabilities in the near-Earth plasma sheet at approximately 10 R_E . These instabilities prevent the cross-tail current from flowing, forcing its redirection down new field-aligned currents forming the SCW (Figure 2.3). These field aligned-currents are closed by a westward travelling current in the ionosphere called the substorm electrojet. In the current disruption model particle injection and depolarization of the near-Earth magnetic field is thought to be due to these instabilities rather than reconnection at the NENL, as postulated in the NENL model. The current disruption process and instabilities produce a rarefaction wave which propagates downtail, causing the plasma sheet to thin behind it, eventually initiating reconnection and the formation of the NENL further downtail.

2.2.3 A Critical Threshold for Substorm Onset and Solar Wind Triggering

Although the tail instabilities described in the NENL and current disruption models are able to explain the observational features of the substorm expansion phase, what triggers these instabilities is still a matter of much debate. While most models agree that the growth phase of the substorm is required to precondition the magnetosphere such that onset can occur, scientists hold differing views as to whether an internal threshold to the magnetosphere (e.g. in open magnetic flux) is a sufficient condition to initiate substorm onset or whether a solar wind trigger is also required. Arguments for both cases are given below.

Kamide *et al.* (1977) studied the dependence of substorm occurrence frequency on the latitude of the equatorward boundary of the nightside auroral oval, which is at best indirectly related to the open magnetic flux (e.g. Coumans *et al.*, 2007). They showed there to be a maximum oval latitude above which substorm onset never occurs and corresponding minimum latitude above which the cumulative probability of onset is 100%, implying a minimum and maximum critical threshold in open magnetic flux for substorm onset.

Recent statistical studies have lent support for the view that a critical threshold in open magnetic flux as a necessary condition for substorm onset. Freeman and Morley (2004) showed that the average occurrence frequency of substorm onset could be replicated using a simple integrate-and-fire model of onset, assuming onset occurs once some critical threshold has been reached in the magnetosphere. Nakai and Kamide (2004) estimated the total pressure in the magnetotail lobes, showing that substorm onsets occur above the upper quartile of the pressure distribution. Shukhtina *et al.* (2005) showed that the magnetic flux stored in the tail lobes at onset was on average ~ 1 GWb, exceeding the typical values during quiet times and SMCs by 50%. Milan *et al.* (2007) quantified the hemispheric open magnetic flux content of the magnetosphere from a total period of 72 hours of observations of the northern polar cap. They found that the open magnetic flux varied between 0.3 and 0.9 GWb, with the occurrence of nightside reconnection events rapidly increasing above ~ 0.5 GWb, suggesting that above 0.5 GWb some critical threshold has been exceeded. A more extensive review of the open

magnetic flux content of the magnetosphere through the substorm process is provided in section 2.4.

These studies have suggested that a critical threshold in open magnetic flux exists as a necessary condition for substorm onset. However, they also show that substorm onsets can occur over a wide range of open flux values, suggesting that any critical threshold is variable. Nakai and Kamide (2004) found that the magnetotail pressure was correlated with the Dst index, and Shukhtina *et al.* (2005) showed that the total magnetic flux in the tail at onset was strongly correlated with the dayside reconnection electric field averaged over the one hour prior to onset. These results suggest that any critical threshold is dependent on the dayside reconnection rate or level of solar wind driving, (which in turn determines the Dst index (Burton *et al.*, 1975)). Other studies have reported the positive correlation between open magnetic flux at onset and the level of solar wind driving, whilst Milan *et al.* (2008, 2009a,b) have shown that the level of open magnetic flux in the magnetosphere remains elevated when the ring current is enhanced, suggested that the ring current stabilises the magnetosphere to tail reconnection, causing the threshold in open magnetic flux to increase.

While the studies above suggest that a critical threshold which is internal to the magnetosphere must be exceeded for substorm onset, other studies have suggested that a trigger in the solar wind is required. For example, the association between interplanetary shocks or solar wind dynamic pressure changes and substorm events has long been studied (e.g. Kawasaki *et al.*, 1971; Burch, 1972; Zhou and Tsunitani, 2001). However, recent statistical studies have shown that only a small percentage (~ 2%) of substorms are associated with solar wind shocks or pressure changes (McPherron *et al.*, 1986). Other studies have found a much larger correlation between a northward turning of the B_z component of the IMF and substorm onset, some studies requiring a period (~30 minutes) of southward IMF (growth phase) prior to substorm onset in addition to a northward turning to classify a substorm as triggered. Caan *et al.* (1975) showed that the onset of mid-latitude positive bays could be associated with northward turnings. Hirshberg and Holzer (1975) noted that in a superposed epoch analysis carried out by Foster *et al.* (1971) the B_z component of the IMF reached a minimum at the onset time of substorms, suggesting triggering. Caan *et al.* (1977) subsequently found that 60% of a study of 18 substorms identified by auroral zone magnetometers could be associated

with a northward turning of IMF B_z . Rostoker (1983), Sergeev *et al.* (1986) and Samson and Yeung (1986) also suggested an association between northward turnings and substorm onset. McPherron *et al.* (1986) studied a six-month interval finding that approximately 44% of all substorms occurring in this period could be associated with a northward turning. Troshichev *et al.* (1986) suggested that the IMF B_y component could also trigger onset events (see also Bae *et al.*, 2001). Lyons *et al.* (1995) suggested that most if not all substorms are triggered by changes in the solar wind and that previous studies had either missed solar wind triggers due to the resolution of solar wind data or the location of the IMF monitor, or that non-triggered substorms were not really substorms. However, Henderson *et al.* (1996) then showed that, although 3 events which had previously been classified as non-triggered events could be associated with a solar wind trigger if better resolution data were used, 6 events clearly occurred during very quiet solar wind conditions. Hsu and McPherron (2003) went on to show that the location of the solar wind monitor does not significantly effect the statistics of triggered and non-triggered events seen and Hsu and McPherron (2009) used high resolution solar wind data to show that small-scale structures in the solar wind cannot account for the 40% of non-triggered events found in the statistical study of Hsu and McPherron (2003).

Lyons *et al.* (1997) studied 20 substorm events finding that 14 could be associated with either a northward turning or B_y trigger. They also estimated that the probability of a chance association between triggers and substorms to be less than 10^{-9} . Hsu and McPherron (2002) studied 145 substorms events and showed that the observed association with northward turning could not be reproduced by a chance association. Hsu and McPherron (2003) found, from a study of some 200 onset events, a ratio of approximately 60:40 between triggered and non-triggered events. They also found that the addition of IMF B_y triggers to the study did not increase this ratio significantly. Liou (2007) have also suggested that a decrease in solar wind dynamic pressure can be associated with substorm onset.

Taking a different tack, Lee *et al.* (2007) considered why some changes in the solar wind which have been shown to be associated with substorm onset do not always trigger onset. They argue that a solar wind trigger will not trigger onset if either: (1) the magnetosphere has not been sufficiently preconditioned by a significant growth phase,

(2) the solar wind trigger is inherently not a substorm trigger or (3) there is a nullifying effect in which two solar wind changes can cancel each other out. Lyons *et al.* (1995) suggested that any change in the solar wind which causes a decrease in the convection strength in the inner plasma sheet will initiate onset. Lee *et al.* (2007) suggested that the solar wind changes not associated with onset in their study are consistent with this idea. Non-triggering changes either acting to increase the convection, or two changes occurring simultaneously, one acting to increase convection, the other to decrease convection, thus cancelling each other out. Russell (2000) suggested a different mechanism by which northward turnings of the IMF could trigger substorm onset. In his model, reconnection on open magnetic field lines at a distant neutral line feeds reconnection on closed magnetic field lines at a NENL. At a northward turning of the IMF reconnection halts at the distant neutral line and stops feeding the NENL with closed flux. Reconnection at the NENL thus moves onto low density open magnetic field lines, where reconnection can occur much faster. When reconnection moves to open magnetic field lines the substorm expansion phase begins.

The studies discussed above clearly show an association between solar wind changes and substorms onset, but whether solar wind triggers are a real substorm phenomena is still a matter of debate. A recent study by Wild *et al.* (2009) found that, while less than 25% of a study 260 substorm events could be associated with a northward turning trigger (which are only considered as a trigger if preceded by a period of southward IMF, a substorm growth phase criterion), most events could be associated with the growth phase criterion used in the definition of a northward turning. Most authors now agree that a substorm growth phase, a common criterion for both triggered and non-triggered events, is a necessary condition of substorms onset. Many examples of substorms occurring independently of any changes in the solar wind suggest that an entirely internal instability (such as in open magnetic flux) is a sufficient condition for onset and that no solar wind trigger is required (see also Morley *et al.*, 2007).

2.3 Identifying the Location of the Open/Closed Magnetic Field Line Boundary in the Ionosphere

As mentioned above, many studies have suggested that a critical threshold in the open magnetic flux content of the magnetosphere exists as a necessary condition for substorm onset. One of the main aims of this thesis is to investigate this claim by carrying out a large statistical study of the open magnetic flux content of the magnetosphere at the time of substorm onset.

Several studies developed empirical relations between the flaring angle of the magnetosphere, tail radius and tail magnetic field strength to estimate the amount of open magnetic flux in the tail lobes at substorm onset (e.g. Petrinec and Russell, 1996; Shukhtina *et al.*, 2004; Shukhtina *et al.*, 2005). However, these studies use observations from a single spacecraft in the magnetotail and do not distinguish between flux of open or closed origin. Currently, the most accurate method for estimating the open magnetic flux content of any one hemisphere is by observing the location of the open/closed magnetic field line boundary (OCB) at all magnetic local times (MLTs) and hence determining the area of the polar cap (the area of the ionosphere threaded by open magnetic field lines). Several ionospheric measurements and techniques have been developed to provide a proxy for the location of the OCB, and these are summarised below.

2.3.1 Particle Precipitation Measurements

In-situ particle precipitation measurements from low-latitude spacecraft (such as the DMSP spacecraft; see section 3.2) provide the most direct and precise determination of the boundaries between different plasma regimes, including the OCB. By identifying different regions of precipitation from electron and ion spectra one can determine where the precipitation transitions from precipitation on closed magnetic field lines to open. On the dayside the best proxy for the OCB is found by searching for the transition between BPS, CPS and LLBL precipitation (closed) to lower energy cusp, mantle and polar rain precipitation (open) (Newell *et al.* 1991a). On the nightside the best proxy for the OCB is at the poleward edge of the sub-visual drizzle region (Newell *et al.*, 1996). These particle precipitation boundaries (PPBs) are thought to be the best proxy for the

OCB but, due to the polar nature of low-altitude spacecraft orbits, can only be determined at two magnetic local times in any one orbit (~100 minutes for the DMSP spacecraft).

2.3.2 All-sky Cameras, Meridian Scanning Photometers, Coherent and Incoherent Scatter Radar and Ground-based Magnetometers

Samson *et al.* (1992) suggested that the location of the OCB may be determined from measurements of the 630 nm auroral emission as a function of latitude. Blanchard *et al.* (1995) demonstrated that a sharp step in the 630 nm emission is seen at the poleward edge of the auroral oval and that this transition between intense and weak emission may be tracked over a relatively large latitudinal range and with high time resolution using a chain of meridian scanning photometers (MSP). By quantitatively locating the emission boundary they compared the poleward edge of the 630 nm aurora with the latitude of the OCB as determined from DMSP PPBs for a total of 10 events. Three of these events occurred during the expansion phase of substorms and showed large differences between the two boundaries of up to 5°. For a further three events the poleward edge of the aurora was located outside of the latitudinal range covered by the photometers. For the remaining four events the DMSP and MSP boundaries coincided with an rms error of $\pm 0.9^\circ$ in latitude. Blanchard *et al.* (1997) expanded on this study using a much larger data set and found that the two boundaries coincided with an accuracy of $\pm 0.54^\circ$.

Until the 1970s the principal information on the structure and dynamics of the auroral oval was inferred from analysis of millions of all-sky camera films (e.g. Feldstein and Galperin, 1985; Sandholt *et al.*, 1998). All-sky cameras use a special fisheye lens to view the entire sky from horizon to horizon (180°) and can be used to view the optical auroral emission. Bond and Akasofu (1979) showed that the poleward edge of the optical emission as viewed by all-sky cameras was in excellent agreement with the location of the poleward edge of emission as seen by satellite imagery.

Measurements of the Doppler spectral width of ionospheric backscatter, measured by coherent scatter radar such as the Super Dual Auroral Radar Network (SuperDARN), may be employed to produce an accurate proxy for the OCB. Baker *et al.* (1995)

showed that enhanced spectral widths were associated with cusp precipitation on open magnetic field lines and that equatorward of this the spectral width was reduced. This implies that the transition between high spectral widths, typically found poleward of the OCB, and low spectral widths, typically found within the auroral oval, may be a good proxy for the position of the OCB. This boundary has been termed the Spectral Width Boundary (SWB). Several studies suggested that the SWB and other radar backscatter properties could be used as proxies for the OCB but that the relationship between the two is not straightforward (e.g. Milan *et al.*, 1999; Blanchard *et al.*, 2001; Chisham *et al.*, 2001, 2002; Lester *et al.*, 2001). Chisham and Freeman (2004) showed that the SWB is a typical feature at all MLTs. However, Chisham and Freeman (2003) demonstrated that accurately identifying this transition can be difficult due to the broad distributions and significant overlap in the regions of high and low spectral width. Chisham and Freeman (2004) developed a threshold method (see also Baker *et al.*, 1997) in which they search poleward along a radar beam until a threshold value in spectral width is exceeded. Using this technique, Chisham *et al.* (2004, 2005a,b) compared the latitude of the SWB from 5 years of SuperDARN data with the OCB as estimated using DMSP PPBs. They found that at most MLTs the SWB gave a good proxy for the OCB except in the 0200-0800 MLT sector, similar to the offsets found between Polar UVI and DMSP OCB proxies by Carbary *et al.* (2003), discussed below.

Incoherent scatter radar may also be used to measure the transition between high density ionospheric electrons found in the auroral oval and low densities poleward of the OCB (e.g. Blanchard *et al.* 2001). See also Chisham *et al.* (2008, 2009).

The polar cap boundary can also be identified with the high-latitude boundary of region 1 field-aligned currents, which can be measured using ground based magnetometers (Iijima and Potemra, 1978; Mishin, 1990).

2.3.3 Satellite Images

All of the above methods suffer from limited spatial and temporal coverage of the OCB. Currently, the best method of determining the global location of the OCB is from global auroral images taken by satellites. However, many studies have shown that the

poleward edge of the auroral emission as determined from imaging spacecraft does not have a simple relationship with the location of the OCB.

The first efforts to find the poleward edge of the auroral oval from satellite images were made by inspecting auroral images taken by simple scanning photometers onboard polar orbiting low-latitude spacecraft (e.g. Lui and Anger, 1973; Lui *et al.*, 1975; Holzworth and Meng, 1975). However, this scanning variety of auroral imager has the drawback that different points within the image are acquired at different times as the photometer scans across the polar cap. The introduction of ultraviolet (UV) imaging cameras, which take a snapshot of the whole auroral oval such that the whole auroral oval is imaged simultaneously, solved this problem. FUV imagers (120-190 nm) are also able to distinguish between high latitude dayglow and auroral oval emission as well as being only minimally contaminated by daylight scattered by clouds and the ground (Mende *et al.*, 2000a).

The first quantitative identification of the poleward edge of the auroral oval from global auroral images was made using observations from the Dynamics Explorer 1 spacecraft (Craven and Frank, 1985, 1987; Frank and Craven, 1988). A technique was employed to determine the edge of the auroral emission such that the poleward edge of the auroral oval is assumed to be located where the auroral intensity drops below some threshold value. Brittnacher *et al.* (1999) used a similar threshold method to determine the global location of the OCB from global auroral observations made by the Polar Ultraviolet Imager (UVI) (Torr *et al.*, 1995). Kauristie *et al.* (1999) used 44 UV images, taken by the Viking spacecraft, of the northern nightside auroral oval and a threshold method to determine the poleward edge of the UV auroral oval. Comparing a small number of these boundaries with DMSP PPB OCB estimates, they found that the poleward edge of UV emission is often found more than 2° equatorward of the location of the equivalent particle boundary, especially in the midnight and morning sector. Baker *et al.* (2000) compared the poleward boundary of the UV aurora as seen by Polar UVI using both a threshold method and ratio method (where the poleward edge of auroral emission is assumed to be located where the auroral intensity drops by a fixed ratio from its peak value at the local time of the boundary). They found that the ratio method had the best correlation with DMSP PPBs and also revealed a systematic latitudinal offset between the UVI and DMSP boundaries of $\sim 1^\circ$ in the evening sector (where most of the

observations were made). Carbary *et al.* (2003) developed a new method of estimating the location of the OCB using Polar UVI auroral images. They fit a Gaussian-like function plus quadratic background term to intensity-latitude profiles across one hour MLT sectors of the UVI auroral oval. The location of the OCB was then assumed to be shifted poleward of the center of the Gaussian function by the full-width-at-half-maximum (FWHM). Comparing over 23,000 UVI and DMSP PPB OCB estimates, they found that the statistical distributions of offsets in each 1-hour MLT bin were Gaussian in nature with a mean close to zero and Gaussian full-width of $\sim 3\text{-}4$ degrees. The mean offsets derived from these distributions show systematic trends in MLT, with the largest offset occurring in the predawn sector ionosphere, where the DMSP OCB is found $\sim 3.5^\circ$ more poleward of the equivalent UVI boundary. A second order harmonic expansion was fit to the mean offsets in order to provide a ‘calibration’ or ‘correction’ to Polar UVI boundaries to provide a more accurate proxy for the OCB. Other studies have suggested that a double Gaussian fit to intensity-latitude profiles provides a better fit to the OCB (e.g. Mende *et al.*, 2003; Gjerloev *et al.*, 2008).

2.4 Summary of Previous Studies on the Polar Cap Flux, Solar Wind and IMF conditions, Geomagnetic Activity and Motion of Auroral Boundaries during the Substorm Cycle

In this thesis we investigate the open magnetic flux content of the magnetosphere, the solar wind and IMF conditions, the auroral and geomagnetic activity, as well as motions of the OCB and equatorward boundary of the auroral oval during the substorm cycle. A detailed summary of the previous studies most relevant to the work in this thesis is given below.

2.4.1 Variations in Open Magnetic Flux

By carrying out the largest statistical study of the open magnetic flux content of the magnetosphere to date, in chapter 5 of this thesis we investigate the idea of a critical threshold in open magnetic flux as a necessary condition for substorm onset. As discussed above, currently, the most accurate method of estimating the hemispheric open magnetic flux content of the magnetosphere is by identifying the global location of the open/closed magnetic field line boundary (OCB) and hence determining the area of

the polar cap. As discussed in section 2.3, several methods have been developed for determining the latitude of the OCB. Once the OCB has been identified, the open magnetic flux can then be easily estimated by integrating the Earth's magnetic field (B) through the area of the polar cap:

$$F_{pc} = \int_{pc} \underline{B} \cdot d\underline{s} . \quad (2.1)$$

Several studies have investigated the size of the polar cap and F_{pc} during substorms for a limited number of events. These are summarised below.

Milan *et al.* (2003) used a combination of auroral images, radar observations and particle precipitation boundaries to identify the global OCB in the northern hemisphere and hence track changes in the polar cap area over two substorm cycles. They found that the polar cap area expanded during the growth phase of both events before decreasing in size immediately (within 10 minutes) after substorm onset. The contraction of the polar cap area continued for up to 100 minutes after onset, some time after auroral activity had faded. Milan *et al.* (2004) used the method of Milan *et al.* (2003) to track the global OCB and estimate F_{pc} in the northern hemisphere, using equation 2.1, for an almost continuous 8 hour period. They estimated that between 2.5-12% (0.2-1.0 GWb) of the total magnetic flux in any one hemisphere (~8 GWb) is connected to the solar wind (i.e. is open) at any one time, with an average value of 8% (0.64 GWb). The extreme value of 0.2 GWb was found after a solar wind pressure step which initiated a large substorm event and was followed by three hours of continuous northward IMF (i.e. little addition of open flux at the dayside magnetopause occurred). Milan *et al.* (2007) used a similar technique to quantify F_{pc} for a total period of 73 hours containing 25 tail reconnection events. They found that F_{pc} varied between 0.2 and 0.9 GWb with a mean value of 0.46 GWb, indicating that between 2.5 and 11% of hemispheric flux is open. The average F_{pc} at the onset of reconnection events was 0.65 GWb and the average F_{pc} at the end of the expansion phase was 0.45 GWb. The amount of F_{pc} closed in each event varied between 0.05 and 0.75 GWb with a mean value of 0.3 GWb (the discrepancy between the average F_{pc} at the start and end of the reconnection events and this value being due to the continued addition of F_{pc} by dayside reconnection in the expansion phases). Milan *et al.* (2008) quantified F_{pc} from auroral

images of the northern hemisphere taken by the FUV Wideband Imaging Camera (WIC) (Mende *et al.*, 2000b) onboard the Imager for Magnetopause-to-Aurora Global Exploration (IMAGE) spacecraft (Burch, 2000) for a near-continuous period of 10 days covering August and September 2005. The distribution of F_{pc} varied between ~ 0.2 and 1 GWb with a mean value of 0.43 GWb.

Frey *et al.* (2004) produced a list of substorm onsets by identifying nightside auroral brightenings and expansion in auroral images made by the IMAGE WIC FUV detector for the entire lifetime of the IMAGE mission (March 2000 to December 2005) using the following criteria:

- (1) a clear local brightening of the auroral oval must be observed,
- (2) the local brightening must expand to the poleward boundary of the auroral oval and spread azimuthally in local time for at least 20 minutes,
- (3) a substorm onset was only accepted as a separate substorm if at least 30 minutes had passed since the previous onset.

The third criterion eliminated closely spaced onsets or multi-onsets and the second criterion was employed to try to eliminate pseudo-breakups which did not develop into a full substorm event. The center of the initial auroral intensification was identified by eye and a computer program used to locate the brightest pixel near this location, defining the latitude and MLT of the initial auroral brightening.

Using the Frey *et al* list of onsets Coumans *et al.* (2006) used auroral images from the IMAGE FUV spectrographic imager SI12 (Mende *et al.*, 2000c) and a threshold method to identify the global OCB to carry out a superposed epoch analysis of the evolution of F_{pc} for 55 substorm events from the time period June 2000 to December 2002. They chose only very isolated events (separated by at least two hours from the previous substorm) and events which showed a significant equatorward motion of auroral boundaries during the substorm growth phase. Of the 55 events, 9 were found to be associated with a northward turning of IMF B_z , 13 were associated with other triggers in the solar wind, and 33 events were non-triggered. The growth phases of all events in the study were found to be very similar. F_{pc} was found to increase from values of ~ 0.5 - 0.6 GWb at the start of the growth phase to values of 0.66 and 0.74 GWb at onset for IMF B_z triggered events and non-triggered events respectively, an average increase

of 33% during the 60 minutes prior to onset. DeJong *et al.* (2007) carried out a superposed epoch analysis of the evolution of F_{pc} for 29 individual sawtooth events, 31 isolated substorms, and 45 steady magnetospheric convection events. They showed that, as expected, F_{pc} during SMC events remains approximately constant with an average F_{pc} of 0.55 GWb. The growth and expansion phases of isolated and sawtooth events showed very similar trends, though the variations in F_{pc} for sawtooth events were found to occur, on average, at values 150% greater in magnitude than for isolated events, suggesting that sawtooth events are more likely to occur when F_{pc} is enhanced. F_{pc} varied between ~ 0.5 and 0.7 GWb for isolated events and ~ 0.8 and 1.0 GWb for sawteeth. Both types of event were found to close $\sim 24\%$ of the onset F_{pc} over the 60 minutes following onset. Huang *et al.* (2009b) carried out a superposed analysis of F_{pc} using auroral images from the IMAGE and Polar spacecraft for a total of 50 individual sawtooth events, 30 isolated substorms and 45 SMC events. Their results showed that F_{pc} varied between ~ 0.3 and 0.8 GWb, that isolated onsets occurred at a mean F_{pc} of 0.68 GWb and that sawtooth events occur at a mean F_{pc} of 1.0 GWb. In both isolated and sawtooth events $\sim 24\text{-}27\%$ of onset F_{pc} was closed during the expansion phase. The result that sawtooth events occur at higher values of F_{pc} is perhaps not unexpected. Sawtooth events tend to occur during period of strong solar wind driving (strongly southward IMF, see section 2.1.4), suggesting that they also occur when the ring current is enhanced. Milan *et al.* (2009a,b) have suggested that the ring current modulates the magnetotail such that substorms occur at higher values of F_{pc} when the ring current is enhanced (see below), thus explained the observations of DeJong *et al.* (2007) and Huang *et al.* (2009b). The strong and steady solar wind driving for sawtooth events also suggests that, although both sawtooth and isolated events close similar amount of F_{pc} during their expansion phases, during sawtooth periods F_{pc} will rise more quickly back to the values at which substorms occur, leading to the periodic nature of these events.

2.4.2 Variations in the Solar Wind, IMF, Auroral Intensity and Geomagnetic Activity During Substorms and Correlation with F_{pc} .

In chapter 5 of this thesis we find that not all substorms show the expected particle injection signature of substorm onset, and we classify substorms into three distinct categories based on their particle injection signatures. In chapter 6 we investigate these

categories in more detail by carrying out the largest superposed epoch analysis to date of the open magnetic flux, the solar wind and IMF conditions, and the geomagnetic activity and auroral luminosity during the substorm cycle for our three distinct categories of substorm.

Previous studies have shown that substorms can occur with a large range of solar wind and IMF conditions. Substorms tend to occur after a prolonged period of southward IMF, the substorm growth phase, although they have also been shown to occur during strongly northward IMF (e.g. Kamide *et al.*, 1977a). An anti-correlation between the magnitude of the IMF B_z component and F_{pc} at onset has been observed. Other studies have shown a positive correlation of F_{pc} or polar cap area with auroral activity (e.g. Feldstein and Starkov, 1967) and geomagnetic activity (e.g. Hardy *et al.*, 1985, 1987). The most relevant studies to the work carried out in this thesis are discussed below.

Zhou and Tsurutani (2001) carried out a statistical study in which substorms, pseudo-breakups and quiescent intervals occurring after interplanetary shocks were associated with strongly southward IMF, near zero IMF and strongly northward IMF respectively. Kullen and Karlson (2004) studied 3 months of data containing 419 substorm events and 330 pseudo-breakups. They found that large substorms most often occur when the IMF is strongly negative, small substorms most often occur when B_z is weakly positive or zero, and pseudo-breakups most often occur for weakly positive B_z and very weak (below average) IMF magnitudes and solar wind density and flow speeds. They also found that substorms occurring with continuous southward IMF in the expansion phase showed no decrease in polar cap size after onset.

Figure 2.7 shows an example of F_{pc} , the maximum nightside auroral intensity, the AL and AU geomagnetic indices, and the IMF B_z variation around four tail reconnection events from Milan *et al.* (2007), and illustrates how tail reconnection events can differ in size and characteristics. The first reconnection event (1) occurs at a southward turning of the IMF (panel d). Both the AL (panel c) and auroral brightness (panel b) show only minimal signatures of onset and F_{pc} (panel a) shows only a slight decline, suggesting that the continued addition of flux on the dayside during southward IMF is balancing the flux closure in the tail to a large extent. The second event (2) shows much

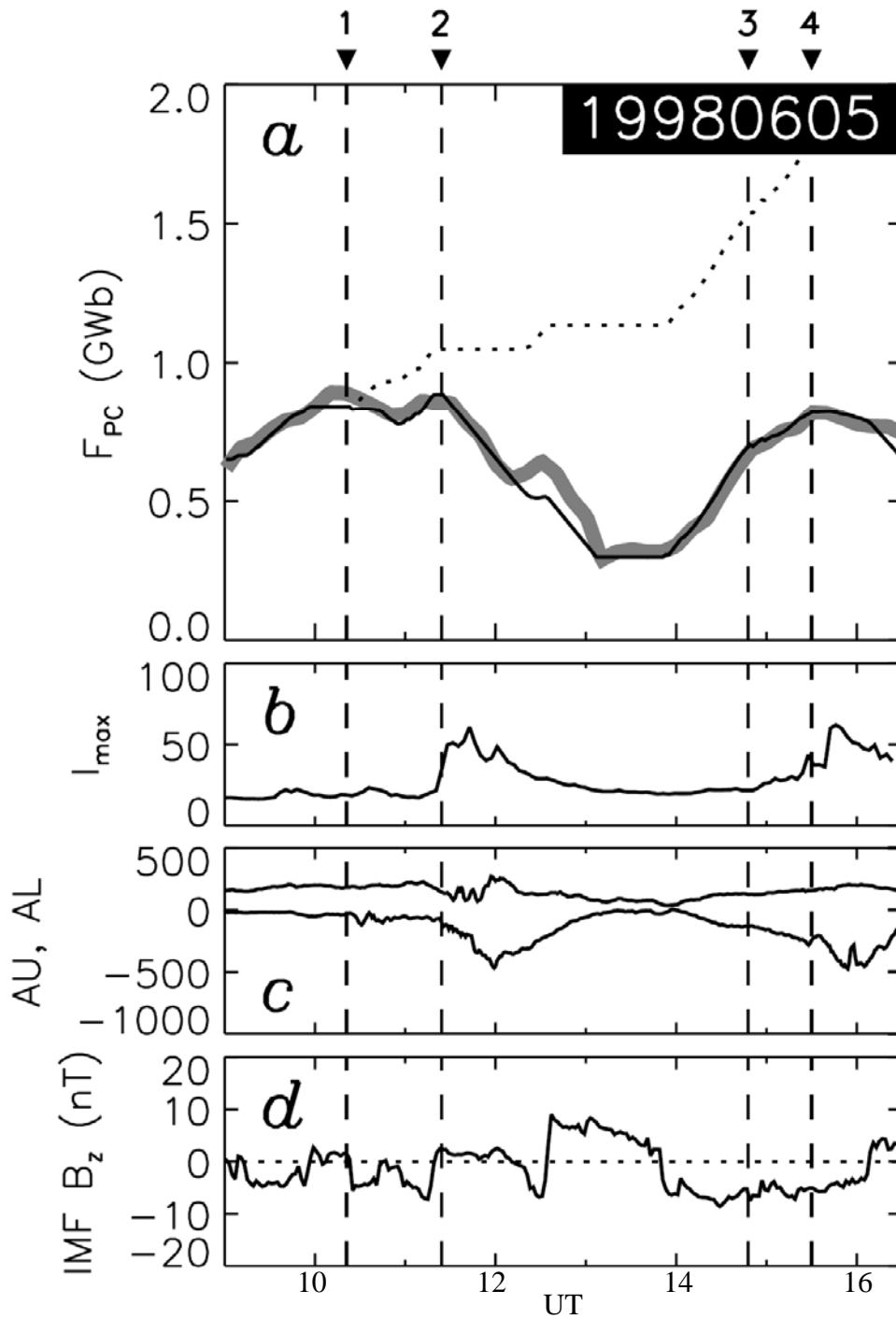


Figure 2.7: Open magnetic flux (thick grey line, panel a) estimated by integrating the radial component of the Earth's magnetic field through the area enclosed by the OCB identified using global auroral imagery (see Milan *et al.*, 2003), maximum nightside auroral intensity (b), geomagnetic indices (c) and IMF B_z lagged to the magnetopause (d) during 4 tail reconnection events (vertical dashed lines) on the 5th of June 1998, from Milan *et al.* (2007). The dashed and bold black lines represent F_{pc} modelled from the dayside reconnection rate only (i.e. F_{pc} variation if there was no nightside reconnection; dashed line) and F_{pc} modelled from measurements of the day and nightside reconnection rates (bold line; see Milan *et al.*, 2007).

larger signatures of onset. A rapid and large brightening of auroral emission is seen (panel b) accompanied by large and typical AL and AU signatures of substorm onset. The event appears to be associated with a northward turning of the IMF (panel d). F_{pc} (panel a) is seen to rapidly decrease after the onset. This decrease is temporally halted when the IMF turns southward for a few minutes at ~ 12 UT. F_{pc} then continues to decrease while the IMF is strongly northward (i.e. no dayside reconnection) before starting to increase again at ~ 14 UT in association with a new southward turning and start of the growth phase of event 3. At the onset of event 3 both the magnitude of the AL and AU indices and the auroral luminosity are increasing. The IMF remains steadily southward but the rate of increase of F_{pc} is slowed indicating that tail reconnection is acting to close magnetic flux, slowing the increase in polar cap size. At the onset of event 4 there is a rapid brightening in auroral emission and clear AL and AU signatures of a substorm event. The IMF remains southward for approximately half an hour following the onset in which time the rise in F_{pc} is halted but a large decrease is not seen. This indicates that even during a large substorm event (as suggested by AL and AU indices and auroral emission, event 4) when the IMF remains steadily southward (indicating that magnetosphere dynamics continue to be largely ‘driven’ by the solar wind) the level of F_{pc} can remain elevated (event 4) or even continue to increase if the dayside reconnection rate is greater than that on the nightside (event 3; see equation 1.1).

Milan *et al.* (2008) studied F_{pc} and the solar wind and IMF conditions for 49 substorm events from late summer 2005. The main findings of their study can be summarised as follows: (1) The substorm frequency and amount of F_{pc} closed for substorms both increase for increased solar wind driving. (2) Despite the fact that the amount of F_{pc} closed during a substorm expansion phase increases for increased solar wind driving, the size of the polar cap is increased for all stages of the substorm cycle when the solar wind driving is enhanced and especially when the intensity of the ring current (as measured by the SYM-H index) is elevated. The authors suggest that there are two factors contributing to this result. Firstly, that there is a delay between the onset (thought to start in the closed magnetic field line region of the plasma sheet) and reconnection on open magnetic field lines in which time open magnetic flux continues to be added to the polar cap. The amount of open flux added in this time will be greater when the solar wind driving is enhanced and hence onset occurs at higher values of F_{pc}

for stronger solar wind driving. The second interpretation of this result is that the magnetotail is more stable to reconnection when the dayside driving is strong and the ring current is enhanced.

The second interpretation was reiterated by Milan *et al.* (2009a) and Milan *et al.* (2009b). Milan *et al.* (2009a) carried out two superposed epoch analyses of magnetospheric dynamics around substorm onset using observations from both the WIC and SI12 auroral imagers onboard the IMAGE spacecraft. The first study consisted of a superposed epoch analysis of F_{pc} , AL and AU indices and the SYM-H index for the 10 day period from the study of Milan *et al.* (2008). The 49 substorm events in this study were sub-divided into four categories by the value of F_{pc} at onset such that approximately even numbers of events were found in each bin (~10 events in each bin of <0.45 GWb, 0.45-0.55, 0.55-0.65 and >0.65 GWb). The second study used all substorms identified in the list of Frey *et al.* (2004) from the two year period of May 2000 to April 2002. This contained some 2000 substorms which were sub-divided into 5 categories by onset latitude (provided in the list of Frey *et al.*, 2004) as a proxy for F_{pc} . The results of both studies are consistent with the following: For increasing values of F_{pc} at onset or lower latitude onsets, (1) auroral brightness increases in all phases of the substorm, (2) IMF B_z is more negative and solar wind velocity, density and dynamic pressure all increase, (3) the AL substorm bay is more pronounced and SYM-H is enhanced.

Milan *et al.* (2009b) estimated the radius of the auroral oval from all auroral images obtained by the IMAGE WIC and SI12 detectors between June 2000 and May 2002. Their results indicate that the radius of the auroral oval (a proxy for F_{pc}) increases for increasing negative SYM-H. Consistent with previous results, they show that, statistically, substorms occurring on expanded auroral ovals are more intense. The authors interpret the increase in auroral oval radius for substorms occurring with enhanced ring current intensity as a stabilisation of the magnetotail to the onset of reconnection due to the magnetic perturbation caused by the ring current. Inside the ring current region, an increase in ring current intensity will result in a negative perturbation in the tail B_z component, seen as a negative perturbation in the SYM-H index. Further downtail, the increase in ring current results in a positive B_z perturbation which acts to maintain depolarization in the tail and hence prevents the thinning of the plasma sheet,

stabilising the magnetotail and allowing F_{pc} to climb to higher levels before the plasma sheet is thinned sufficiently enough for reconnection to initiate.

The results of Milan *et al.* (2008; 2009a,b) are consistent with both a maximum threshold in F_{pc} at which substorm onset is induced and a minimum threshold in F_{pc} at which reconnection ceases in the tail at the end of the expansion phase which are both modulated by the strength of the ring current; this is represented schematically in Figure 2.8. Panel a represents the characteristic perturbation of the SYM-H index, a measure of the north south perturbation of the Earth's magnetic field strength at the equator, and hence a measure of the strength of the ring current (see section 3.6), during a geomagnetic storm. A geomagnetic storm is usually defined by a main phase in which a rapid, lasting less than 12 hours, depression of the SYM-H index is seen followed by a slow recovery lasting several days. During the main phase the IMF turns strongly southward resulting in enhanced dayside reconnection and the rapid increase in the strength of the ring current (particularly on the nightside and seen as a large southward perturbation in the surface magnetic field strength at the equator of the Earth and a depression in SYM-H). The main phase of storms are often preceded by a pressure step in the solar wind resulting in the enhancement of the dayside ring current and northward perturbation in the Earth's magnetic field at the equator (positive SYM-H perturbation seen in Figure 2.8). Panel b shows the typical behaviour of the radius of the auroral oval, which can be assumed to have a direct relation to the size of polar cap and hence open magnetic flux, during the storm. Prior to the storm the oval radius increases and decreases during substorm growth and expansion phases. In the main phase of the storm the oval radius rapidly increases due to the increased dayside reconnection as the IMF turns southward. Subsequently the oval radius gradually decreases as SYM-H slowly declines. Throughout this recovery the oval continues to expand and contract with the substorm cycle and the maximum and minimum oval radius slowly decreases with decreasing SYM-H.

The superposed epoch results of Huang *et al.* (2009a) also showed that F_{pc} at onset increased for increased dayside merging electric field (a measure of the dayside reconnection rate) and with the Dst index (a measure of the ring current), consistent with the results of Milan *et al.* (2008, 2009a,b). Huang *et al.* (2009b) studied the total pressure and lobe magnetic field strength during sawtooth events. They showed that

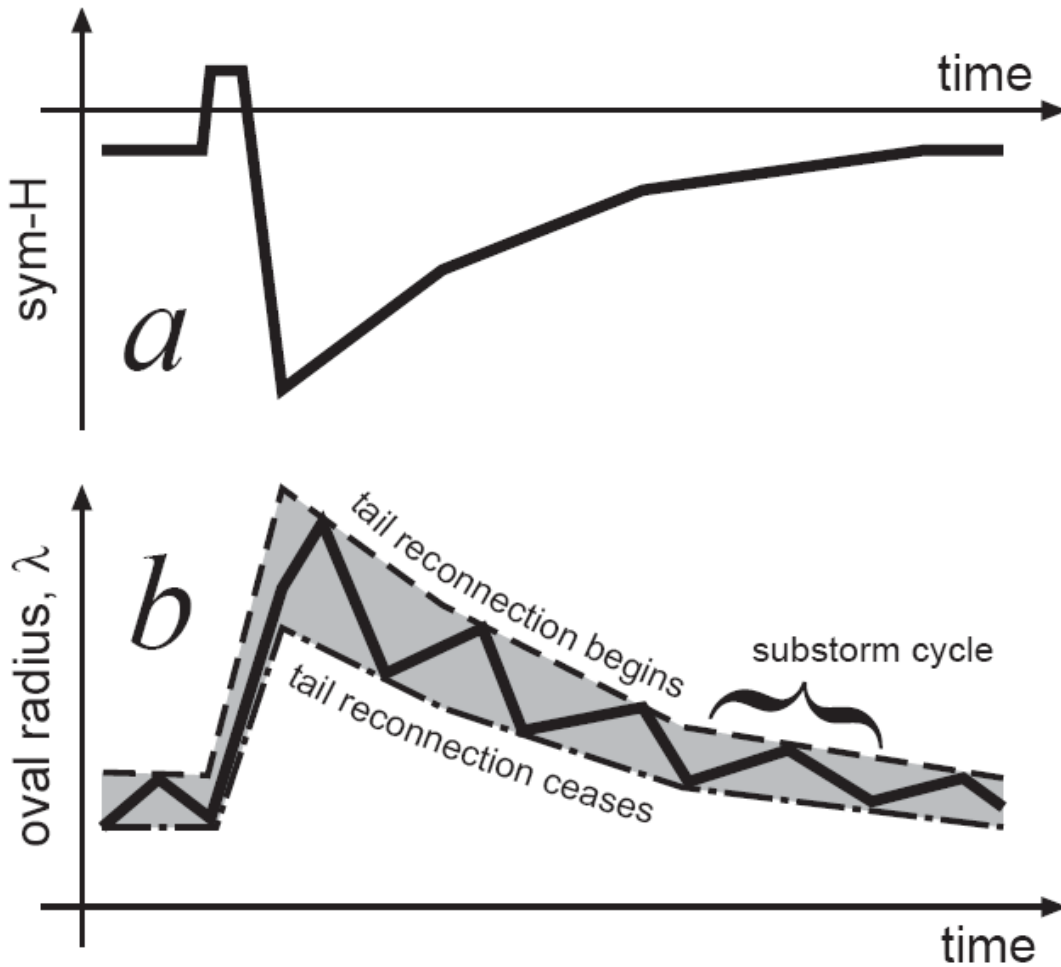


Figure 2.8: Representation of how the strength of the ring current (as measured by the SYM-H index) may modulate the level of open magnetic flux (approximated by auroral oval radius) during substorms as postulated by Milan *et al.* (2009b).

both lobe field and total pressure are increased at the onset of sawtooth events for increasing magnitudes of solar wind driving, suggesting that sawtooth events occur once some critical state in the magnetotail has been reached and that this state depends on the solar wind parameters.

Several studies have shown there to be a good correlation between various solar wind-magnetosphere coupling functions and F_{pc} at onset (e.g. Shukhtina *et al.*, 2005). Blockx *et al.* (2009) studied the correlation between F_{pc} , the nightside auroral intensity (integrated between 18-6 MLT) and the Akasofu energy input parameter for a total of 256 Frey onset events. The ε parameter is an empirically determined fraction of the solar wind Poynting flux through the dayside magnetopause (Perreault & Akasofu, 1978) and is thus a measure of the solar wind energy input into the magnetosphere due to dayside reconnection, given by:

$$\varepsilon = l_0^2 V_{sw} B^2 \sin^4(\theta_c / 2), \quad (2.2)$$

where V_{sw} is the solar wind flow speed, B is the strength of the IMF, θ_c is the IMF clock angle and l_0 is a length constant of $\sim 7 R_E$. They found a very low correlation between the nightside auroral intensity averaged over the expansion phase and the value of F_{pc} at onset (0.06), the amount of F_{pc} accumulated in the growth phase (0.27) and the rate of increase of F_{pc} during the growth phase (0.26). Thus they conclude that F_{pc} does not control the amount of kinetic energy of auroral particles released during substorms. They found a much better correlation between the nightside intensity and the ε parameter integrated over the growth phase of the substorms (0.9) than ε integrated over the expansion phases (0.66). These results suggest that the loading-unloading process (in which energy stored in the magnetosphere during the substorm growth is released during the expansion phase) is statistically more dominant in controlling the energy released in substorm onsets than the directly driven process (in which solar wind energy is directly released in the ionosphere and ring current).

As discussed earlier, one indicator of the substorm strength are the AL and AU geomagnetic indices. Weimer (1994) carried out a superposed epoch analysis of the AL and AE indices of 55 substorm events, showing that the peak activity was reached

between +25 and +34 minutes relative to onset, after which the indices decayed with a time constant of 1.78-2.42 hours. The results also showed that the peak in intensity was reached sooner for events with a larger magnitude at onset and that the following decay was faster for larger magnitude events.

Mende *et al.* (2003) carried out a superposed study of the maximum auroral intensity of WIC images across 1 hour MLT sectors of the auroral oval from 91 substorm events selected from a period of ~ 1 year starting in June 2000. They found that the intensity at the MLT of the initial onset rapidly increased around onset from approximately 800 to 4000 counts (see section 3.1.3), reaching a peak at +5 minutes.

2.4.3 Auroral Boundary Motions

As discussed above, the OCB is an important diagnostic tool for magnetospheric physics. The location and motion of the equatorward boundary of the auroral oval also provides important information on the state and dynamics of the magnetosphere and is thought to map to the Earthward edge of the plasma sheet and/or ion isotropy boundary (Mende *et al.*, 2003 and references therein). Although the global expansion and contraction of the auroral oval during substorms has been confirmed by several studies, there are relatively few detailed studies of the local motion of the OCB and equatorward boundary of the auroral oval during substorms.

In chapter 6 of this thesis we further investigate the three distinct categories of substorms discussed earlier, by carrying out the largest superposed epoch analysis of the motion of the OCB and equatorward boundary of the auroral oval in separate MLT sectors during the substorm cycle, to date. A review of previous studies relevant to this work is given below.

The classic substorm definition of Akasofu (1964) states that the aurora drift equatorward in the growth phase of the substorm, before rapidly expanding poleward in the expansion phase. The equatorward motion of the boundaries during the growth phase is an indication that the magnetotail is becoming more stretched, while the poleward expansion after onset is an indication that the field becomes more dipolar. Observations of the global auroral oval from spacecraft have since confirmed that both

the poleward and equatorward boundaries of the auroral oval drift to lower latitudes by several degrees during the growth phase of substorms before recovering to higher latitudes during the expansion phase (e.g. Craven and Frank, 1987; Brittnacher *et al.*, 1999; Milan *et al.*, 2003). These studies have also shown this average behaviour to be highly variable. For example, the drift of the poleward boundary towards lower latitudes during the growth phase is not concurrent at all MLTs. Brittnacher *et al.* (1999) showed that the poleward boundary moves faster than the equatorward boundary in all stages of the substorm process.

To date, few and limited statistical studies of auroral boundary motions during substorms have been carried out. Jayachandran *et al.* (2005) studied the equatorward motion of the equatorward boundary of the proton aurora through 68 substorm growth phases using the SuperDARN E-region backscatter boundary as a proxy for the equatorward boundary of the auroral oval (Jayachandran *et al.*, 2002). They classified the equatorward motions into two categories; a global equatorward motion seen over several hours of MLT (47 of 68 events) and a more localised motion seen over only a few hours of MLT encompassing the onset MLT (21 events). Coumans *et al.* (2007) studied the motion of the OCB and equatorward boundary of the proton auroral emission, as observed by the SI12 detector onboard the IMAGE spacecraft, for 55 substorm events. They showed that the equatorward motion of the boundaries tends to increase for increasing negative values of B_z . This result is not unexpected as previous studies have shown that the polar cap size and rate of increase of F_{pc} during the growth phase of substorms is larger for events with stronger solar wind driving. They also found a correlation of 0.54 between various solar wind-magnetosphere coupling functions integrated over the growth phase of the substorm and the equatorward motion of the OCB, suggesting that the dayside driving plays a role in determining the motion of the boundaries. They found that the equatorward boundary mostly moved with a global motion (either with a similar latitudinal change at all MLTs or with variable degrees of movement at differing MLT sectors) and that the OCB most often moved with a non-uniform equatorward global motion, that is a equatorward motion of the OCB at all MLTs but of differing magnitudes, finding no correlation between the MLT of the largest boundary motion and the MLT of onset. Gjerloev *et al.* (2007) used observations from 116 substorm events to show that the average equatorward boundary at the onset MLT continues to drift equatorward after onset for up to half an hour before

turning poleward by only 0.5° over the next hour and a half. They also showed that the poleward edge of the auroral substorm bulge expanded poleward by $\sim 5^\circ$ in the expansion phase, before slowly recovering towards lower latitudes after ~ 1 hour.

The largest statistical study of boundary motions to date has been carried out by Mende *et al.* (2003) using global auroral images from the WIC and SI12 detectors onboard IMAGE (see section 3.1) and is shown in Figure 2.9. They studied the boundary motions at the MLT of the initial auroral brightening and at both ± 2 (green and yellow lines Figure 2.9) and ± 4 MLT (blue and red lines Figure 2.9) from the onset MLT. Their results showed that both poleward (top set of traces Figure 2.9) and equatorward boundaries (bottom set of traces Figure 2.9) slowly drifted equatorward during the growth phase by $\sim 1\text{-}2^\circ$ at all MLTs, the poleward boundary moving slightly faster than the equatorward boundary. At onset the poleward boundary moved rapidly to higher latitudes by between $2\text{-}5^\circ$, the response being greater and more rapid the closer to the MLT of onset. The motion of the equatorward boundaries at onset is much less pronounced, with the poleward response to onset not occurring until 5-30 minutes after onset, the delay increasing the further from the MLT of onset. The relative motions of the boundaries result in thinning of the auroral oval during the growth phase of the substorm and subsequent thickening in the expansion phase. The results of this study are discussed in more detail in section 6.2 of this thesis.

2.5 Summary

Since the first definition of the growth and expansion phases of the substorm (Akasofu, 1964), substorms have been the subject of a substantial amount of research for over 40 years. Yet they are still one of the fundamental magnetospheric processes yet to be fully understood. In particular relation to this thesis, there still remains much controversy over the trigger mechanism for substorm onset with some scientists arguing that a solar wind trigger is a necessary requirement for substorm onset, whilst others argue for a critical threshold internal to the magnetosphere.

One of the main aims of this thesis is to investigate the idea of a fixed critical threshold in the open magnetic flux content of the magnetosphere as a necessary and/or sufficient condition for substorm onset. Firstly, in order to accurately estimate the open magnetic

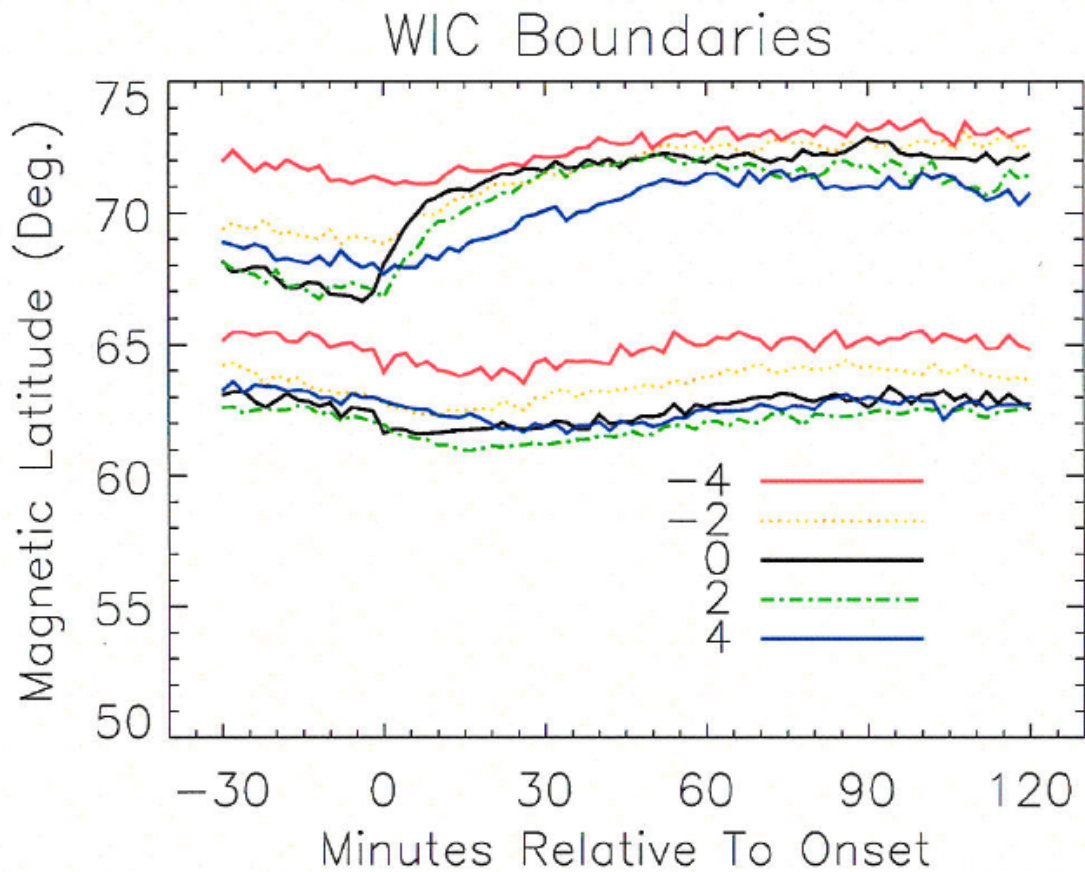


Figure 2.9: The latitude of the poleward (top set of traces) and equatorward (bottom set of traces) boundaries of the WIC auroral oval from approximately 30 minutes prior to substorm onset to 120 minutes after, at the MLT of the initial auroral onset (black line) and at -2 (yellow), +2 (green), -4 (red) and +4 (blue) MLTs from this location, from a study of 91 substorms by Mende *et al.*, 2003.

flux content of the magnetosphere, in chapter 4 of this thesis we develop an automated method of identifying the global location of the open/closed magnetic field lines boundary in the ionosphere from global auroral images taken by the IMAGE spacecraft. Using this method, in chapter 5, we carry out the largest statistical study of the open magnetic flux content of the magnetosphere, to date. The idea of a critical threshold in open magnetic flux for substorm onset is investigated and discussed. We also find that not all substorms show the expected particle injection signature of substorm onset. We sub-categorise substorms into three distinct sub-categories by their particle injection signatures and investigate the open magnetic flux, solar wind and IMF, geomagnetic activity, auroral luminosity and auroral oval boundary motions for the three distinct categories in chapter 6 of this thesis in the largest superposed epoch analysis of its type to date. A suite of both ground-based and space-based instrumentation has been used in the completion of this thesis. These instruments are discussed in the following chapter.

Chapter 3. Instrumentation

A range of data from both space and ground-based instrumentation has been used in the completion of this thesis. In this chapter the main features of these instruments are summarised.

3.1 IMAGE FUV

The bulk of the work in this thesis is based on imagery of the auroral oval in the far ultraviolet band of the electromagnetic spectrum by the Far Ultra-Violet (FUV) instrument onboard the Imager for Magnetopause-to-Aurora Global Exploration (IMAGE) spacecraft. The IMAGE spacecraft was launched on the 25th March 2000 and was operational between May 2000 and December 2005 when the spacecraft failed. The spacecraft was launched into a highly elliptical polar orbit with an apogee of $7 R_E$ and perigee a of 1000 km (Burch, 2000). Apogee was initially over the northern hemisphere (see Figure 3.1), directly over the northern pole in 2001. Apogee precessed into the southern hemisphere in 2003. In this thesis observations of the northern hemisphere during the winter months of 2000-2002 are used. During this time the spacecraft spent most of its time far from the Earth and thus mostly observed the aurora from or near apogee with a temporal resolution of 2 minutes due to the spin period of the spacecraft. Global auroral imaging was achieved through two FUV imagers, the Wideband Imaging Camera (WIC) and Spectrographic Imager (SI).

3.1.1 The Wideband Imaging Camera

The Wideband Imaging Camera (WIC) (Mende *et al.*, 2000b) was designed to observe broad band ultraviolet auroral emission. A downward-pointing auroral imager in the 140-190 nm wavelength range will be minimally contaminated by daylight scattered from clouds and the ground and the aurora can be observed in the presence of high latitude dayglow (Mende *et al.*, 2000a). Figure 3.2 shows the typical auroral emission features in the ultraviolet. The WIC detector covers the region populated by weak Lyman-Birge-Hopfield (LBH) lines (140-190 nm). This emission is primarily caused by the excitation and subsequent decay of N_2 to the ground state via a forbidden transition.

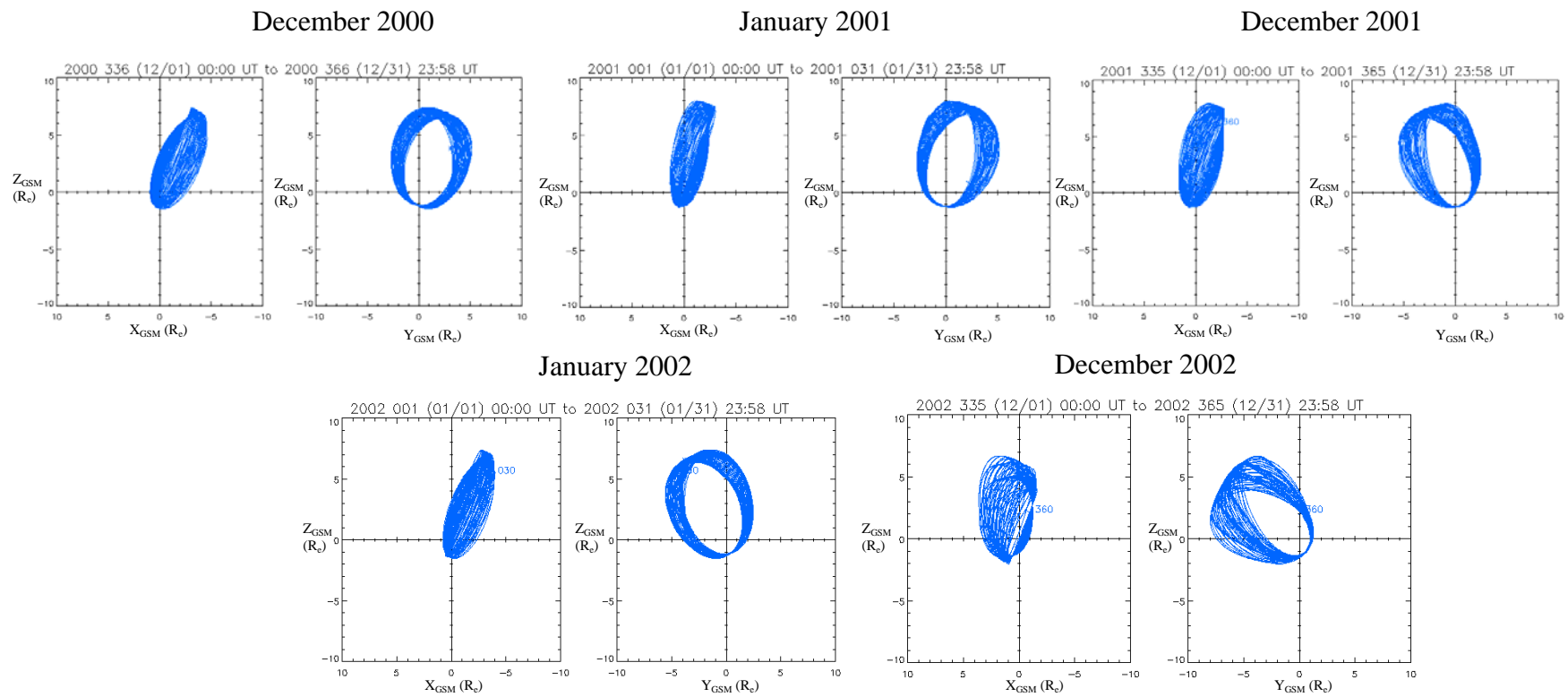


Figure 3.1: Orbit of the IMAGE spacecraft for the five months used in this thesis.

FUV Auroral Spectrum

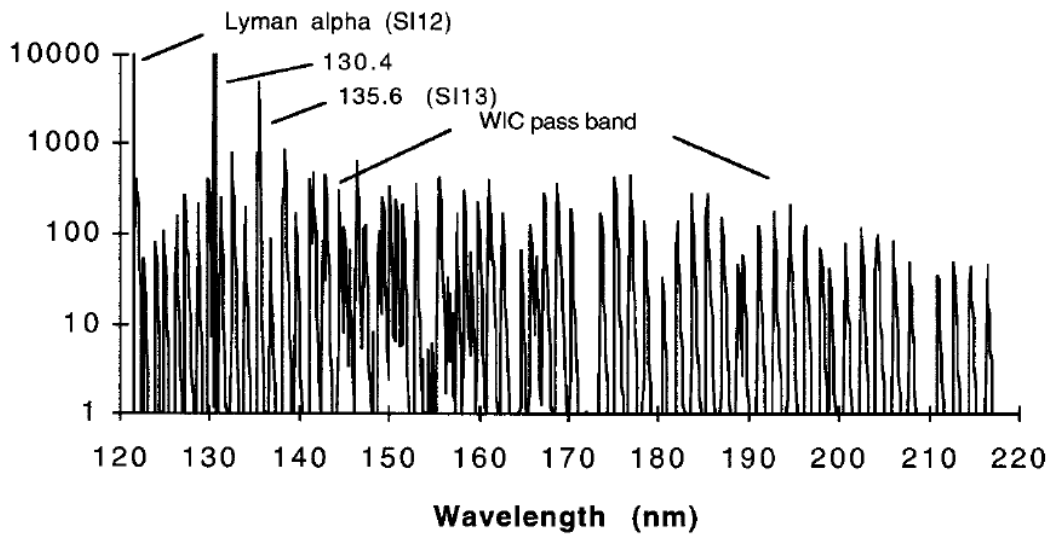


Figure 3.2: Model of the ultraviolet auroral emissions and the geocorona (from Mende *et al.* (2000a)).

The excitation of N_2 is principally caused by precipitating electrons but up to 20-25% of nightside emission can be caused by precipitating protons (Dashkevich *et al.*, 1996). It should also be noted that secondary electrons produced by the proton aurora have a small contribution to this emission.

In order to provide global imagery of the auroral oval the imager must have a field of view greater than 15° (the angle subtended by the Earth at $7 R_E$). This is achieved with a field of view of $17^\circ \times 17^\circ$ (13300×13300 km). WIC has a nominal pixel field of 256×256 . A nominal pixel at apogee corresponds to an ionospheric footprint of 52×52 km and 1.2×1.2 km at perigee.

WIC used a Cassegrain Burch type camera (Burch, 1947) to image the aurora. A basic schematic of the WIC detector is shown in Figure 3.3. Light enters from the left and is reflected by a small primary mirror. The secondary mirror reflects the light towards a microchannel plate (MCP). In order to filter out wavelengths below 140 nm, a BaF_2 entrance window is placed in front of the MCP. Photons interact with a photocathode at the front of the MCP, emit photoelectrons through the photoelectric effect which are then accelerated down the channels of the MCP by an accelerating voltage of $\sim +4000V$ placed across the MCP. A CsI photocathode is used to minimize contamination from wavelengths longer than 190 nm. An electron cascade is created as secondary photoelectrons are produced by collisions with the walls of the MCP. To avoid reflection of electrons back into the MCP, an aluminium coated phosphor is located at the rear of the MCP where the photons emitted are directed along a fiberoptic system to the charge-couple detector (CCD). The CCD outputs the information digitally in the form of A-D converted counts, one 8-bit byte per pixel.

3.1.2 The Spectrographic Imager

At the shortest wavelengths in the FUV spectrum (see Figure 3.2) is the Lyman-alpha emission consisting of two components, the cold Lyman-alpha (at 121.5667 nm), caused by geocoronal emission, and the hot, Doppler-shifted emission (121.8 nm) caused by protons precipitating into the upper atmosphere. When a proton enters the upper atmosphere it may collide with the neutral atmospheric molecules (mostly N_2 , O_2 , and O) capturing an electron through charge exchange. It then becomes a fast down-

going H atom with an excited electron, which, when the electron subsequently spontaneously decays to a lower energy level, may emit hot Lyman-alpha emission. In subsequent collisions the H atom may lose another electron, at which point the cycle can repeat itself. The resultant Lyman-alpha emission is Doppler shifted away from the detector. The spectrographic imager SI12 (Mende *et al.*, 2000c) images this Doppler shifted Lyman-alpha, the proton auroral emission.

The brightest emission feature in the aurora is the 130.4 nm OI emission line. However, this is multiply-scattered in the atmosphere. The 135.6 nm line (caused by precipitating electrons) is less scattered and it is this which the SI13 detector observes (Mende *et al.*, 2000c).

The requirement to observe the whole auroral oval, separate the Doppler-shifted Lyman-alpha from the cold Lyman-alpha geocoronal emission and to separately image the 135.6 nm OI emission line from the multiply scattered 130.4 nm line requires special engineering solutions to achieve the highest possible photon collection and efficiency. This is achieved using a novel Imaging Monochromator system, shown schematically in Figure 3.4. Light enters through a slit grill and is reflected by the collimator which produces parallel light from any point on the slit. The grating then disperses the light by wavelength. The wavelength separated light is then directed toward two exit slits, one located where the 135.6 nm line appears (this contains a wide open slit for maximizing the light throughput) and the second where the Lyman-alpha emission appears (this slit contains a grill to filter out the geocoronal Lyman-alpha at 121.56 nm that would otherwise dominate the signal). Two reflecting surfaces are required to provide sufficient aberration correction without lengthening the instrument. Finally, the split light is detected at two microchannel plate detectors. To achieve the required global imaging, the field of view of the SI instrument is $15^\circ \times 15^\circ$, giving a nominal resolution of 92×92 km per pixel at apogee (Mende *et al.*, 2000c).

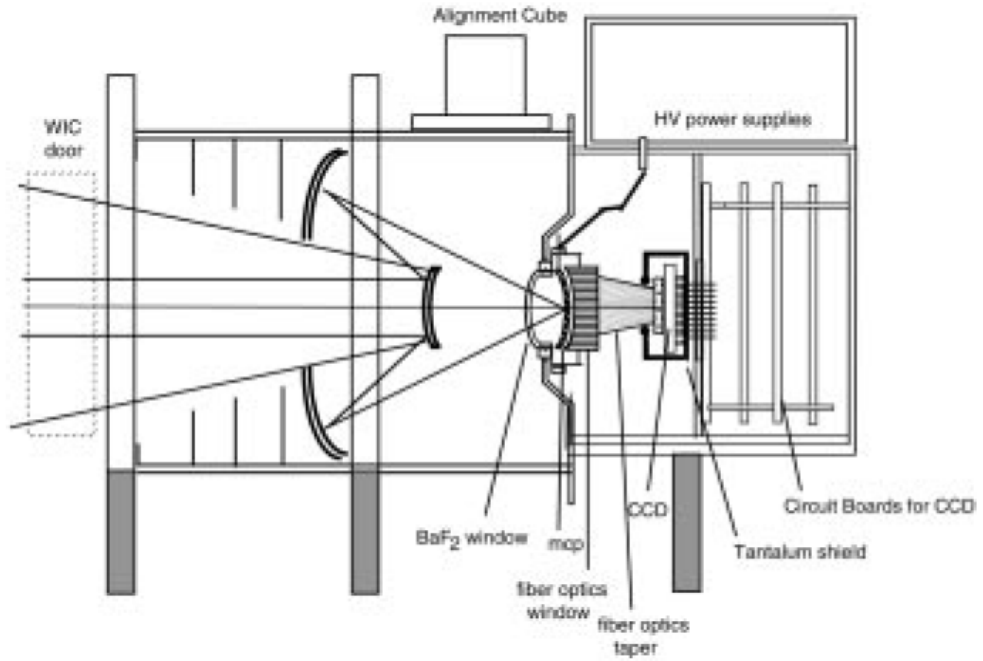


Figure 3.3: Cross section of IMAGE WIC detector (from Mende *et al.*, 2000b).

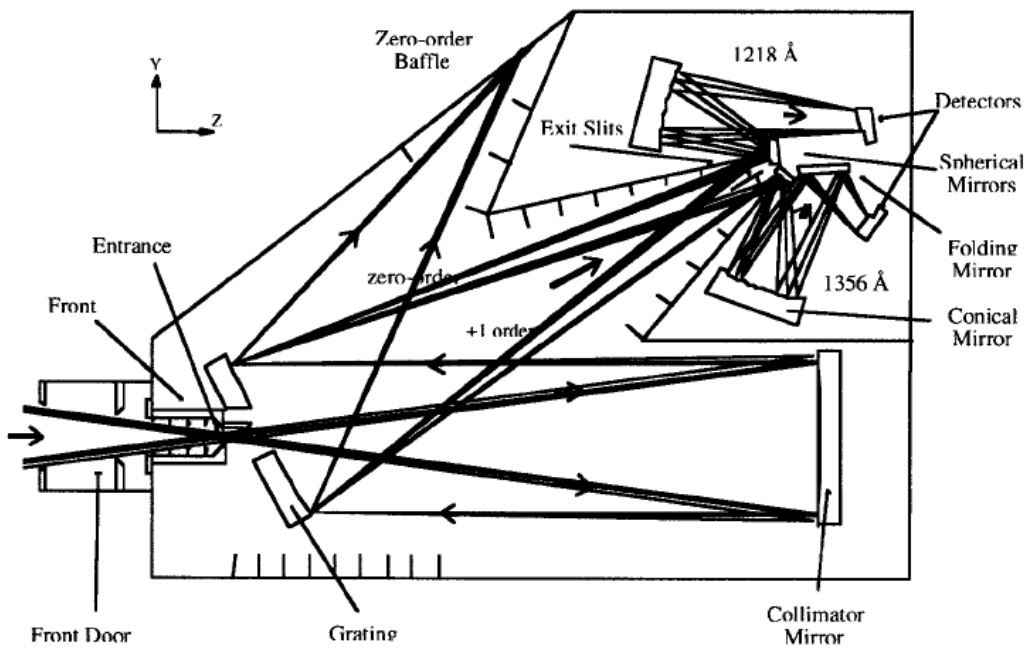


Figure 3.4: Schematic of the IMAGE Spectrographic Imager (from Mende *et al.*, 2000c).

3.1.3 Image Processing

The greatest challenge the FUV instruments face is the difficulty in taking high resolution and high sensitivity images during the short period that the Earth is in the field of the view of the FUV camera due to the spin of the spacecraft. The FUV camera points radially outward from the spin axis of the spacecraft, which has a spin period of two minutes. In each two minute rotation a point on the Earth will be in the field of view of the WIC detector for ~ 10 seconds and the field of view of the SI camera for ~ 5 seconds. The WIC camera images the FUV aurora using a high-speed CCD, read out at 30 frames per second. WIC takes approximately 300 separate video frames while the Earth rotates in its field of view, at an exposure time of 33 ms. The distortion caused by the spin of the spacecraft is minimal for this time. All images are then superimposed on each other, offset to account for the spacecraft rotation, and electronic distortion correction is applied. Thus one image is taken in each two minute spin period over an integration period of 10 seconds. The SI detector works in a similar manner, but processes individual photons rather than whole images.

Throughout this thesis corrected counts from the IMAGE data are used, where corrections for flatfield, gain of the MCP, etc., have been applied so that one Rayleigh of emission always produces the same number of counts wherever in the CCD or MCP.

3.2 DMSP

Estimations of the latitude of the OCB from measurements of the down-going precipitating auroral particles on closed and open magnetic field lines taken by five of the Defense Meteorological Satellite Program (DMSP) satellites (F11-15) have been used in this thesis. Each satellite has a 101 minute, sun-synchronous near-polar orbit at an altitude of 830 km. The location of the OCB has been estimated by identifying the transition between precipitation originating from closed and open magnetic field lines (these regions are described in more detail in section 1.3 of this thesis). The energy of precipitating particles are measured by the Precipitating Electron and Ion Spectrometer (SSJ/4) (Hardy *et al.*, 1984).

The SSJ/4 instrument consists of four electrostatic analyzers which record the electron and ion fluxes in the range 30 eV to 30 keV. The analyzers are split into two pairs, one measuring ions and the other electrons. In each pair one detector measures the low energy fluxes while the other is the high energy detector. Each detector cycles through 10 logarithmically spaced energy channels, dwelling on each channel for 0.09 seconds and completing a full energy spectrum in one second.

3.3 LANL Spacecraft

Energetic particle measurements made by the Synchronous Orbit Particle Analyzers (SOPA) onboard the Los Alamos National Laboratory (LANL) spacecraft (Belian *et al.*, 1992) are used in this thesis to classify substorms into three categories based on their energetic particle injection signatures.

The LANL spacecraft are a set of satellites located at geosynchronous orbit ($6.6 R_E$), approximately evenly spaced in longitude around the Earth. At the time of writing over 10 satellites are currently in near-earth orbit with typically data from 3-4 satellites received simultaneously. Each spacecraft has a spin axis aligned so that it points towards the center of the Earth and has a spin period of ~ 10 seconds. The SOPA instrument (Belian *et al.*, 1992) consists of three, nearly identical, silicon solid-state-detector telescopes accepting particles from three different angles relative to the spacecraft spin axis (30° , 90° and 120°), each with a field of view of $\sim 11^\circ$. Each detector consists of a thin, $4 \mu\text{m}$, 10 mm^2 front detector followed by a thick, $3000 \mu\text{m}$, 25 mm^2 back detector surrounded by aluminium and copper shielding to exclude side-penetrating particles. Electron fluxes are measured in 10 energy channels from 50 keV to above 1.6 MeV and proton fluxes are measured in 12 channels measuring particles of 50 keV to 50 MeV. Low energy electron (6 energy channels in the range 50-500 keV, 50-75, 75-105, 105-150, 150-225, 225-315 and 315-500 keV respectively) and proton (5 energy channels from 50-400 keV, 50-75, 75-113, 113-170, 170-250 and 250-400 keV respectively) summary plots are used in chapter 5 of this thesis and examples plots are shown in Figures 5.2 to 5.4.

3.4 Measurement of Magnetic Fields

Data from several different spacecraft and ground-based observatories are used in this thesis to provide information on the strength and orientation of IMF and Earth's magnetic field. Similar measurement techniques are used in all magnetic field instrumentation used in this thesis. These techniques are summarised below.

3.4.1 The Fluxgate Magnetometer

Magnetic fields may be measured in a variety of different ways but by far the most common used today is the fluxgate magnetometer. A fluxgate magnetometer sensor is essentially a transformer wound around a high-permeability core. Two identical primary coils are wound in opposite directions around separate cores. An AC current of equal strength is passed through each coil, oppositely directed in each. The current and permeability of the cores are chosen so that the cores will reach saturation (any induced magnetic field in the cores will no longer increase with increasing current) on every one-half cycle. A secondary coil is wound around both cores such that a voltage will be induced in the secondary coil if the magnetic field produced by the two primary coils is different. In the presence of no external field the AC current will induce a magnetic field of equal strength but opposite sign in the two cores. The net field across the two cores will thus be zero and no output will be detected. However, in reality there is always a background magnetic field which will induce a background magnetic field of equal strength in the two cores. Depending on the direction of the current, the field induced by the primary coil current will add to the magnetic field of one of the cores and decrease the magnetic field in the other. This causes saturation to occur more quickly in one core, introducing a changing non-zero net field which is measured as a voltage induced in the secondary coil. Knowledge of the permeability of the cores, strength of the AC current and output voltage allows the strength of the background magnetic field parallel to the primary coil axis to be determined. In order to obtain a full 3-D picture of the magnetic field is it thus necessary to have three sensors aligned orthogonally to each other. Such magnetometers are called triaxial fluxgate magnetometers.

3.4.2 Search Coil Magnetometers

Search coil magnetometers consist of a single coil which when placed in a changing magnetic field, by Faraday's law (see Prölss, 2004), will have an induced voltage associated with it. As a voltage will only be induced in a changing magnetic field, search coil magnetometers can only provide information on the variation of the field, and not its strength.

3.5 Solar Wind Monitoring Spacecraft

In chapter 6 of this thesis we investigate the solar wind plasma and IMF conditions around substorm onset. The one-minute resolution OMNI data set has been used (see the OMNIweb page for full details of the data set and its creation; see also King and Papitashvili, 2005). The data set consists of one-minute resolution solar wind plasma and IMF data mapped to the location of the Earth's bow shock nose using the Weimer minimum variance technique (see Weimer *et al.*, 2003; Weimer, 2004; Weimer and King, 2008). Data from three spacecraft were used in the production of the data used in this thesis; the Advanced Composition Explorer (ACE), Wind and Geotail spacecraft.

3.5.1 ACE

The ACE spacecraft (Stone *et al.*, 1998), launched on the 25th of August 1997, orbits the first Lagrangian point (L1) located at $\sim 240 R_E$ sunward of the Earth. Spacecraft located at the L1 point will remain in an approximately fixed location on the Earth-Sun line allowing the constant monitoring of upstream solar wind data. Data from two of the suite of instruments onboard ACE are used in this thesis. The ACE Magnetic Field Experiment (MAG) (Smith *et al.*, 1998) provides information on the strength and orientation of the IMF. Twin triaxial fluxgate magnetometers controlled by a common CPU are mounted on the end of two separate 4.19 m long booms emanating from the center of the spacecraft. This minimises magnetic effects caused by the spacecraft. The MAG instrument takes 6 magnetic field vector measurements every second. The Solar Wind Electron Proton Alpha Monitor (SWEPAM) instrument (McComas *et al.*, 1998) provides electron and ion plasma data. Separate electrostatic analysers measure the ion

fluxes in the range 0.26-36 keV and electrons from 1-1350 eV. A full 3-D energy spectrum is produced every 64 seconds.

3.5.2 Wind

The Wind spacecraft (Franz *et al.*, 2001) was launched in November 1994 to investigate the solar wind and bow shock region. Since 2004, Wind has been in a small circular orbit at the L1 point. Prior to this the orbit varied with a closest approach to Earth of $\sim 4.5 R_E$ and apogee of $\sim 250 R_E$. The IMF is measured by the Magnetic Field Investigation (MFI) instrument (Lepping *et al.*, 1995). MFI uses the same boom-mounted dual triaxial fluxgate magnetometer system as ACE. One detector is placed at the end of a 12 m long boom, with the second half way down the boom. It is thought that the field produced by the main body of the spacecraft at this distance is only ± 0.1 nT. The solar wind plasma data are measured by the Solar Wind Experiment (SWE) instrument (Ogilvie *et al.*, 1995). Electron and proton distributions in the energy/charge range 7 V to 24.8 kV are provided by the Vector Electron and Ion Spectrometer (VEIS). Consisting of two sets of 3 small electrostatic analyzers, the ions and electrons are measured sequentially by reversing the analyzer electric field and are subsequently detected by channel electron multipliers. The plasma ‘key parameters’ (velocity, density, temperature) of solar wind ions are measured by a Faraday Cup (FC) system. A FC system essentially consists of a metal cup which will have a current induced across it when a stream of ions enters it. This current is then read and gives information on the ion flux striking the detector. Two voltages are applied across the device so that only ions which satisfy $V1 < E/Q < V2$, where $V1$ and $V2$ are the applied voltages and E and Q are the energy and charge of the incident ions, are passed to the detector allowing a full energy spectrum to be taken. The Wind FC system has an energy/charge range of 150 V to 8 kV.

3.5.3 Geotail

The Geotail spacecraft (Nishida *et al.*, 1992) was launched on the 24th of July 1994. Launched into an eccentric orbit near the ecliptic plane ($9 \times 30 R_E$ since 1995) the primary mission of the Geotail spacecraft was to investigate the structure and dynamics

of the Earth's deep tail. However, Geotail has several annual solar wind 'seasons' in which apogee is near the dayside of the Earth and Geotail enters the near-Earth solar wind. Magnetic field data are provided by the Magnetic Field Experiment (MFE), consisting of two dual fluxgate magnetometers and one search coil magnetometer which measure the magnetic field over 7 dynamic ranges from ± 16 nT to ± 65536 nT (Kokubun *et al.*, 1994).

Plasma data from the Comprehensive Plasma Instrument (CPI) was used for the data used in this thesis. In particular, the Solar Wind Ion Analyzer measures cool solar wind plasma over 64 passbands covering the range 145-6830 V (Frank *et al.*, 1994).

3.6 Ground Based Magnetometers and Geomagnetic Indices

One minute resolution AL, AU and SYM-H indices are used in chapter 6 to investigate the magnetic field signatures of substorm onset and the ring current. Data are provided by the Kyoto World Data Center for geomagnetism.

The substorm indices, AU and AL, were defined by Davis and Sugiura (1966) and provide a measure of the auroral electrojets relatively uncontaminated from effects of the ring current (Kivelson and Russell, 1995). The indices are derived from a chain of approximately 12 ground-based magnetometers, located in the polar regions (Figure 3.5 lists typical stations used and shows their location on the Earth). Traces of the H component of the magnetic field measured at each station are made. The monthly mean value from all stations is subtracted from each individual trace so that they are plotted relative to a common baseline. The AL index is then defined at any one instant as the largest negative excursion of any of the traces from the baseline, and the AU index is defined as the maximum positive excursion. Negative excursions in the H component occur under a westward travelling current and positive excursions occur under an eastward travelling current, therefore the AU and AL indices provide a measure of the strength of the eastward and westward electrojets respectively.

The SYM-H index measures the perturbation of the north south component of the Earth's magnetic field at the equator and is essentially the same as the hourly Dst index but with one-minute resolution (Wanliss *et al.*, 2006). At the equator the ring current

TABLE 1 - List of AE(12) Stations.

Observatory	IAGA Code	Geographic Coord.		Geomagnetic Coord.	
		Lat.(°N)	Long.(°E)	Lat.(°N)	Long.(°E)
Abisko	ABK	68.36	18.82	66.04	115.08
Dixon Island	DIK	73.55	80.57	63.02	161.57
Cape Chelyuskin	CCS	77.72	104.28	66.26	176.46
Tixie Bay	TIK	71.58	129.00	60.44	191.41
Cape Wellen	CWE	66.17	190.17	61.79	237.10
Barrow	BRW	71.30	203.25	68.54	241.15
College	CMO	64.87	212.17	64.63	256.52
Yellowknife	YKC	62.40	245.60	69.00	292.80
Fort Churchill	FCC	58.80	265.90	68.70	322.77
Poste de la Baleine	PBQ	55.27	282.22	66.58	347.36
Narsarsuaq (Narssarsuaq)	NAQ	61.20	314.16	71.21	36.79
Leirvogur	LRV	64.18	338.30	70.22	71.04

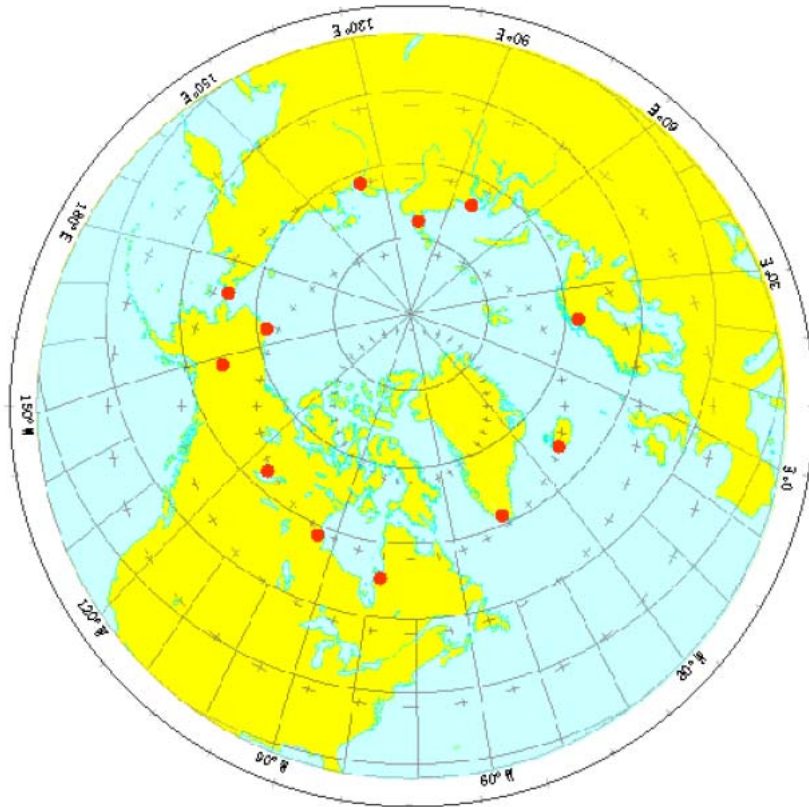


Figure 3.5: Typical polar geomagnetic observatories used in determining the AL and AU substorm indices (from Auroral Electrojet (AE) Indices for January – December 1992 (provisional), WDC for Geomagnetism, Kyoto).

causes the largest perturbations in the magnetic field and thus the SYM-H index is a measure of the strength of the ring current. The SYM-H index is essentially determined in the same way as the AL and AU indices using a set of approximately 12 magnetometer stations distributed over the Earth in non-polar regions. Figure 3.6 shows properties of typical stations used in the calculation of SYM-H and their location. The calculation of a baseline value becomes more complicated for SYM-H as the secular and diurnal magnetic field fluctuations can be as large as fluctuations caused by large geomagnetic storms. For a full explanation of this procedure see Kivelson and Russell (1995).

TABLE 1.

STATION NAME	ABB CODE	G.G. LAT.	G.G. LONG.	G.M. LAT.	G.M. LONG.	INVARIANT LAT.	ROTATION ANGLE
San Juan	SJG	18.4	293.9	29.1	5.2	32.5	-8.9
Fredericksburg	FRD	38.2	282.6	49.1	352.2	50.4	0.4
Boulder	BOU	40.1	254.8	48.7	319.0	49.1	2.5
Tucson	TUC	32.3	249.2	40.4	314.6	39.7	2.7
Honolulu	HON	21.3	202.0	21.5	268.6	20.2	0.5
Memambetsu	MMB	43.9	144.2	34.6	210.2	34.9	-16.1
Urumqi	WMQ	43.8	87.7	33.7	162.0	36.5	7.66
Alibag	ABG	18.6	72.9	9.9	145.8	—	6.8
Martin de Vivies	AMS	-37.8	77.6	-46.9	142.8	48.6	-32.4
Hermanus	HER	-34.4	19.2	-33.7	82.7	43.6	-10.1
Chambon-la-Foret	CLF	48.0	2.3	50.1	85.7	45.7	13.6

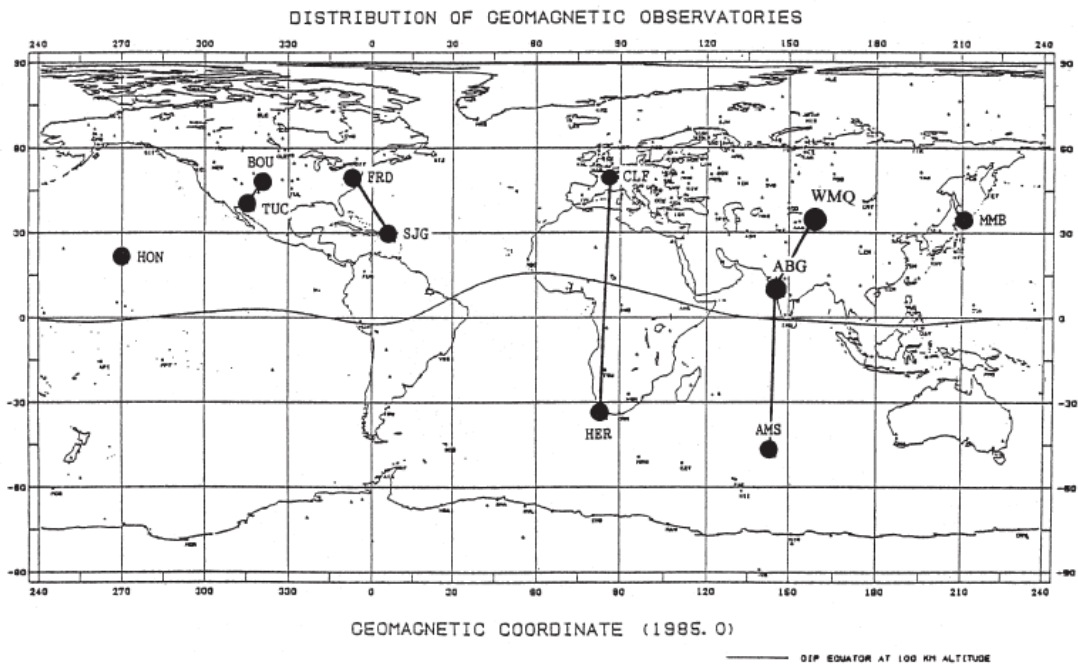


Figure 3.6: Typical geomagnetic observatories used in determining the SYM-H index (from Mid-latitude Geomagnetic Indices “ASY” and “SYM” (Provisional) No. 19 (2008), Data Analysis Center for Geomagnetism and Space Magnetism Graduate School of Science Kyoto

Chapter 4. Estimating the Latitude of the Open/Closed Magnetic Field Line Boundary in the Ionosphere

The location of the open/closed magnetic field line boundary (OCB) is an important diagnostic tool for magnetospheric physics. Observations of its motion and location are widely used in theories of solar wind-magnetospheric-ionospheric coupling and dynamics. For example, it may be used to determine global and local day and nightside reconnection rates (e.g. Milan *et al.*, 2003; Hubert *et al.*, 2006) as well as provide estimates of the open magnetic flux content of the magnetosphere (e.g. Milan *et al.*, 2004, 2008), one of the main aims of this thesis. The accurate determination of its location is therefore of prime importance.

Many different ionospheric measurements have been used over the years to provide a proxy for the location of the OCB. A summary of these techniques is given in section 2.3 of this thesis. Particle precipitation boundaries (PPBs) measured by low-altitude spacecraft (such as the Defence Meteorological Satellite Program (DMSP) spacecraft) provide the most direct and precise determination of boundaries between different plasma regions, including the OCB. However, these spacecraft only cross the OCB in two magnetic local time (MLT) sectors in each hemisphere in any one orbit (~100 minutes for the DMSP satellites) and therefore cannot be used to determine the global location of the OCB.

Currently, the best method for estimating the global location of the OCB in any one hemisphere is from global auroral imagery provided by orbiting spacecraft (e.g. Carbary *et al.*, 2003; Milan *et al.*, 2003, 2004, 2008; Hubert *et al.*, 2006). However, recent studies have shown that systematic offsets of up to a few degrees exist between the location of the OCB as estimated from satellite imagery and as estimated from PPBs (e.g. Kauristie *et al.*, 1999; Baker *et al.*, 2000; Carbary *et al.*, 2003). Carbary *et al.* (2003) studied the statistical discrepancy between the DMSP OCB proxies and an OCB proxy derived from auroral images taken in the Lyman-Birge-Hopfield “long” (LBHL) band (164-178 nm) by the Ultra-Violet Imager (UVI) on the Polar spacecraft. They showed that the largest discrepancy occurs in the predawn sector ionosphere, with the DMSP proxy found up to ~ 3.5° poleward of the UVI proxies at 0500 MLT. A very

similar discrepancy was found in the predawn sector ionosphere by Chisham *et al.* (2005a,b), comparing the DMSP OCB proxy with an OCB proxy provided by the Super Dual Auroral Radar Network (SuperDARN) Spectral Width Boundary (SWB). Wild *et al.* (2004) presented a case study in which the latitudes of both the SWB OCB proxy and the OCB estimated using the Wideband Imaging Camera (WIC) (140-160 nm) onboard the Imager for Magnetopause-to-Aurora Global Exploration (IMAGE) spacecraft were placed several degrees equatorward of the OCB PPB proxies determined from Cluster, DMSP and FAST spacecraft measurements obtained simultaneously in the predawn sector. However they showed that the OCB determined from the Spectrographic Imager SI13 (~133-138 nm) on board IMAGE was closely co-located with the OCB PPB proxies. They concluded that in the dawn sector ionosphere the SWB and the poleward boundary of auroral emissions measured by WIC were unreliable proxies for the OCB in this case, with the poleward boundary of SI13 emissions providing a more accurate proxy. Other studies have used the poleward boundary of SI12 auroral emission (~119-124 nm) in preference to WIC or SI13 OCB proxies due to the reduced level of dayglow, making boundary estimation possible even in summer months (Hubert *et al.*, 2006). However, these studies did not consider if SI12 gave the most reliable estimation of the OCB location. Using IMAGE FUV data, Mende *et al.* (2003) also noted that the proton aurora was found to be displaced equatorward of the electron aurora for dusk local times and poleward for dawn local times during all phases of substorms.

The aim of this chapter is to investigate the accuracy of using IMAGE FUV observations of the global auroral oval to determine the location of the OCB. Based on the work of Carbary *et al.* (2003) with Polar UVI auroral images, we firstly develop an automated method of identifying the OCB from IMAGE FUV images. A statistical comparison of the OCB as estimated from the three different FUV detectors onboard IMAGE is then performed. To assess the accuracy of the FUV OCB estimation method we then compare the FUV OCB proxies with OCB proxies determined from direct measurement of precipitating particles made by the DMSP satellites. Combining the results of these two studies, we find systematic offsets between the FUV and DMSP OCB proxies which can be used to 'correct' FUV OCB proxies to give a more accurate estimation of the location of the OCB in any one MLT sector.

4.1 A Method for Identifying the Location of the Open/Closed Magnetic Field Line Boundary in the Ionosphere from IMAGE FUV Auroral Images

4.1.1 Instrumentation and Data Set

Auroral imagery of the northern polar cap made by the three FUV detectors onboard the IMAGE spacecraft are used in this study. The Wideband Imaging Camera (WIC) and spectrographic imagers, SI12 and SI13, are described in detail in chapter 3. WIC views the aurora in the 140-180 nm wavelength range, auroral emissions in this bandwidth are largely from electron transitions. The Spectrographic Imager SI12 observes the proton aurora with a pass band of 5 nm centered on 121.82 nm and the spectrographic imager SI13 observes the ‘excited electron aurora’ with a pass band of 5 nm centered on the 135.6 nm. WIC offers the best spatial resolution of approximately 50 km at apogee, compared to approximately 100 km offered by both spectrographic imagers.

The IMAGE spacecraft was operational from May 2000 to December 2005, when the spacecraft failed. In this study we use northern hemisphere data from December 2000 and the January and December months of 2001 and 2002 (see Figure 3.1). After this date the camera pointing became less reliable such that the position of the auroral oval may be offset from its true position by up to 1° of latitude. This resulted from the development of a complicated wobble in the spin axis of the spacecraft (the IMAGE spacecraft had four long (250 m) antennas positioned 90° apart protruding from the main body of the spacecraft and kept stable by the centripetal force of the 2 minute spin period. At times these antennas had a tendency to snap, causing the weight distribution of the spacecraft to become uneven and resulting in a hard to characterise wobble in the spin axis). We only use images from December and January as dayglow is much less prominent in these months; whilst in other months dayglow often swamps the dayside auroral oval, particularly in the WIC data, making the estimation of the dayside OCB latitude impossible.

4.1.2 Methodology

The method used by Carbary *et al.* (2003) to identify the location of the OCB from Polar UVI (Torr *et al.*, 1995) global auroral imagery forms the basis of the method we

develop to identify the OCB from IMAGE FUV auroral imagery. Although this method was developed using data from the Polar spacecraft, Lam *et al.* (2006) have shown that the same method can be successfully applied to other auroral imagers.

The first step is to create intensity-latitude profiles of the IMAGE FUV auroral oval by averaging intensities (corrected counts are used throughout this thesis, see section 3.1.3) in bins of one degree of magnetic latitude and one hour of MLT. Examples of intensity-latitude profiles are shown in Figure 4.1 (a-c), where the binned data are represented by diamonds. AACGM coordinates (Baker and Wing, 1989) are used throughout this thesis. The solid curves in Figure 4.1 (a-c) represent a fit to the binned data using a non-linear least-square fit (using the IDL Gaussfit routine) to the following function:

$$T(\lambda) = A_0 \exp\left[-\frac{1}{2}\left(\frac{\lambda - A_1}{A_2}\right)^2\right] + A_3 + A_4\lambda + A_5\lambda^2 \quad (4.1)$$

where λ is the magnetic latitude and A_0 - A_5 are coefficients of the fit. The Gaussian part of equation 4.1 is assumed to represent the auroral oval and the quadratic background is assumed to include extraneous airglow, off-axis radiance, or unwanted non-oval aurora. A fit is assumed to be successful if the following criteria are satisfied:

1. The intensity of the Gaussian peak, A_0 , exceeds 5 counts.
2. The magnetic latitude of the peak of the Gaussian, A_1 , is between 50° and 85° magnetic latitude.
3. The Gaussian full-width-at-half-maximum (FWHM) ($\Delta\lambda = 2A_2\sqrt{2\ln 2}$, where A_2 is the width of the Gaussian) exceeds 1° .
4. The ratio of the background at the center of the Gaussian ($B = A_3 + A_4.A_1 + A_5.A_1^2$) to the peak of the Gaussian, A_0 , does not exceed 0.2.
5. The Gaussian width spans less than 30% of the latitude bins which have non-zero intensity, $\Delta\lambda < 0.3(\lambda_{\max} - \lambda_{\min})$.

The latitude of the OCB, λ_{OCB} (shown by the vertical lines in Figure 4.1 (a-c) and overplotted on the auroral images (Figure 4.1 (d-f)) by diamonds), is assumed to be displaced poleward of the centre of the Gaussian by the Gaussian FWHM such that

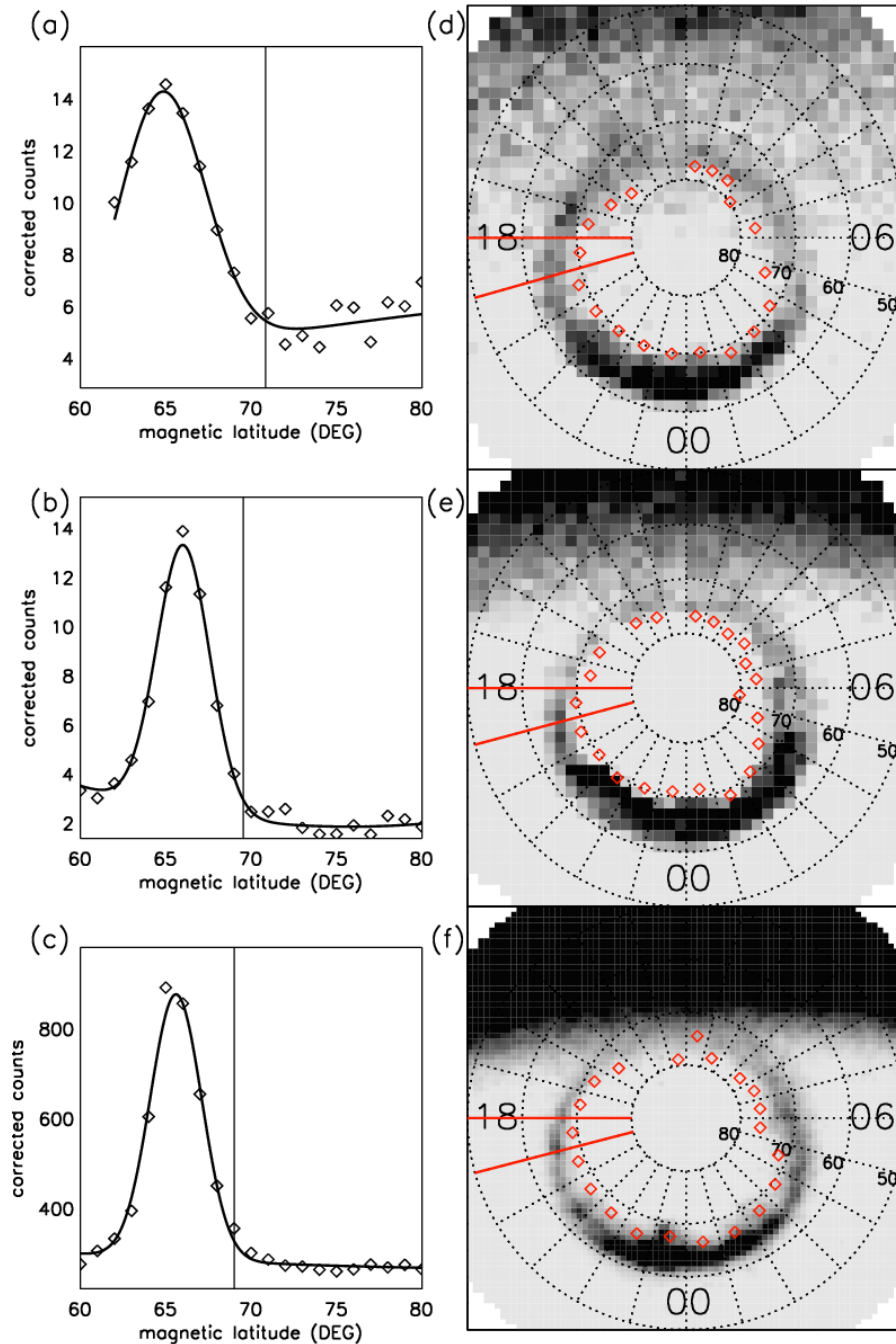


Figure 4.1: (a-c) Intensity-latitude profiles (left-hand column) across a 1 hour MLT sector (1800-1900 MLT) and (d-f) images of the auroral oval (right-hand column), with magnetic local noon at the top of the figure, for 20:40:09 on 26 December 2000. Rows correspond to data from three different IMAGE FUV detectors, SI12 (top), SI13 (middle) and WIC (bottom). Average intensities in bins of one degree magnetic latitude are shown by diamonds and the Gaussian plus quadratic background fits to these points are shown by the solid curves. The position of the OCB proxies are marked by the vertical solid lines and overplotted on the auroral images by red diamonds.

$$\lambda_{OCB} = A_1 + \Delta\lambda . \quad (4.2)$$

By visually inspecting the data, it can be seen that on occasion the FUV OCB estimation method produces a latitude profile meeting the given criteria above but which results in an apparently inaccurate boundary estimation (displaced several degrees in latitude from the location estimated by eye). Two particular reasons have been identified as contributing to this error and these have been correct for in the following manner:

(1) The auroral oval can often display a double oval configuration (Elphinstone *et al.*, 1995), particular on the nightside, where the auroral oval consists of two bright bands or partial ovals of emission separated by a dark band. This causes the intensity-latitude profiles to have a multiple peaked nature with two or more Gaussian like components. Normally the Gaussian fitting procedure will fit to the most equatorward peak and include the more poleward peaks in the quadratic background part of the fit. To find the most accurate location of the OCB these poleward peaks must be included in the Gaussian part of the fit. This is achieved by searching for the most poleward peak meeting the criteria 1-5 as follows. The intensity-latitude profile must decrease in intensity over at least two degrees of magnetic latitude in the poleward direction from the latitude of the last peak found, followed by an increase over at least two degrees of latitude. Once a new maximum in intensity is found the intensity must decrease again over at least two degrees of magnetic latitude. The Gaussian fitting procedure is then applied to the most poleward peak identified below 85° magnetic latitude by including only latitudes more poleward of the minimum between the most poleward peak and the previous peak in the fitting routine. This will also effectively remove dayglow from intensity-latitude profiles when a clear drop in intensity exists between the poleward edge of dayglow and the equatorward edge of the auroral oval.

(2) Dayglow often extends close to or onto the auroral oval, often completely swamping it in the summer months. The noise associated with the dayglow can be larger than the auroral signature itself. In most cases the criteria 1-5 reject any identification of the OCB. However occasionally this is not the case and the Gaussian function is fit to the

dayglow emission rather than the auroral oval emission, placing the OCB estimate at the poleward edge of the dayglow, as seen at 1100-1200 MLT in Figure 4.1 (f). Extra criteria are used to try to eliminate these cases as follows. On the dayside (0600-1800 MLT) an OCB proxy is rejected if it has been placed over five degrees poleward or equatorward of the proxy found in the previous MLT sector. If the previous MLT sector has not produced a proxy the nearest MLT within 4 MLT sectors that has produced a proxy is used. If there are no previous estimations of the OCB within four MLTs of the tested MLT sector the MLT sector tested is rejected.

If an OCB proxy has not been identified at this point, in a bid to remove dayglow, the lower limit of latitudes included in the fitting procedure is increased in steps of one degree until an estimation of the OCB can be found (by reapplying all the above FUV OCB estimation method) up to a maximum latitude lower limit of 80° . A similar correction as above is applied on the nightside, 0000-0600 MLT and 1800-2400 MLT, if the OCB is located over 8° poleward or equatorward of adjacent MLTs. The larger value on the nightside is used as we find, from visual inspection, that the latitude of the OCB can genuinely change by between 5-8 degrees, particularly around the auroral bulge where at substorm onset the latitude of the OCB is rapidly changing.

These extra criteria remove many erroneous OCB estimations. However, not all bad estimations are caught, as seen in Figure 4.1 (f) 1100-1200 MLT, where the OCB proxy is placed equatorward of the poleward edge of the WIC auroral emission but is just within the five degree condition. These criteria will also not catch poorly estimated OCB proxies if several poorly estimated proxies have been made in several adjacent MLT bins.

4.2 Statistical Comparison of IMAGE FUV OCB proxies

In this section we compare the estimate of the OCB latitude from the three different FUV detectors, WIC, SI12 and SI13. The FUV OCB estimation method described above is applied to every FUV auroral image obtained by the IMAGE spacecraft from the months of December 2000 and December and January 2001-2002. Comparing FUV OCB proxies from different detectors at the same UT and MLT gives a total of 499273 comparisons between WIC and SI12 OCB proxies, 543505 comparisons between WIC

and SI13 OCB proxies and 408753 comparisons between SI12 and SI13 OCB proxies, with over 4000 comparisons at each hour of MLT.

Let us define the latitude of WIC, SI12 and SI13 OCB proxies as λ_{WIC} , λ_{SI12} and λ_{SI13} respectively. Figure 4.2 shows distributions of the latitude differences between matched WIC and SI12 OCB proxies ($\lambda_{WIC} - \lambda_{SI12}$) for four 1-hour MLT bins. Positive values of latitude difference are defined such that the WIC OCB proxy is at higher latitudes than the SI12 OCB proxy. Crosses in Figure 4.2 represent the number of occurrences of latitude differences between WIC and SI12 OCB proxies in bins of 0.2° magnetic latitude. In order to reduce small statistical uncertainty smoothing has been applied to the distributions three times using boxcar averaging over five points. Large boundary differences can be seen in the tails of these distributions. Visual inspection of these points shows that they occur when a poor boundary estimation has been made, and has not been caught by the criteria discussed above, in one or both of the FUV cameras. We characterise the latitude difference between the FUV OCB proxies by the mode of the distribution (shown by the red vertical lines in Figure 4.2), since this is insensitive to the presence of these outliers. Black vertical lines represent the mean of the distributions.

Figure 4.3 shows the variation of the modal FUV OCB proxy latitude differences with MLT, for $\lambda_{WIC} - \lambda_{SI12}$ (blue), $\lambda_{WIC} - \lambda_{SI13}$ (black) and $\lambda_{SI13} - \lambda_{SI12}$ (orange). To put the variation in context we also provide some information on the width of the distributions and the error on the mode. The width of the latitude difference distributions (Figure 4.2) is estimated by moving out from the mode (red line Figure 4.2) in steps of one 0.2 degree bin in both positive and negative directions to find the latitude range within which 68% of the points lie (which would be equal to the standard deviation for a Gaussian). We estimate the error on the mode by dividing the width by \sqrt{N} , where N is the number of points in each bin of MLT (equivalent to the standard error on the mean for a Gaussian). The estimated widths are approximately 2° and the estimated errors on the mode are $<0.01^\circ$.

The modal latitude differences between WIC and SI13 OCB proxies (black curve Figure 4.3) are relatively small, $<0.8^\circ$. This is not unexpected as both view auroral emission excited by electron emission. Larger latitude differences are found between

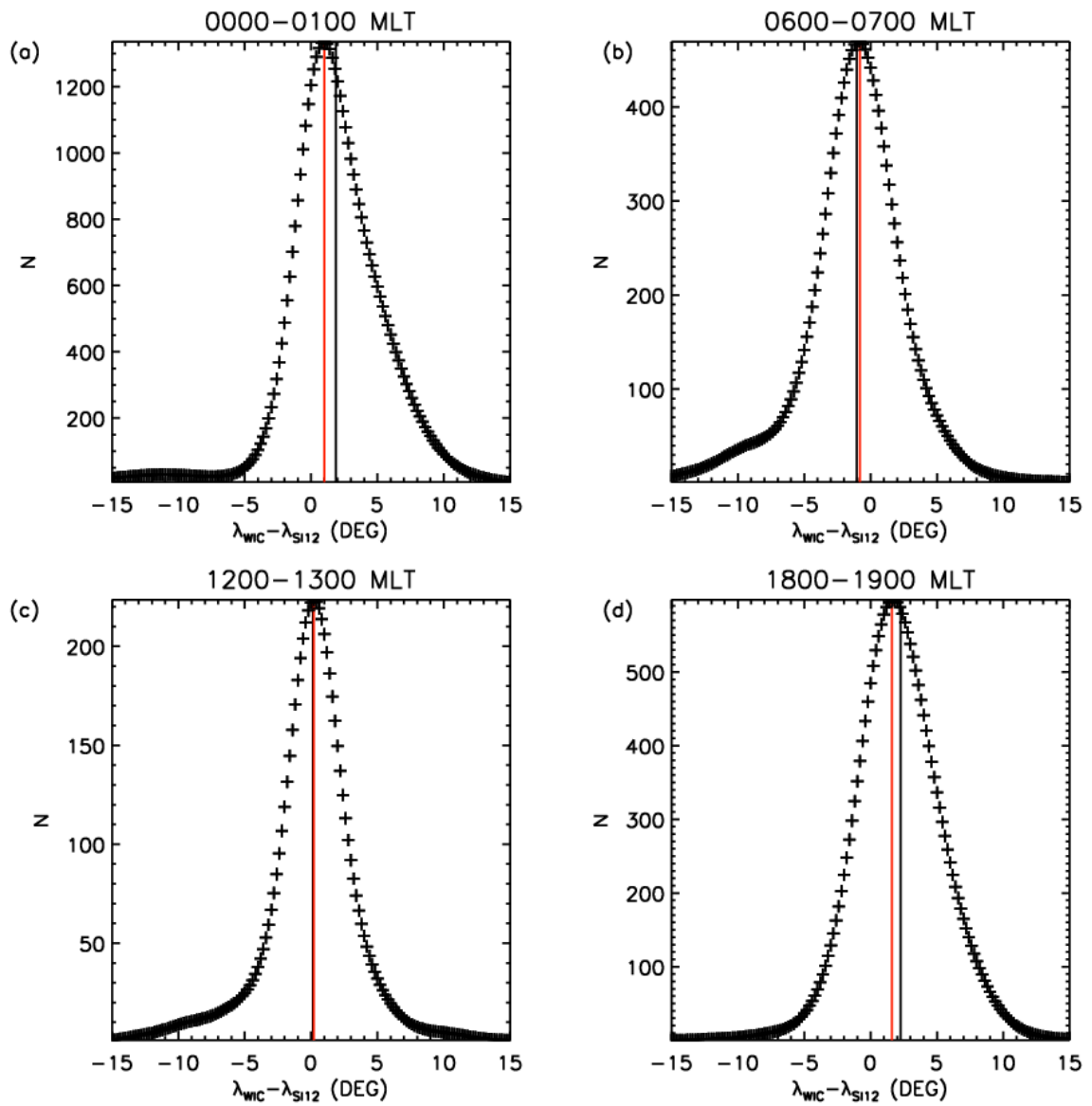


Figure 4.2: Frequency distribution of the difference between the latitude of WIC and SI12 OCB proxies for 0000-0100, 0600-0700, 1200-1300 and 1800-1900 MLT. Crosses represent the number of boundary differences in 0.2° bins of magnetic latitude, red vertical lines represent the mode of the distribution and black vertical lines the mean.

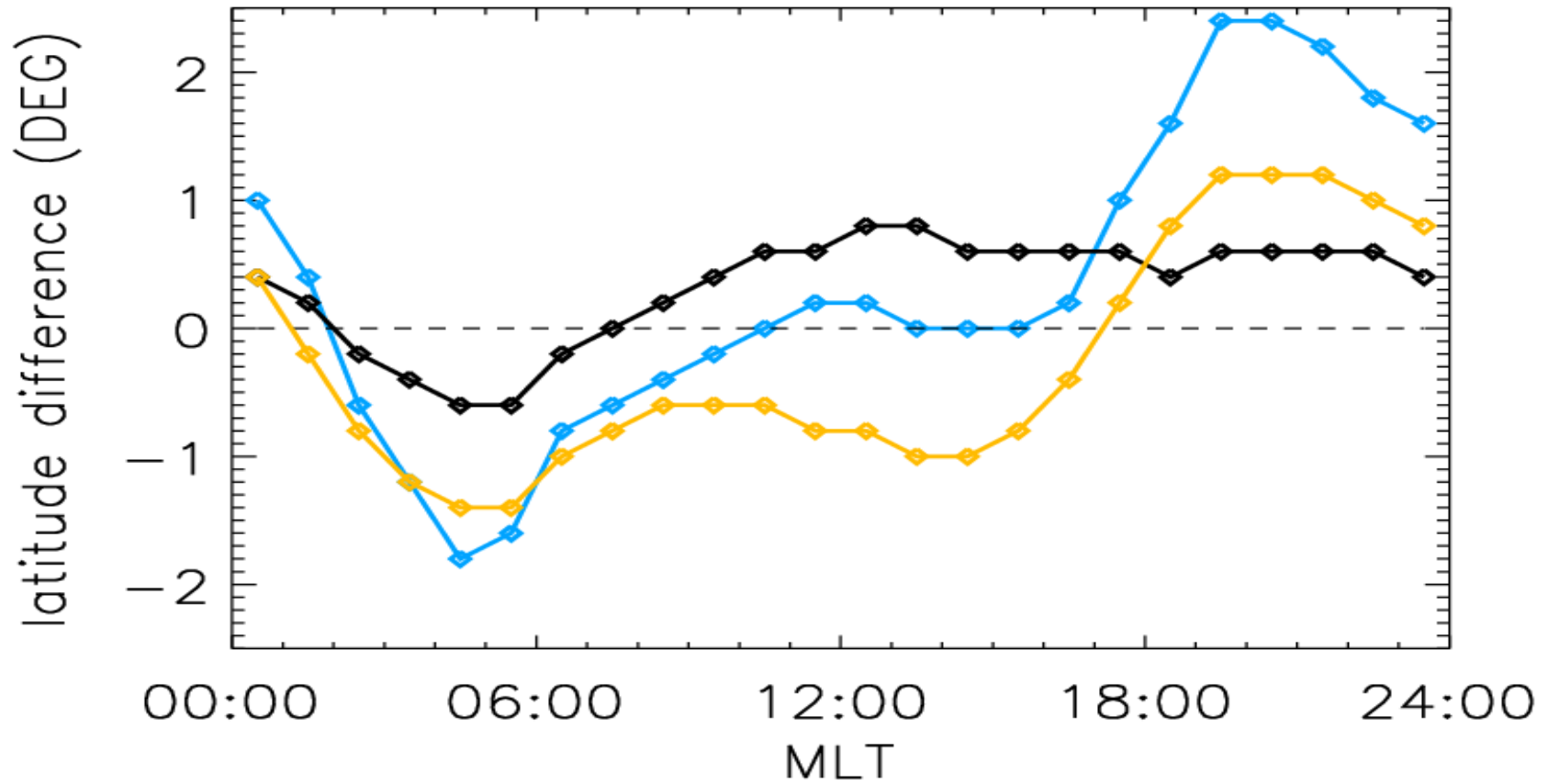


Figure 4.3: Mode of OCB proxy latitude differences for $\lambda_{WIC}-\lambda_{SI12}$ (blue), $\lambda_{WIC}-\lambda_{SI13}$ (black) and $\lambda_{SI13}-\lambda_{SI12}$ (orange). The estimated widths of the distributions (explained in the text) are of order 2° and the estimated errors on the modes are $< 0.01^\circ$.

the proton aurora OCB proxies (SI12) and the SI13 or WIC OCB proxies (electrons aurora). Modal latitudinal differences between WIC and SI12 OCB proxies and between SI13 and SI12 OCB proxies (blue and orange curves respectively) are small in the 0700-1700 MLT range. In the predawn sector SI12 boundaries are found to be located poleward of both WIC and SI13 by between 1° - 2° . Conversely SI12 boundaries are also found to be located at greater than 1 degree equatorward of both WIC and SI13 in the 1800-2300 MLT range. We discuss these offsets further in section 4.5.

4.3 Comparison with DMSP Auroral Boundaries

Global auroral imagery is currently the only method via which the entire auroral oval of one hemisphere can be viewed simultaneously by a single instrument and is hence currently the best method of accurately estimating the global location of the OCB. However, as discussed above, recent studies have shown that systematic offsets of up to a few degrees exist between the latitude of the OCB as estimated from global auroral imagery in the FUV wavelength range and the latitude of the OCB as estimated from PPBs (thought to be the most direct and precise measurement of the OCB). In this section we compare the latitude of the OCB as estimated by our IMAGE FUV method and the latitude of the OCB as estimated from PPBs from the DMSP spacecraft.

Sotirelis and Newell (2000) used automated techniques to identify the location of different auroral boundaries (including the OCB) from the energy flux of down-going polar precipitating particles as seen by particle analyzers onboard the DMSP satellites. The location of the OCB was determined using the definition of different ionospheric precipitation regions described by Newell *et al.* (1991a) and Newell *et al.* (1996), discussed in section 1.3 and summarised in Figure 1.10 of this thesis. On the nightside, the OCB is given by the b6 boundary of Newell *et al.* (1996), which marks the transition from the poleward edge of the sub-visual drizzle region to particle fluxes below detectable levels or the first encounter with polar rain (see Figure 1.10). On the dayside the OCB is given by the doc (dayside open/closed) boundary, located where there is an unambiguous transition between precipitation characteristic of open and closed field lines. The central plasma sheet, boundary plasma sheet and low latitude boundary layer (LLBL) are considered to be closed, and cusp, mantle, open LLBL, polar rain and void (a lack of precipitating particles) are considered to be open. If any of

these transitions are not clear, because of ambiguities in the region, then an OCB proxy is not identified (Chisham *et al.*, 2005b). Data from five DMSP spacecraft (F11-15) for the years 2000-2001 were used in this study. For a full description of the DMSP satellites and their SSJ/4 particle analyzers see section 3.2 of this thesis.

DMSP OCB proxies are compared to the closest (in both UT and MLT) FUV OCB proxy within ± 0.5 hours of MLT and ± 10 minutes of UT, producing over 1700 comparisons for each FUV detector. However, due to the orbit of the DMSP spacecraft, no DMSP boundaries are available in the northern hemisphere between 2200 and 0500 MLT.

The latitude differences are binned into bins of 0.5° . To reduce the statistical uncertainty and produce a smooth distribution with one clear peak the distributions have been smoothed three times using a boxcar average over five points. Figure 4.4 shows example distributions of latitude differences between DMSP and WIC OCB proxies for four 1-hour MLT bins, where λ_{DMSP} is the latitude of the DMSP OCB proxy. The smoothed latitude differences are shown by the crosses and vertical lines show the mean (black) and modes (red) of the distributions. The distributions are skewed to the right such that there is a higher probability of finding a DMSP OCB proxy at a significantly higher latitude than the equivalent FUV proxy than there is of finding an FUV OCB proxy at a higher latitude. We find three possible factors which may contribute to these large differences:

1. The method of FUV OCB proxy estimation. When a poor FUV OCB proxy estimation is made (and is not caught by the criteria discussed in section 4.1.2) it is nearly always placed equatorward of the poleward edge of the auroral oval emission and is therefore more equatorward of the equivalent DMSP boundary than should be the case.
2. The use of finite MLT and UT windows in the comparison procedure. The fine scale structure of the OCB may change by small amounts over these window sizes. Reducing the size of the windows reduces the width of the distributions but also reduces the number of comparisons available.

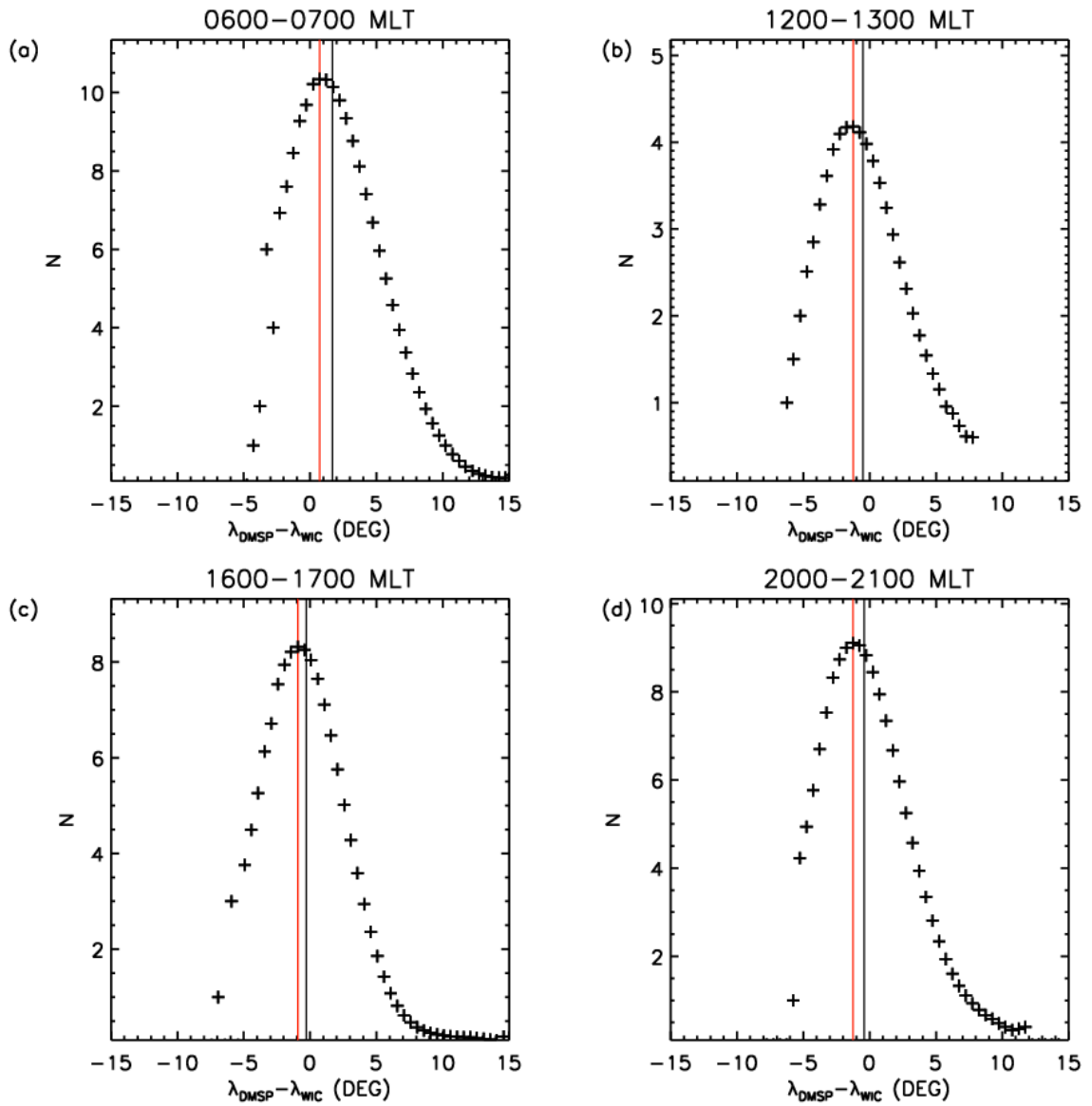


Figure 4.4: Smoothed frequency distributions for $\lambda_{DMSP} - \lambda_{WIC}$ for (a) 0600–0700 MLT, (b) 1200–1300 MLT, (c) 1600–1700 MLT and (d) 2000–2100 MLT in bins of 0.5° magnetic latitude. Vertical black lines show the mean of the distributions and red lines represent the mode.

3. Failure of the DMSP OCB estimation procedure. The DMSP OCB estimation is made using an automatic algorithm which will occasionally fail.

The mean of the distributions, shown by the black vertical lines, is shifted towards this tail. We therefore use the mode of the distributions, shown by the red vertical lines, to characterise the centre of the distribution.

Figure 4.5 (a-c) shows the variation with MLT of the modal latitude differences between the FUV and DMSP OCB proxies. The horizontal lines at the center of the estimated error bars represent the mode of the latitude differences in bins of 1 hr MLT. Thin error bars represent the estimated width and the thick error bars represent the estimated error on the mode as explained in section 4.2. Due to the relatively low number of DMSP-FUV OCB proxy comparisons the estimated widths are fairly large (3° - 4°), exceeding the size of the offsets themselves, although the estimated error on the mode is smaller ($<1^{\circ}$).

Following the method set out by Carbary *et al.* (2003), a continuous function is fitted to the data which extrapolates into MLTs where no DMSP boundaries are available. A weighted second-order harmonic fit is applied to the modal latitude differences using a least squares fit,

$$L(\varphi) = C_0 + C_1 \cos \varphi + D_1 \sin \varphi + C_2 \cos 2\varphi + D_2 \sin 2\varphi \quad (4.3)$$

where φ is the angle associated with the MLT ($\equiv MLT \times 15^{\circ}$), and C and D are coefficients of the fit. Weights are $n/\max(n)$ where n is the number of boundary comparisons in each one hour MLT bin. The harmonic coefficients determined by Carbary *et al.* (2003) were used as initial starting values for the fitting routine and are listed with the final coefficients in Table 4.1 along with the number of OCB proxies compared for each detector (N). Figure 4.5 (d) shows the resultant fits and the fit of Carbary *et al.* (2003) for the case of DMSP and Polar UVI OCB proxies (dashed blue line).

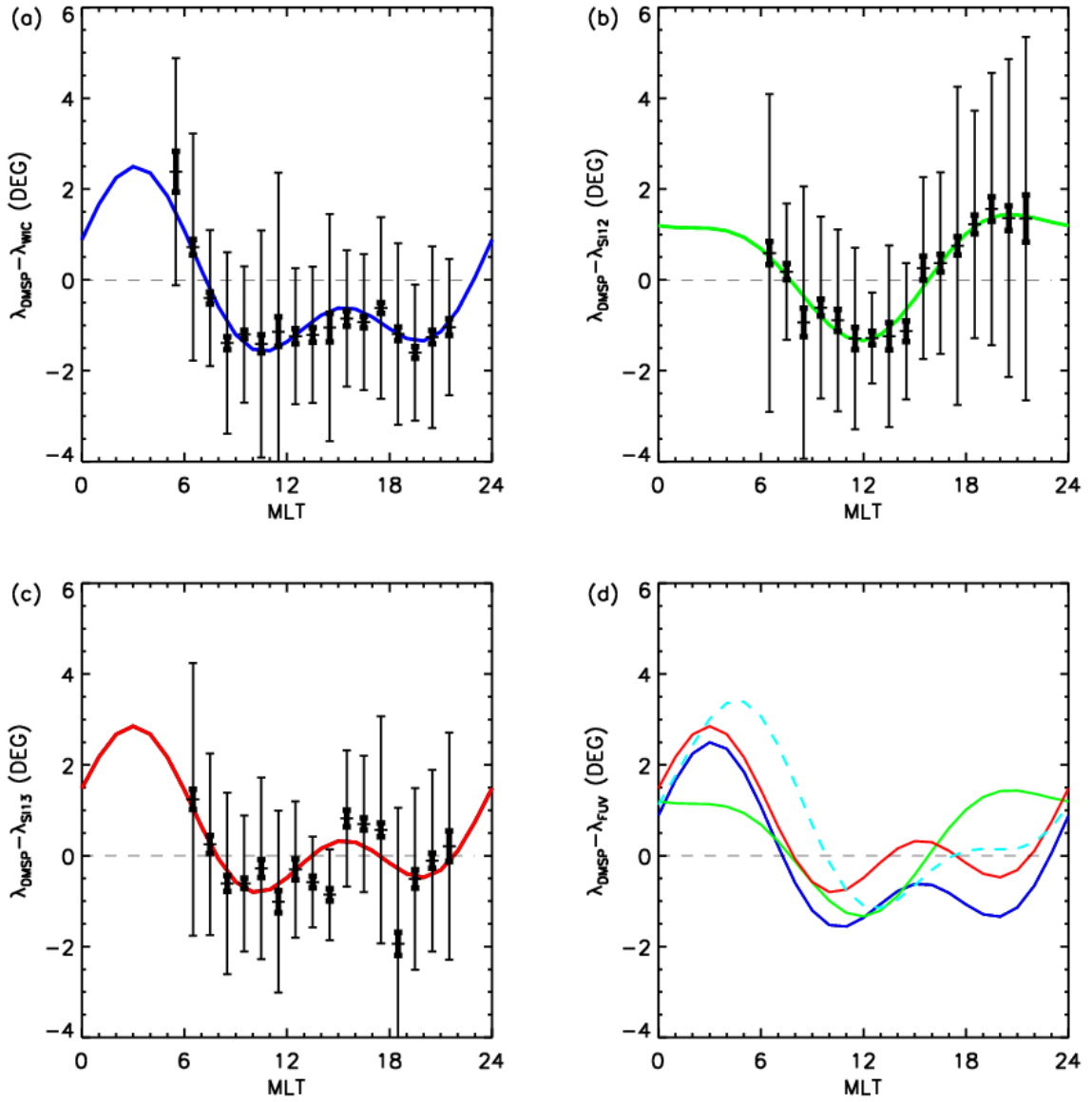


Figure 4.5: Modes of OCB proxy latitude differences between FUV and DMSP, (a) $\lambda_{DMSP} - \lambda_{WIC}$, (b) $\lambda_{DMSP} - \lambda_{SI12}$ and (c) $\lambda_{DMSP} - \lambda_{SI13}$. Bold error bars represent the estimated error on the mode and thin error bars represent the estimated widths (see text for details). Second order harmonic fits to the OCB proxy latitude differences are shown by solid curves and compared to the fit of Carbary *et al.* (2003) (dashed light blue line) in Figure (d).

Table 4.1: Coefficients of the weighted second-order fit to modal latitude differences between DMSP OCB proxies and Polar UVI proxies (from Carbary *et al.*, 2003) and IMAGE FUV OCB proxies. N is the number of OCB proxies compared in each comparison.

	Carbary <i>et al.</i> (2003)	WIC	SI12	SI13
C ₀	0.80	-0.12	0.39	0.57
C ₁	1.11	1.13	1.27	0.99
D ₁	1.48	1.08	-0.17	0.80
C ₂	-0.79	-0.12	-0.46	-0.07
D ₂	0.38	1.06	-0.03	1.02
N	11244	2462	1704	1838

Latitude differences between DMSP and WIC or SI13 OCB proxies display systematic deviations grossly consistent with the previous DMSP-UVI study (Carbary *et al.*, 2003), with the largest deviations occurring in the predawn sector. Between 0700 and 2300 MLT the fits to latitude differences typically differ by less than a degree. In contrast the average latitude difference between DMSP and SI12 is larger in the evening sector (1600-2400 MLT) and smaller in the morning sector (0-7 MLT), by up to 2°.

4.4 Boundary Optimization

In order to test the validity of our IMAGE FUV OCB approximation method, we wish to compare the latitude of the OCB as estimated by our method with the true location of the OCB. Above, we find systematic offsets between the FUV and DMSP OCB proxies consistent with previous studies (e.g. Carbary *et al.*, 2003). Assuming the DMSP OCB proxy to be the best estimate of the OCB, we believe that these offsets give a good approximation to the offset between FUV OCB proxies and the true location of the OCB and may be used to provide a ‘correction’ to FUV OCB proxies to provide a more accurate global estimation of the OCB. However, at individual MLTs there are inconsistencies between the DMSP-FUV comparisons and the inter-FUV comparisons. That is, if both results were completely consistent, then the curves of Figure 4.5 should be consistent with the curves of Figure 4.3, such that the curve of $(\lambda_{DMSP} - \lambda_{SI12})$ minus the curve of $(\lambda_{DMSP} - \lambda_{WIC})$ from Figure 4.5 should lie exactly on top of the curve of $(\lambda_{WIC} - \lambda_{SI12})$ of Figure 4.3. However, this is not seen with small discrepancies found at several MLTs. Given the considerably larger number of comparisons used in the inter-FUV comparisons it is desirable to use these results to enhance our best estimate of the systematic offsets of the FUV OCB proxies from the (unknown) true location of the OCB. We do this by considering characteristic latitudinal offsets of the WIC, SI12, SI13 and DMSP proxies, which we designate as W , P , E , and D respectively.

Relating the characteristic latitudinal offsets W , P , E , and D at each MLT to the values shown in Figures 4.3 and 4.5 produces the following set of equations;

$$W - P = \langle \lambda_{WIC} - \lambda_{SI12} \rangle + a = x_1 + a \quad (4.4)$$

$$W - E = \langle \lambda_{WIC} - \lambda_{SI13} \rangle + b = x_2 + b \quad (4.5)$$

$$P - E = \langle \lambda_{SI12} - \lambda_{SI13} \rangle + c = x_3 + c \quad (4.6)$$

$$D - W = \langle \lambda_{DMSP} - \lambda_{WIC} \rangle + d = x_4 + d \quad (4.7)$$

$$D - P = \langle \lambda_{DMSP} - \lambda_{SI12} \rangle + e = x_5 + e \quad (4.8)$$

$$D - E = \langle \lambda_{DMSP} - \lambda_{SI13} \rangle + f = x_6 + f \quad (4.9)$$

where a , b , c , d , e , and f are unknown measurement errors and $\langle \rangle$ indicate an ensemble property, for which the mode has been used. Comparing the curves in Figure 4.3 shows that the unknown errors, a , b , and c are insignificant (that is, for the blue, black and orange curves in Figure 4.3 respectively, $(\lambda_{WIC} - \lambda_{SI12}) - (\lambda_{WIC} - \lambda_{SI13}) = (\lambda_{SI13} - \lambda_{SI12})$), and so these were set to zero (however, if a , b , and c are considered to be non-zero, a full treatment leads to the same result). The optimally estimated characteristic latitudinal offsets were calculated by minimizing the sum squared error, $G = d^2 + e^2 + f^2$ by setting $dG/dD = 0$, assuming W , P and E are known. This gives,

$$D = (W + P + E + x_4 + x_5 + x_6)/3 \quad (4.10)$$

Rearranging equation 4.10 and substituting for equations 4.4-4.6 gives:

$$W - D = (x_1 + x_2 - x_4 - x_5 - x_6)/3 \quad (4.11)$$

$$P - D = (-x_1 + x_3 - x_4 - x_5 - x_6)/3 \quad (4.12)$$

$$E - D = (-x_2 - x_3 - x_4 - x_5 - x_6)/3 \quad (4.13)$$

Figure 4.6 presents these optimised FUV offsets relative to the DMSP proxy (equations 4.11-4.13). The reference DMSP OCB proxy is shown by the orange circle and the characteristic latitudinal offsets for the WIC (blue), SI13 (red) and SI12 (green) proxies are shown relative to the DMSP proxy. Latitude difference is shown by the radial coordinates. These optimised boundary offsets can be applied to the FUV OCB boundaries to give a more accurate global location of the OCB.

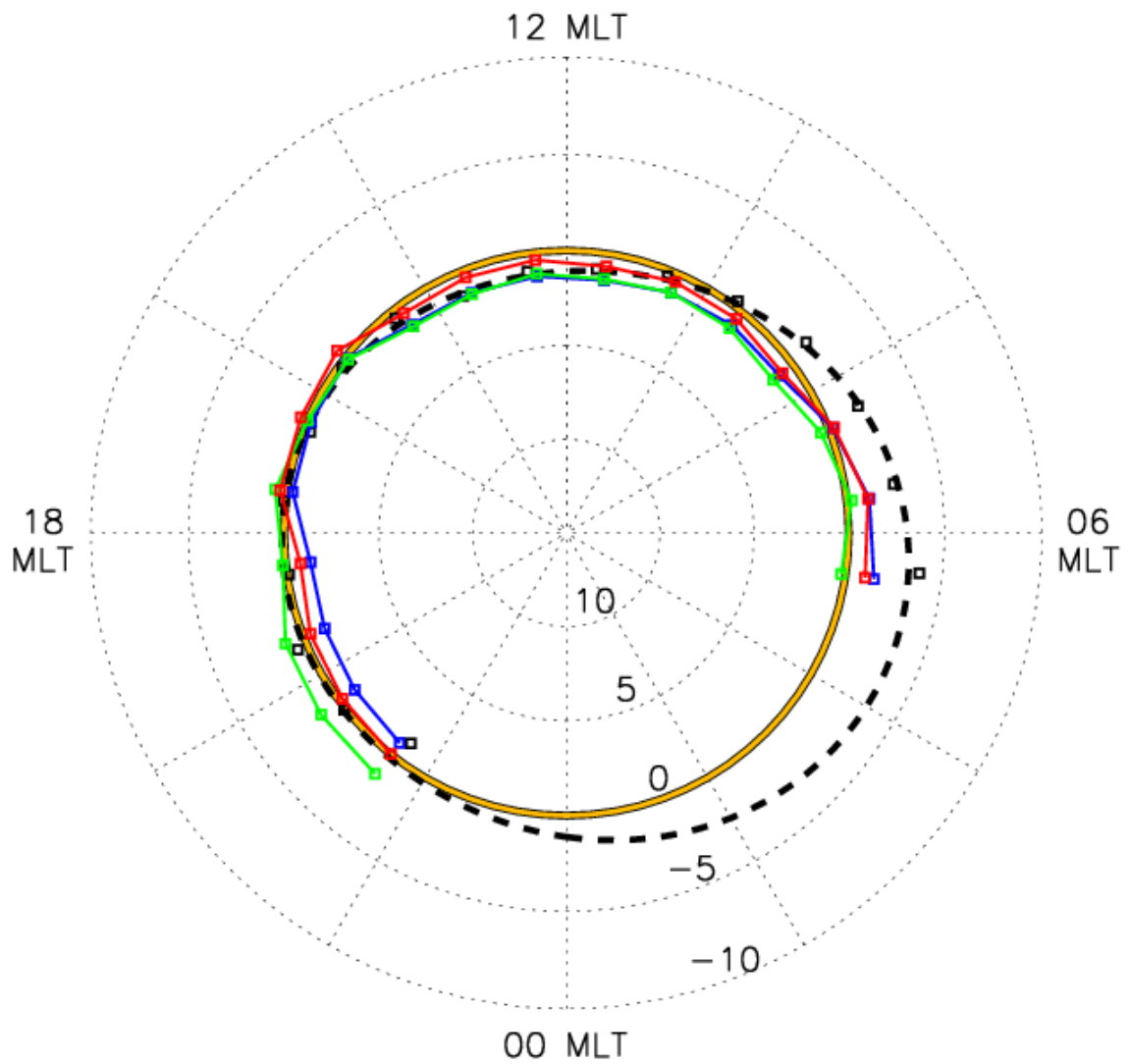


Figure 4.6: Optimally estimated latitude differences between WIC (dark blue), SI13 (red) and SI12 (green) OCB proxies relative to the latitude of the DMSP OCB proxy (orange). Latitude differences between DMSP and Polar UVI OCB proxies from Carbary *et al.* (2003) are shown by black rectangles and the black dashed line shows the extrapolated fit to all MLTs. Radial coordinates represent latitude difference relative to the DMSP OCB proxy in degrees.

4.5 Discussion

In this chapter the latitude of the OCB as estimated from auroral images from the WIC, SI12 and SI13 FUV detectors onboard the IMAGE satellite and from particle precipitation measurements from the DMSP spacecraft have been compared.

Figures 4.3 and 4.6 show that at most MLTs the average modal difference in the latitude between the WIC, SI12 and SI13 OCB proxies is statistically small ($<1^\circ$), although in any one MLT bin differences may be larger. Larger average discrepancies are seen in the evening and predawn sectors. In the evening (1800-2300 MLT) sector SI12 OCB proxies can be located between 1-2 degrees equatorward of WIC and SI13 OCB proxies and 1-2 degrees poleward of WIC and SI13 OCB proxies in the predawn (0300-0600 MLT) sector. These offsets may be explained by the morphology of the magnetospheric current systems, discussed below.

In the dawn sector ionosphere region-1 Field Aligned Currents (FACs) are directed downward into the ionosphere and vice-versa in the evening sector (see Figure 1.9b). Equatorward of region-1 currents are region-2 FACs directed oppositely to region-1 FACs (Iijima and Potemra, 1978; see Figure 1.9b). Upward FACs are associated with down-going electrons and are therefore associated with the WIC and SI13 electron auroral emission (although these also have a small contribution from secondary electrons produced by the proton aurora). The dominant charge carrier associated with downward FACs is less clear but if they are assumed to be associated with down-going protons (Cran-McGreehin and Wright, 2005) then we may expect downward FACs to be associated with the SI12 auroral emission. We would therefore expect to see WIC and SI13 auroral emission poleward of SI12 emission in the evening sector and equatorward in the dawn sector, as seen in this study. It is also interesting to note that the offsets between FUV proxies are small on the dayside and do not follow the morphology of the FACs. However, it is known that the location at which region-1 and region-2 currents switch from upwards to downwards varies over a large MLT range in this sector depending on the orientation of the IMF B_y component (Weimer, 2001). Over large time scales the average of the IMF B_y component is close to zero and therefore the boundary offsets seen are also close to zero in this MLT sector.

Figures 4.5 and 4.6 show that in the predawn sector the SI12 OCB proxy is in better agreement with DMSP OCB proxy than either the WIC or SI13 OCB proxies, but is still located over 1° equatorward of the DMSP proxy, which is thought to be the best proxy for the OCB. Previous studies (Wild *et al.*, 2004) have suggested that WIC may be an unreliable proxy for the OCB in the predawn sector whilst others (Hubert *et al.*, 2006) have used SI12 in preference to SI13 or WIC when determining the global OCB due to the reduced dayglow in SI12 rather than the accuracy of the detector in determining the location of the OCB. The work in this chapter confirms that SI12 may be a better estimation for the OCB in the predawn sector. However, Figures 4.5 and 4.6 show that at all later magnetic local times the WIC and SI13 OCB proxies are either in better agreement with DMSP proxies or as good as the SI12 proxy. The most accurate global determination of the OCB may therefore be obtained by using the individual FUV detector which has the best correlation with the DMSP OCB proxy in any one MLT sector. For example SI12 in the 0100-0700 MLT range, WIC at 0700-0800, SI13 at 0800-1600 MLT, SI12 at 1600-1700 MLT, SI13 at 1700-2200 and WIC at 2200-0100 MLT. For single instrument studies WIC may produce the best proxies for the global OCB due to its good global correlation with the DMSP OCB proxy and its better spatial resolution. It should also be noted that the FUV OCB proxies are found poleward of the equivalent DMSP proxy at dayside MLTs. Near noon there is frequently more particle flux on open field lines (cusp, mantle, etc, see section 1.3.4 and Figure 1.10a) than closed, particularly in SI12 which is likely seeing cusp protons. Cusp precipitation, in particular, is of a much higher energy than that of polar rain and can cause bright auroral emission well above the FUV background level. The resolution of the WIC detector is such that a sharp transition is not seen between cusp and the main auroral oval precipitation. Instead this boundary is 'smoothed' in the WIC intensity-latitude profiles such that cusp precipitation may be included in the Gaussian part of the fitting routine described in section 4.1, increasing the Gaussian half width and thus shifting the OCB proxy to higher latitudes. DMSP is able to see the direct transition between the cusp and main oval precipitation. Counting the cusp precipitation as occurring on open field lines, this places the DMSP OCB proxy at a lower latitude than that equivalent WIC OCB proxy. Conversely, on the nightside and particularly in the dawn-sector ionosphere a region of low-energy precipitation thought to be on closed magnetic field lines is often found poleward of the main auroral oval (see section 1.3), its intensity decreasing poleward and towards the dayside. This low energy precipitation is not much

stronger than polar rain on open field lines, and produces only weak auroral emission. This weak auroral emission is therefore included in the background part of the Gaussian fitting procedure described above such that sub-visual precipitation is considered open. The higher spatial resolution of the DMSP particle analysers are able to directly determine the sharp transition between polar rain and the sub-visual drizzle region, resulting in the DMSP OCB proxy being placed at a higher latitude than the equivalent FUV proxy on the nightside.

Figures 4.5 and 4.6 confirm that systematic differences exist between estimations of the OCB from DMSP particle precipitation measurements and FUV auroral imagers, similar to the differences seen between DMSP and radar derived OCB proxies as presented by Chisham *et al.* (2007). These systematic differences may be used to ‘correct’ auroral boundaries to give a more accurate determination of the OCB. Unfortunately due to the low number of comparisons available at each hour of MLT between the DMSP and FUV OCB proxies and the lack of data available in the predawn sector (where the extrapolated offsets are largest) the uncertainties involved in this correction are not insignificant. To produce the most reliable distributions the modes of the OCB proxy latitude differences have been used and smoothing has been applied. However, using the mean of the latitude differences, or applying different degrees of smoothing, can change the fits to the DMSP-FUV OCB proxy differences in the predawn sector (where the fit is interpolated) by up to a degree. Therefore, we can only reliably trust the DMSP correction where DMSP data are available (0600-2100 MLT). However, as a best guess of the location of the OCB, we believe that applying this correction will statistically give a more accurate result than using the uncorrected FUV OCB proxies.

4.6 Summary

In this chapter we have developed a method of identifying the location of the open/closed magnetic field line boundary from IMAGE FUV auroral images and have assessed its validity.

By comparing over 400000 OCB proxies estimated from the IMAGE WIC, SI13 and SI12 FUV detectors and from auroral images obtained in December 2000 and

December and January 2001-2002, it has been shown that systematic differences exist between the latitude of the OCB as estimated by the three detectors. Statistically the OCB proxy differences are small ($<1^\circ$) except in the predawn sector where the SI12 OCB proxy is found, on average, to be located up to 2° poleward of the WIC and SI13 OCB proxies and in the evening sector where the SI12 OCB proxy can be located up to 2° equatorward of SI13 and WIC OCB proxies.

Correlating FUV OCB proxies with the DMSP OCB proxy confirms that the SI12 OCB proxy is found poleward of the WIC and SI13 OCB proxies in the predawn sector, in better agreement with the DMSP OCB proxy. The WIC and SI13 OCB proxies are found to be in better agreement with the DMSP OCB proxy at all other MLTs. Systematic offsets are found between the DMSP and FUV OCB proxies which may be used to 'correct' FUV OCB proxies to give a more accurate estimation of the true location of the OCB. In the following chapter we develop this method to produce an automated method of identifying the global location of the OCB from IMAGE FUV auroral images, allowing us to accurately determine the area of the ionospheric polar cap and hence estimate the open magnetic flux content of the magnetosphere.

Chapter 5. A Statistical Study of the Open Magnetic Flux Content of the Magnetosphere at the time of Substorm Onset

In the previous chapter we developed an automated method of identifying the location of the open/closed magnetic field line boundary (OCB) in the ionosphere at any one MLT from global auroral images taken by the IMAGE spacecraft. In this chapter we further develop this method to produce a semi-automated technique of accurately identifying the global location of the OCB, allowing us to determine the size of the polar cap and hence estimate the open magnetic flux content of the magnetosphere. This method is then applied to over 12,000 auroral images of the northern polar cap to produce the distribution of the average open magnetic flux content of the magnetosphere, which we hereon name the parent distribution, the largest such study to date. From this parent distribution we select the distribution of open magnetic flux at the time of substorm onset using the Frey list of substorm onset times (see section 2.4.1). We compare the average open magnetic flux content of the magnetosphere to that at the time of substorm onset and discuss in terms of various triggering mechanisms for substorm onset.

We also find that not all substorms in this study show the expected particle injection signature of substorm onset. Splitting substorms into three categories based on their particle injection signatures we find that those substorms which show a clear particle injection signature occur, on average, at higher values of open magnetic flux than those showing no activity.

5.1 Methodology

5.1.1 Estimating the Open Magnetic Flux Content of the Magnetosphere

We estimate the hemispheric open magnetic flux content of the magnetosphere (F_{pc}) by determining the global location of the OCB from global auroral images taken by the IMAGE spacecraft. Since the OCB marks the delineation between magnetic field lines of open and closed topology, the dark region poleward of the OCB, known as the polar

cap, is threaded by open magnetic flux. Thus by simply summing the radial component of the Earth's magnetic field through the area of the polar cap gives us an estimate of F_{pc} .

In the previous chapter we developed an automated method of identifying the OCB in any one MLT sector using global auroral imagery taken by the three FUV detectors onboard the IMAGE spacecraft. Comparing the latitude of the OCB as estimated by FUV auroral images and as estimated from direct measurements of down-going precipitating particles as measured by the DMSP satellite, thought to provide the best proxy for the OCB, showed that systematic offsets exist between the two methods. OCB estimates from the spectrographic imager SI12 were found to be in better agreement with DMSP OCB proxies in the dawnward ionosphere, but OCB estimates from the Wideband Imaging Camera (WIC) and SI13 detector gave at least as good a proxy for the OCB, if not better, at other MLTs. WIC provides a better spatial resolution (~50 km at apogee) than either spectrographic imager (~100 km at apogee) and it is data from WIC which we use in this study. The same data set as used in the previous chapter is utilised. That is, we use all auroral images taken by WIC of the northern hemispheric polar cap for the months of December 2000 and December and January 2001-2002. After this date the WIC data became less reliable (as explained in chapter 4). During the summer months dayglow obscures much of the dayside auroral oval making the determination of the dayside OCB difficult if not impossible from FUV auroral images. Thus we use images from winter months only. During this period the IMAGE spacecraft can image the northern polar cap with a temporal resolution of 2 minutes due to the spin period of the spacecraft and for approximately 10 hours of its' ~14 hour orbit (see Figure 3.1). Thus our primary data set consists of some 77,000 images.

The method to identify the OCB at individual MLTs is described in detail in section 4.1 of this thesis and briefly summarised below. Each auroral image is divided into 24 latitudinal profiles, each 1 hour of MLT wide. The latitudinal variation of the longitudinally-averaged intensity within each profile is fitted by a Gaussian plus quadratic function. Here, the Gaussian is expected to fit to the latitudinal profile of the auroral oval, whereas the quadratic fits to any background luminosity, including dayglow. The fit is accepted if the criteria given in section 4.1.2 of this thesis are met. The auroral oval intensity-latitude profiles often display a double Gaussian-like feature

with more than one peak in intensity. Thus extra criteria are employed to search for the most poleward peak in auroral intensity. The OCB is then assumed to be placed poleward of the center of the most poleward Gaussian fit meeting the fitting criteria by the Gaussian full-width-at-half-maximum. We then ‘correct’ these boundary estimations by applying the systematic offsets found between DMSP particle precipitation boundaries and the IMAGE WIC boundary estimations as shown by the blue curve in Figure 4.5.

Figure 5.1 shows three examples of auroral images from WIC with differing values of F_{pc} . The positions of the OCB estimated in each hour of MLT are shown by diamonds. Visual inspection shows that this method gives a good estimate of the expected OCB latitude at most MLTs. However this is not always the case, as seen, for instance, at 04-05 MLT in Figure 5.1b. Here the OCB estimation has been placed at a higher latitude than its position as suggested by eye. Also, the fitting procedure can fail at several MLTs, as seen between 10-15 MLT in Figure 5.1c, resulting in no boundary identifications. Linear interpolation is used to provide an estimate of the OCB in such cases. However, if the boundary estimation fails in more than six MLT sectors we reject the image (approximately 5/6 of the available auroral images are rejected in this way). In order to smooth out the poor estimations and increase the statistical reliability of the OCB estimates we apply a truncated six-point Fourier Transform, equivalent to a least squares fit of a sixth order Fourier series (*Hamming, 1989*), to the boundary estimations to give the final global estimation of the OCB, shown by the thick dashed line in Figure 5.1a-c. This returns 48 separate estimations of the OCB latitude around the auroral oval, separated by a half hour of MLT.

To calculate F_{pc} for each image, we numerically integrate the radial component of an assumed dipolar magnetic field along 48 latitudinal meridians, each a half hour of MLT in width, in steps of 0.5° of latitude from the magnetic pole to the OCB latitude. That is:

$$F_{pc} = \int_{pc} \underline{B} \cdot d\underline{s} = \int_{pc} B_r ds , \quad (5.1)$$

where B_r is the radial component of the Earths magnetic field, which at the height of the aurora, r (which we take to be 150 km), is given by

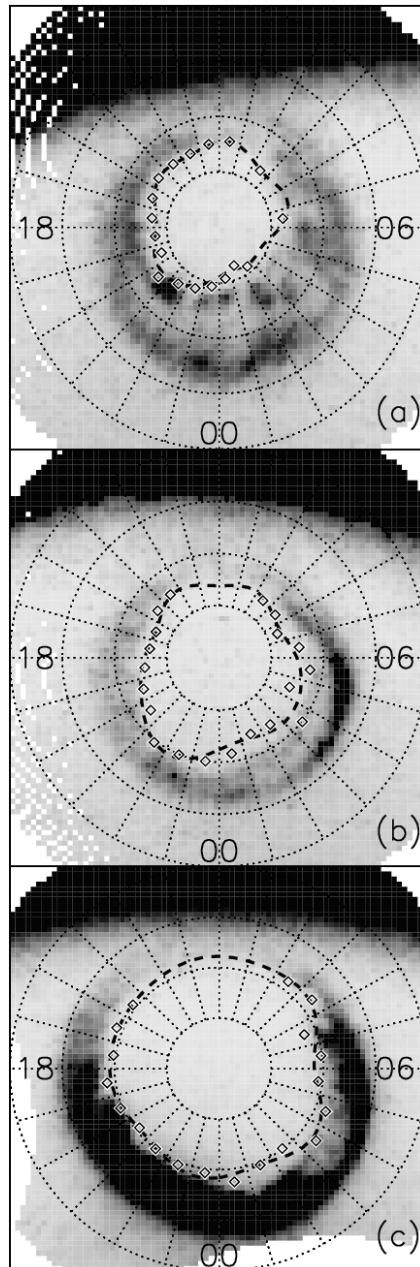


Figure 5.1: Auroral images from the IMAGE WIC FUV detector for three different values of open magnetic flux, (a) 13th January 2002 08:54:41 UT, $F_{pc} = 0.36$ GWb, (b) 26th December 2001 02:02:07 UT, $F_{pc} = 0.57$ GWb, (c) 23rd December 2000 04:49:49 UT, $F_{pc} = 0.97$ GWb. Diamonds represent the OCB estimates at 1 MLT intervals with the thick dashed line showing the final global OCB estimate. Local noon is located at the top of the plots with dotted lines representing lines of constant MLT at 1 MLT intervals. Concentric dotted circles represent lines of constant magnetic latitude at 10° intervals centered on 90° . The dark region at the top of the plots is the result of dayglow swamping the auroral imager.

$$B_r = 2B_{eq} \cos(\theta) \left(\frac{R_E}{r} \right)^3, \quad (5.2)$$

where B_{eq} is the equatorial field strength at the surface of the Earth (31,000 nT), R_E is the radius of the Earth (6370 km) and θ is the colatitude (as measured from the pole). Approximating each small 0.5° by 0.5 hr MLT element to be rectangular, the area of each element is given by

$$A = dh \times dw = \left(2\pi R_E \left(\frac{0.5}{360} \right) \right) \times \left(2\pi R_E \sin(\theta) \left(\frac{1}{48} \right) \right), \quad (5.3)$$

where dh and dw are the height and width of the elements. Running from the pole to the observed latitude of the OCB at the appropriate MLT in steps of 0.5° colatitude and around 48 MLT sectors, we sum the product $A \times B_r$ for each element such that the total polar cap flux is given by

$$F_{pc} = \sum_{n=1}^N A_n \times B_{r,n}, \quad (5.4)$$

where N is the number of elements.

It is difficult to estimate the uncertainty in the flux calculation, but, as an extreme example, if we assumed the latitude of the OCB at all MLTs to be systematically under or over estimated by 1° then this would lead to an increase or decrease of open magnetic flux of about $\pm 10\%$ (Milan *et al.*, 2003). If we assumed that the latitudinal differences between the WIC OCB proxies and the DMSP OCB proxies, as presented in Figure 4.5, represented the errors on the OCB estimation then for a circular polar cap with a constant latitude of 70° at all MLTs, corresponding to an F_{pc} of ~ 0.88 GWb, this would induce an error of $\sim 4\%$ on the F_{pc} estimation. For a circular OCB with constant latitude of 75° , corresponding to an F_{pc} of ~ 0.51 GWb, the error is $\sim 6\%$. Both of these are lower than the 10% suggested by a systematic over or under estimation of 1° .

5.1.2 Selection of Parent and Substorm Distributions

Applying the above method to all WIC auroral images from December 2000 and December and January of 2001 and 2002 returns an estimate of F_{pc} from 12731 auroral images, the occurrence distribution of which we shall hereafter call the parent distribution.

Using the list of substorm onsets compiled by *Frey et al.* (2004), we find the subset of F_{pc} occurring at the time of substorm onset, the occurrence distribution of which we hereafter call the substorm distribution. *Frey et al.* identified onsets from auroral images taken by the IMAGE FUV detectors using the following criteria using the criteria listed in section 2.4.1.

We are unable to determine F_{pc} for many of the images at onset due to a failure to determine the latitude of the OCB in a sufficient number of MLT bins. Thus to increase the size of the substorm distribution, we take the average of F_{pc} from all available values within 4 minutes of every onset time such that a value of F_{pc} at the onset time is not required. Of the 451 substorms in the Frey onset list for the months of this study, we are able to determine F_{pc} for 173 substorm onsets. Note that these averaged estimates include those times when an F_{pc} estimate has been made at the onset time. Comparing the values of F_{pc} using this averaging method and obtained at the onset time only we find that the averaging process adds an additional uncertainty on estimates of F_{pc} of ~ 0.03 GWb and adds an additional 48 events to the substorm distribution.

5.1.3 LANL Substorm Classification

Another signature of substorm onset is the enhancement of energetic particle fluxes at geosynchronous orbit (see section 2.1.2). A typical example of an isolated substorm injection signature, as seen by particle analysers onboard three of the LANL spacecraft (see section 3.3) is shown in Figure 5.2. Panel a shows electron fluxes and panel b proton fluxes. The time of substorm onset is marked by the vertical white line and the times the spacecraft are located at midnight and noon MLTs are shown by the vertical

blue and yellow lines respectively. The MLT of the spacecraft at the time of substorm onset is marked on each panel. At the onset MLT (22 MLT in Figure 5.2), prior to substorm onset a drop-out in energetic particle fluxes is seen. It is thought that this is caused by the thinning of the plasma sheet during the growth phase, causing the spacecraft to move out of the plasma sheet region (e.g. Moldwin *et al.*, 1996). At onset, a dispersionless injection of energetic particles is seen in all energy channels, raising the flux levels well above nominal values. The injection signature becomes dispersed as the particle subsequently gradient and curvature drift around the Earth (see Figure 1.4). Electrons drift eastward and protons drift westwards around the Earth such that the dispersed signature is seen at the LANL spacecraft located at 10 MLT in Figure 5.2 prior to the spacecraft located at 16 MLT for electrons, and vice-versa for protons. We classify substorms into three distinct categories depending on their particle injection signatures:

1. 'Classical' substorm injection signature.
2. Unclear activity.
3. No activity.

Substorms falling in category 1 will normally have a clear dispersionless enhancement in the midnight sector, followed by dispersed enhancements seen in other satellites (typically two or more) at other local times (*Belian et al.*, 1978; *Baker et al.*, 1979). Events when no satellite data are available in the midnight sector but a dispersed signature is seen by at least three other satellites, consistent with gradient-curvature drift from a dispersionless enhancement at midnight, are also included in this category. Figure 5.2 is an example of such an event. Category 2 covers all other energetic particle fluctuations not falling within category 1, an example of a category 2 onset is shown in Figure 5.3. Category 3 events show no fluctuations in any of the LANL spacecraft. To be included in this category data must be available in the midnight sector. An example of a category 3 event is shown in Figure 5.4. Both electron and proton data are used in the classification process.

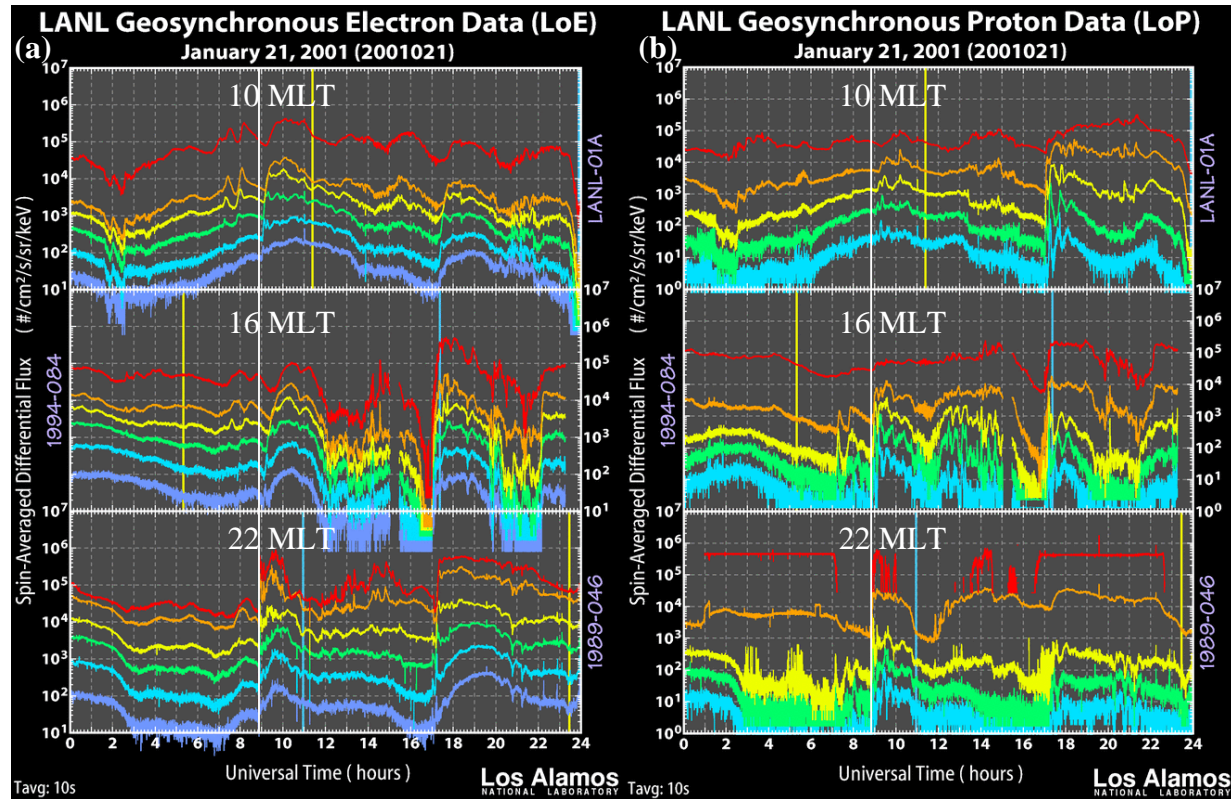


Figure 5.2: Example of a typical category 1 event (a ‘classical’ substorm injection signature) in energetic electrons (a) and protons (b). Data from three LANL spacecraft, located at geosynchronous orbit are shown, from top to bottom, LANL-01A, 1994-084 and 1989-046. Vertical white lines show the time of substorm onset: 08:50:03 on January 21st 2001. Vertical yellow and blue lines show the time at which the spacecraft are located at local noon and midnight respectively. The approximate MLT of each spacecraft at the time of onset is shown in each panel. Electrons are measured in 6 energy channels in the range 50-500 keV (from top to bottom of each channel (red to blue) 50-75, 75-105, 105-150, 150-225, 225-315 and 315-500 keV). Protons are measured in 5 energy channels from 50-400 keV (50-75, 75-113, 113-170, 170-250 and 250-400 keV). This event is described in more detail in section 2.1.2 of this thesis.

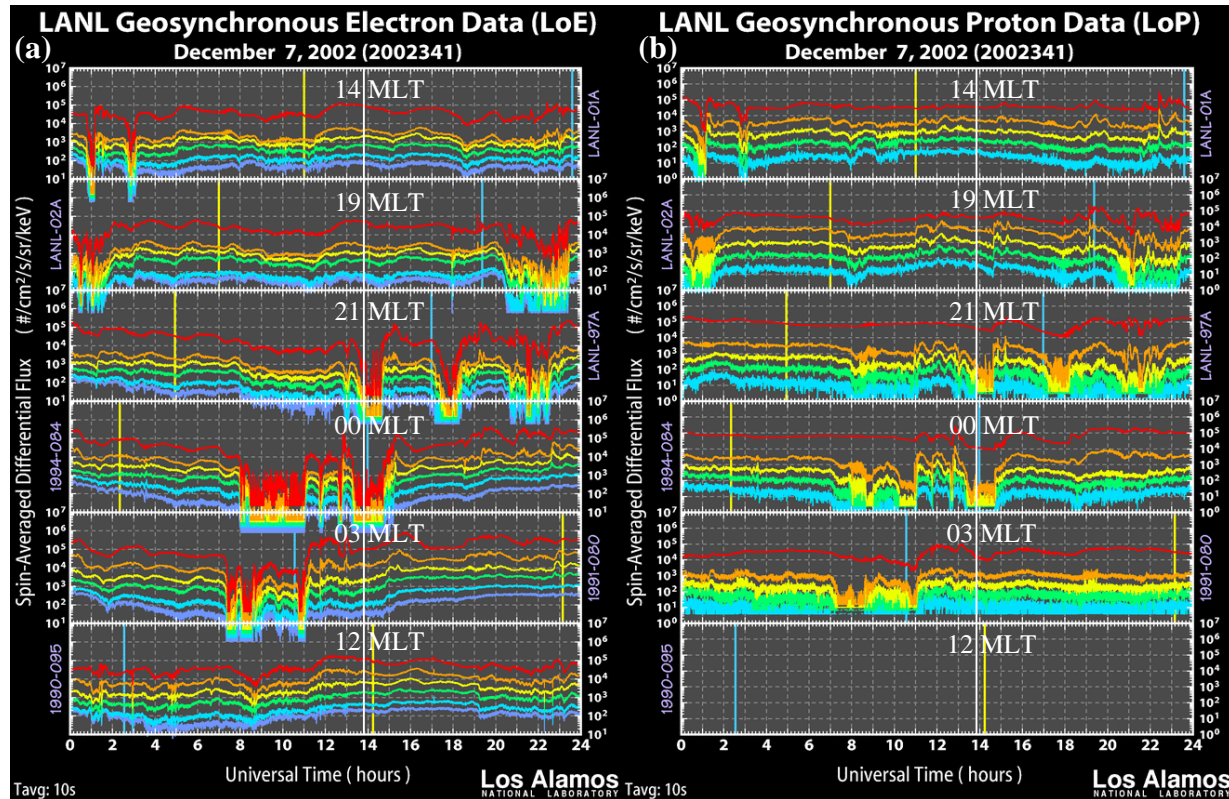


Figure 5.3: Example of a category 2 event (unclear injection activity) in energetic electrons (a) and protons (b). Data from six LANL spacecraft, located at geosynchronous orbit are shown, from top to bottom, LANL-01A, LANL-02A, LANL-97A, 1994-084, 1991-080 and 1990-095. Vertical white lines show the time of substorm onset: 13:47:14 on December 07th 2002. Vertical yellow and blue lines show the time at which the spacecraft are located at local noon and midnight respectively. The approximate MLT of each spacecraft at the time of onset is shown in each panel. Electrons are measured in 6 energy channels in the range 50-500 keV (from top to bottom of each channel (red to blue) 50-75, 75-105, 105-150, 150-225, 225-315 and 315-500 keV). Protons are measured in 5 energy channels from 50-400 keV (50-75, 75-113, 113-170, 170-250 and 250-400 keV). At the onset time a large dropout in fluxes is seen near the onset MLT (~00 MLT). A substorm like injection is not seen until after 14 UT.

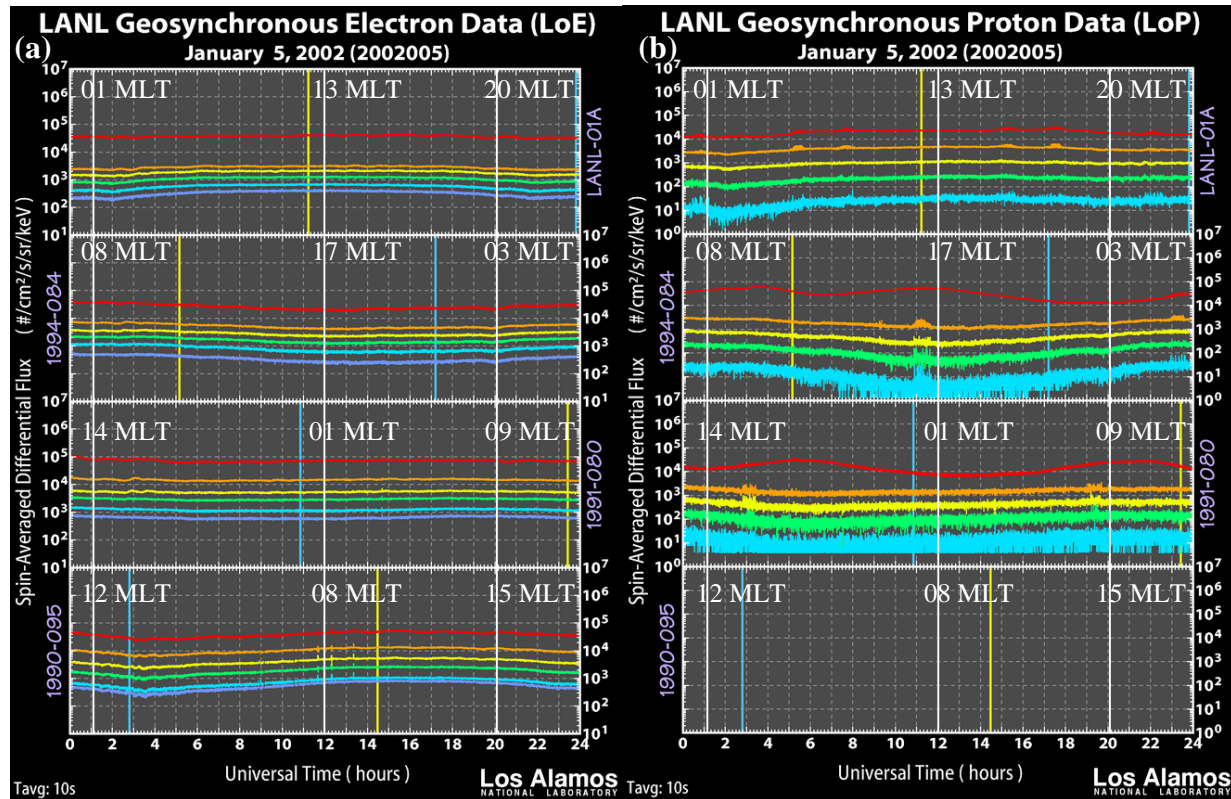


Figure 5.4: Examples of three category 3 events (no injection activity) in energetic electrons (a) and protons (b). Data from four LANL spacecraft, located at geosynchronous orbit are shown, from top to bottom, LANL-01A, 1994-084, 1991-080 and 1990-095. Vertical white lines show the times of substorm onset: 01:07:18, 11:59:52 and 20:05:42 UT on January 05th 2002. Vertical yellow and blue lines show the time at which the spacecraft are located at local noon and midnight respectively. The approximate MLT of each spacecraft at the time of onset is shown in each panel. Electrons are measured in 6 energy channels in the range 50-500 keV (from top to bottom of each channel (red to blue) 50-75, 75-105, 105-150, 150-225, 225-315 and 315-500 keV). Protons are measured in 5 energy channels from 50-400 keV (50-75, 75-113, 113-170, 170-250 and 250-400 keV).

5.2 Results

5.2.1 The Open Magnetic Flux at the Time of Substorm Onset

The parent probability distribution of open magnetic flux $p(F_{pc})$ is shown by the unfilled histograms in Figures 5.5a-e. The substorm probability distribution, $p(F_s) = p(F_{pc}|s)$, is shown by the shaded histogram in Figure 5.5a. The open magnetic flux of the parent distribution is seen to vary between ~ 0.2 and 0.9 GWb with a mean value of $\overline{F}_{pc} = 0.52$ GWb. The open magnetic flux at substorm onset varies between 0.3 and 0.9 GWb with a mean value of $\overline{F}_s = 0.58$ GWb. Applying the Kolmogorov-Smirnov (K-S) statistical test (Press *et al.*, 2007) to the two distributions verifies that the probability of rejecting the null hypothesis that the two distributions are the same is greater than 0.999.

The shaded histograms in Figures 5.5b-e show the distributions of open magnetic flux for category 1, 2, 3 and category 1&2 substorms respectively, determined from the LANL spacecraft as defined above. We combine categories 1 and 2 so as to include all possible onset signatures. Of the 173 substorm onsets in the total substorm distribution, 135 have available LANL spacecraft data. Of these, 61 (45%) fall within category 1, 39 (29%) fall in category 2 and 35 (26%) fall in category 3. Substorms occurring in categories 1 and 2 tend to occur at higher values of F_{pc} than those occurring in category 3, with all three categories being significantly different from one another, and from the parent distribution, according to the K-S test. The mean values of F_{pc} for the different substorm categories are as follows; $\overline{F}_1 = 0.66$ GWb, $\overline{F}_2 = 0.59$ GWb, $\overline{F}_{1\&2} = 0.63$ GWb and $\overline{F}_3 = 0.48$ GWb.

5.2.2 Probability of Substorm Onset as a Function of Open Magnetic Flux

From Bayes' theorem (see Press, 2007), the probability $p(s|F_{pc})$ of substorm onset occurring in an image at a given value of open magnetic flux can be derived from the probability distributions shown in Figures 5.5a-e according to

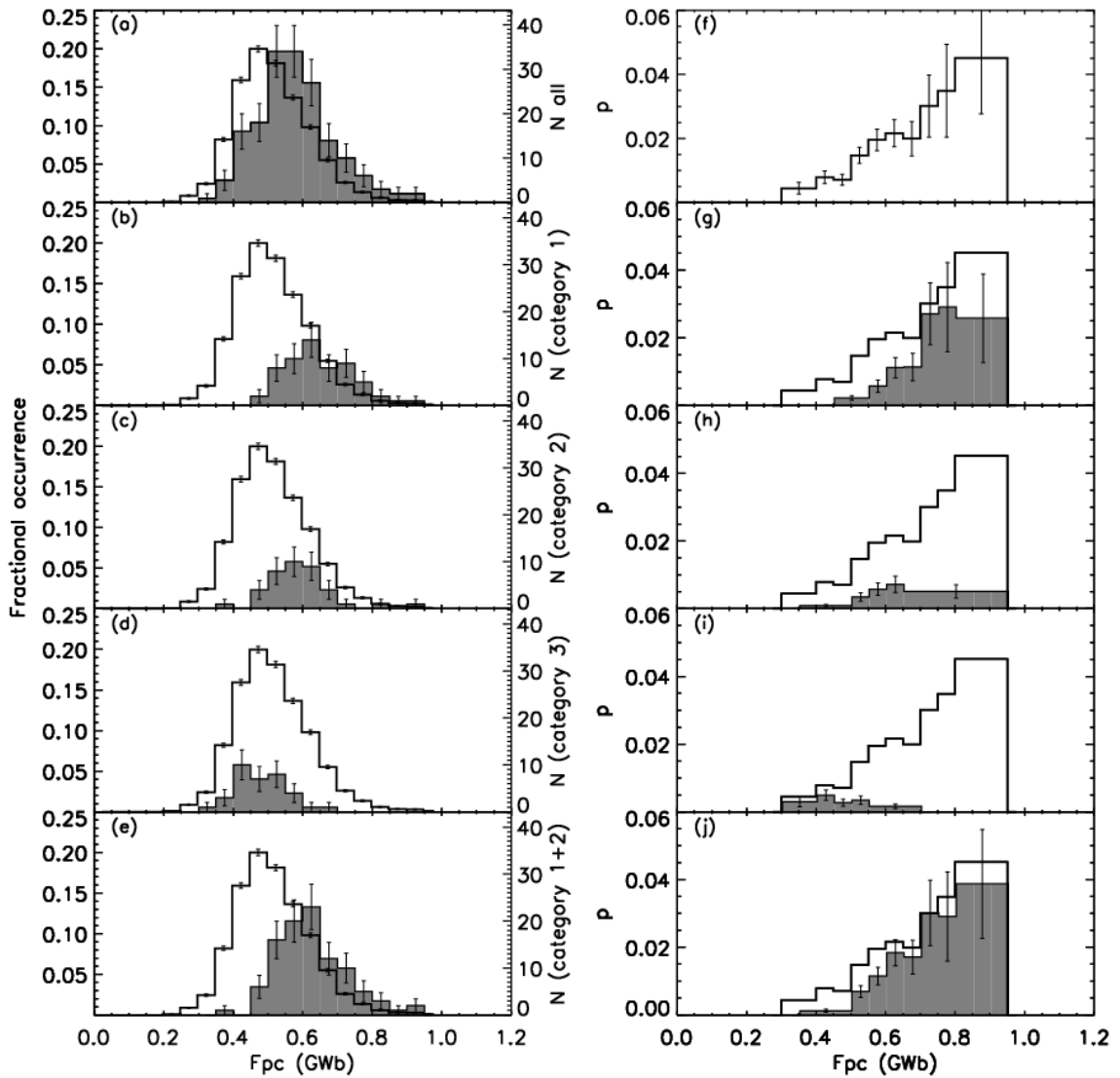


Figure 5.5a-e: Fractional occurrence, left axis, of parent distribution of open magnetic flux (unfilled histogram in all panels) and for (a) all substorms, (b) category 1, (c) category 2, (d) category 3 and (e) category 1&2 (shaded histograms). The right hand axis shows the number in each bin for the relevant substorm distribution. (f-i) Probability of substorm onset as a function of open magnetic flux for, (f) all substorms (unfilled histogram repeated in all panels), (g) category 1, (h) category 2, (i) category 3 and (j) category 1&2 substorms (shaded histograms). Error bars are calculated from \sqrt{N} errors. Note that of the 173 substorms in the distribution of 5a and 5f we are able to sub-categorise 135 into categories 1, 2 and 3. Consequently the sum of the shaded probability distribution in figures 5g-i does not equal the unshaded probability distribution in figure 5f.

$$p(s|F_{pc}) = \frac{p(s)p(F_s)}{p(F_{pc})} = \frac{n(F_s)}{n(F_{pc})}, \quad (5.5)$$

where n denotes occurrence frequency and $p(s)$, $p(F_s)$, and $p(F_{pc})$ are the probability of a substorm occurring independently, the probability that the magnetosphere will be at a given value of open magnetic flux given there is a substorm, and the probability that the magnetosphere will be at that value of open magnetic regardless of there being a substorm or not. Figure 5.5f shows the function $p(s|F_{pc})$ derived from the parent and all-substorm frequency distributions shown in Figure 5.5a and is repeated in panels g to j by the unshaded histograms. Similarly, the shaded histograms in Figures 5.5g-j show $p(s|F_{pc})$ for the substorm categories shown in Figures 2b-e. In all cases we have used bins of 0.05 GWb and combined bins in which there are less than 5 events occurring. For all substorms, and for category 1&2, the probability of substorm onset is negligible for fluxes below ~ 0.3 GWb, increases almost linearly until $F_{pc} \sim 0.9$ GWb, and is undefined above 0.9 GWb, as fluxes are not observed in this study with values that exceed this. These results are discussed below.

5.3 Discussion & Conclusions

5.3.1 Are All Frey Substorm Events Substorms?

In this study we use substorm onset times derived by *Frey et al.* (2004) from nightside auroral brightenings in IMAGE FUV observations. It is well known that other magnetospheric phenomena, such as pseudo-breakups (see section 2.1.6), can cause auroral brightenings similar to those seen at the time of substorm onset and it is not unlikely that a number of these may have been erroneously included in Frey's substorm list. Therefore, as a secondary indicator of substorm onset we looked for energetic particle injections measured by the LANL spacecraft, subdividing the substorm distribution into three categories based on these signatures. We found that a significant number of substorms fall into each of the three categories, and showed that the mean of F_{pc} decreases as the injection signature becomes less obvious (see Figures 5.5b-d).

One interpretation of this result is that the probability of energetic particles reaching, or being generated at, geosynchronous orbit following substorm onset decreases for smaller values of F_{pc} . Indeed it has been shown that substorms occurring with contracted polar caps (corresponding to smaller open magnetic fluxes) are statistically less energetic than substorms occurring with larger auroral ovals (e.g. Akasofu, 1975; Milan *et al.*, 2008).

An alternative view of these results is that category 1 events are almost certainly substorms, with category 2 including both substorm events as well as other phenomena which cause auroral brightenings such as pseudo-breakups or solar wind pressure enhancements (which have been shown to be associated with auroral brightenings and energetic particle enhancements at geosynchronous orbit). Events falling into category 3 may not be substorms or may be pseudo-breakups or very weak substorms. We further investigate the properties of these three distinct categories in the following chapter.

5.3.2 What do the Distributions Tell Us About Substorm Onset?

We have shown that the occurrence distribution of F_{pc} in the magnetosphere varies between 0.2 and 0.9 GWb, with a mean of 0.52 GWb, in good agreement with the values found by previous studies (e.g. Milan *et al.*, 2004, 2007, 2008). The occurrence distribution of F_{pc} at substorm onset also varies between values consistent with previous studies (Coumans *et al.*, 2007; DeJong *et al.*, 2007; Milan *et al.*, 2007, Huang *et al.*, 2009b) and occurs with a significantly higher mean (0.59 GWb) than the parent distribution. No substorm onsets are seen to occur below a minimum of 0.3 GWb, showing that the magnetosphere must be preloaded with open magnetic flux as a requirement for substorm onset. If category 1 is considered to be the true substorm distribution then a minimum threshold of 0.4 GWb must be reached before substorm onset is induced, more strongly supporting this view.

Freeman and Morley (2004) developed a theoretical model in which the occurrence distribution of substorm onsets, and the distribution of substorm magnitudes (Morley *et al.*, 2007), could be reproduced if substorm onset only depended on a fixed critical threshold in the open magnetic flux. If this were so then we would expect the probability distribution of F_{pc} at substorm onset to be a delta function centered on the

threshold value and a sharp cut-off in the parent distribution of F_{pc} at this value. However, Figures 5.5a-j do not show this. For all substorm categories, onset can occur over a range of open magnetic fluxes (confirming results found by other smaller statistical studies) with the parent distribution extending over this entire range. Here we must also consider whether the distributions can be consistent with a fixed threshold within measurement errors. Using the extreme example of an uncertainty in the open magnetic flux of $\sim 10\%$, this gives a maximum error in open magnetic flux of ~ 0.1 GWb, much smaller than the spread seen in our distributions.

Whilst most studies agree that the preloading of the magnetosphere is required for substorm onset, others suggest that a further condition must also exist, such as a solar wind trigger (e.g. a northward turning of the IMF B_z) (Lyons *et al.*, 1997; Hsu and McPherron, 2002; Hsu and McPherron, 2003). Other studies showing clear examples of substorm onsets occurring during very steady solar wind conditions (e.g. Hsu and McPherron, 2003; Henderson *et al.*, 2006) suggest that an entirely internal threshold (such as in open magnetic flux), whose value may be modulated by other factors such as the strength of the ring current (e.g. Milan *et al.*, 2009a,b), is the only requirement of substorm onset (see also section 2.2.3).

If we assume that a solar wind trigger is required to trigger onset once some minimal open magnetic flux threshold has been reached, that triggers occur uniformly randomly with time, and that the open magnetic flux increases linearly ($B_z < 0$) until a trigger occurs, then we would expect the probability of substorm onset as a function of open magnetic flux to show a step function from zero probability of onset below the minimal flux threshold and a decreasing (geometric) distribution above this. This is not seen in our distribution. In fact we may expect the probability to decrease even faster than this because Hsu and McPherron (2002) showed that triggers are not uniformly distributed, such that the longer it has been since the last southward turning of the IMF B_z , the longer the time expected until a northward turning. Thus a simple model of flux accumulation followed by the triggering of substorm onset by the solar wind, where the triggers are either independent or distributed as found by Hsu and McPherron (2002), cannot explain the results presented in this thesis.

Milan *et al.* (2009a,b) suggested that the ring current may stabilise the magnetotail to reconnection such that when the ring current is enhanced substorms occur at higher values of open magnetic flux (see Figure 2.8). Our results are not inconsistent with a variable open magnetic flux threshold for substorm onset, whose value depends on the strength of the ring current or some other magnetospheric property.

In this study we have concentrated on the relationship of substorm onset to the amount of open magnetic flux in the magnetosphere. However, it may be that there exists another quantity for which a fixed threshold is a necessary and sufficient condition for substorm onset (e.g. the Kappa parameter (Büchner and Zelenyi, 1987)) and that the relationship between this and open flux is multi-valued. That is, various configurations of open magnetic flux could exist for a given critical value of this quantity. What magnetospheric property this quantity may be is still a matter of speculation and enquiry.

5.4 Summary

In this chapter we have carried out the largest statistical study of the open magnetic flux content of the magnetosphere to date, and compared the average open magnetic flux content of the magnetosphere with that at the time of substorm onset. The results show that, on average, substorms occur at the upper end of the average open magnetic flux distribution, showing how the magnetosphere must be preloaded with open magnetic flux prior to substorm onset.

The large numbers of open magnetic flux estimates allow us, for the first time, to determine the probability of substorm onset as a function of open magnetic flux. The results show that substorms can occur over a large range of open magnetic flux values and that a fixed critical threshold in open magnetic flux does not exist. The results are also not consistent with a model in which a solar wind trigger is required to trigger onset once some minimal threshold in open magnetic flux has been reached. The results are, however, consistent with a model in which a variable threshold in open magnetic flux exists as a requirement of substorm onset. The distributions shown in Figure 5.5 place important constraints on any future similar models of substorm onset.

Searching for the energetic particle injection signatures of substorm onset in geosynchronous satellite data, we have found that not all substorms identified in the list of Frey *et al.* (2004) show the characteristic injection signature of substorms. Dividing substorms into three categories based on their particle injection signatures, we find that substorms showing the ‘classical’ particle injection signature expected at substorm onset occur, on average, at higher values of open magnetic flux than those showing varied particle enhancement signatures. Events showing no energetic particle enhancements occur at even lower values of open magnetic flux. In the following chapter we investigate these three distinct particle injection categories of substorms in more detail by carrying out a superposed epoch analysis of the open magnetic flux, solar wind and IMF conditions, geomagnetic activity, auroral luminosity and auroral oval boundary motions during each type of event.

Chapter 6. A Superposed Epoch Analysis of Substorm Dynamics

In the previous chapter we demonstrated that substorms showing a ‘classic’ substorm particle injection signature at geosynchronous orbit (category 1) occur, on average, at higher values of open magnetic flux than those showing varied activity (category 2) or no particle injection activity (category 3). In the first half of this chapter we investigate this finding in more detail by carrying out a superposed epoch analysis of the open magnetic flux, solar wind and IMF conditions, auroral luminosity and geomagnetic activity around the time of substorm onset for the three distinct particle injection categories. In the second half of this chapter we carry out a superposed epoch analysis of the latitude of the OCB, the latitude of the equatorward boundary of the auroral oval and the derived width of the auroral oval for all substorms and for the three distinct particle injection substorm categories.

6.1 Open Magnetic Flux, Auroral Intensity, IMF and Solar Wind Conditions and Geomagnetic Indices

6.1.1 Methodology

In the previous chapter we calculated F_{pc} from over 12,000 auroral images from the December and January months of 2000-2002. We now use these estimates of F_{pc} and the Frey list of substorms to perform a superposed epoch analysis of F_{pc} , the maximum nightside auroral intensity and the solar wind conditions and geomagnetic activity within ± 5 hours from the time of substorm onset.

Firstly, we categorise all Frey substorm onsets from December and January 2000-2002 using the LANL classification system as described in the previous chapter. That is, we split the onsets in to three categories based on particle injection signatures at geosynchronous orbit as seen by the LANL spacecraft:

Category 1: Substorms showing a classic substorm particle injection signature.

Category 2: Those substorms exhibiting energetic particle fluctuations which do not fall within category 1 (unclear activity).

Category 3: Substorms which show no energetic particle fluctuations at any MLTs.

The availability of LANL data and the location of the LANL spacecraft limits our ability to classify the substorms in this way (as described in the previous chapter). Of the 451 onsets in the Frey database from December and January 2000-2002 we are able to classify a total of 306 onsets into the three LANL categories. We find that relatively even numbers of onsets lie in each of the three categories, 114 in category 1, 100 in category 2 and 92 in category 3. To produce a time-series of F_{pc} relative to the onset time, the following procedure is used: for each LANL category and for each Frey onset within the category we find all values of F_{pc} from the parent distribution which fall within ± 5 hours of the onset time. The data are then binned in bins of 13 minutes such that at the onset time values are binned from 6 minutes prior to onset to 6 minutes proceeding onset. The mean of all values in each 13 minute bin and across all substorms within the relevant category is then taken. A similar procedure is carried out on the maximum nightside auroral intensity, solar wind magnetic field and plasma properties and the geomagnetic indices AL, AU and SYM-H.

The maximum nightside auroral intensity is taken to be the maximum count rate found between 18-06 MLT and 50-90° magnetic latitude from each IMAGE WIC FUV auroral image. Any counts found above a value of 4000 are considered to be due to anomalies in the data, that is we set a maximum limit of 4000 counts. Solar wind data are provided by the OMNI Definitive, 1 AU 1 minute IMF and Plasma database courtesy of CDAWeb. Plasma and magnetic field data from the ACE, WIND and Geotail spacecraft were used to produce averaged 1 minute resolution plasma and IMF datasets shifted to the Earth's bow shock nose using a minimal variance technique (see Weimer *et al.*, 2003). All solar wind data used in this thesis are in GSM coordinates (see Figure 1.2). One minute resolution AL, AU and SYM-H indices were provided courtesy of the World Data Center for Geomagnetism, Kyoto University, from a chain of high latitude magnetometers.

The Akasofu epsilon parameter is an empirically determined fraction of the solar wind Poynting flux through the dayside magnetopause (Perreault & Akasofu, 1978) and is thus a measure of the solar wind energy input into the magnetosphere due to dayside reconnection. Here we define the epsilon parameter as:

$$\varepsilon = V_x B^2 \sin^4(\theta_c / 2), \quad (6.1)$$

where B is the total IMF strength ($B = \sqrt{B_x^2 + B_y^2 + B_z^2}$), V_x is the x component of the solar wind flow speed and θ_c is the IMF clock angle (see Figure 1.2). This has the same functional form as equations derived for the dayside reconnection rate (e.g. Milan *et al.*, 2007; Milan *et al.*, 2008) and thus its magnitude also gives an indication of the level of dayside reconnection. Here we have left out the length constant, l_0 , so that ε has units of power per unit area.

Figure 6.1 shows the superposed epoch traces for the three LANL categories. Category 1 events are shown by the green trace, category 2 by the red and category 3 by the blue. Also overplotted in each panel is a null line (grey) representing the average conditions and variations for the whole period of study not keyed to substorm onset. This is calculated by combining the onset times from all three categories, adding one IMAGE orbit period (14.2 hrs) to each onset time and carrying out the same superposed epoch methodology to find F_{pc} and the solar wind and magnetic indices within ± 5 hrs of this shifted time. Shifting the onset times by one IMAGE orbit means that no biases will be introduced by the viewing angle of the WIC detector as this will remain consistent between the LANL categories and null line. Progressing through each panel, a-n, in turn we have the superposed traces for (a) F_{pc} , (b) the maximum nightside auroral intensity (I), (c) the IMF B_z component in nT, (d) the transverse component of the IMF ($B_t = \sqrt{B_y^2 + B_z^2}$), (e) IMF B_y , (f) the absolute value of B_y , (g) IMF B_x , (h) the absolute value of B_x , (i) the solar wind proton number density (N_{sw}), (j) the solar wind flow pressure (P), (k) the x component of the solar wind flow speed (V_x), (l) the SYM-H index, (m) the Akasofu parameter (ε) given by equation 6.1, and finally (n) the AU and AL indices.

To give us a better understanding of the significance of any fluctuations in the superposed traces we also plot the LANL categories separately in Figures 6.2-6.4, along with a null line (grey line) representing the average conditions. Each null line is calculated in the same manner as for Figure 6.1 using only the onset times relevant to

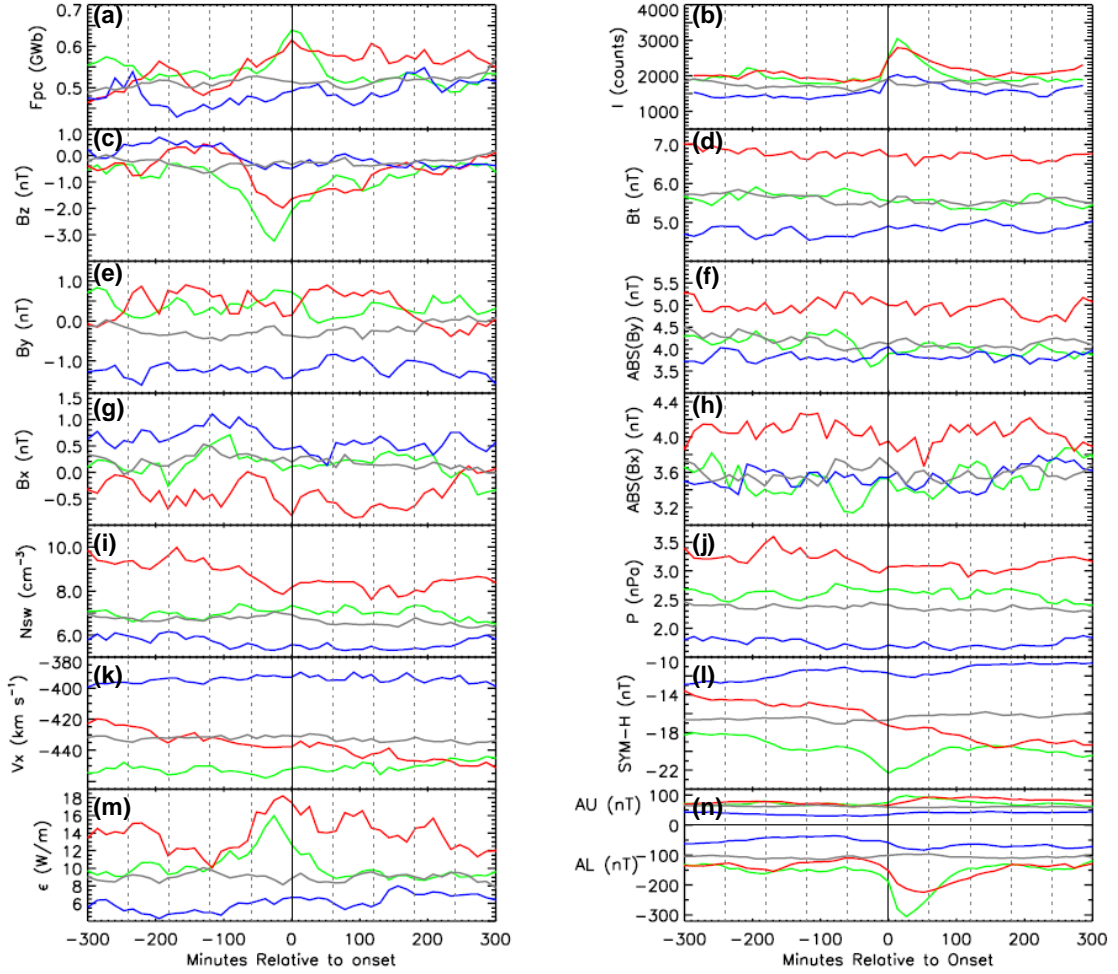


Figure 6.1: Superposed epoch analysis of (a) open magnetic flux, (b) maximum nightside auroral intensity, (c) IMF B_z , (d) transverse component of the IMF $B_t = \sqrt{(B_y^2 + B_z^2)}$, (e) IMF B_y , (f) the absolute value of IMF B_y , (g) IMF B_x , (h) the absolute value of IMF B_x , (i) solar wind proton number density, (j) the solar wind flow pressure, (k) the x component of the solar wind flow speed, (l) the SYM-H index (m) the Akasofu ϵ parameter and (n) the AU and AL geomagnetic indices keyed to the time of substorm onset for the three distinct particle injection categories of substorms. Green represents category 1 (classical substorm injection signature substorms, 100 events), red represents category 2 (all substorms showing energetic particle enhancements not falling within category 1, 114 events) and blue represents category 3 (substorms occurring with no energetic particle enhancements, 92 events). The grey lines represent the average conditions of each parameter for the period of study. The bold vertical line represents the time of substorm onset and dashed vertical lines show hours from onset time.

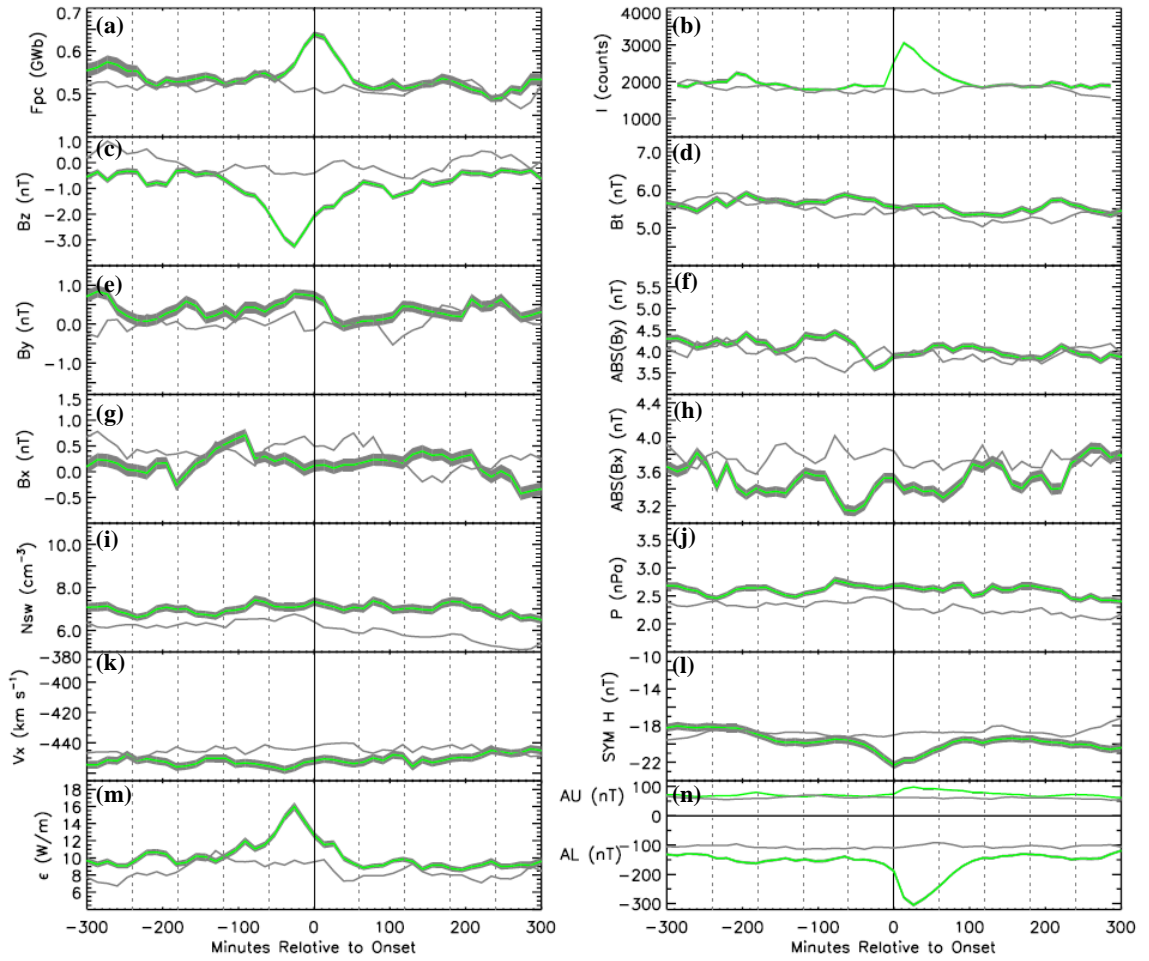


Figure 6.2: Superposed epoch analysis of 100 category 1 events (‘classic’ substorm particle injection signatures), green line. The grey shaded regions represent the standard error on the mean and the grey line represents the average conditions for the period of study. Panel (a) open magnetic flux, (b) maximum nightside auroral intensity, (c) IMF B_z , (d) transverse component of the IMF $B_t = \sqrt{(B_y^2 + B_z^2)}$, (e) IMF B_y , (f) the absolute value of IMF B_y , (g) IMF B_x , (h) the absolute value of IMF B_x , (i) solar wind proton number density, (j) the solar wind flow pressure, (k) the x component of the solar wind flow speed, (l) the SYM-H index (m) the Akasofu ϵ parameter and (n) the AU and AL geomagnetic indices. The bold vertical line represents the time of substorm onset and dashed vertical lines show hours from onset time.

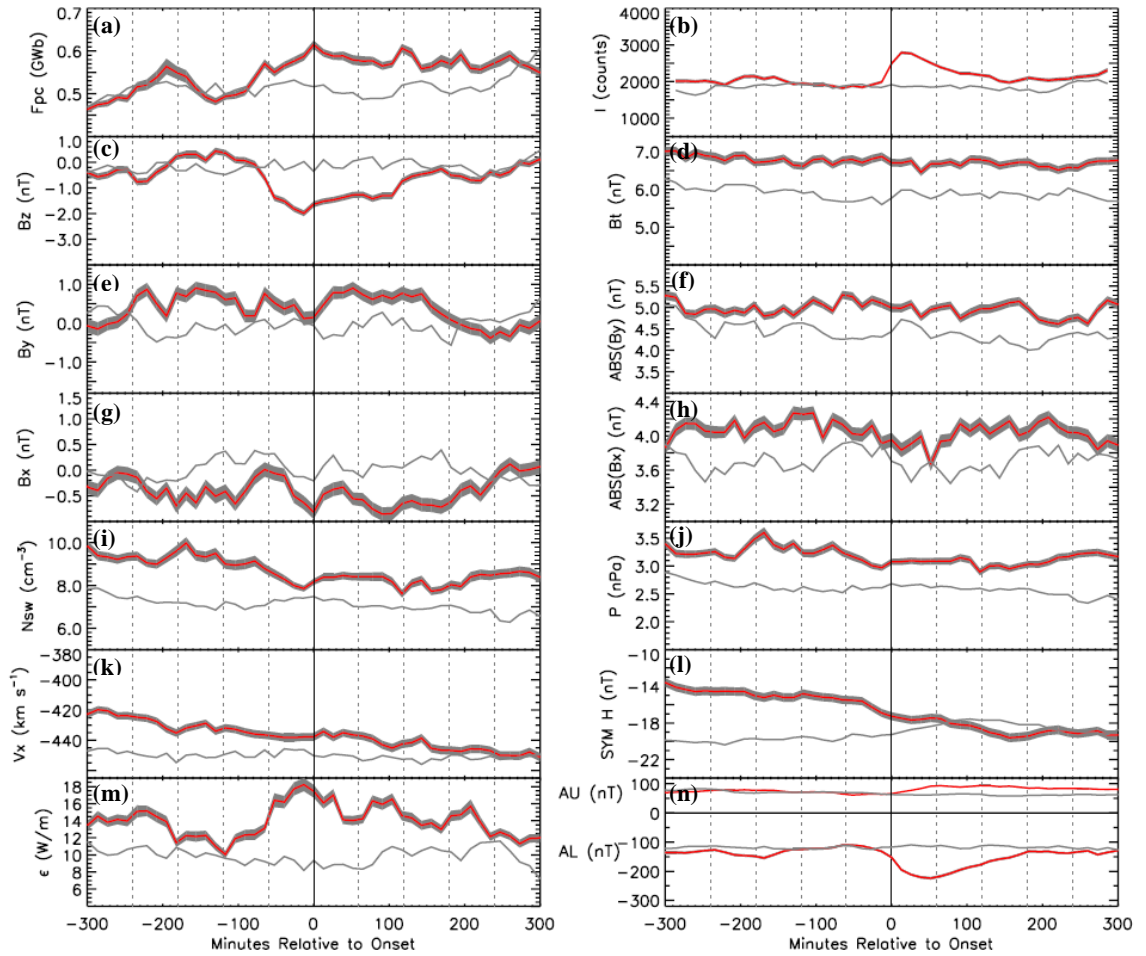


Figure 6.3: Superposed epoch analysis of 114 category 2 events (unclear particle injection activity), red line. The grey shaded regions represent the standard error on the mean and the grey line represents the average conditions for the period of study. Panel (a) open magnetic flux, (b) maximum nightside auroral intensity, (c) IMF B_z , (d) transverse component of the IMF $B_t = \sqrt{(B_y^2 + B_z^2)}$, (e) IMF B_y , (f) the absolute value of IMF B_y , (g) IMF B_x , (h) the absolute value of IMF B_x , (i) solar wind proton number density, (j) the solar wind flow pressure, (k) the x component of the solar wind flow speed, (l) the SYM-H index (m) the Akasofu ϵ parameter and (n) the AU and AL geomagnetic indices. The bold vertical line represents the time of substorm onset and dashed vertical lines show hours from onset time.

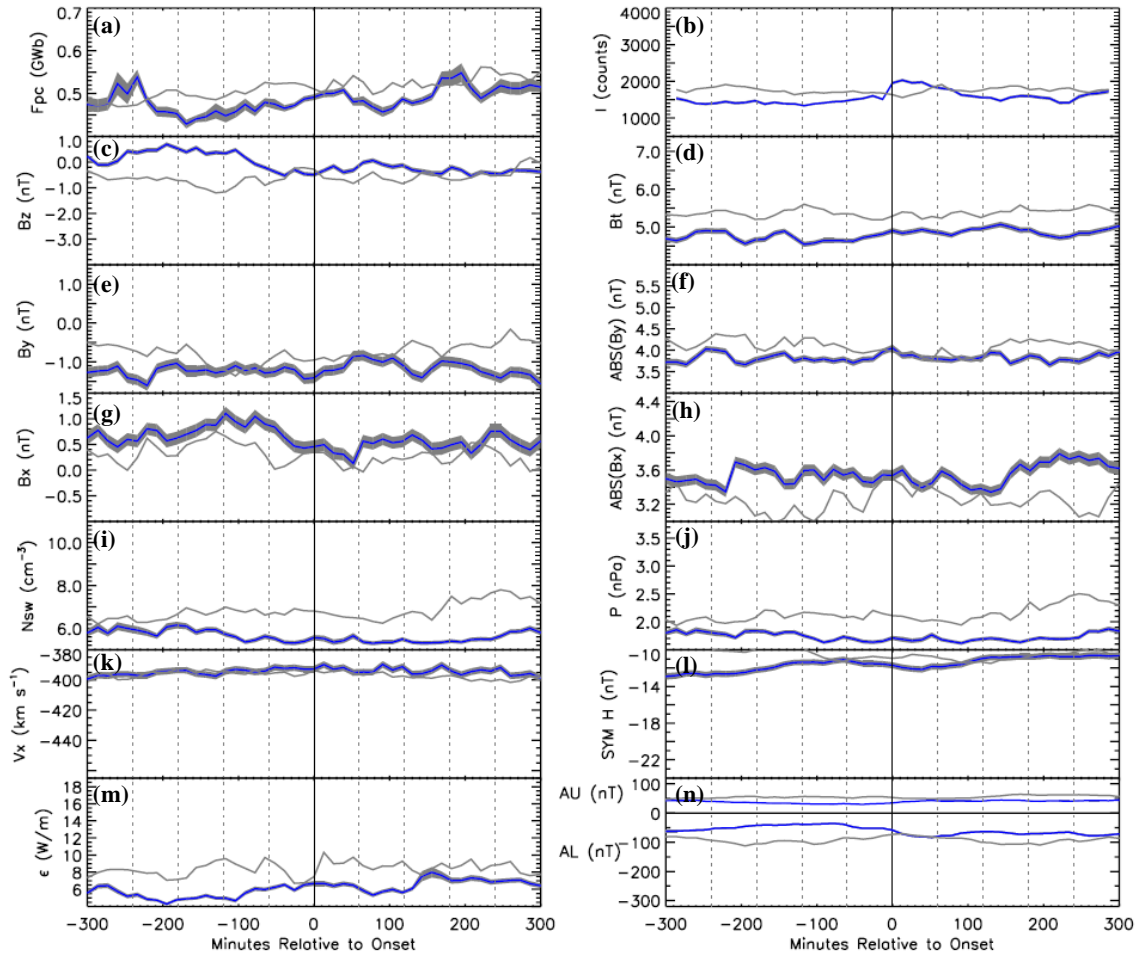


Figure 6.4: Superposed epoch analysis of 92 category 3 events (no substorm injection signature), blue line. The grey shaded regions represent the standard error on the mean and the grey line represents the average conditions for the period of study. Panel (a) open magnetic flux, (b) maximum nightside auroral intensity, (c) IMF B_z , (d) transverse component of the IMF $B_t = \sqrt{(B_y^2 + B_z^2)}$, (e) IMF B_y , (f) the absolute value of IMF B_y , (g) IMF B_x , (h) the absolute value of IMF B_x , (i) solar wind proton number density, (j) the solar wind flow pressure, (k) the x component of the solar wind flow speed, (l) the SYM-H index (m) the Akasofu ϵ parameter and (n) the AU and AL geomagnetic indices. The bold vertical line represents the time of substorm onset and dashed vertical lines show hours from onset time.

each category. To give some indication of the statistical significance of the superposed results, we also plot the standard error on the mean for all parameters, shown by the grey shaded region. Repeating all plots using the medians in the binning process does not effect any of the curves significantly.

6.1.2 Observations and Discussion

6.1.2.1 Overview of Category 1 and 2 Events

Initial inspection of Figure 6.1 shows that the fluctuations seen in category 1 and 2 events occur with relatively similar magnitudes and show similar trends in many of the parameters whilst category 3 events tend to occur with much weaker fluctuations. We therefore firstly summarise the variations and trends seen in category 1 and 2 events, taking each parameter in turn, before discussing the very different category 3 events in the next section.

Panel a: Open Magnetic Flux

In the previous chapter we showed that category 1 events occur, on average, at higher values of F_{pc} than either category 2 or category 3 events. This is confirmed in the superposed plot, green line Figure 6.1a and 6.2a, with F_{pc} reaching its highest value for the whole ± 5 hours at the onset time (from hereafter referred to as $t = 0$) with a value of ~ 0.64 GWb. F_{pc} remains relatively unchanged between ~ -3.5 hrs and ~ -60 minutes, fluctuating between ~ 0.52 and 0.54 GWb. At ~ -60 minutes F_{pc} begins to rise sharply away from the null line from a value of ~ 0.53 GWb to 0.64 GWb at $t = 0$, an increase of 21%. Following onset F_{pc} rapidly falls, decreasing to a value of 0.51 GWb at $+78$ minutes, a drop of $\sim 20\%$. F_{pc} then continues to fluctuate between ~ 0.48 and 0.54 GWb for the remainder of the period.

The variation of F_{pc} for category 2 events is shown by the red trace of Figures 6.1a and 6.3a. Although F_{pc} starts to increase at ~ -2 hours, we take the beginning of the growth phase to be where a sharp increase is seen in the F_{pc} accumulation rate at -91 minutes. This growth phase is approximately 30 minutes longer than the growth phase seen for category 1 events and increases F_{pc} from a value of ~ 0.50 GWb to a value of 0.61 GWb

at $t = 0$, an increase of 22%. The expansion phase is much less pronounced but more prolonged than for category 1. Lasting for approximately 90 minutes and reducing F_{pc} by ~ 0.045 GWb. That is, F_{pc} decreases by only $\sim 7\%$ in the expansion phase. Following the end of the expansion phase F_{pc} continues to fluctuate between 0.55 and 0.6 GWb for the remainder of the period, comfortably above the null line flux, which has a mean of 0.51 GWb, and F_{pc} prior to substorm onset. The fluctuations are comparable in size to the fluctuations seen in the null lines and we thus consider them to be insignificant.

The values of F_{pc} for both category 1 and 2 events are consistent with the values found by previous studies (e.g. Coumans *et al.*, 2007; DeJong *et al.*, 2007; Milan *et al.*, 2007; Huang *et al.*, 2009). Previous studies (e.g. DeJong *et al.*, 2007; Huang *et al.*, 2009) have found a reduction of between 24-30% of the total open magnetic flux stored in the system during the expansion phase of isolated and sawtooth substorm events. Category 1 events show a similar reduction in the total F_{pc} content of the system (20%), whilst category 2 events do not (7%). Panel m of Figure 6.1 shows the superposed Akasofu ε parameter (equation 6.1), a measure of the dayside driving, for the three categories. Category 1 ε decreases rapidly around the onset time, suggesting that the addition of energy to the magnetosphere through dayside reconnection, and the addition of open magnetic flux to the system, slows dramatically. Coupled with the large flux closure due to substorm onset on the nightside, this results in a large reduction of the total flux of the system for this category. For category 2, ε (red trace) remains elevated after onset as compared to category 1 events (green trace), suggesting that dayside reconnection and the addition of open magnetic flux to the system continues at a steady rate throughout the substorm expansion phase for category 2 events, balancing the ongoing closure of flux on the nightside (see also I below). This results in only a moderate reduction of the total flux of the system for this category.

Panel b: Auroral Intensity

The green trace in panel b Figures 6.1 and 6.2 shows the superposed maximum nightside auroral intensity (I), in counts, for category 1 events. Between -5 hrs and -13 minutes the intensity fluctuations are small and of a similar size to the random fluctuations seen in the null lines. At -13 minutes the intensity sharply increases, at a rate of ~ 52 counts/min, from a value of ~ 1890 to a peak of ~ 3051 counts at

+13 minutes. Following the peak I falls at a rate of 11 counts/min until $\sim +2$ hours, where after it fluctuates around the null line at a fairly constant intensity for the remainder of the period.

The intensity of category 2 events (red trace Figure 6.1b and 6.3b) fluctuates at similar values to that of the category 1 intensity and the null lines from -5 hrs to -13 minutes. At -13 minutes the intensity rapidly rises at a rate of ~ 32 counts/min. As with category 1 events, the peak in intensity is reached at +13 minutes with a value of 2800 counts. Thereafter, similarly to F_{pc} (Figure 6.1a), the intensity shows a slow decline lasting for ~ 30 minutes longer than the decline of I for category 1 events. Also similarly to F_{pc} , for the remainder of the period I remains elevated as compared to the category 1 intensity and the null lines. The values found in this study are somewhat lower in intensity than those found by Mende *et al.* (2003) at the MLT of the initial onset. The higher background levels in our study suggest that the brightest part of the auroral oval is not necessarily at the onset MLT prior to substorm onset. The more extreme peak values of the Mende study may be explained by the increased intensity of the aurora in summer months, not used in this study.

Blockx *et al.* (2009) found a very good correlation between the maximum nightside auroral intensity during the substorm process and the ε parameter, a measure of the dayside reconnection rate. They found that the maximum nightside auroral intensity integrated over the expansion phase is better correlated with the ε parameter integrated over the growth phase ($r=0.9$) than ε integrated over the expansion phase ($r=0.6$), suggesting that the loading-unloading process (in which energy is first stored in the magnetosphere during the growth phase and subsequently released during substorm expansion) plays a bigger role in the substorm onset than the directly driven process (where solar wind energy is directly dissipated into the ionosphere and ring current). Milan *et al.* (2006) carried out a multi-instrument study of a substorm interval occurring during a period of continued southward IMF and hence inferred continuous dayside driving. They found that following the second substorm event of their study F_{pc} remained elevated for the remainder of the substorm interval and that the maximum auroral intensity averaged between 20:00 and 04:00 MLT, after showing a rapid brightening around the onset time, slowly declined over the next 2.5 hours. Measurements of the magnetic field in the magnetotail made by the Cluster

(Escoubet *et al.*, 1997, 2001) and Double Star (Liu *et al.*, 2005) spacecraft suggested that the tail dynamics during the substorm is strongly driven by the on-going dayside creation of open magnetic flux. We suggest that category 2 events are similar to the event of this study in that they are highly influenced by the continued dayside solar wind-magnetosphere driving, and that there is a larger contribution in their driving from the directly driven process whilst category 1 events depend more heavily on the loading-unloading process.

Panels c-k and m: IMF and Solar Wind Conditions

The green trace in panels c-h of Figure 6.1 and 6.2 show the superposed IMF data for category 1 events. B_z fluctuates between ~ -0.3 and -0.9 nT from -5 hrs to -130 minutes. This is followed by a rapid and large increase to more negative values, -3.2 nT being reached at -26 minutes. The decrease of B_z slightly increases at -78 minutes from ~ 0.017 nT/min between -130 and -78 minutes to 0.033 nT/min between -78 and -26 minutes. Over the next 40 minutes B_z turns sharply towards less negative values, a value of -0.8 nT reached at $\sim +1$ hr. For the remainder of the 5 hr study the B_z component slowly progresses towards less negative values but is always more negative than the null lines. The ϵ parameter (panels m) closely anti-correlates with the variation of the B_z component of the IMF. Between -5 hrs and -130 minutes ϵ varies between approximately 5.5 and 8.6 W/m, before rapidly increasing in conjunction with the large negative excursion of B_z . ϵ reaches its maximum value of ~ 11.2 W/m at -26 minutes, the same time as B_z reaches its most negative value. Subsequently ϵ drops rapidly until $+91$ minutes following the rapid return of B_z to less negative values. Thereafter ϵ slowly declines as B_z slowly moves towards less negative values for the remainder of the period. The close anti correlation between the IMF B_z and ϵ variations suggests that B_z plays the dominant role in the driving of dayside reconnection for category 1 events.

The category 1 B_t , B_x and absolute values of B_x and B_y (panels d, g, h and f) show no deviation from the typical non-substorm IMF behaviour as represented by the null lines. The category 1 B_y component (panels e) is mildly positive and fluctuates with a slightly higher mean, $\mu = 0.3$ nT, than its null line, $\mu = 0.1$ nT. The size of the fluctuations seen in the category 1 B_y trace are of a similar size to the fluctuations seen in the

category 1 null line (grey line Figure 6.2e), suggesting that these fluctuations are not significant.

Both the category 1 solar wind proton density (Figure 6.1i and 6.2i) and pressure (panels j) have a slightly higher mean than their average values as represented by the null lines, the mean values being $\bar{N}_{SW_{Cat1}} \approx 7.0 \text{ cm}^{-3}$, $\bar{N}_{SW_{Cat1Null}} \approx 6.0 \text{ cm}^{-3}$, $\bar{P}_{Cat1} = 2.6 \text{ nPa}$, $\bar{P}_{Cat1null} \approx 2.3 \text{ nPa}$. The category 1 solar wind velocity, V_x , (panels k) is also slightly higher than its equivalent null line, $\bar{V}_{x_{Cat1}} \approx -451 \text{ km s}^{-1}$, $\bar{V}_{x_{Cat1null}} \approx -444 \text{ km s}^{-1}$.

The category 2 IMF data are shown by the red lines of Figures 6.1c-h and 6.3c-h. Between -5 and -3.5 hrs the B_z component of the field varies around values similar to the category 1 events and the null line before moving to slightly positive values between ~ -3 and ~ -2 hours. The negative magnitude of B_z then starts to increase at the same time as the excursion seen in the category 1 events, with the rate of change rapidly increasing at -78 minutes to a rate of $\sim 0.02 \text{ nT/min}$. The most negative value of $\sim -2 \text{ nT}$ is reached at -13 minutes, approximately ten minutes later than for category 1 events. The recovery towards less negative magnitudes occurs much less rapidly than for category 1 events over the subsequent 3 hours, thereafter B_z slowly progresses towards less negative values and the null line for the remainder of the period.

The category 2 transverse component of the field (B_t) is elevated from the null line and category 1 events by $\sim 1 \text{ nT}$, the K-S statistical test returns a probability of 0.98 that the distribution of B_t for category 2 events is significantly different to that of category 1 events and the null line. The K-S test returns a probability of 0.2 that the category 1 B_t distribution is significantly different to its null line, suggesting that category 1 events occur during average solar wind B_t conditions. The category 2 B_y component fluctuates at similar values to the category 1 events, whilst the absolute value suggests that the category 2 events occur with elevated magnitudes of IMF B_y . Figure 6.5 shows the distributions of B_y and the absolute value of B_y averaged over the half hour prior to onset for the three LANL categories. Several large magnitude B_y events ($> \pm 10 \text{ nT}$) are seen in the category 2 distribution. Removing these events from the superposed study

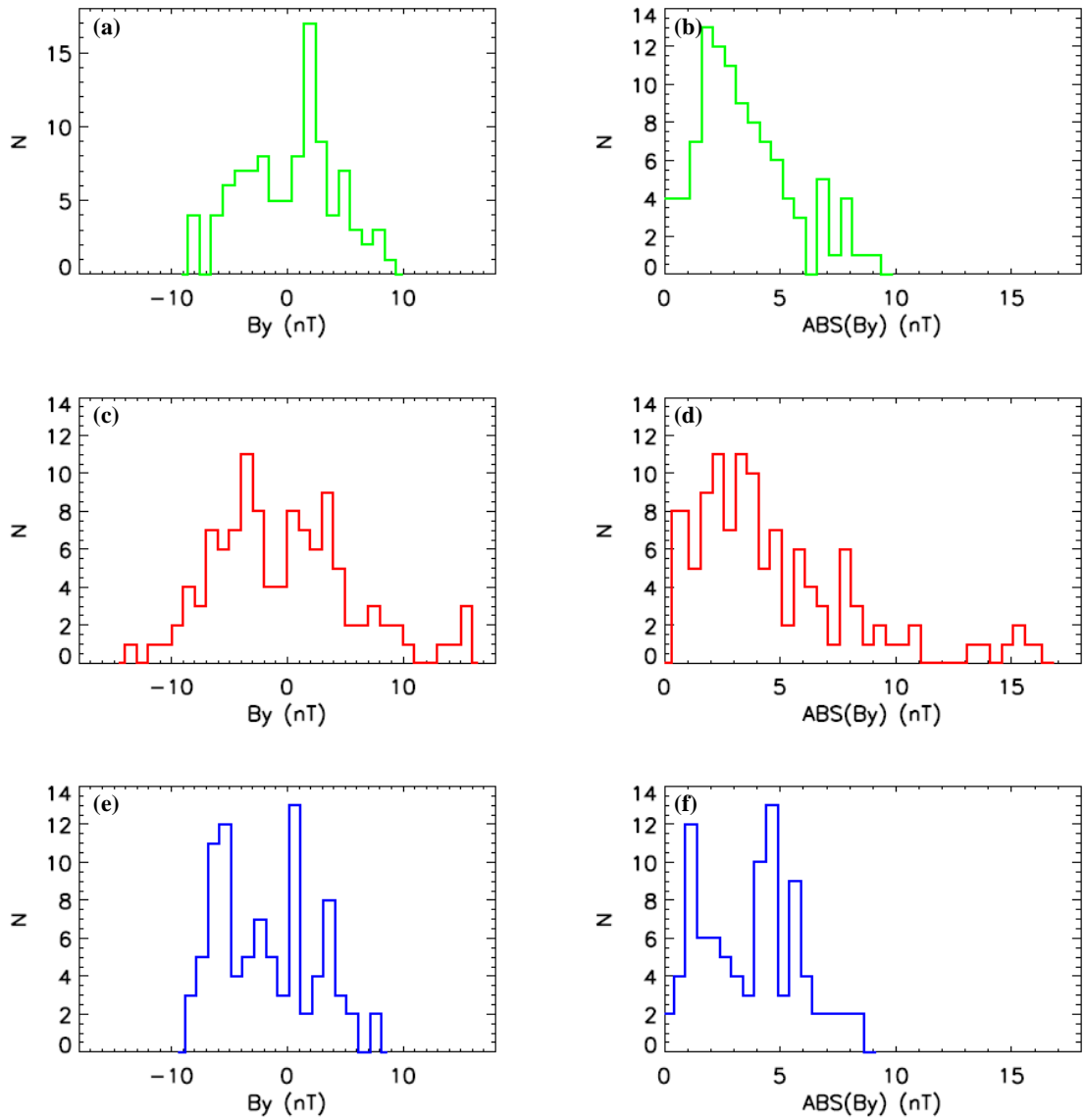


Figure 6.5: Distributions of IMF B_y (a, c and e) and absolute value of IMF B_y (b, d and f) averaged over the half hour prior to substorm onset for the three distinct categories of substorm injection. Category 1 (clear injection signature, 100 events): green panels a and b. Category 2 (unclear activity, 114 events): red panels c and d. Category 3 (no injection signature, 92 events): blue panels e and f.

reduces the size of the $ABS(B_y)$ shift to higher magnitudes, but it remains elevated as compared to category 1 and 3 events showing that this offset is statistically significant. The B_x component, Figure 6.1 and 6.3 panel g, fluctuates at more negative values than the null line or category 1 events and has an elevated magnitude as shown by the absolute value, panel h.

Category 2 events also occur with elevated solar wind proton density (red line Figure 6.1i and 6.3i), $\bar{N}_{SW_{Cat2}} \approx 8.7 \text{ cm}^{-3}$, $\bar{N}_{SW_{cat2null}} \approx 7.1 \text{ cm}^{-3}$, and solar wind pressure (Figure 6.1j and 6.3j), $\bar{P}_{Cat2} \approx 3.2 \text{ nPa}$, $\bar{P}_{Cat2null} \approx 2.6 \text{ nPa}$, as compared to category 1 events and the null lines, whilst the solar wind speed (V_x panels k) is slightly lower than for category 1 events, $\bar{V}_{x_{Cat2}} \approx -437 \text{ km s}^{-1}$ and $\bar{V}_{x_{Cat2null}} \approx -437 \text{ km s}^{-1}$.

As for category 1 events, category 2 events show a close anti-correlation between IMF B_z and ε (red trace Figures 6.1c and m), with B_z and ε remaining elevated in magnitude throughout the expansion phase. However, the ε parameter is a function of the solar wind flow speed, V_x , the total IMF strength, $B = (B_x^2 + B_y^2 + B_z^2)^{1/2}$, and the IMF clock angle. Both V_x and B_z are stronger for category 1 events, whilst B_y and B_x are elevated for category 2. While the driving for category 1 events appears to be largely governed by the B_z component of the field, the elevated driving for category 2 events appears to originate from the elevated magnitudes of the B_y component of the field.

Panels l-n: Magnetic Indices

The category 1 superposed SYM-H, AU and AL indices are shown by the green lines in Figures 6.1 and 6.2 panels l and n respectively. The SYM-H index gradually increases in negative magnitude from $\sim -18 \text{ nT}$ at -5 hours to $\sim -19.6 \text{ nT}$ at $\sim -1 \text{ hrs}$. From $\sim -1 \text{ hrs}$ to $T=0$ SYM-H increases more quickly to a minimum of -22 nT at $T=0$. Immediately following $T=0$ SYM-H begins to recover, recovering to $\sim -19 \text{ nT}$ at +91 minutes. For the entire period of study category 1 SYM-H has a greater magnitude than the null lines. The category 2 SYM-H index occurs at slightly reduced levels compared to category 1 and steadily increases between -14 and -20 nT over the 10 hrs of study. This is consistent with the continued enhancement of the ring current throughout the expansion

phase of these events due to the continued dayside reconnection. The enhancement of the SYM-H index (a measure of the ring current) for substorm events with larger values of F_{pc} is consistent with results of previous superposed studies (Milan *et al.*, 2008, 2009a, b; Huang *et al.*, 2009).

Category 1 AL and AU indices show the expected bays associated with the onset of substorms. As for SYM-H, both AL and AU values are enhanced as compared to the null lines. The peak in AL and AU magnetic bays for category 2 events is slightly smaller than that seen for category 1 events. The magnetic bays suggest the onset of substorms, but as with F_{pc} , the intensity and the IMF B_z , the recovery occurs more gradually over ~ 3 hours.

The peak in category 1 AL and AU activity is reached at +26 minutes, consistent with the findings of Weimer *et al.* (1994). Category 2 activity reaches a peak at $\sim +52$ minutes, somewhat later than the times suggested by the Weimer study. However, the magnitudes of the AL and AU indices are on average much smaller than those seen in the Weimer study and are consistent with the result that the greater the magnitude of the substorm bay the quicker the peak in activity is reached.

Substorm periodicity

Initial inspection of the category 1 superposed F_{pc} suggests that F_{pc} may reach a significant peak at both $\sim \pm 5$ hours, suggesting a possible substorm periodicity of 5 hours for these events. A second peak in the superposed F_{pc} trace of category 2 events is seen at ~ -3 hours, with F_{pc} rising and falling by ~ 0.09 GWb between -5 and ~ -2.1 hours. Small secondary peaks are also seen following onset, although these are of a similar size to the fluctuations seen in the null line. Borovsky *et al.* (1993) studied the average time interval between substorms (Δt) for every pair of consecutive substorms identified from energetic particle enhancements at geosynchronous orbit by the LANL spacecraft from the 1st of October 1982 to the 29th of September 1983. 1001 values of Δt were used. They found an average waiting time between substorms occurring cyclically (e.g. sawtooth events) of ~ 2.75 hours and a Δt of ~ 5 hours for substorms occurring randomly (outside of cyclic periods). This leads to the question of whether category 1 events are isolated random substorm events occurring with a mean periodicity of

~ 5 hours, similar to the mean time found between ‘random’ substorms by Borovsky *et al.* (1993), and whether category 2 events are periodic substorms occurring with the average substorm periodicity of ~ 2.75 hours. To investigate this further we searched through the Frey database of onsets for all substorms occurring within the ± 5 hour period of the superposed study. We find that there is little difference between the number of substorms occurring within this time period for category 1 and 2 events. In fact only 50% of the substorms in either category 1 or 2 have another substorm within +5 hours or -5 hours. For category 3 events (see below) this number is reduced to ~ 36%, which may be expected due to the lower general activity seen for category 3 events. This also suggests that category 3 events are not largely made up of pseudo-breakups or very weak substorms occurring in the growth or expansion phases of larger events. We conclude that there is no difference in the substorm periodicity for category 1 and 2 events. We may also draw the conclusion that sawtooth events (approximately 3 hourly substorm events defined by the nature of their particle injection signatures) do not determine the properties of either category 1 or 2 events. The secondary peak in the category 2 superposed plot is due to a small number of very large onsets occurring at this time.

Substorm Triggering

The large northward turning of the IMF B_z component (green trace Figure 6.1a and 6.2a) in the half hour preceding substorm onset for category 1 events may lead some observers to suggest that these events could be triggered by a northward turning of the IMF. With only a small rise in B_z seen for category 2 events, conversely observers may also suggest that most category 2 events are non-triggered events. Morley and Freeman (2007) developed an automated technique to identify northward triggers using the quantitative rules defined by Lyons *et al.* (1997) (see Morley and Freeman (2007) for the list of criteria used in identifying a northward turning). We used this automated technique to identify northward turnings occurring within the 50 minutes prior to the onset time, finding that 72% of category 1, 54% of category 2 events and 41% of category 3 events are associated with a northward turning. For a time window of 30 minutes prior to onset 57% of category 1, 40% of category 2 events and 33% of category 3 events are associated with a northward turning. For a time window of 15 minutes before onset (as used by Lyons *et al.* (1997) in their definition of a

northward trigger) 44% of category 1, 29% of category 2 and 17% of category 3 events are associated with a northward turning. It is clear that category 1 events do not have exclusivity on northward triggering events and it is more likely that the increased number of ‘triggered’ events in this category and the large northward turning seen in the superposed trace is a consequence of the form of the growth phase and the dayside driving for these events rather than a real association between northward turning triggered events and energetic particle injections. Moreover, Coumans *et al.* (2007) suggested that northward triggered events occur at lower values of F_{pc} than non-triggered events such that if category 1 events were triggered by the solar wind they would occur at lower values of F_{pc} than category 2, which is the opposite of what is seen in the present study.

6.1.2.2 Summary and Discussion of Category 3 Events

In the previous chapter we showed that category 3 events occur, on average, at lower values of F_{pc} than either category 1 or 2 events. This is confirmed in the superposed study, blue trace Figure 6.1a and 6.4a, with an F_{pc} at onset of 0.49 GWb. This value is below the null line value of F_{pc} at onset and the mean value of the category 3 null line flux (grey trace Figure 6.4), 0.51 GWb. This value is also somewhat lower than the average value of the onset F_{pc} found in previous studies (e.g. Coumans *et al.*, 2007; DeJong *et al.*, 2007; Milan *et al.*, 2007; Huang *et al.*, 2009). F_{pc} rises from a value of ~ 0.43 GWb at -169 minutes to a peak of ~ 0.51 GWb reached at +39 minutes. Approximately 0.05 GWb of flux is then closed over the next 50 minutes. For the majority of the 10 hour period F_{pc} is located below the average F_{pc} represented by the null lines, which is the opposite to what is expected for substorms. The maximum nightside auroral intensity of category 3 events, blue trace Figures 6.1b and 6.4b, is also located below the average intensity of the null line for the entirety of the 10 hours except for a short period of ~ 1 hour starting around the onset time. This is evidently the auroral brightening identified by Frey *et al.* (2004) as the start of substorm onset. The IMF B_z component, blue Figures 6.1c and 6.4c, is also found at smaller magnitudes than the average B_z for the majority of the ± 5 hours. There is no large southward turning of B_z which would normally lead to a substorm growth phase. The Category 3 B_t , blue trace Figures 6.1d and 6.4d, and the absolute B_y , Figures 6.1f and 6.4f, components of the field are also found at smaller magnitudes than the null lines.

The B_y component, blue trace Figure 6.1e and 6.4e, is shifted towards negative values, fluctuating between -1.6 and -0.8 nT for the entire period. To investigate this apparent shift further, we plot the distributions of B_y averaged over the half hour before onset for the three LANL categories in panels a,c and e of Figure 6.5. It is quite clear from the figure that both category 1 and 2 distributions are fairly symmetric around 0 nT, as one would expect in the average solar wind, with means of ~ 0.67 and 0.18 nT respectively. However, the category 3 distribution is skewed towards negative values of B_y , with a mean of -1.34 nT. Figure 6.6 shows the distributions of B_y for each of the five months used in this study. The distributions for December 2000, December 2002 and January 2001 are fairly symmetric around 0 nT, with slightly positive means. December 2001 has a slightly negative shift while January 2002 exhibits a large peak at ~ -5 nT, shifting the mean towards a larger negative value. Category 1 events are fairly evenly spread throughout these months. 54% of category 2 events occur in the negatively shifted months of December 2001 and January 2002, with 26% (30 events) falling within the largely negative January 2002. In comparison, 59% of category 3 events are found in these months with 38% (35 events) falling within January 2002. Removing all January 2002 onsets from the superposed study has no significant effect on the trends and variations seen in any of the panels of Figures 6.1-6.4 for any of the three categories, with the negative magnitude of category 3 events reduced to a mean value -0.52 nT from -1.19 nT previously. We also note that the mean of the category 3 null line (-0.77 nT) is much more negative than the mean of either category 1 (0.07 nT) or category 2 (-0.05 nT). That is, the negative shift in B_y for category 3 substorms is due to a bias in IMF orientation during parts of our study interval and not a characteristic of substorm events showing no particle injection signatures.

Previous studies have shown that substorm onsets most often occur in the pre midnight sector of the auroral oval in the northern hemisphere but that the onset location shifts towards dawn for events occurring during periods of more negative IMF B_y , (e.g. Gerard *et al.*, 2004; Liou *et al.*, 2001b). To investigate whether our results are consistent with this result, we plot the distribution of onset MLTs (the MLT of the auroral brightening identified by Frey *et al.* (2004) by visual inspection of IMAGE FUV auroral images) for the three categories in Figure 6.7. Both category 1 and 2 distributions (green and red respectively) are very similar, both having a mean of

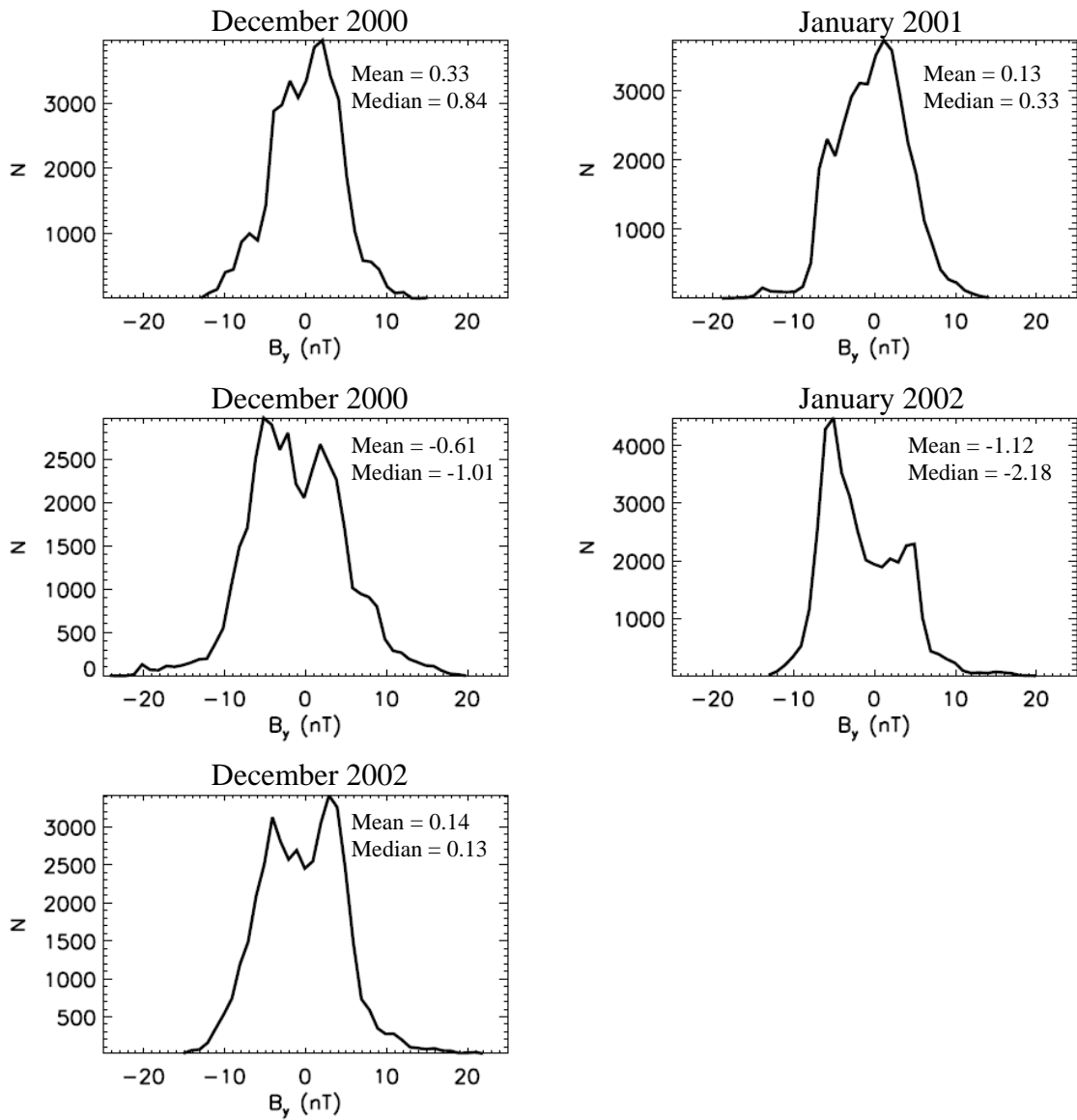


Figure 6.6: Distributions of IMF B_y for the 5 months used in this study. Distributions are produced from all 1 minute resolution values (provided by the OMNI Definitive, 1 AU 1 minute IMF and Plasma database, courtesy of CDAWeb) from each day of the relevant month.

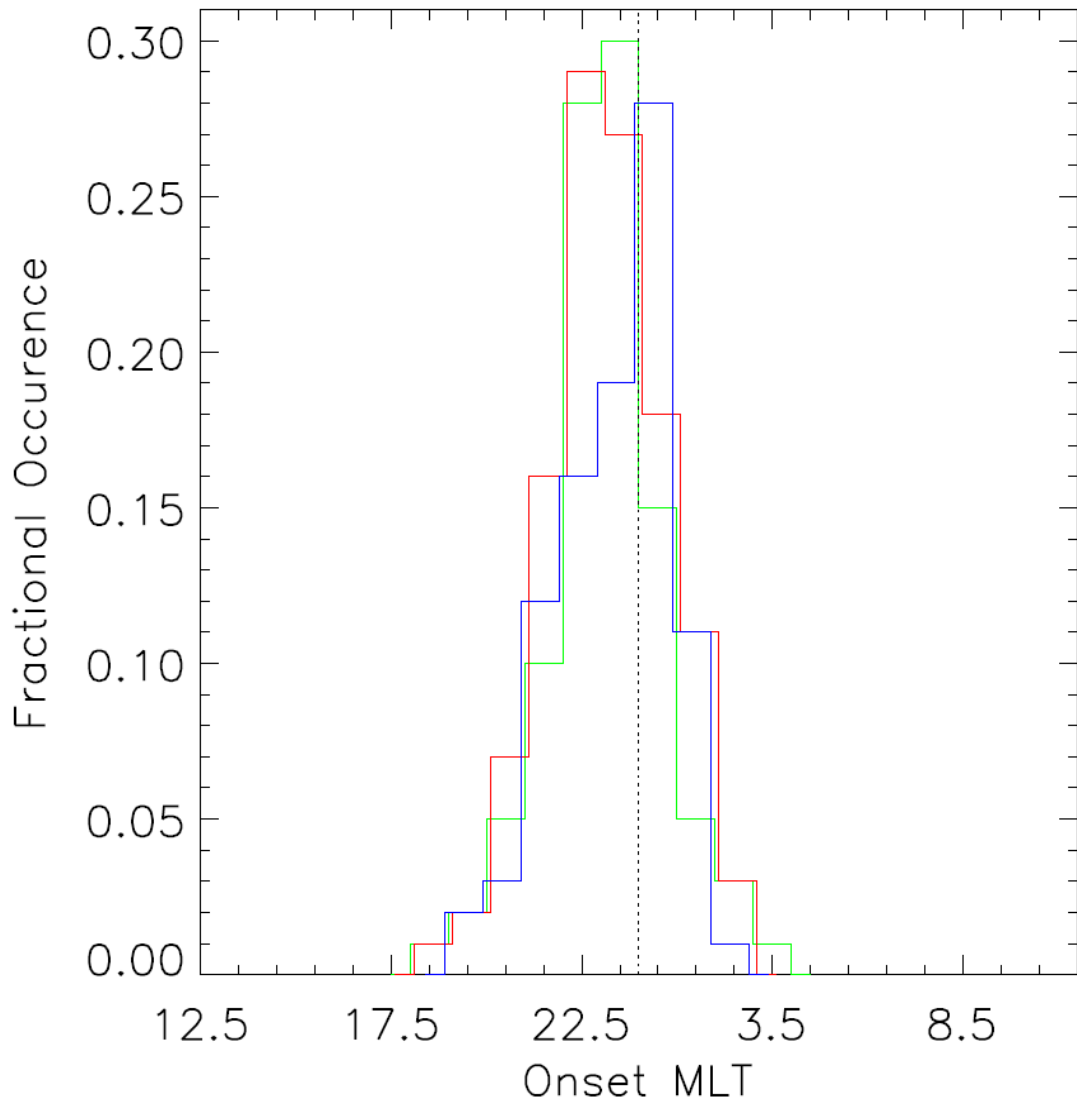


Figure 6.7: Distribution of onset MLTs for category 1 (green), category 2 (red) and category 3 (blue) substorm events.

~ 23.1 MLT, consistent with the average onset location found in previous studies. Applying the K-S statistical test to the two distributions returns a probability of 0.98 that the two distributions are the same. Category 3 events are shifted towards more positive MLTs, although this is not largely reflected in the mean, with a mean of 23.5 MLT. The K-S test returns a probability that category 3 events are the same as category 1 or 2 of less than 0.06. This result is consistent with the shifting of onset MLTs toward dawn for substorms occurring with more negative IMF B_y . However, it also suggests that category 3 events are not the same as category 1 and 2. That is, they may be a different type of process.

The category 3 B_x component, blue Figures 6.1g and 6.4g, is found at slightly more positive values than the null line, as would be expected to accompany the negative B_y shift due to anti correlation between B_x and B_y in the Parker spiral. The category 3 solar wind proton density, pressure and flow speed are all significantly reduced compared to category 1 and 2 events and the average null lines.

The category 3 SYM-H, AL and AU indices (blue Figures 6.1n and 6.4n) are much reduced compared to category 1 and 2 events, suggesting that category 3 events occur during quiet geomagnetic conditions. The AL and AU indices both show slight deviations at the onset time suggesting that very small geomagnetic disturbances are occurring.

Previous studies have shown that very weak substorms and pseudo-breakups occur with very weak IMF B_z , solar wind proton density and pressure (e.g. Kullen and Karlsson, 2004) and show very weak magnetic activity (see McPherron *et al.*, 2008 and references therein). The results of this study suggest that category 3 may contain both very weak substorms as well as other events which may cause nightside auroral brightenings such as pseudo-breakups (however, as discussed above, they are not dominated by pseudo-breakups occurring during the growth phase of substorms).

6.2 Auroral Boundaries

The OCB in the ionosphere marks the transition from magnetic field lines with an open topology to a closed topology and hence represents the mapped location of the dayside

and nightside reconnection sites. Tracking changes in the latitude of the OCB thus gives important insights into the reconnection process. The equatorward boundary of the electron auroral oval has been shown to be co-located with inner edge of the plasma sheet (e.g. Eather and Mende, 1972). Tracking latitudinal changes in the equatorward boundary of the auroral oval is therefore an important diagnostic tool for the state of the magnetosphere.

In the classic definition of a substorm (see section 2.1 of this thesis) the aurora drift equatorward in the growth phase of the substorm before rapidly expanding poleward during the expansion phase. Ground and space-based auroral imagery have confirmed this general motion of the aurora during substorms, but have also shown that this average behaviour is highly variable and dynamic. For example, the aurora may remain at a relatively constant latitude when open magnetic flux continues to be added to the polar cap during the expansion phase. Other studies have shown that the motion of the poleward and equatorward boundary of the auroral oval is not concurrent at all MLTs (e.g. Jayachandran *et al.*, 2005; Coumans *et al.*, 2007). To date few and limited statistical studies of the poleward and equatorward motion of auroral boundaries during substorms have been carried out. By far the most extensive of these was carried out by Mende *et al.* (2003); this study is summarised below and in Figures 6.8 and 6.9.

Using both WIC and SI12 observations of the auroral oval Mende *et al.* (2003) carried out a superposed epoch analysis of the poleward (top set of traces Figure 6.8) and equatorward (bottom set of traces Figure 6.8) auroral boundary motions at the onset MLT ($RMLT = 0$; black line Figure 6.8) and at ± 2 ($\pm 2 RMLT$; yellow and green lines Figure 6.8) and ± 4 MLT ($\pm 4 RMLT$; red and blue lines Figure 6.8) from the onset MLT. Here we have introduced the notation $RMLT$ to denote the MLT at which the boundary motion takes place relative to the MLT of the initial auroral brightening, determined from the location of the initial auroral brightening in the IMAGE data. Their data set consisted of 112 substorm onsets from the time period 23 June 2000 to 14 May 2001. Their results show that prior to substorm onset the poleward boundary moves slowly equatorward by $\sim 1-2^\circ$ in all MLT sectors. At onset ($t=0$) the poleward boundary moves rapidly to higher latitudes. At $RMLT=0$ (black line top set of traces Figure 6.8) the response of the poleward boundary to onset is rapid and large, the poleward motion appearing to start $\sim 4-5$ minutes before onset, and moving rapidly poleward by $\sim 4-5^\circ$

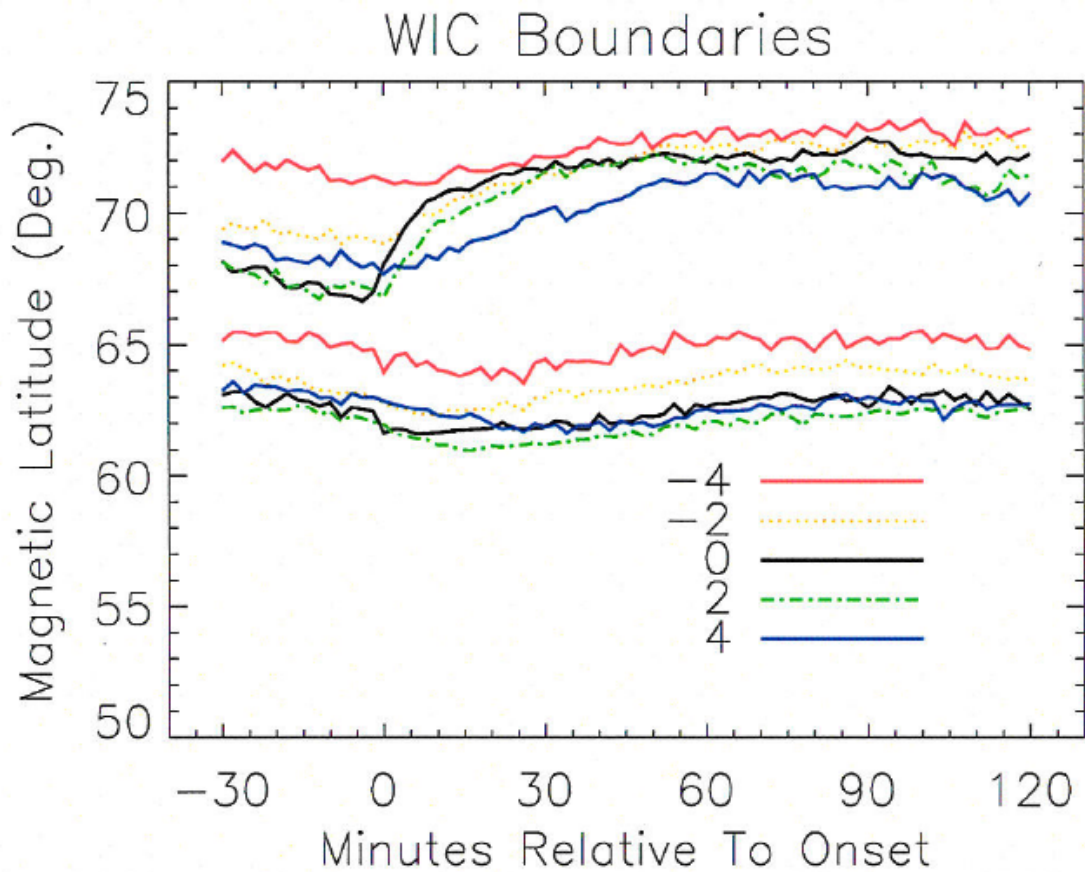


Figure 6.8: The latitude of the poleward (top set of traces) and equatorward (bottom set of traces) boundaries of the WIC auroral oval from approximately 30 minutes prior to substorm onset to 120 minutes after, at the MLT of the initial auroral onset (black line) and at -2 (yellow), +2 (green), -4 (red) and +4 (blue) MLTs from this location, from a study of 91 substorms by Mende *et al.*, 2003.

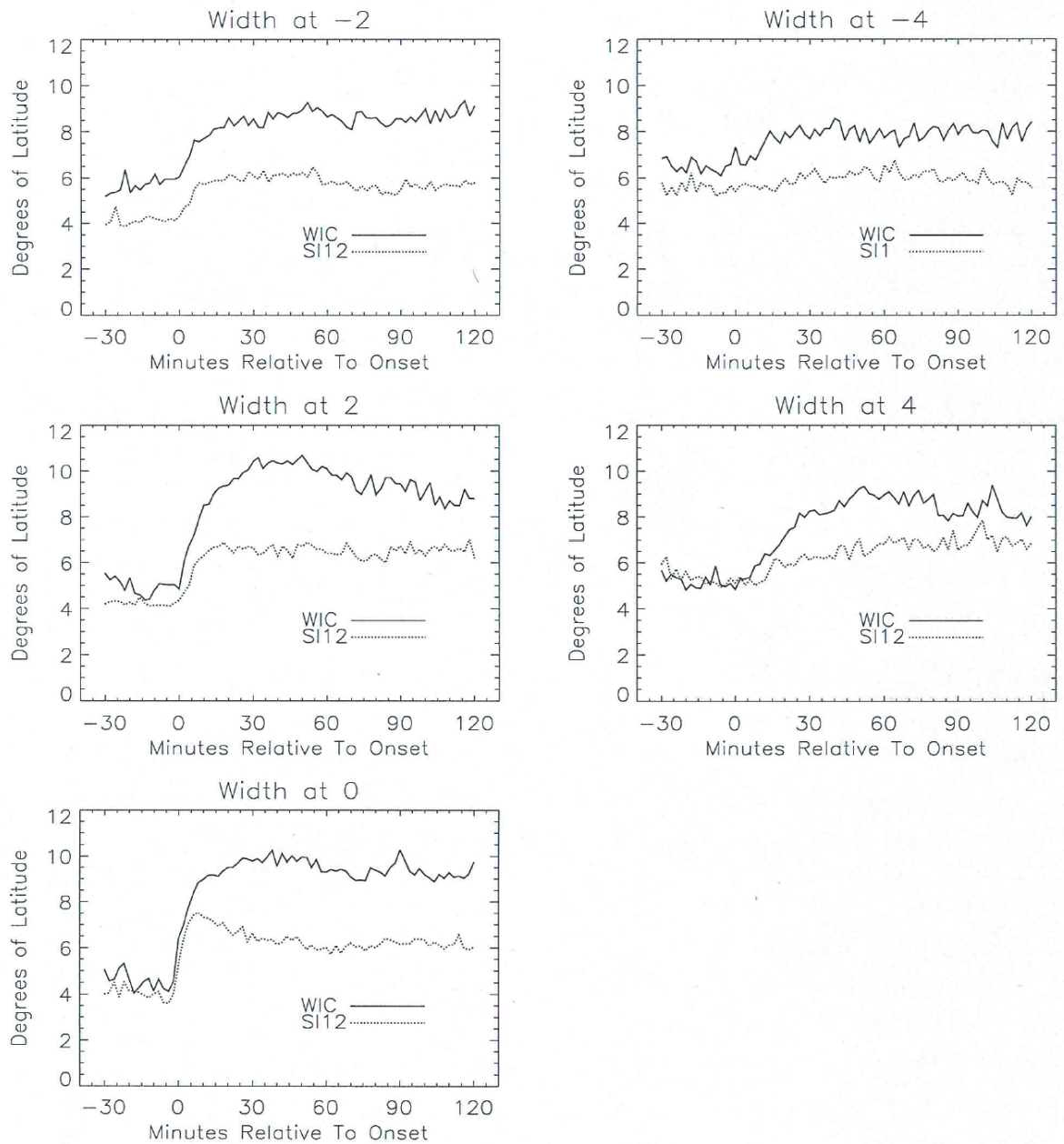


Figure 6.9: The variation in the width of the auroral oval at the onset MLT of the initial auroral brightening (0) and at -2, +2, -4 and +4 MLTs from this location from a study of 92 substorms by Mende *et al.*, (2003). The solid lines show the width as calculated from boundary estimations of the WIC (electron) auroral oval (see Figure 6.8) and dashed lines from boundary estimations of the SI12 (proton) auroral oval.

until ~ 10-15 minutes after the onset. The boundary then drifts poleward by ~ 1° over the next hour. At both ± 2 *RMLT* the poleward motion begins immediately at $t=0$. The poleward motion is less rapid for both MLT sectors, with an expansion of ~ 5° over ~ 30 minutes seen at +2 *RMLT* (green line top set of traces Figure 6.8) and a more sluggish motion of 3-4° over ~ 50 minutes for -2 *RMLT* (yellow line top set of traces). The response to onset at +4 *RMLT* (blue line top set of traces Figure 6.8) is slow but there is still a poleward motion of up to 4° over the first hour from onset. At -4 *RMLT* (red line top set of traces Figure 6.8) the response seen is minimal, with a poleward motion of ~ 2° over the first hour and a delay of ~5-10 minutes seen between $t=0$ and the start of the poleward motion.

The equatorward boundary's response to onset was found to be much less pronounced than the poleward boundary and to show a very similar motion at all MLTs. As expected, the equatorward boundary was found to slowly drift to lower latitudes in the growth phase, this equatorward motion continuing for several minutes after onset, a delay of ~5 minutes at *RMLT*=0 (black line bottom set of traces Figure 6.8), 10-15 minutes at ± 2 *RMLT* and 20-30 minutes at ± 4 *RMLT*. The equatorward boundary is found at slightly higher latitudes (up to ~ 3-4°) at premidnight MLTs (-4 and -2 *RMLT*; red and yellow lines respectively bottom set of traces Figure 6.8) than in the dawnward sector (+4 and +2 MLT; blue and green lines respectively bottom set of traces Figure 6.8). The authors suggest that this may be explained by the symmetry of the auroral oval. If the auroral oval is located at its lowest latitude at midnight (00 MLT), and as most onsets occur between 22-23 MLT, the lowest boundaries should be found at ~ +2 MLT, with +4 MLT boundaries at approximately the same latitude as the onset MLT. Boundaries at both -2 and -4 MLTs will be found at higher latitudes, as is seen in their study.

The response of the auroral oval width to these boundary motions is shown in Figure 6.9. In response to the motions of the poleward and equatorward boundaries, a slight narrowing of the auroral oval width during the growth phase is seen in most MLT sectors. In the first 5-10 minutes following onset a rapid thickening of ~5° is seen at *RMLT*=0 followed by a further thickening of ~1° over the next 30 minutes. At +2 *RMLT* a rapid thickening of ~3.5° is seen in the first 10 minutes after onset, followed by a thickening of ~2° over the next half hour. At -2 *RMLT* the response is less

pronounced, with a rapid thickening of $\sim 2^\circ$ seen in the first 5-10 minutes followed by a further thickening of $\sim 1^\circ$ in the next half hour. The response at ± 4 *RMLT* is much more gradual with a total widening of $\sim 4^\circ$ over the 50 minutes proceeding onset for +4 *RMLT* and a smaller widening of $\sim 2^\circ$ over 30 minutes for -4 *RMLT*. Following the oval widening, the oval then remains at approximately the same width for the remainder of their time window (up to 120 minutes after onset) for all MLT sectors.

In summary, this study has shown that both the OCB and equatorward boundary of the auroral oval near the MLT of substorm onset slowly drift equatorward during the growth phase before rapidly expanding poleward after substorm onset but that these motions are variable depending upon the specific MLT from onset. In general, the boundary motions after substorm onset are reduced and slower to respond the further from the onset MLT. The motion of the OCB is much more pronounced than that the equatorward boundary.

In this study we firstly carry out the largest superposed epoch analysis to date of the motion through the substorm process of the OCB, equatorward auroral boundary and auroral oval width as seen by the WIC detector from all substorms identified in the December and January months of 2000-2002 by Frey *et al.* (2004), a total of 451 events. We then divide the study into the three distinct LANL particle injection categories, giving us new insights into these different types of events including their global extent.

6.2.1 Methodology

Using the technique described in chapter 4 of this thesis, we have identified the location of the OCB at 24 separate MLT sectors around the auroral oval from over 12000 auroral images taken by the IMAGE WIC detector in the months of December 2000 and December and January of 2001-2002. The location of the equatorward boundary (λ_{Eq}) of the auroral oval has similarly been determined. The equatorward boundary is assumed to be displaced by one FWHM equatorward of the center of the Gaussian fit to the intensity-latitude profiles across 1 hour MLT sectors of the auroral oval from 50-90° magnetic latitude. That is:

$$\lambda_{Eq} = A_1 - \Delta\lambda, \quad (6.2)$$

where A_1 is the latitude of the peak of the Gaussian and $\Delta\lambda$ is the Gaussian FWHM. We do not search for the most poleward Gaussian fit, as described in chapter 4 for the OCB. The fit is made over the entire 50-90° latitude range and if the first fit does not meet the criteria 1-5 of section 4.1.2 of this thesis then we do not make a boundary estimation. By visual inspection of the auroral images, we determine that this method gives a good estimation of latitude of the WIC equatorward boundary on the nightside auroral oval (18-06 MLT). We are unable to estimate the location of the equatorward boundary on the dayside due to dayglow causing errors in the fitting procedure (as described in section 4.2.2 of this thesis). It is important to note that a DMSP correction is not applied to the equatorward boundaries. For a comparison of the latitude of the auroral image equatorward boundary and DMSP equatorward boundary see Carbary *et al.* (2003). A similar study is beyond the scope of this work. The superposed epoch analysis of the boundaries is carried out in the same manner as for F_{pc} and solar wind described above, with boundaries averaged in bins of 13 minutes. The width of the auroral oval is also determined from the individual OCB and equatorward boundary proxies and binned in 13 minute bins.

6.2.2 Superposed Study of All Substorms

Figure 6.10 shows the superposed epoch OCB, equatorward boundary and oval width within ± 5 hours from $t=0$ determined from all December 2000 and December and January 2001-2002 Frey listed substorms (a total of 451 events). The black trace represents the boundaries at $RMLT=0$, green $+2 RMLT$, orange $-2 RMLT$, blue $+4 RMLT$ and red $-4 RMLT$. There is a minimum number of 702 boundary estimates in any one of the 13 minute time bins. The standard deviations vary between 2.5 and 3.5° for the OCB, 2.4-4.5° for the equatorward boundary and 3.1-4.8° for the oval width. The standard errors on the means vary from 0.06-0.12 for the OCB, 0.05-0.14 for the equatorward boundary and 0.07 to 0.18 for the oval width.

As expected the OCB gradually moves to lower latitudes during the growth phase of the substorm (lasting for approximately 100 minutes), the motion being very similar in all

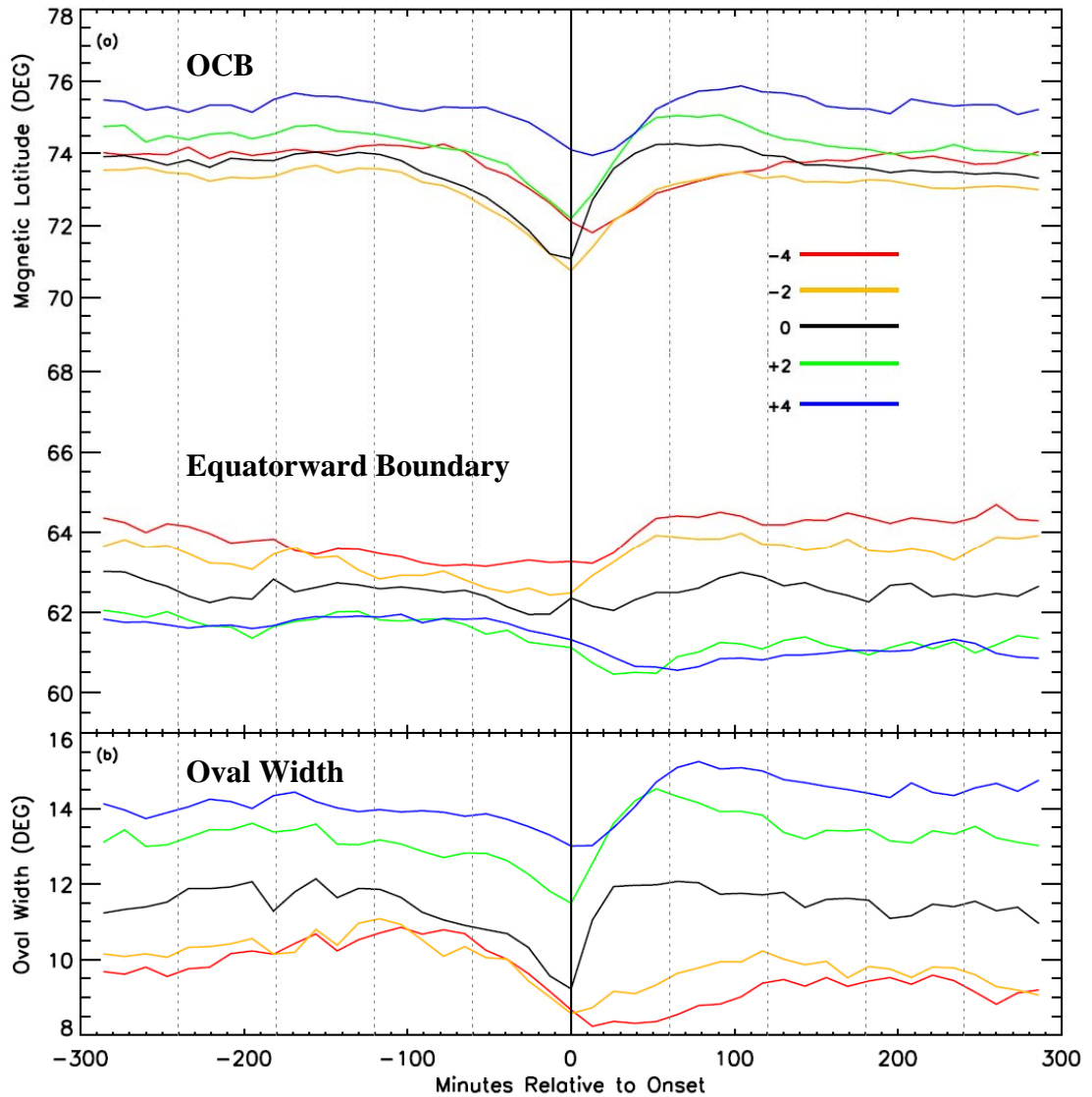


Figure 6.10: Superposed epoch analysis of auroral oval boundary motions keyed to substorm onset time for all substorms identified by Frey *et al.* (2004) for the months of December 2000 and December and January 2001-2002, a total of 451 events. Panel a shows the motion of the OCB and equatorward boundary of auroral oval (top and bottom set of traces respectively) and panel b the derived auroral oval width. Black lines represent the motions in the 1 hour MLT sector of the initial auroral brightening identified by Frey *et al.* (2004). Green, blue, orange and red traces represent the motions in MLT sectors at +2, +4, -2 and -4 MLTs from the onset MLT. The bold vertical line represents the onset time and dashed vertical lines represent hours of UT from onset.

MLT sectors. At $RMLT=0$ the OCB immediately responds to the onset, rapidly moving poleward by approximately 3° in the first 30 minutes. The response at $\pm 2 RMLT$ is also immediate, $+2 RMLT$ showing an expansion of $\sim 3.5^\circ$ over the first 50 minutes and $-2 RMLT$ showing a motion of $\sim 3^\circ$ over the first 90 minutes. There is a slight delay of up to 10 minutes between the onset and the response of the poleward movement at $\pm 4 RMLT$, presumably due to the time it takes for the reconnection to move to later and earlier MLTs from $RMLT=0$. The poleward motion in these MLT sectors is smaller and more gradual, with the poleward movement continuing for up to +2 hours compared to the general halt of the poleward movement at +1 hour at other MLT sectors. A poleward motion of $\sim 2^\circ$ is seen in both MLT sectors over approximately the first 100-130 minutes after onset.

The motion of the equatorward boundary is much less pronounced than for the OCB. As expected, the equatorward boundary slowly drifts to lower latitudes during the growth phase. The response of the poleward motion at $-2 RMLT$ is immediate, while a delay of a few minutes is seen at $RMLT=0$ and $-4 RMLT$. This delay increases towards the dawnward sector, with a 30 minute delay at $+2 RMLT$ and an hour delay at $+4 RMLT$. After the poleward motion the duskward equatorward boundary (-2 and $-4 RMLT$) is located at slightly higher latitudes than its pre-onset values. At $+2$ and $+4 RMLT$ the equatorward motion in the growth phase is larger and more prolonged, continuing for up to an hour after onset. The subsequent poleward motion is reduced compared to other MLTs, leaving the boundary $\sim 1^\circ$ equatorward of its pre-onset values.

The motions of the OCB and equatorward boundary are reflected in the oval width, shown in Figure 6.10b. At $RMLT=0$, $+2$ and $+4 RMLTs$ a very similar thinning of the oval in the growth phase is followed by a rapid thickening in the expansion phase. A delay in the widening of the oval is seen at $+4 RMLT$ due to the delay in the poleward motion of the OCB in this MLT sector. At -2 and $-4 RMLTs$ the widening after onset is much reduced due to the larger poleward motion of the equatorward boundary in the expansion phase. The boundary and oval width variations are grossly similar to the study of Mende *et al.* (2003) but reduced in size and response time. This may be due to the possible inclusion of non-substorm events in our study (i.e. category 3).

Similar to the result of Mende *et al.* (2003), we find that the equatorward boundary is located at higher latitudes duskward of the onset MLT (-2 and -4 *RMLTs*, orange and red traces) and at lower latitudes more dawnward of onset (+2 and +4 *RMLTs*, green and blue traces). As suggested by Mende *et al.* this may be explained by the symmetry of the auroral oval. The average onset MLT of all the onsets in this study is 23.26 MLT. This suggests that, on average the equatorward boundary of the WIC auroral oval for December 2000 and December and January 2001-2002 is at its lowest latitude at ~01-02 MLT (+2 *RMLT*), followed by 03-04 MLT (+4 *RMLT*), 23-00 MLT (*RMLT*=0), 21-22 MLT (-2 *RMLT*) and finally 19-20 MLT (-4 *RMLT*). In the study of Mende *et al.* (2003) the OCB is also located at higher latitudes in the duskward MLT sectors. However, this situation is almost reversed for the location of the OCB in this study, with the OCB found at its lowest latitude at -2 *RMLT* (orange), followed by *RMLT*=0 (black), -4 *RMLT* (red), +2 *RMLT* (green) and finally +4 *RMLT* (blue). This is also reflected in the oval widths. In the dawnward sector (green and blue traces), prior to substorm onset, the auroral oval is up to 4-5° thicker than at duskward MLTs (orange and red traces). Due to the motions of the equatorward boundary and OCB during the expansion phase, this situation is exaggerated following onset. Post-onset the auroral oval becomes thinner in the duskward sector and thicker at dawnward MLTs, with the post-onset dawnward oval being up to 6-7° thicker than in the duskward sector. Visual inspection of the WIC auroral ovals confirms this result.

We attribute this result to the low energy precipitation region often seen to cover several degrees of latitude poleward of the main auroral oval at dawnward MLTs. This is the so-called sub-visual drizzle region, which extends away from the main oval precipitation in the post-midnight sector towards the dayside. Mende *et al.* (2003) estimated the high latitude boundary of WIC auroral emission by fitting a double Gaussian like function to intensity-latitude profiles across 1 hour MLT sectors of the auroral oval. They then assume the upper boundary is located at the most poleward point at which the fitted Gaussian is above 50% of the pre-onset averaged maximum auroral intensity (averaged from 30-12 minutes before onset). In chapter 4 of this thesis we have shown that the DMSP particle precipitation estimations of the OCB are found several degrees poleward of the equivalent IMAGE WIC OCB boundary in the dawnward sector of the auroral oval. Directly observing the precipitating particles by DMSP allows the transition between the low energy sub-visual drizzle region on closed

magnetic field lines and the low-energy polar rain on open magnetic field lines to be directly determined. Fitting a Gaussian function to the intensity-latitude profiles is much weaker at defining this transition, often smoothing the sub-visual drizzle region into the background part of the fit. The DMSP OCB is therefore found poleward of the WIC OCB in the dawnward sector, where the sub-visual drizzle region is prominent, and we have applied a correction to our WIC OCB estimations to account for this. A similar correction has not been applied in the study of Mende *et al.* (2003), and, as they state, they are studying the poleward edge of poleward auroral emission rather than the true location of the OCB.

This DMSP correction is likely to be the biggest factor affecting the offsets seen, but we must also consider whether a smaller effect may be induced by the viewing angle of the IMAGE spacecraft. Figure 3.1 shows the orbit of the IMAGE spacecraft for the five months of this study. Over the first four months the average viewing angle of the spacecraft is located directly over the northern polar cap, with apogee slightly duskward in December 2000 and January 2001 and slightly dawnward in December 2001 and January 2002. Only in December 2002 is the apogee significantly shifted towards the dawnward side. This may cause a slight elongating of the dawn side auroral oval to higher latitudes (as seen by the imager), placing the dawnward OCB at higher latitudes, and an elongating of the duskward oval to lower latitudes, placing the duskward equatorward boundary at a lower latitude. However, we would expect this effect to be minimal and only significant in the final month of the study. Removing the boundary estimations of December 2002 from the superposed study does not significantly change the offsets seen.

6.2.3 Superposed Boundary Movements of LANL Categories

Figure 6.11 shows the superposed epoch boundary and oval width movement for the three LANL categories, green category 1, red category 2 and blue category 3, at $RMLT=0$ and ± 2 and ± 4 $RMLT$. There is a minimum of 108 boundary estimates in any of the 13 minute time bins. The standard deviations vary between 2.2-4.2° for the OCB, 1.8-5.9° for the equatorward boundary and 2.6-5.2° for the oval width. The standard deviations vary between 0.09-0.36° for the OCB, 0.08-0.39° for the equatorward boundary and 0.13-0.49° for the oval width. Figure 6.12 shows the superposed latitude

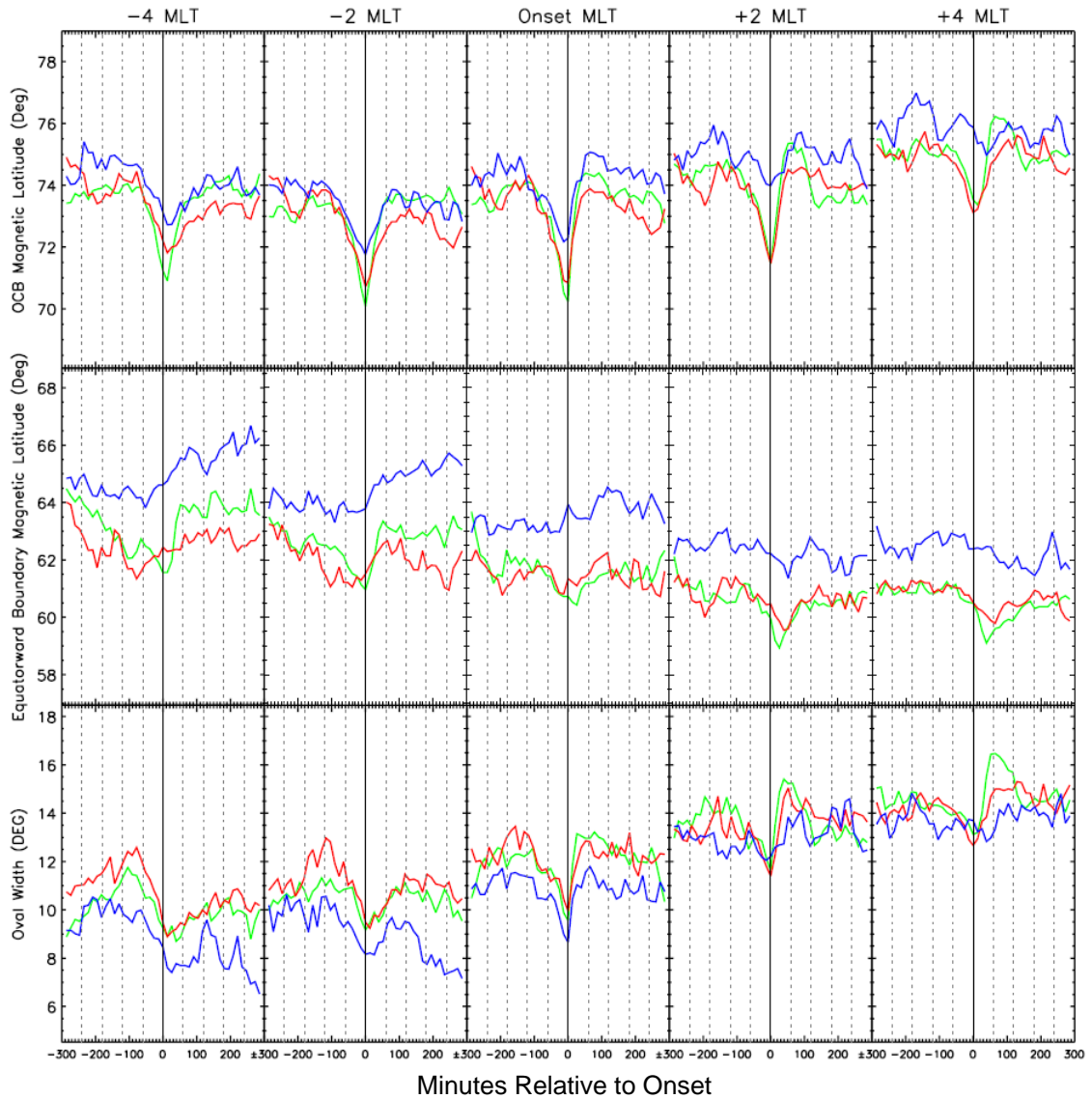


Figure 6.11: Superposed epoch analysis of the motion of OCB, equatorward boundary of the auroral oval and auroral oval width keyed to substorm onset time for category 1 (green), category 2 (red) and category 3 (blue) substorm events at the MLT sector of the initial auroral brightening (Onset MLT) and at ± 2 and ± 4 MLTs from the onset MLT. The bold vertical line represents the time of onset and dashed grey vertical lines represent hours from onset.

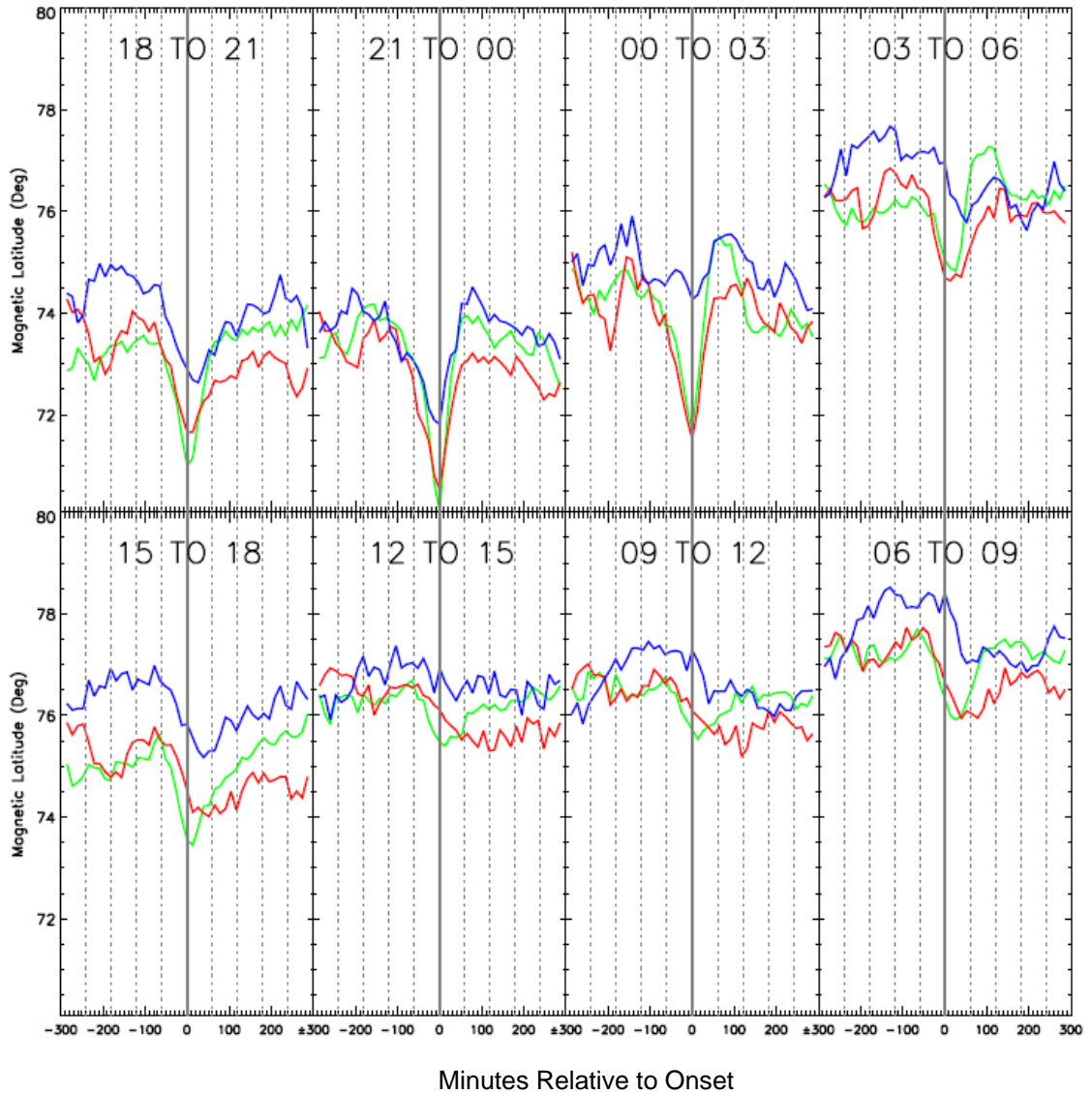


Figure 6.12: Superposed epoch analysis of the motion of the OCB for the entire auroral oval. OCB estimates have been averaged over 3 hours of MLT. Category 1 events are shown by green, category 2 by red and category 3 by blue. The vertical solid line at 0 minutes shows the time of onset and the dashed vertical lines show hours from onset.

variation of the OCB averaged over 3 MLT sectors around the entire auroral oval. Standard deviations are of the order 2-4° and standard errors 0.1-0.3°. A similar plot is not possible for the equatorward boundary due to the lack of accurate estimates of the equatorward boundary on the dayside due to low-latitude dayglow swamping the equatorward edge of the auroral oval.

6.2.3.1 Motion of the OCB

The OCB motion for category 1 and 2 events is very similar and follows the general trends seen for all substorms at all MLT sectors. Category 3 events (blue) show smaller OCB motions in all MLT sectors. The equatorward motion and subsequent poleward expansion of the OCB is seen at all MLT sectors for category 1 events shown in Figure 6.12, showing these events to be truly global in nature. The poleward and equatorward boundary motions varying between ~ 1-4°, with the largest boundary motions closer to midnight.

Category 2 events (red) show the expected equatorward and poleward motions on the nightside (18-06 MLT, Figure 6.12). A poleward expansion is also evident in the 06 to 09 MLT sector after an ~ 1 hour delay from onset. In the 15-18 MLT sector the OCB drifts equatorward during the growth phase, remains at an almost constant latitude between the onset time and +2 hours, before moving poleward by less than 1°. In both the 09-12 and 12-15 MLT sectors the OCB continues to move to lower latitudes for ~ 2 hours after onset, indicating that open magnetic flux is still being added on the dayside. This is not seen for category 1 events (green) and is consistent with the increased dayside driving suggested by the elevated levels of the ε parameter for category 2 events (Figure 6.1m, see section 6.1.2.1).

Category 3 events show a clear equatorward and poleward motion around onset between 15-00 MLT. The movement is much less clear at 00-15 MLT, with the fluctuations around onset of a similar magnitude to those of the rest of the period of study, suggesting that these are not significant. These results suggest that category 3 events are highly localised reconnection events which do not become a global phenomenon.

Many previous studies have shown that the initial onset region is located within the closed magnetic field line region of the auroral oval, some distance from the OCB (e.g. Gérard *et al.*, 2004). We therefore might expect to see a short delay between the poleward motion of the OCB and substorm onset due to the time it takes for the reconnection to eat through closed magnetic flux before proceeding onto open magnetic field lines. However, and as reported in previous studies (Mende *et al.*, 2003), this is not seen in the superposed boundary plots. The OCB is seen to respond immediately to substorm onset at midnight MLTs with a short delay only evident at 3-18 MLT in Figure 6.12 and ± 4 *RMLT* in Figure 6.11. This short delay is presumably due to the time it takes for the reconnection to travel to earlier and later MLTs from the onset MLT. One explanation of this lack of delay at midnight could be due to the timing of substorm onset in our study. Due to the temporal resolution of the IMAGE spacecraft we can only determine the time of the initial brightening to within 2 minutes. However, as pointed out by Voronkov *et al.* (2003), the initial auroral brightening (as may be seen by ground-based all-sky cameras) is often below the threshold of UV detectors such that there may be a time delay of up to ~5 minutes between the true onset time and the first auroral brightening seen by UV auroral imagers. Reducing the bin size of the superposed study does not effect the trends seen, but does significantly increase the size of the standard deviations and standard errors.

6.2.3.2 Motion of Equatorward Boundary

The motion of the category 1 equatorward boundary (green Figure 6.11, middle row) very closely follows the motions seen for all substorms. That is, a smaller poleward motion and longer delay between onset and the poleward turning of the boundary for further dawnward MLTs (+2 and +4 *RMLT*). Category 1 events show the largest boundary movements of the three categories. Category 2 events show the same general trends as for all substorms and category 1 events, but with, in general, smaller poleward movements after onset. Category 2 events also show a slightly longer delay between the onset time and poleward turning of the equatorward boundary at +2 and +4 *RMLTs* as compared to category 1 events. As expected, the category 3 equatorward boundary is found at higher latitudes than category 1 or 2 due to the contracted auroral ovals for this category. The equatorward boundary of category 3 events does not follow the typical boundary movements expected around substorm onset. At -4 and -2 *RMLT* the category

3 equatorward boundary continually moves towards higher latitudes from approximately $T=0$ until the end of the period of study. At +4 and +2 *RMLT* this motion is generally reversed.

6.2.3.3 Oval Width Variation

The oval width of category 1 and 2 events also follow each other closely at all MLTs and show the general trends of all substorms. The category 3 oval width is more complicated due to the less typical motions of the OCB and equatorward boundaries. At the onset MLT the oval width variation is similar to that of category 1 and 2, showing the expected thinning and thickening motion typical of a substorm. Due to the poleward motion of the equatorward boundary at -4 and -2 *RMLT*, the oval width generally decreases for the whole period of study in the duskward sector. At +2 and +4 *RMLT* the oval width remains relatively constant. The boundary motions suggest that category 3 events are much smaller, much more localised events than either category 1 or 2.

6.3 Discussion

In order to have confidence in any conclusions drawn from this study it is important to discuss the statistical significance of the trends and variations seen in the superposed plots. To give an indication of the error on the mean for each LANL category, we plot the standard error on the mean (the standard deviation divided by the root of the total number of events in each 13 minute bin, grey shaded region) on the superposed plots of Figures 6.2-6.4 along with the null lines for each category (representing the average variations of the parameters for the period of study, grey line). Further, we find a small number of events in each category which occur during relatively enhanced solar wind conditions from the average behaviour seen in each category. Removing these events from the superposed analysis does not effect the average trends seen in any of the categories and we conclude that the variations and trends seen in Figures 6.1-6.4 are true representations of the differing LANL categories.

The standard deviations of the superposed boundary plots in Figures 6.8, 6.9 and 6.10 vary from $\sim 2-4^\circ$ for the OCB, $2-6^\circ$ for the equatorward boundary and $\sim 3-5^\circ$ for the oval width. The standard error on the mean varies between $0.06-0.36^\circ$ for the OCB,

0.05-0.39° for the equatorward boundary and 0.07-0.49 for the oval width, less than the deviations in boundary movements which we consider to be significant.

Here let us bring together the main findings of the superposed F_{pc} , solar wind and IMF, geomagnetic activity, maximum nightside auroral intensity and auroral boundary motions and discuss their implications for the three LANL categories.

The category 1 superposed F_{pc} , solar wind and IMF conditions and geomagnetic activity are shown by the green traces of Figures 6.1-6.2. Category 1 events are the largest and most energetic of the three LANL categories. They occur with the highest F_{pc} at onset (panel a Figures 6.1 and 6.2) and show the largest peaks in auroral intensity (panels b) and magnetic indices (panels l and n). They show the most obvious growth and expansion phases in F_{pc} and geomagnetic indices. They close the most F_{pc} during the expansion phase, ~20% consistent with the amount of F_{pc} closed in previous substorm studies (e.g. Caan *et al.*, 1978; McPherron and Hsu, 2002; Huang *et al.*, 2009). They show the sharpest increase and subsequent decrease in auroral intensity and AL and AU indices. They occur in periods of enhanced geomagnetic activity (AL, AU and SYM-H) but average IMF and solar wind conditions (pressure, proton density and IMF B_y , B_x , B_t , panels e, g and d respectively). The dayside reconnection is strongly controlled by the IMF B_z component (panel c), which shows a significant southward turning and subsequent northward recovery typical of a ‘classical’ substorm onset growth phase (McPherron *et al.*, 1973). The superposed boundary study (green traces Figures 6.9-6.10) shows that the category 1 events are truly global in nature, with the typical boundary movements expected around substorm onset seen at all MLTs. In conclusion, category 1 events show all the expected signatures of a ‘classic’ substorm event. It seems likely that category 1 events are large, energetic substorms occurring due to a large southward turning of the IMF B_z component during otherwise average IMF and solar wind conditions.

The superposed category 2 F_{pc} , solar wind, IMF and geomagnetic activity is shown by the red traces of Figures 6.1 and 6.3. Category 2 events occur at slightly lower values of F_{pc} than category 1 events, with a more gradual increase in F_{pc} during the growth phase, which lasts for approximately 30 minutes longer than for category 1 events. After onset the decrease in F_{pc} (panels a), auroral intensity (panels b) and geomagnetic indices

(panels l and n) is also more gradual, with the recovery lasting for up to 2 hours after the onset. F_{pc} remains elevated after onset due to the continued dayside driving (ϵ panels m) continuing to add open magnetic flux to the polar cap balancing the flux closed by nightside reconnection. The continued dayside driving appears to be more driven by the elevated IMF B_y component (panels e) for these events. Category 2 events also occur with elevated solar wind pressure and proton density (panels i and j). As with category 1 events, category 2 events show the expected OCB, equatorward boundary and oval width motions (red traces Figures 6.9 and 6.10) around onset typical of substorm onsets. These boundary motions are reduced in size compared to category 1 events, perhaps suggesting that these events are smaller or less energetic than category 1. However, the reduced size of boundary motions can also be explained by the continued driving of these events by the solar wind and continued addition of F_{pc} during the expansion phase.

The category 3 F_{pc} , solar wind, IMF and geomagnetic activity is shown by the blue traces of Figures 6.1 and 6.4. Category 3 events do not show the typical growth and expansion phases in F_{pc} (panels a), with F_{pc} continuing to rise after the onset time despite the very low dayside driving (ϵ , panels m), suggesting that nightside reconnection does not progress to open magnetic field lines. There is no large southward turning of the IMF B_z component (panels c) expected in the growth phase of a classical substorm onset. A slight increase and subsequent slow decline is seen in the maximum nightside auroral intensity. This is evidently the auroral brightening identified by Frey *et al.*, (2004) as substorm onset. Small-scale magnetic bays are also seen in the AL (<100 nT) and AU (<50 nT) indices, but these are below the average activity as represented by the null lines (grey lines Figures 6.1-6.4). Pseudo-breakups are known to be associated with small geomagnetic bays of less than 100 nT (Koskinen *et al.*, 1993), suggesting that pseudo-breakups may be included in this category. As well as occurring during quiet geomagnetic conditions (AL, AU and SYM-H Figures 6.1 and 6.4 l and n), they also occur during periods of weak solar wind flow (pressure, proton density, B_r , B_z and V_x Figure 6.1 and 6.4) also typical of very weak substorms or pseudo-breakups (e.g. Zhou and Tsurutani 2001; Kullen and Karlson 2004). The average IMF B_y component (panels e) is shifted toward negative values, though this appears to be at least partly due to a bias in a portion of our solar wind data.

The category 3 OCB (blue Figure 6.11 and 6.10) shows the expected equatorward motion in the growth phase and poleward recovery during the expansion phase. However, this motion is much reduced in latitudinal extent compared to category 1 and 2 events and is only evident close to the onset MLT. This suggests that category 3 events are relatively small, localised events. The motions of the equatorward boundary is atypical of classically defined substorm onsets.

The Frey onset list may include a number of events which are not true substorm events (see chapter 5), and this list may include a number of weaker events which may cause substorm-like auroral brightenings such as pseudo-breakups or Poleward Boundary Intensifications (PBIs). The reduced activity in all parameters of this study for category 3 events and lack of typical substorm onset signatures suggests that these events may not all be substorms. The superposed boundary movements suggest that some of these events may be very small, localised low energy reconnection events, while the small geomagnetic bays suggest that they may be pseudo-breakup events or failed substorms. Another phenomenon which may cause nightside auroral brightenings are Poleward Boundary Intensifications (see McPherron *et al.*, 2008 and references therein). PBIs are nightside auroral intensifications which occur on the poleward edge of the auroral oval, which may or may not subsequently move equatorward with time and have been observed to occur during SMC events as well as often occurring during the expansion phase of substorms. One way of distinguishing PBI events from true substorms might be to look at the ‘onset latitude’ relative to the locations of the OCB and equatorward boundary of the auroral oval.

We have estimated the latitude of both the OCB and equatorward boundary of the auroral oval for all substorms used in this study, allowing us to investigate the location of the onset relative to these boundaries. Figure 6.13a shows the fractional occurrence distribution of the difference between the latitude of the OCB averaged over 6 minutes prior to substorm onset at the onset MLT, and the initial onset arc (provided in the substorm list of Frey *et al.*, 2004). Both category 1 (green) and category 2 (red) show a larger fraction of events occurring within 2° of the OCB than do category 3. If PBI events are present in the Frey substorm list, then these are not exclusively found within category 3. Only 9 category 3 events occur within 2° of the OCB. Gérard *et al.* (2004) found the location of the onset latitude relative to the OCB for 78 substorm onsets from

November 2000 to January 2001, overlapping our dataset. They found that the latitude difference varied between 0 and $\sim 15^\circ$ with the majority of the events below 5° (see their Figure 4a). Our results are consistent with these findings. Gérard *et al.* (2004) also noted that the average latitude difference between the onset location and the equatorward boundary is most often between $2-6^\circ$, which is also consistent with our results. However, Gérard *et al.* (2004) do not present the latitude differences as a fraction of the auroral oval width or discuss the location of the onset within the auroral oval.

Figure 6.13b shows the fractional occurrence distribution of the OCB-onset latitude difference as a fraction of the oval width. Rather surprisingly the onset location is on average closer to the OCB than the equatorward boundary of the auroral oval for all three LANL categories, all with approximately the same mean of 0.4 and with a skew towards the onset latitude being closer to the OCB. A DMSP correction has been applied to the OCB in this study so we should consider whether this effects the offsets seen. The onset MLTs of the substorms in this study vary from $\sim 17.5-3.5$ MLT. Between 23 and 3.5 MLT the DMSP correction (Figure 4.5) shifts the OCB poleward by between $1-2^\circ$. Between 17 and 23 MLT the OCB is shifted equatorward by $\sim 1^\circ$. We expect half of the OCBs will be shifted poleward by the DMSP correction and half equatorward by approximately the same amount. Therefore we do not expect the DMSP correction to effect the overall mean of the OCB-onset latitude distribution. We also consider whether the Gaussian fitting routine results in the offsets seen. At onset there is rapid brightening of the auroral oval at the latitude of the initial onset arc. The peak intensity at this latitude will be much greater than the intensity at other latitudes within the auroral oval. Although we use the most poleward fitted Gaussian to find the OCB and the most equatorward to find the low latitude boundary, at substorm onset the rapid brightening may cause only one Gaussian fit to be made to the data with the peak located at the latitude of the onset brightening. Thus the onset latitude would be found half way between the OCB and equatorward boundaries (both located a FWHM poleward and equatorward of the Gaussian peak respectively). However, if this were the case the rapid increase in the peak of the Gaussian intensity would cause a rapid thinning of the Gaussian width of the fitted Gaussians and thus a rapid movement of the OCB towards lower latitudes and a rapid movement of the equatorward boundary towards higher latitudes would be seen. However, this is not seen in the superposed

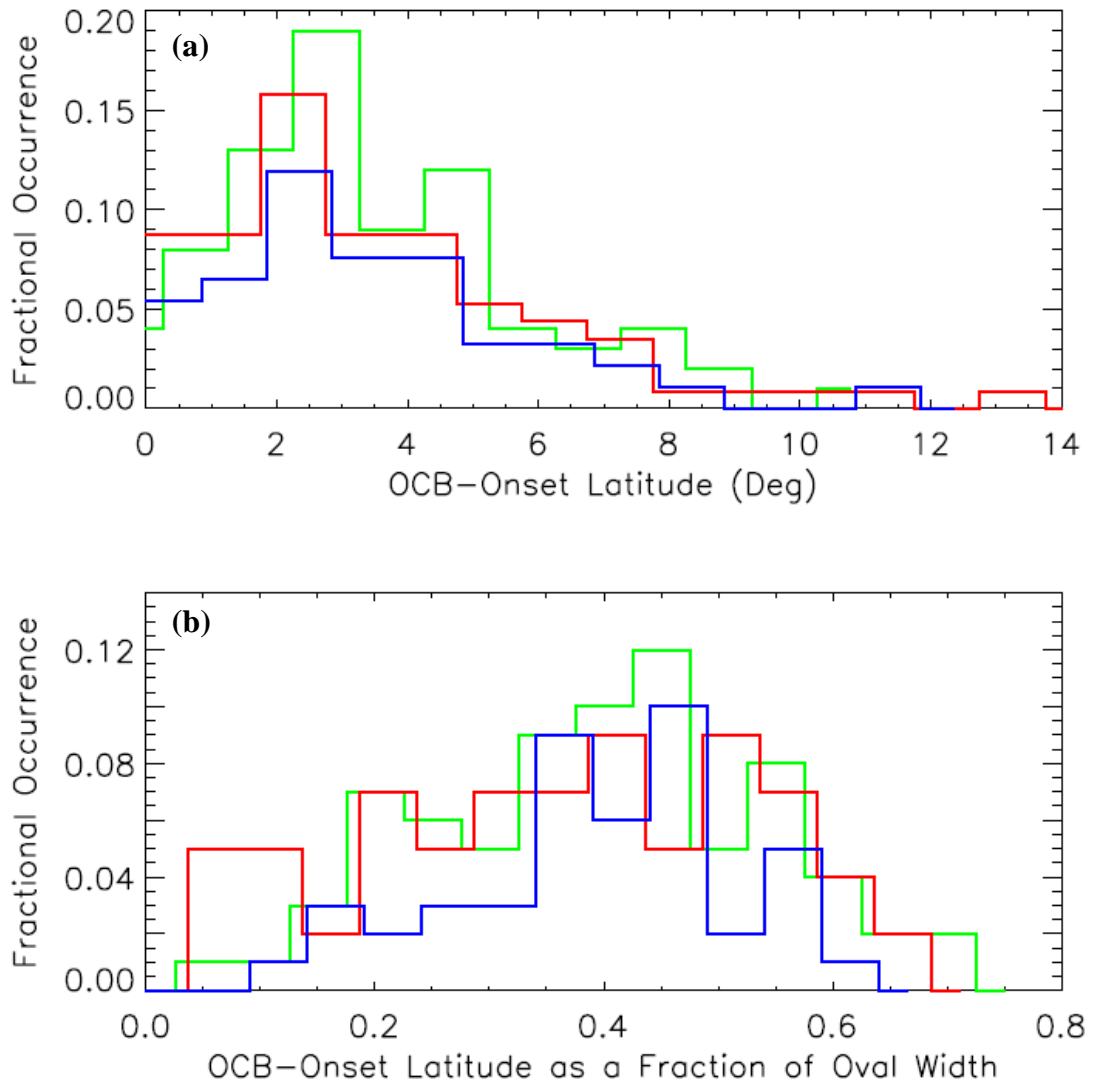


Figure 6.13 : Fractional occurrence distributions of (a) the latitude difference between the OCB at the MLT of the initial auroral brightening and the onset latitude of the initial auroral brightening; (b) the latitude difference between the OCB and onset latitude as a fraction of auroral oval width. Category 1 events are shown by green, category 2 by red and category 3 by blue.

boundary movements. Moreover, we have averaged the OCB location over the 6 minutes prior to substorm onset to negate any effect this may have.

Previous studies have suggested that the initial onset arc is located several degrees equatorward of the OCB, closer to the equatorward edge of the auroral oval than poleward edge (e.g. Murphree *et al.*, 1993; Lyons *et al.*, 2002). However our results are consistent with the findings of Gérard *et al.* (2004) in which for the majority of cases the onset location is less than 5° from the OCB. Murphree *et al.* (1993) used Viking UV auroral images to identify the location of the onset within the auroral oval. They found that the onset was located in the poleward part of the diffuse aurora. Sotirelis and Newell (2000) have shown that approximately half of the auroral oval is made up of discrete auroral precipitation and half by diffuse emission. Initial plots of the total electron flux-latitude profile across the auroral oval as measured by the SOPA instrument onboard the LANL spacecraft suggest that our estimation of the OCB from WIC is located at the poleward edge of the discrete electron precipitation and that the estimation of the equatorward edge of the WIC auroral oval is roughly located at the equatorward edge of the diffuse electron precipitation. If the onset is indeed located at the poleward edge of the diffuse precipitation (approximately half way between our OCB and equatorward boundary) then this may explain the offsets seen. Unfortunately, there are no coincident crossing of the auroral oval at the MLT of onset for any of the substorms in our study to investigate this further.

Caution should also be taken for, as pointed out by Voronkov *et al.* (2003), the initial onset arc as seen by ground-based observations has a thickness of only tens of kilometres, similar to the size of the smallest structure which can be resolved by WIC (Mende *et al.* 2000b). The initial onset arc brightens for several minutes before expanding poleward and may only have a slightly enhanced intensity compared to pre-existing growth phase arcs (e.g. Lyons *et al.* (2002) and references therein). Thus the resolution of space-based imagery may not be able to resolve the initial onset arc until it has brightened significantly. Onset arcs can exhibit a large range of intensities (e.g. Voronkov *et al.*, 2000) and coupled with the 2 minute resolution of the WIC auroral images, it is unclear at what stage the onset arc becomes resolvable in the WIC auroral image. Thus the arc may have travelled several degrees poleward by the time it

is seen using visual inspection of auroral images. A more extensive study of the onset location within the auroral oval is beyond the scope of this present work.

Three distinctly different categories of particle injection events have been indentified, each with their own distinct characteristics. Here let us discuss what these characteristics may tell us about the injection process for these different events.

Category 1 events are defined by their ‘classic’ substorm particle injection signatures and show all the expected signatures of large classically defined substorm onsets. That is, they have a typical growth phase in which large amounts of open magnetic flux is added to polar cap. This should result in a thinning of the plasma sheet. LANL spacecraft near midnight observe a dropout in particle fluxes which we interpret as the spacecraft moving out of the thinning plasma sheet and the expansion of the cold dense plasmasphere to geosynchronous orbit due to tail field line stretching (e.g. Moldwin *et al.*, 1996). At onset the formation of the NENL or current disruption creates an Earthward travelling injection boundary behind which particles of all energies are injected simultaneously (e.g. Birn *et al.*, 1997). A spacecraft located near midnight, in the injection region, observes a dispersionless enhancement of both energetic electrons and protons. Electrons subsequently drift eastward and protons westward due to gradient and curvature drift and are detected as a dispersed energy signature by spacecraft located at later and earlier MLTs. Dispersion increases in the eastward direction for electrons and in the westward direction for protons. The evolution of particle injection in such a manner is defined as a ‘typical’ or ‘classic’ substorm injection signature.

Category 2 events cover all events which show energetic particle enhancements at geosynchronous orbit, as seen by LANL, not showing the expected evolution of a substorm injection event described above. LANL data shows that these events often occur during periods of very active and complicated energetic particle fluctuations. This includes events where the signature is being confused with the signature of other processes, for example drift echoes from previous substorms, enhancements related to solar wind pressure pulses (Lee *et al.*, 2005) or large flux dropouts as the spacecraft leave the plasma sheet. Category 2 events may be substorms associated with or triggered by these other events, or may in fact be these non-substorm events themselves.

However, the solar wind and IMF data (see Figures 6.1 and 6.3) suggest that category 2 events are highly driven by the solar wind and IMF B_y component, suggesting that the continued driving of the magnetosphere during the expansion phase of these events has a direct impact on energetic particle injection into geosynchronous orbit. It seems likely that the more active energetic particle fluctuations seen around the time of onset for category 2 events is a result of this continued driving and that the injection signature of these events is masked or complicated due to this increase in activity.

Category 3 events show no enhancement of energetic particles at any MLTs, i.e. they lack substorm injections. Figure 6.14 shows the distribution of the magnetic latitude of the initial auroral brightening identified by Frey *et al.* (2004). One may argue that category 3 events occur at higher latitudes than either category 1 and 2 events (although there is significant overlap) and that therefore their reconnection sites map to further down tail. Miyashita *et al.* (2004) used observations of the tail magnetic field variations during substorms to show that the initial reconnection site of intense substorms (e.g. category 1) tend to be located closer to the Earth than weaker events (e.g. category 3). Nagai *et al.* (2005) also showed that substorms occurring with stronger or more efficient solar wind energy input (i.e. category 1/2) have their onset location closer to the Earth than those with weaker driving (i.e. category 3). If the reconnection region for category 3 events did indeed map to far down the magnetotail then we may expect that any subsequent particle injection associated with these events may not be energetic enough to reach geosynchronous orbit. However, a tail magnetic field line fixed at a constant latitude will become more stretched as more open magnetic flux is added to the tail lobes and its L-shell value (a value describing the distance from the centre of the Earth to the location at which a field line crosses the equatorial plane of the Earth) increases (as represented in Figure 6.15). The tail is thus expected to be less stretched for category 3 events compared to the higher flux at onset events of category 1 and 2. Although the initial onset of category 3 events appears to occur at higher latitudes in the ionosphere than either category 1 or 2, the reconnection site (which occurs in the plasma sheet in the equatorial plane of the Earth and is thus located at a distance from the Earth given by the L-shell value) may in fact map to smaller L-shells, and closer to the Earth, than either category 1 or 2 events. We also note that the ring current as measured by the SYM-H index is very low for category 3 events and therefore we would not expect injections to be impeded from reaching geosynchronous orbit. Investigating the

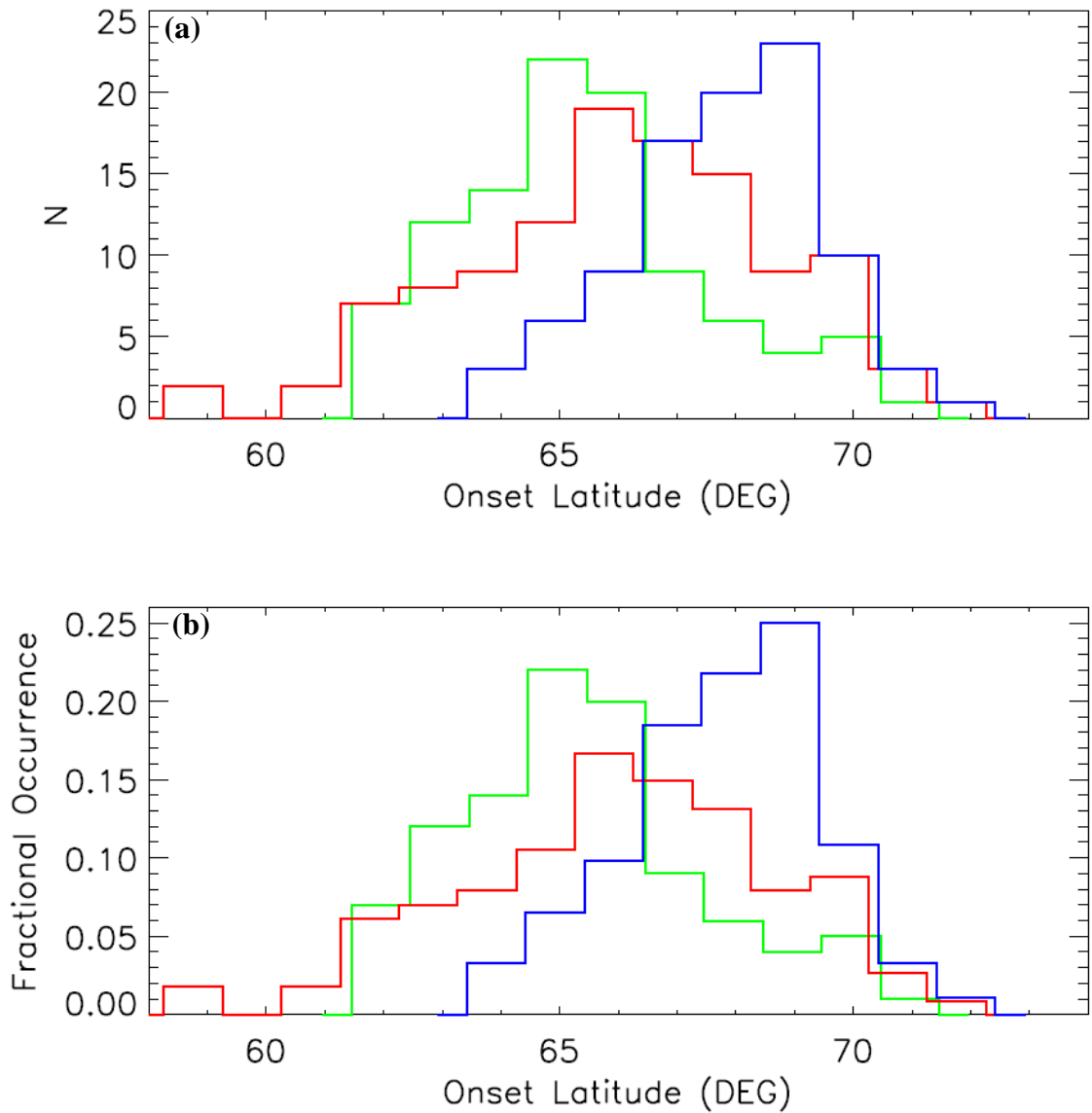


Figure 6.14: Number, (a), and fractional, (b), occurrence distributions of the latitude of the initial onset arc identified by Frey *et al.* (2004) as the start of substorm onset for category 1 events (green), category 2 events (red) and category 3 events (blue).

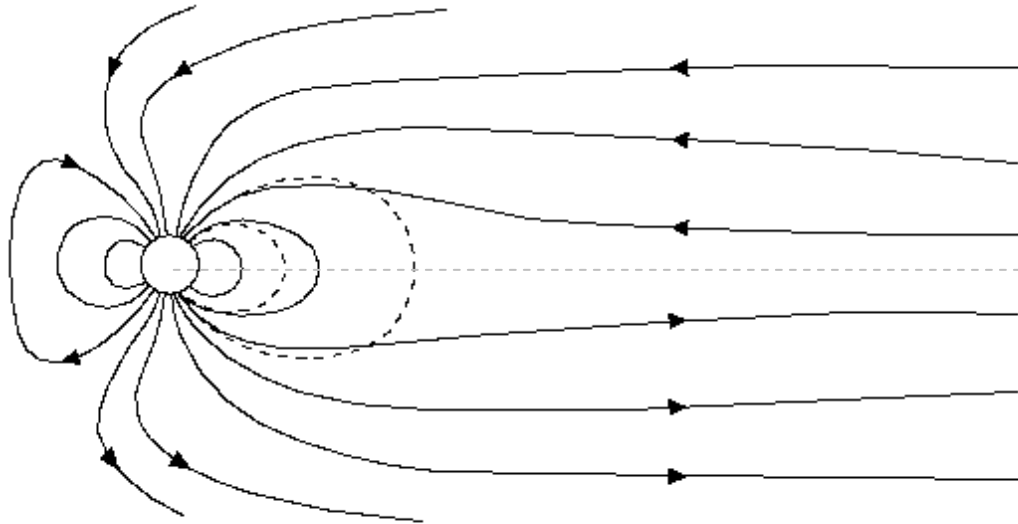


Figure 6.15: Schematic of how the magnetotail becomes more stretched and less dipolar when more open magnetic flux is added to the system. The solid lines represent the magnetosphere in its loaded state, that is, with large open magnetic flux content, and dashed lines show how field lines fixed at a constant latitude would become more dipolar, and move closer to the Earth in the equatorial plane (shown by the dashed horizontal line), when the open magnetic flux content decreases.

magnetotail field line stretching and tail field variations during these events may allow us to determine the onset location with some degree of accuracy and provide important insights into the tail dynamics and injection processes for the three distinct categories. Such a study is beyond the scope of this thesis.

6.4 Summary and Conclusions

6.4.1 Auroral Boundary Motions

We have carried out the largest superposed study to date of the WIC OCB, equatorward auroral oval boundary and oval width motions around the time of substorm onset from 451 Frey substorm events from the December and January months of 2000-2001. The offsets and variations seen are grossly consistent with the study of the poleward edge of WIC auroral emission by Mende *et al.* (2003), giving us confidence in the validity of our method. However, converse to the results of Mende *et al.* (2003) we find that the OCB is located at higher latitudes dawnward of the onset MLT. We attribute this result to the DMSP correction applied in our study and used to give a better determination of the true OCB location, shifting the OCB poleward by up to 2° in the dawnward sector and by equatorward by up to 1° in the duskward sector. We summarise the results of our study as follows:

- (1) Both OCB and equatorward boundaries drift equatorward in the growth phase of the substorm, the motions being very similar in all MLT sectors.
- (2) The OCB shows a rapid poleward expansion at the time of substorm onset, the motion being very similar at the onset MLT and $+2$ RMLT. The response at -2 RMLT is also immediate, but the poleward motion is less rapid. There is a delay of ~ 10 minutes between onset and the poleward response at ± 4 RMLT and the extent of the motion is reduced.
- (3) The equatorward boundary moves to higher latitudes immediately after onset at -2 RMLT. The equatorward motion continues for a few minutes after onset at the onset MLT and -4 RMLT before a rapid poleward motion is seen. This delay increases to ~ 30 and ~ 60 minutes for $+2$ and $+4$ RMLT respectively.
- (4) The latitude difference between the OCB and equatorward edge of the auroral oval (oval width) is larger dawnward of the onset MLT ($+2$ and $+4$ MLT).

(5) The OCB-equatorward boundary latitude difference increases after onset at dawnward MLTs and decreases at duskward MLTs.

6.4.2 Study of LANL Categories

Using all substorm onsets from the months of December and January 2000-2002 identified by Frey *et al.* (2004), in chapter 5 of this thesis we identified three differing categories of substorms defined by their particle injection signatures as seen by the LANL spacecraft. We showed that substorms showing a ‘classic’ particle injection signature of substorm onset (category 1) occur on average at higher values of open magnetic flux than those showing varied (category 2) or no activity (category 3). In this chapter we have investigated these LANL categories in more detail by carrying out a superposed epoch analysis of F_{pc} , solar wind and IMF conditions, geomagnetic activity and motions of the OCB and equatorward boundary of the auroral oval.

We summarise our current understanding of the three LANL categories below:

- (1) Category 1 events show all the expected signatures of large energetic substorm events occurring due to a large southward turning of the IMF B_z component during otherwise average solar wind and geomagnetic activity.
- (2) The variations and trends of all category 2 parameters are consistent with substorms occurring during continuous solar wind driving, i.e. these events are highly driven by the solar wind and they occur during periods of stronger solar wind flow. The IMF B_y component appears to play a large role in the dayside driving for these events.
- (3) Category 3 events do not show the expected signatures of true global substorm events. It is likely that this category consists of very weak substorm events, pseudo-breakups or other events which may cause nightside auroral brightenings.
- (4) These results have important implications for those wishing to use the Frey onset list for future substorm studies. Splitting substorm studies by these LANL categories may provide important insights into different types of substorm events and energetic particle injections. For example, our results suggest that the level of solar wind driving and continued energy input during substorms has a direct impact on the evolution and signature of substorm injections. Substorms showing the classical substorm injection signature may be more controlled by the loading-unloading scheme, whilst more varied energetic particle fluctuations may be an indication of a more directly driven event.

Chapter 7. Summary and Future Work

7.1 Summary

In this thesis we have investigated the relationship between the open magnetic flux content of the magnetosphere and substorm onsets. In chapter 4 we developed an automated method of identifying the global location of the open/closed magnetic field line boundary (OCB) in the ionosphere from global auroral images of the northern polar cap taken in the far ultraviolet (FUV) by the IMAGE spacecraft. Comparing the latitude of the OCB as approximated by the three different FUV detectors onboard IMAGE, the Wideband Imaging Camera (WIC; 140-190 nm) and spectrographic imagers SI12 (~121.82 nm) and SI13 (~ 135.6 nm), we found that the modal latitude differences are small ($<1^\circ$) except in the evening and predawn sectors. In the evening sector SI12 OCB proxies are found between 1-2° poleward of WIC and SI13 OCB proxies and vice-versa in the dawnward magnetic local time (MLT) sectors (see Figure 4.6).

In-situ measurements of precipitating particles from low-latitude spacecraft, such as the DMSP spacecraft, currently provide the most direct and precise determination of the location of the OCB at any one MLT but are, however, unable to produce a global proxy due to their limited spatial coverage. In chapter 4 we also compared the FUV OCB proxies with the OCB as estimated by DMSP measurements. We found systematic offsets (see Figure 4.5) between the two OCB estimation methods consistent with previous studies which used more limited data sets or auroral imagery from different spacecraft and for only one wavelength (e.g. Carbary *et al.*, 2003 and references therein). Previous studies have suggested that the WIC detector may be an unreliable proxy for the OCB in the predawn sector (e.g. Wild *et al.*, 2004) and we indeed find that the SI12 OCB proxies give a closer match to the DMSP OCB proxies in the dawnward MLT sector. However, we also show that at other MLTs the WIC and SI13 OCB proxies give a good as, if not better, correlation with DMSP OCBs. Hence, the best method for identifying the global OCB from the IMAGE FUV detectors may be to use the FUV detector which produces the closest statistical match to DMSP OCB proxies at each individual MLT. For studies using a single instrument, WIC images may provide

the best global proxy for the OCB due to its higher spatial resolution (~ 50 km at apogee) compared to either of the spectrographic imagers (~ 100 km at apogee).

Assuming that the DMSP OCB proxies give the best estimation of the true location of the OCB, the systematic offsets found between the FUV and DMSP OCB proxies can be used to ‘correct’ the FUV OCB proxies to give a more accurate global proxy for the OCB. Since the OCB delineates the open magnetic field lines of the polar cap and more equatorward closed magnetic field lines, once the global location of the OCB has been determined it is a simple matter to estimate the open magnetic flux content of the hemisphere (F_{pc}) by summing the radial component of the Earth’s magnetic field through the area of the polar cap. In chapter 5 of this thesis, we developed the method of chapter 4 to estimate the global location of the OCB and open magnetic flux in such a manner. Applying this method to all WIC auroral images of the northern polar cap from the December and January months of 2000 to 2002 returned the distribution of the average open magnetic flux content of the northern polar cap (F_{pc}) from 12,731 separate auroral images. From this parent distribution we extracted the distribution of F_{pc} at the time of substorm onset using the Frey list of substorm onsets (Frey *et al.*, 2004). The parent distribution varied between ~ 0.2 and ~ 0.9 GWb with a mean flux value of ~ 0.52 GWb (Figure 5.5, unshaded histogram panels a-e). The substorm distribution (173 events) varied between ~ 0.3 and 0.9 GWb, with a mean of ~ 0.58 GWb (Figure 5.5, shaded histogram panel a). From these large datasets, we were able, for the first time, to determine the probability of substorm onset as a function of open magnetic flux (Figure 5.5f). The probability of substorm onset is negligible below ~ 0.3 GWb, increases almost linearly until an F_{pc} of ~ 0.9 GWb, and is undefined above this as fluxes above this value are not observed in this study.

We also found that not all substorms within the substorm distribution showed the expected signature of energetic particle injection for substorm onsets. Splitting the substorm distribution into three categories based on their injection signatures as seen at geosynchronous orbit by the LANL spacecraft we found that, on average, substorms showing a clear and classic injection signature of substorm onset (category 1) occur at higher values of open magnetic flux than those showing varied (category 2, all energetic enhancements not following the expected substorm evolution) or no (category 3) injection activity (Figure 5.5. panels b-e and g-j).

The results of this study show that the substorm distribution occurs at the upper end of the parent distribution, as not unexpected due to the growth phase requirement of substorm onset, and that no substorms occur below ~ 0.3 GWb, suggesting a minimal threshold in open magnetic flux required for substorm onset. The distributions also show that there is no fixed critical threshold in open magnetic flux as a necessary condition for substorm onset, as suggested by some models (e.g. Freeman and Morley, 2004). Other models for substorm onset suggest that a change in the solar wind is required to trigger substorm onset (e.g. Lyons *et al.*, 1995; Hsu and McPherron, 2002). Our distributions are not consistent with a model in which once some minimal critical threshold in open magnetic flux has been reached a solar wind trigger must be waited for. However, they may be consistent with a threshold in open magnetic flux whose value depends on other magnetospheric or ionospheric conditions (e.g. the strength of the ring current, see Milan *et al.*, 2009a,b).

In chapter 6 we investigated the three distinct particle injection categories of substorm events further by carrying out a superposed epoch analysis of F_{pc} , solar wind and IMF conditions, maximum nightside auroral intensity, geomagnetic activity and motions of the OCB and equatorward auroral boundary during these events (Figures 6.1-6.4, 6.9 and 6.10). Category 1 events clearly show the expected signatures of large energetic substorms in all parameters. The growth phase of these events is characterised by a large southward turning of the IMF and subsequent recovery. They occur in otherwise average IMF and solar wind conditions. These events appear to be largely driven by the B_z component of the IMF. While the loading-unloading scheme seems to dominate the category 1 events, the directly driven process would appear to be more important for category 2 events. The IMF B_z , though not reaching the magnitudes of category 1 events, remains negative throughout the expansion phase suggesting that dayside reconnection is ongoing throughout. The IMF B_y component would also appear to play a larger role in the driving of these events. They also occur under stronger solar wind flow in general. Finally, category 3 events do not show the expected signatures of substorms, occur with very weak solar wind conditions and IMF driving, and appear to be highly localised tail reconnection events. We conclude that category 3 events are either very weak substorms or pseudo-breakups. This relationship between the level of solar wind driving and particle injection signatures is a new and unexpected result.

These categories provide an important sub-categorisation of the Frey onset list and future investigation of these categories may provide more important insights into the substorm process.

In summary, this thesis has produced several important results which have increased our understanding of magnetospheric substorms and which have important implications for, and place important constraints on, future models of substorm onset.

7.2 Future Work

In chapter 4 of this thesis we developed an automated method of identifying the location of the OCB in the ionosphere from global auroral images taken by the three FUV detectors onboard the IMAGE spacecraft. In chapters 5 and 6 we used this method to estimate the open magnetic flux content of the magnetosphere from auroral images of the northern polar cap for the December and January months of 2000-2002. In this study we chose to use only winter months due to the much reduced levels of dayglow and general reduction in background noise during the winter. A natural extension of the work carried out in this thesis would be to extend the datasets to other seasons. However, the automated method of OCB identification was developed using auroral images from winter months. We found that applying the automated method, as is, to other months returned many more erroneous boundary estimations passing the fitting criteria than during December and January. We attribute this result to the much increased levels of dayglow and background noise during summer. A condition of the boundary fitting routine is that the background noise must be below a particular ratio of the maximum image intensity. This condition often fails in the summer, also resulting in much fewer boundary estimations. This condition also means that boundaries are only estimated for particularly bright auroral ovals in the summer, when they are much more intense than the background FUV emission, thus biasing any results returned. It is clear that there are several issues when applying the automated method to summer months and that the method needs significant, but not unachievable, modification to produce accurate and unbiased results for summer. This would allow the comparison of the average F_{pc} content of the magnetosphere and F_{pc} for substorms, as well as LANL particle injection events, for different seasons.

In this thesis we have investigated the open magnetic flux and auroral dynamics of the northern polar cap. During 2003 the apogee of the IMAGE spacecraft moved from the northern to southern hemispheres, with auroral imagery mostly coming from the southern pole after 2003. Another natural extension of the work carried out in this thesis would be the investigation of the southern open magnetic flux and auroral dynamics during substorms. However, at the time of the work carried out in this thesis it was known that there were several issues with the quality of the data from the southern hemisphere. Namely, a complicated wobble developed along the spin axis of the IMAGE spacecraft which was hard to characterise such that the error in the camera pointing direction was increased. It is believed that this wobble may cause the auroral oval to be apparently displaced by up to 1° from its true location. This would significantly change the values of F_{pc} returned from these images. The pointing for these months has since been improved and the extension of this work to the southern hemisphere may be possible.

To date, very few conjugate studies of the northern and southern auroral ovals have been possible due to the very limited number of conjugate observations made by imaging spacecraft. However, the few studies which have been carried out have shown that there can be significant differences in the aurora and onset location of substorms in the two hemispheres (e.g. Østgaard *et al.*, 2006). The IMAGE spacecraft is, in general, only able to image the aurora of one hemisphere at any one time and thus conjugate studies are not possible. The proposed KuaFu mission (Tu *et al.*, 2007) will consist of two auroral imagers on separate spacecraft, allowing the simultaneous observation of both southern and northern FUV auroral ovals. Application of the methods described in this thesis to auroral images from KuaFu, or similar future missions, would allow the open magnetic flux evolution and auroral dynamics during substorms to be compared between hemispheres.

In chapters 5 and 6 of this thesis we have defined three distinct categories of substorms depending on their particle injection signatures. The apparent relation between substorm injection signatures and the level and type of solar wind driving is a new and unexpected result. Further investigation of these categories (for example investigating the tail magnetic field morphology during these events) may provide important insights into the substorm and particle injection processes.

References

- Abel, G. A., Freeman, M. P., Smith, A. J., and Reeves, G. D., Association of substorm chorus events with drift echoes, *J. Geophys. Res.*, *111*, A11220, 2006.
- Akasofu, S. I., Roles of North-South Component of Interplanetary Magnetic-Field on Large-Scale Auroral Dynamics Observed by DMSP Satellite, *Planet. Space Sci.*, *23*, 1349-1354, 1975.
- Akasofu, S. I., The Development of the auroral substorm, *Planet. Sp. Sci.*, *12*, 273-282, 1964.
- Arnoldy, R. L., and Chan, K. W., Particle substorms observed at the geostationary orbit, *J. Geophys. Res.*, *74*, 5019-5028, 1969.
- Asano, Y., Mukai, T., Hoshino, M., Saito, Y., Hayakawa, H., and Nagai, T., Statistical study of thin current sheet evolution around substorm onset, *J. Geophys. Res.-Sp. Phys.*, *109*, 2004.
- Aubry, M. P., Russell, C. T., and Kivelson, M. G., Inward Motion of Magnetopause before a Substorm, *J. Geophys. Res.*, *75*, 7018-7031, 1970.
- Axford, W. I., The interaction between the solar wind and the earth's magnetosphere, *J. Geophys. Res.*, *67*, 3791-3796, 1962.
- Bae, S. H., Lee, D. Y., Lee, E., Min, K. W., and Choi, K. H., Substorms associated with azimuthal turnings of the interplanetary magnetic field, *J. Atmos. Solar Terr. Phys.*, *63*, 1763-1774, 2001.
- Baker, D. N., Pulkkinen, T. I., Angelopoulos, V., Baumjohann, W., and McPherron, R. L., Neutral line model of substorms: Past results and present view, *J. Geophys. Res.*, *101*, 12975-13010, 1996.

Baker, D. N., Belian, R. D., Higbie, P. R., and Hones, E. W., High-Energy Magnetospheric Protons and their Dependence on Geomagnetic and Inter-Planetary Conditions, *J. Geophys. Res.*, *84*, 7138-7154, 1979.

Baker, D. N., Higbie, P. R., Hones, E. W., and Belian, R. D., High-Resolution Energetic Particle Measurements at 6.6-Re .3. Low-Energy Electron Anisotropies and Short-Term Substorm Predictions, *J. Geophys. Res.*, *83*, 4863-4868, 1978.

Baker, J. B., Clauer, C. R., Ridley, A. J., Papitashvili, V. O., Brittnacher, M. J., and Newell, P. T., The nightside poleward boundary of the auroral oval as seen by DMSP and the Ultraviolet Imager, *J. Geophys. Res.*, *105*, 21267-21280, 2000.

Baker, K. B., Rodger, A. S., and Lu, G., HF-radar observations of the dayside magnetic merging rate: A Geospace Environment Modeling boundary layer campaign study, *Journal of Geophysical Research-Space Physics*, *102*, 9603-9617, 1997.

Baker, K. B., Dudeney, J. R., Greenwald, R. A., Pinnock, M., Newell, P. T., Rodger, A. S., Mattin, N., and Meng, C. I., Hf Radar Signatures of the Cusp and Low-Latitude Boundary-Layer, *J. Geophys. Res.*, *100*, 7671-7695, 1995.

Baker, K. B., and S. Wing, A new magnetic coordinate system for conjugate studies at high latitude, *J. Geophys. Res.*, *94*, 9139, 1989.

Baumjohann, W. and Treumann, R. A., Basic Space Plasma Physics, Imperial College Press, London, 1997.

Biermann, L., Kometschweife und solare Korpuskularstrahlung, *Z. Astrophys.*, *29*, 274-286, 1951.

Belian, R. D., Cayton T. E., and Reeves G. D., Quasi-periodic, substorm associated, global flux variations observed at geosynchronous orbit, in *Space Plasmas: Coupling Between Small and Medium Scale Processes*, edited by M. Ashour-Abdalla, T. Chang, and P. Dusenber, 143, AGU, Washington, D.C., 1995.

Belian, R. D., Gisler, G. R., Cayton, T., and Christensen, R., High-Z Energetic Particles at Geosynchronous Orbit during the Great Solar Proton Event Series of October 1989, *J. Geophys. Res.*, *97*, 16897-16906, 1992.

Belian, R. D., Baker, D. N., Hones, E. W., Higbie, P. R., Bame, S. J., and Asbridge, J. R., Timing of Energetic Proton Enhancements Relative to Magnetospheric Substorm Activity and its Implication for Substorm Theories, *J. Geophys. Res.*, *86*, 1415-1421, 1981.

Belian, R. D., Baker, D. N., Higbie, P. R., and Jones Jr., E. W., High resolution energetic particle measurements at 6.6 Re, 2, High-energy proton drift echoes, *J. Geophys. Res.*, *83*, 4857-4862, 1978.

Birkeland, K., "Are the Solar Corpuscular Rays that penetrate the Earth's Atmosphere Negative or Positive Rays?", *Videnskapsselskapets Skrifter, I Mat Naturv. Klasse No.1*, Christiania, 1916.

Birkeland, K. B., The Norwegian Aurora Polaris Expedition, 1902-1903, H. Aschehoug & Co., Christiania, 1909.

Birn, J., Thomsen, M. F., Borovsky, J. E., Reeves, G. D., McComas, D. J., Belian, R. D., and Hesse, M., Substorm ion injections: Geosynchronous observations and test particle orbits in three-dimensional dynamic MHD fields, *J. Geophys. Res.*, *102*, 2325-2341, 1997.

Blanchard, G. T., Ellington, C. L., Lyons, L. R., and Rich, F. J., Incoherent scatter radar identification of the dayside magnetic separatrix and measurement of magnetic reconnection, *J. Geophys. Res.*, *106*, 8185-8195, 2001.

Blanchard, G. T., Lyons, L. R., and Samson, J. C., Accuracy of using 6300 angstrom auroral emission to identify the magnetic separatrix on the nightside of earth, *J. Geophys. Res.*, *102*, 9697-9703, 1997.

Blanchard, G. T., Lyons, L. R., delaBeaujardiere, O., Doe, R. A., and Mendillo, M., Measurement of the magnetotail reconnection rate, *J. Geophys. Res.*, *101*, 15265-15276, 1996.

Blanchard, G. T., Lyons, L. R., Samson, J. C., and Rich, F. J., Locating the Polar-Cap Boundary from Observations of 6300 Angstrom Auroral Emission, *J. Geophys. Res.*, *100*, 7855-7862, 1995.

Blockx, C., Gerard, J. C., Coumans, V., Hubert, B., and Meurant, M., Contributions of the driven process and the loading-unloading process during substorms: A study based on the IMAGE-SI12 imager, *J. Geophys. Res.*, *114*, 2009.

Bond, F. R. and Akasofu, S. I., Comparison of Auroral Ovals from All-Sky Camera Studies and from Satellite Photographs, *Planet. Space Sci.*, *27*, 541-549, 1979.

Borovsky, J. E., Nemzek, R. J., and Belian, R. D., The Occurrence Rate of Magnetospheric-Substorm Onsets - Random and Periodic Substorms, *J. Geophys. Res.*, *98*, 3807-3813, 1993.

Brittnacher, M., Fillingim, M., Parks, G., Germany, G., and Spann, J., Polar cap area and boundary motion during substorms, *J. Geophys. Res.*, *104*, 12251-12262, 1999.

Büchner, J., and Zelenyi, L. M., Chaotization of the Electron Motion as the Cause of an Internal Magnetotail Instability and Substorm Onset, *J. Geophys. Res.*, *92*, 13456-13466, 1987.

Burch, C. R., Reflecting microscopes, *Proc. Physical Society*, *59*, 41-46, 1947.

Burch, J. L., IMAGE mission overview, *Space Science Reviews*, *91*, 1-14, 2000.

Burch, J. L., Preconditions for Triggering of Polar Magnetic Substorms by Storm Sudden Commencements, *J. Geophys. Res.*, *77*, 5629- 5632, 1972.

Burton, R. K., Mcpherron, R. L., and Russell, C. T., Empirical Relationship between Interplanetary Conditions and Dst, *J. Geophys. Res.*, 80, 4204-4214, 1975.

Caan, M. N., Mcpherron, R. L., and Russell, C. T., Statistical Magnetic Signature of Magnetospheric Substorms, *Planet. Space Sci.*, 26, 269-279, 1978.

Caan, M. N., Mcpherron, R. L., and Russell, C. T., Characteristics of Association between Interplanetary Magnetic-Field and Substorms, *J. Geophys. Res.*, 82, 4837-4842, 1977.

Caan, M. N., Mcpherron, R. L., and Russell, C. T., Substorm and Interplanetary Magnetic-Field Effects on Geomagnetic Tail Lobes, *J. Geophys. Res.*, 80, 191-194, 1975.

Carbary, J. F., Sotirelis, T., Newell, P. T., and Meng, C. I., Auroral boundary correlations between UVI and DMSP, *J. Geophys. Res.*, 108, 1018, 2003.

Chao, J. K., Kan, J. R., Lui, A. T. Y., and Akasofu, S. I., Model for Thinning of Plasma Sheet, *Planet. Space Sci.*, 25, 703-710, 1977.

Chapman, S., and Ferraro, V. C. A., A new theory of magnetic storms, Part 1, The initial phase, *Terrest. Magnetism and Atmospheric Elec.*, 36, 171-186, 1931.

Chapman, S., and Ferraro, V. C. A., A new theory of magnetic storms, *Nature*, 126, 129-130, 1930.

Chisham, G., Freeman, M. P., Abel, G. A., Bristow, W. A., Marchaudon, A., Ruohoniemi, J. M., and Sofko, G. J., Spatial distribution of average vorticity in the high-latitude ionosphere and its variation with interplanetary magnetic field direction and season, *J. Geophys. Res.*, 114, A09301, 2009.

Chisham, G., Freeman, M. P., Abel, G. A., Lam, M. M., Pinnock, M., Coleman, I. J., Milan, S. E., Lester, M., Bristow, W. A., Greenwald, R. A., Sofko, G. J., and Villain, J.

P., Remote sensing of the spatial and temporal structure of magnetopause and magnetotail reconnection from the ionosphere, *Rev. Geophys.*, *46*, RG1004, 2008.

Chisham, G., Lester, M., Milan, S. E., Freeman, M. P., Bristow, W. A., Grocott, A., McWilliams, K. A., Ruohoniemi, J. M., Yeoman, T. K., Dyson, P. L., Greenwald, R. A., Kikuchi, T., Pinnock, M., Rash, J. P. S., Sato, N., Sofko, G. J., Villain, J. P., and Walker, A. D. M., A decade of the Super Dual Auroral Radar Network (SuperDARN): scientific achievements, new techniques and future directions, *Surv. Geophys.*, *28*, 33-109, 2007.

Chisham, G., Freeman, M. P., Lam, M. M., Abel, G. A., Sotirelis, T., Greenwald, R. A., and Lester, M., A statistical comparison of SuperDARN spectral width boundaries and DMSP particle precipitation boundaries in the afternoon sector ionosphere, *Ann. Geophys.*, *23*, 3645-3654, 2005a.

Chisham, G., Freeman, M. P., Sotirelis, T., Greenwald, R. A., Lester, M., and Villain, J. P., A statistical comparison of SuperDARN spectral width boundaries and DMSP particle precipitation boundaries in the morning sector ionosphere, *Ann. Geophys.*, *23*, 733-743, 2005b.

Chisham, G. and Freeman, M. P., An investigation of latitudinal transitions in the SuperDARN Doppler spectral width parameter at different magnetic local times, *Ann. Geophys.*, *22*, 1187-1202, 2004.

Chisham, G., Freeman, M. P., and Sotirelis, T., A statistical comparison of SuperDARN spectral width boundaries and DMSP particle precipitation boundaries in the nightside ionosphere, *Geophys. Res. Lett.*, *31*, L02804, 2004.

Chisham, G. and Freeman, M. P., A technique for accurately determining the cusp-region polar cap boundary using SuperDARN HF radar measurements, *Ann. Geophys.*, *21*, 983-996, 2003.

Chisham, G., Pinnock, M., Coleman, I. J., Hairston, M. R., and Walker, A. D. M., An unusual geometry of the ionospheric signature of the cusp: implications for magnetopause merging sites, *Ann. Geophys.*, *20*, 29-40, 2002.

Chisham, G., Pinnock, M., and Rodger, A. S., The response of the HF radar spectral width boundary to a switch in the IMF B-y direction: Ionospheric consequences of transient dayside reconnection?, *J. Geophys. Res.*, *106*, 191-202, 2001.

Clauer, C. R., Cai, X., Welling, D., DeJong, A., and Henderson, M. G., Characterizing the 18 April 2002 storm-time sawtooth events using ground magnetic data, *J. Geophys. Res.*, *111*, A04S90, 2006.

Coumans, V., Blockx, C., Gerard, J. C., Hubert, B., and Connors, M., Global morphology of substorm growth phases observed by the IMAGE-SI12 imager, *J. Geophys. Res.*, *112*, A11211, 2007.

Cowley, S. W. H. and Lockwood, M., Excitation and Decay of Solar Wind-Driven Flows in the Magnetosphere-Ionosphere System, *Ann. Geophys.*, *10*, 103-115, 1992.

Cran-McGreehin, A. P. and Wright, A. N.: Electron acceleration in downward auroral field-aligned currents, *J. Geophys. Res.*, *110*, A10S15, 2005.

Craven, J. D. and Frank, L. A., 'Diagnosis of Auroral Dynamics Using Global Auroral Imaging with Emphasis on Large-Scale Evolution', in *Auroral Physics*, edited by C.-I Meng, M. J. Rycroft and L. A. Frank, 273, Cambridge Univ. Press, New York, 1991.

Craven, J. D. and Frank, L. A., Latitudinal Motions of the Aurora during Substorms, *J. Geophys. Res.*, *92*, 4565-4573, 1987.

Craven, J. D. and Frank, L. A., The Temporal Evolution of a Small Auroral Substorm as Viewed from High-Altitudes with Dynamics Explorer-1, *Geophys. Res. Lett.*, *12*, 465-468, 1985.

Dashkevich, Z. V., Kozelov, B. V., and Ivanoc, I. Y., Lyman-Birge-Hopfeld bands in proton auroras, *Geomagnetism and Aeronomy*, 35, 1996.

Davis, T. N., and Sugiura, M., Auroral electrojet index AE and its universal time variations, *J. Geophys. Res.*, 71, 785–801, 1966.

Deforest, S. E. and McIlwain, C. E., Plasma Clouds in Magnetosphere, *J. Geophys. Res.*, 76, 3587-3611, 1971.

DeJong, A. D., Cai, X., Clauer, R. C., and Spann, J. F., Aurora and open magnetic flux during isolated substorms, sawteeth, and SMC events, *Ann. Geophys.*, 25, 1865-1876, 2007.

Dungey, J. W., The length of the magnetospheric tail, *J. Geophys. Res.* 70, 1753-1753, 1965.

Dungey, J. W., The structure of the exosphere or adventures in velocity space. In: C. De Witt, J. Hieblot and L. Le Beau, Editors, *Geophysics, The Earth's Environment*, Gordon and Breach, New York, 503–550, 1963.

Dungey, J. W., Interplanetary Magnetic Field and the Auroral Zones, *Phys. Rev. Lett.*, 6, 47-48, 1961.

Eastman, T. E., Hones, Jr., E. W., Bame, S. J., and Asbridge, J. R., The magnetospheric boundary layer: Site of plasma, momentum, and energy transfer from the magnetosheath into the magnetosphere, *Geophys. Res. Lett.*, 3, 685-688, 1976.

Eather, R. H. and Mende, S. B., Systematics in Auroral Energy Spectra, *J. Geophys. Res.*, 77, 660 - 673, 1972.

Elphinstone, R. D., Murphree, J. S., Hearn, D. J., Cogger, L. L., Sandahl, I., Newell, P. T., Klumpar, D. M., Ohtani, S., Sauvaud, J. A., Potemra, T. A., Mursula, K., Wright, A., and Shapshak, M., The Double Oval Uv Auroral Distribution .1. Implications for the Mapping of Auroral Arcs, *J. Geophys. Res.*, 100, 12075-12092, 1995.

Escoubet, C. P., Fehringer, M., and Goldstein, M., The Cluster mission - Introduction, *Ann. Geophys.*, *19*, 1197-1200, 2001.

Escoubet, C. P., Schmidt, R., and Goldstein, M. L., Cluster-science and mission overview, *Sp. Sci. Rev.*, *79*, 11-32, 1997.

Fairfield, D. H., and Scudder, J. D., Polar rain: Solar coronal electrons in the Earth's magnetosphere, *J. Geophys. Res.*, *90*, 1985.

Fairfield, D.H., Polar magnetic disturbances and the interplanetary magnetic field, *Space Res.* *8*, 107, 1967.

Fairfield, D. H. and Cahill Jr., L.J., Transition region magnetic field and polar magnetic disturbances, *J. Geophys. Res.*, *71*, 155, 1966.

Feldstein, Y. I. and Galperin, Y. I., The Auroral Luminosity Structure in the High-Latitude Upper-Atmosphere - its Dynamics and Relationship to the Large-Scale Structure of the Earth's Magnetosphere, *Rev. Geophys.*, *23*, 217-275, 1985.

Feldstein, Y. I. and Starkov, G. V., Dynamics of auroral belt and polar geomagnetic disturbances, *Planet. Space Sci.*, *15*, 209, 1967.

Franz, H., Sharer, P., Ogilvie, K., and Desch, M., WIND nominal mission performance and extended mission design, *J. Astronaut. Sci.*, *49*, 145-167, 2001.

Foster, J. C., Fairfield, D.H., Ogilvie, K. W., and Rosenber, T.J., Relationship of Interplanetary Parameters and Occurrence of Magnetospheric Substorms, *J. Geophys. Res.*, *76*, 6971, 1971.

Frank, L. A., Ackerson, K. L., Paterson, W. R., Lee, J. A., English, M. R., and Pickett, G. L., The Comprehensive Plasma Instrumentation (Cpi) for the Geotail Spacecraft, *J. Geomag. Geoelec.*, *46*, 23-37, 1994.

Frank, L. A. and Craven, J. D., Imaging Results from Dynamics Explorer-1, *Rev. Geophys.*, *26*, 249-283, 1988.

Frank, L. A., On the extraterrestrial ring current during geomagnetic storms, *J. Geophys. Res.*, *72*, 3753, 1967.

Freeman, M. P. and Morley, S. K., A minimal substorm model that explains the observed statistical distribution of times between substorms, *Geophys. Res. Lett.*, *31*, L12807, 2004.

Frey, H. U., Mende, S. B., Angelopoulos, V., and Donovan, E. F., Substorm onset observations by IMAGE-FUV, *J. Geophys. Res.*, *109*, A10304, 2004.

Fujimoto, M., Mukai, T., Kawano, H., Nakamura, M., Nishida, A., Saito, Y., Yamamoto, T., and Kokubun, S., Structure of the low-latitude boundary layer: A case study with Geotail data, *J. Geophys. Res.*, *103*, 2297-2308, 1998.

Gérard, J.-C., Hubert, B., Grard, A., Meurant, M., and Mende, S. B., Solar wind control of auroral substorm onset locations observed with the IMAGE-FUV imagers, *J. Geophys. Res.*, *109*, A03208, 2004.

Gjerloev, J. W., Hoffman, R. A., Sigwarth, J. B., Frank, L. A., and Baker, J. B. H., Typical auroral substorm: A bifurcated oval, *Journal of Geophysical Research-Space Physics*, *113*, A03211, 2008.

Gjerloev, J. W., Hoffman, R. A., Sigwarth, J. B., and Frank, L. A., Statistical description of the bulge-type auroral substorm in the far ultraviolet, *J. Geophys. Res.*, *112*, 2007.

Gringauz, K. I., Bezrukikh, V. V., Ozerov, V. D., and Rybchinskii, R.E., A study of the interplanetary ionized gas, high-energy electrons, and corpuscular radiation from the sun by means of the three-electrode trap for charged particles on the second Soviet cosmic rocket, *Soviet Phys. Dokl.*, *5*, 361–364, 1960.

Haerendel, G., and G. Paschmann, Entry of solar wind plasma into the magnetosphere, in *Physics of the Hot Plasma in the Magnetosphere*, ed. B. Hultqvist and L. Stenflo, p. 23, Plenum, New York, 1975.

Hamming, R. W., *Digital Filters (3rd ed)*, Prentice Hall International (UK) Ltd, Hertfordshire, UK, 1989.

Hardy, D. A., Gussenhoven, M. S., Raistrick, R., and Mcneil, W. J., Statistical and Functional Representations of the Pattern of Auroral Energy Flux, Number Flux, and Conductivity, *J. Geophys. Res.*, *92*, 12275-12294, 1987.

Hardy, D. A., Gussenhoven, M. S., and Holeman, E., A Statistical-Model of Auroral Electron-Precipitation, *J. Geophys. Res.*, *90*, 4229-4248, 1985.

Hardy, D. A., Yeh, H. C., Schmitt, L. K. Schumaker, T. L., Gussenhoven, M. S., Huber, A., Marshall, F. J., and Pantazis, J.: Precipitating electron and ion detectors (SSJ/4) on the block 5D/Flights 6-10 DMSP satellites: Calibration and data presentation, Tech. Rep. AFGL-TR-84- 0317, Air Force Geophys. Lab., Hanscom Air Force Base, Mass., 1984.

Heikkila, W. J., and Winningham J. D., Penetration of magnetosheath plasma to low altitudes through the dayside magnetospheric cusps, *J. Geophys. Res.*, *76*, 883, 1971.

Henderson, M. G., Reeves, G. D., Skoug, R., Thomsen, M. F., Denton, M. H., Mende, S. B., Immel, T. J., Brandt, P. C., and Singer, H. J., Magnetospheric and auroral activity during the 18 April 2002 sawtooth event, *J. Geophys. Res.*, *111*, A01S90, 2006.

Henderson, M. G., The May 2-3, 1986 CDAW-9C interval: A sawtooth event, *Geophys. Res. Lett.*, *31*, 2004.

Henderson, M. G., Reeves, G. D., Belian, R. D., and Murphree, J. S., Observations of magnetospheric substorms occurring with no apparent solar wind IMF trigger, *J. Geophys. Res.*, *101*, 10773-10791, 1996.

Hirshberg, J. and Holzer, T. E., Relationship between Interplanetary Magnetic-Field and Isolated-Substorms, *J. Geophys. Res.*, *80*, 3553-3556, 1975.

Hoffmeister, C., Physikalische Untersuchungen an Kometen I. Die Beziehungen der primären Schweifstrahls zum Radiusvektor, *Z. Astrophys.*, *22*, 265-285, 1943.

Holzer, R. E. and Slavin, J. A., Correlative Study of Magnetic-Flux Transfer in the Magnetosphere, *J. Geophys. Res.*, *84*, 2573-2578, 1979.

Holzworth, R. H. and Meng, C. I., Mathematical Representation of Auroral Oval, *Geophys. Res. Lett.*, *2*, 377-380, 1975.

Hones, E. W., Jr., Plasma sheet behaviour during substorms, in *Magnetic Reconnection in Space and Laboratory Plasmas, Geophysical Monograph 30*, ed. E. W. Hones, Jr., AGU, Washington DC, 178, 1984.

Hsu, T. S. and McPherron, R. L., A statistical study of the spatial structure of interplanetary magnetic field substorm triggers and their associated magnetic response, *J. Geophys. Res.*, *114*, A02223, 2009.

Hsu, T. S. and McPherron, R. L., Occurrence frequencies of IMF triggered and nontriggered substorms, *J. Geophys. Res.*, *108*, 1307, 2003.

Hsu, T. S. and McPherron, R. L., An evaluation of the statistical significance of the association between northward turnings of the interplanetary magnetic field and substorm expansion onsets, *J. Geophys. Res.*, *107*, 1398, 2002.

Hubert, B., Milan, S. E., Grocott, A., Blockx, C., Cowley, S. W. H., and Gérard, J.-C., Dayside and nightside reconnection rates inferred from IMAGE FUV and Super Dual Auroral Radar Network data, *J. Geophys. Res.*, *111*, A03217, 2006.

Huang, C. S. and Cai, X., Magnetotail total pressure and lobe magnetic field at onsets of sawtooth events and their relation to the solar wind, *J. Geophys. Res.*, *114*, A04204, 2009.

Huang, C. S., DeJong, A. D., and Cai, X., Magnetic flux in the magnetotail and polar cap during sawteeth, isolated substorms, and steady magnetospheric convection events, *J. Geophys. Res.*, *114*, A07202, 2009.

Iijima, T. and Potemra, T. A., Large-Scale Characteristics of Field-Aligned Currents Associated with Substorms, *J. Geophys. Res.*, *83*, 599-615, 1978.

Imber, S. M., Milan, S. E., and Hubert, B., Observations of significant flux closure by dual lobe reconnection, *Ann. Geophys.*, *25*, 1617-1627, 2007.

Imber, S. M., Milan, S. E., and Hubert, B., The auroral and ionospheric flow signatures of dual lobe reconnection, *Ann. Geophys.*, *24*, 3115-3129, 2006.

Jayachandran, P. T., Donovan, E. F., MacDougall, J. W., Moorcroft, D. R., Liou, K., Newell, P. T., and St-Maurice, J. P., Global and local equatorward expansion of the ion auroral oval before substorm onsets, *J. Geophys. Res.*, *110*, A05204, 2005.

Jayachandran, P. T., Donovan, E. F., MacDougall, J. W., Moorcroft, D. R., St Maurice, J. P., and Prikryl, P., SuperDARN E-region backscatter boundary in the dusk-midnight sector - tracer of equatorward boundary of the auroral oval, *Annales Geophysicae*, *20*, 1899-1904, 2002.

Kamide, Y., Perreault, P. D., Akasofu, S. I., and Winningham, J. D., Dependence of Substorm Occurrence Probability on Interplanetary Magnetic-Field and on Size of Auroral Oval, *J. Geophys. Res.*, *82*, 5521-5528, 1977.

Kamide, Y. and Winningham, J. D., Statistical Study of Instantaneous Nightside Auroral Oval - Equatorward Boundary of Electron-Precipitation as Observed by Isis-1 and 2 Satellites, *Journal of Geophysical Research-Space Physics*, *82*, 5573-5588, 1977.

Kauristie, K., Weygand, J., Pulkkinen, T. I., Murphree, J. S., and Newell, P. T., Size of the auroral oval: UV ovals and precipitation boundaries compared, *J. Geophys. Res.*, *104*, 2321-2331, 1999.

Kawasaki, K., Akasofu, S. I., Yasuhara, F., and Meng, C. I., Storm Sudden Commencements and Polar Magnetic Substorms, *J. Geophys. Res.*, *76*, 6781-6789, 1971.

Kelley, C. K., with contributions from Heelis R. A., The Earth's Ionosphere: Plasma Physics and Electrodynamics, *Academic Press*, San Diego, CA, 1989.

Kellogg, P. J., Flow of plasma around the earth, *J. Geophys. Res.*, *67*, 3805-3811, 1962.

King, J. H. and Papitashvili, N. E., Solar wind spatial scales in and comparisons of hourly Wind and ACE plasma and magnetic field data, *J. Geophys. Res.*, *110*, A02104, 2005.

Kivelson, M. G. and Russell, C. T., An Introduction To Space Plasma Physics, Cambridge University Press, Cambridge, 1995.

Kivelson, M. G., Kaye, S.M., and Southwood, D. J.: The Physics of plasma injection events, in Dynamics of the Magnetosphere, edited by: Akasofu, S.-I., D. Reidel, Norwell Mass., 385-405, 1980.

Kokubun, S., Yamamoto, T., Acuna, M. H., Hayashi, K., Shiokawa, K., and Kawano, H., The Geotail Magnetic-Field Experiment, *J. Geomag. Geoelec.*, *46*, 7-21, 1994.

Koskinen, H., Lopez, R., Pellinen, R., Pulkkinen, T., Baker, D., and Bosinger, T., Pseudobreakup and substorm growth phase in the ionosphere and magnetosphere, *J. Geophys. Res.*, *98*, 5801, 1993.

Krimigis, S. M., Gloeckler, G., McEntire, R. W., Potemra, T. A., Scarf, F. L., and Shelley, E. G., Magnetic Storm of September 4, 1984 - a Synthesis of Ring Current Spectra and Energy Densities Measured with Amptec Cce, *Geophys. Res. Lett.*, *12*, 329-332, 1985.

Kullen, A. and Karlsson, T., On the relation between solar wind, pseudobreakups, and substorms, *J. Geophys. Res.*, *109*, A12218, 2004.

Lam, M. M., M. Pinnock, and E. F. Donovan, Observations of nightside magnetic reconnection during substorm growth and expansion phases, *J. Geophys. Res.*, *111*, A05209, 2006.

Lee, D. Y., Lyons, L. R., Weygand, J. M., and Wang, C. P., Reasons why some solar wind changes do not trigger substorms, *J. Geophys. Res.*, *112*, A06240, 2007.

Lee, D. Y., Lyons, L. R., and Reeves, G. D., Comparison of geosynchronous energetic particle flux responses to solar wind dynamic pressure enhancements and substorms, *J. Geophys. Res.*, *110*, A09213, 2005.

Lepping, R. P., Acuna, M. H., Burlaga, L. F., Farrell, W. M., Slavin, J. A., Schatten, K. H., Mariani, F., Ness, N. F., Neubauer, F. M., Whang, Y. C., Byrnes, J. B., Kennon, R. S., Panetta, P. V., Scheifele, J., and Worley, E. M., The Wind Magnetic-Field Investigation, *Sp. Sci. Rev.*, *71*, 207-229, 1995.

Lester, M., Milan, S. E., Besser, V., and Smith, R., A case study of HF radar spectra and 630.0 nm auroral emission in the pre-midnight sector, *Ann. Geophys.*, *19*, 327-339, 2001.

Lester, M., Murdin, P., Magnetosphere of Earth: Substorms, in *Encyclopedia of Astronomy and Astrophysics*, Edited by Paul Murdin, article 2351, Bristol: Institute of Physics Publishing, 2001.

Liemohn, M. W., and Chan, A.A., Unravelling the mechanisms responsible for radiation belt enhancements, *EOS*, *88*, 425-426, 2007.

Liou, K., Large, abrupt pressure decreases as a substorm onset trigger, *Geophys. Res. Lett.*, *34*, L14107, 2007.

Liou, K., Meng, C. I., Newell, P. T., Lui, A. T. Y., Reeves, G. D., and Belian, R. D., Particle injections with auroral expansions, *J. Geophys. Res.*, *106*, 5873-5881, 2001a.

Liou, K., Newell, P. T., Sibeck, D. G., Meng, C. I., Brittnacher, M., and Parks, G., Observation of IMF and seasonal effects in the location of auroral substorm onset, *J. Geophys. Res.*, *106*, 5799-5810, 2001b.

Liou, K., Meng, C. I., Newell, P. T., Takahashi, K., Ohtani, S. I., Lui, A. T. Y., Brittnacher, M., and Parks, G., Evaluation of low-latitude Pi2 pulsations as indicators of substorm onset using Polar ultraviolet imagery, *J. Geophys. Res.*, *105*, 2495-2505, 2000.

Liu, W. L.; Li, X.; Sarris, T.; Cully, C.; Ergun, R.; Angelopoulos, V.; Larson, D.; Keiling, A.; Glassmeier, K. H.; Auster, H. U., Observational and modelling of the injection observed by THEMIS and LANL satellites during the 23 March 2007 substorm event, *J. Geophys. Res.*, *114*, A00C18, 2009.

Liu, Z. X., Escoubet, C. P., Pu, Z., Laakso, H., Shi, J. K., Shen, C., and Hapgood, M., The Double Star mission, *Ann. Geophys.*, *23*, 2707-2712, 2005.

Lockwood, M., Moen, J., van Eyken, A. P., Davies, J. A., Oksavik, K., and McCrea, I. W., Motion of the dayside polar cap boundary during substorm cycles: I. Observations of pulses in the magnetopause reconnection rate, *Ann. Geophys.*, *23*, 3495-3511, 2005.

Lockwood, M. and Cowley, S. W. H., Ionospheric Convection and the Substorm Cycle, in: Proceedings of the International Conference on Substorms (ICS-1), *ESA SP-335*, 99-109, 1992.

Lopez, R. E., Sibeck, D. G., McEntire, R. W., and Krimigis, S. M., The Energetic Ion Substorm Injection Boundary, *J. Geophys. Res.*, *95*, 109-117, 1990.

Lui, A. T. Y., Current disruption in the Earth's magnetosphere: Observations and models, *J. Geophys. Res.*, *101*, 13067-13088, 1996.

- Lui, A. T. Y., A Synthesis of Magnetospheric Substorm Models, *J. Geophys. Res.*, *96*, 1849-1856, 1991.
- Lui, A. T. Y., Anger, C. D., Venkatesan, D., Sawchuk, W., and Akasofu, S. I., Topology of Auroral Oval as seen by Isis 2 Scanning Auroral Photometer, *J. Geophys. Res.*, *80*, 1794-1805, 1975.
- Lui, A. T. Y. and Anger, C. D., Uniform Belt of Diffuse Auroral Emission seen by Isis-2 Scanning Photometer, *Planet. Space Sci.*, *21*, 799-799, 1973.
- Lyons, L. R., Voronkov, I. O., Donovan, E. F., and Zesta, E., Relation of substorm breakup arc to other growth-phase auroral arcs, *J. Geophys. Res.*, *107*, 1390, 2002.
- Lyons, L. R., Blanchard, G. T., Samson, J. C., Rouhoniemi, J. M., Greenwald, R. A., Reeves, G. D., Scudder, J. D., Near Earth Plasma Sheet Penetration and Geomagnetic Disturbances, in *New Perspectives on the Earth's Magnetotail. Geophys. Monogr.*, vol. 105, Edited by A. Nishida, D. N. Baker and S. W. H. Cowley, 241, AGU, Washington, D. C., 1998.
- Lyons, L. R., Blanchard, G. T., Samson, J. C., Lepping, R. P., Yamamoto, T., and Moretto, T., Coordinated observations demonstrating external substorm triggering, *J. Geophys. Res.*, *102*, 27039-27051, 1997.
- Lyons, L. R., A New Theory for Magnetospheric Substorms, *J. Geophys. Res.*, *100*, 19069-19081, 1995.
- Mauk, B. H. and Meng, C. I., Characterization of Geostationary Particle Signatures Based on the Injection Boundary Model, *J. Geophys. Res.*, *88*, 3055-3071, 1983.
- McComas, D. J., Bame, S. J., Barker, P., Feldman, W. C., Phillips, J. L., Riley, P., and Griffee, J. W., Solar Wind Electron Proton Alpha Monitor (SWEPAM) for the Advanced Composition Explorer, *Sp. Sci. Rev.*, *86*, 563-612, 1998.

McIlwain, C. E., Substorm injection boundaries, in *Magnetospheric Physics*, edited by B. M. McCormac, 143-154, D. Reidel Publishing Co., 1974.

McPherron, R. L., Weygand, J. M., and Hsu, T. S., Response of the Earth's magnetosphere to changes in the solar wind, *J. Atmos. Solar Terr. Phys.*, *70*, 303-315, 2008.

McPherron, R. L., O'Brien, T. P., and Thompson, S., Solar wind drivers for steady magnetospheric convection, in *Multiscale Coupling of Sun-Earth Processes*, Editors Lui *et al.*, Elsevier, Amsterdam, 113-124, 2005.

McPherron, R. L. and Hsu, T. S., A comparison of substorms occurring during magnetic storms with those occurring during quiet times, *J. Geophys. Res.*, *107*, 1259, 2002.

McPherron, R. L., Terasawa, T., and Nishida, A., Solar-Wind Triggering of Substorm Expansion Onset, *J. Geomagn. Geoelectr.*, *38*, 1089-1108, 1986.

McPherron, R. L., Russell, C. T., and Aubry, M. P., Satellite Studies of Magnetospheric Substorms on August 15, 1968 .9. Phenomenological Model for Substorms, *Transactions-American Geophysical Union*, *54*, 206-206, 1973.

McPherron, R. L., Growth phase of magnetospheric substorms, *J. Geophys. Res.*, *75*, 5592-5599, 1970.

Mende, S. B., Frey, H. U., Morsony, B. J., and Immel, T. J., Statistical behavior of proton and electron auroras during substorms, *J. Geophys. Res.*, *108*, 1339, 2003.

Mende, S. B., Heeterks, H., Frey, H. U., Lampton, M., Geller, S. P., Habraken, S., Renotte, E., Jamar, C., Rochus, P., Spann, J., Fuselier, S. A., Gerard, J. C., Gladstone, R., Murphree, S., and Cogger, L., Far ultraviolet imaging from the IMAGE spacecraft. 1. System design, *Space Sci. Rev.*, *91*, 243-270, 2000a.

Mende, S. B., Heeterks, H., Frey, H. U., Lampton, M., Geller, S. P., Abiad, R., Siegmund, O. H. W., Tremsin, A. S., Spann, J., Dougani, H., Fuselier, S. A.,

Magoncelli, A. L., Bumala, M. B., Murphree, S., and Trondsen, T., Far ultraviolet imaging from the IMAGE spacecraft. 2. Wideband FUV imaging, *Space Sci. Rev.*, *91*, 271-285, 2000b.

Mende, S. B., Heetderks, H., Frey, H. U., Stock, J. M., Lampton, M., Geller, S. P., Abiad, R., Siegmund, O. H. W., Habraken, S., Renotte, E., Jamar, C., Rochus, P., Gerard, J. C., Sigler, R., and Lauche, H., Far ultraviolet imaging from the IMAGE spacecraft. 3. Spectral imaging of Lyman-alpha and OI 135.6 nm, *Space Sci. Rev.*, *91*, 287-318, 2000c.

Milan, S. E., Grocott, A., Forsyth, C., Imber, S. M., Boakes, P. D., and Hubert, B., A superposed epoch analysis of auroral evolution during substorm growth, onset and recovery: open magnetic flux control of substorm intensity, *Ann. Geophys.*, *27*, 659-668, 2009a.

Milan, S. E., Hutchinson, J., Boakes, P. D., and Hubert, B., Influences on the radius of the auroral oval, *Ann. Geophys.*, *27*, 2913-2924, 2009b.

Milan, S. E., Boakes, P. D., and Hubert, B., Response of the expanding/contracting polar cap to weak and strong solar wind driving: Implications for substorm onset, *J. Geophys. Res.*, *113*, A09215, 2008.

Milan, S. E., Provan, G., and Hubert, B., Magnetic flux transport in the Dungey cycle: A survey of dayside and nightside reconnection rates, *J. Geophys. Res.*, *112*, A01209, 2007.

Milan, S. E., Wild, J. A., Hubert, B., Carr, C. M., Lucek, E. A., Bosqued, J. M., Watermann, J. F., and Slavin, J. A., Flux closure during a substorm observed by Cluster, Double Star, IMAGE FUV, SuperDARN, and Greenland magnetometers, *Annales Geophysicae*, *24*, 751-767, 2006.

Milan, S. E., Cowley, S. W. H., Lester, M., Wright, D. M., Slavin, J. A., Fillingim, M., Carlson, C. W., and Singer, H. J., Response of the magnetotail to changes in the open flux content of the magnetosphere, *J. Geophys. Res.*, *109*, A04220, 2004.

Milan, S. E., Lester, M., Cowley, S. W. H., Oksavik, K., Brittnacher, M., Greenwald, R. A., Sofko, G., and Villain, J. P., Variations in the polar cap area during two substorm cycles, *Ann. Geophys.*, *21*, 1121-1140, 2003.

Milan, S. E., Lester, M., Cowley, S. W. H., and Brittnacher, M., Dayside convection and auroral morphology during an interval of northward interplanetary magnetic field, *Ann. Geophys.*, *18*, 436-444, 2000.

Milan, S. E., Lester, M., Cowley, S. W. H., Moen, J., Sandholt, P. E., and Owen, C. J., Meridian-scanning photometer, coherent HF radar, and magnetometer observations of the cusp: a case study, *Ann. Geophys.*, *17*, 159-172, 1999.

Mishin, V. M., The Magnetogram Inversion Technique and some Applications, *Sp. Sci. Rev.*, *53*, 83-163, 1990.

Miyashita, Y., Kamide, Y., Machida, S., Liou, K., Mukai, T., Saito, Y., Ieda, A., Meng, C. I., and Parks, G. K., Difference in magnetotail variations between intense and weak substorms, *J. Geophys. Res.*, *109*, A11205, 2004.

Moldwin, M. B., Thomsen, M. F., Bame, S. J., McComas, D. J., Weiss, L. A., Reeves, G. D., and Belian, R. D., The appearance of plasmaspheric plasma in the outer magnetosphere in association with the substorm growth phase, *Geophys. Res. Lett.*, *23*, 801-804, 1996.

Moore, T. E., Arnoldy, R. L., Feynman, J., and Hardy, D. A., Propagating Substorm Injection Fronts, *J. Geophys. Res.*, *86*, 6713-6726, 1981.

Morley, S. K. and Freeman, M. P., On the association between northward turnings of the interplanetary magnetic field and substorm onsets, *Geophys. Res. Lett.*, *34*, L08104, 2007.

Morley, S. K., Freeman, M. P., and Tanskanen, E. I., A comparison of the probability distribution of observed substorm magnitude with that predicted by a minimal substorm model, *Ann. Geophys.*, *25*, 2427-2437, 2007.

Murphree, J. S., Elphinstone, R. D., Henderson, M. G., Cogger, L. L., and Hearn, D. J., Interpretation of Optical Substorm Onset Observations, *J. Atmos. Terr. Phys.*, *55*, 1159-1170, 1993.

Nakai, H. and Kamide, Y., A critical condition in magnetotail pressure for leading to a substorm expansion onset: Geotail's observations, *J. Geophys. Res.*, *109*, A01205, 2004.

Nagai, T., Fujimoto, M., Nakamura, R., Baumjohann, W., Ieda, A., Shinohara, I., Machida, S., Saito, Y., and Mukai, T., Solar wind control of the radial distance of the magnetic reconnection site in the magnetotail, *J. Geophys. Res.*, *110*, A09208, 2005.

Nagai, T., Fujimoto, M., Saito, Y., Machida, S., Terasawa, T., Nakamura, R., Yamamoto, T., Mukai, T., Nishida, A., and Kokubun, S., Structure and dynamics of magnetic reconnection for substorm onsets with Geotail observations, *J. Geophys. Res.*, *103*, 4419-4440, 1998.

Newell, P. T., Feldstein, Y. I., Galperin, Y. I., and Meng, C. I., Morphology of nightside precipitation, *J. Geophys. Res.*, *101*, 10737-10748, 1996.

Newell, P. T. and Meng, C. I., Mapping the Dayside Ionosphere to the Magnetosphere According to Particle-Precipitation Characteristics, *Geophys. Res. Lett.*, *19*, 609-612, 1992.

Newell, P. T., Burke, W. J., Sanchez, E. R., Meng, C. I., Greenspan, M. E., and Clauer, C. R., The Low-Latitude Boundary-Layer and the Boundary Plasma Sheet at Low Altitude - Prenoon Precipitation Regions and Convection Reversal Boundaries, *J. Geophys. Res.*, *96*, 21013-21023, 1991a.

Newell, P. T., Wing, S., Meng, C. I., and Sigillito, V., The Auroral Oval Position, Structure, and Intensity of Precipitation from 1984 Onward - an Automated Online Data-Base, *J. Geophys. Res.*, *96*, 5877-5882, 1991b.

Nishida, H., Uesugi, K., Nakatani, I., Mukai, T., Fairfield, D. H., and Acuña, M. H., Geotail mission to explore Earth's magnetotail, *EOS, Trans. AGU*, *73*, No. 40, 1992.

O'Brien, T. P., Thompson, S. M., and McPherron, R. L., Steady magnetospheric convection: Statistical signatures in the solar wind and AE, *Geophys. Res. Lett.*, *29*, 1130, 2002.

Ogilvie, K. W., Chornay, D. J., Fritzenreiter, R. J., Hunsaker, F., Keller, J., Lobell, J., Miller, G., Scudder, J. D., Sittler, E. C., Torbert, R. B., Bodet, D., Needell, G., Lazarus, A. J., Steinberg, J. T., and Tappan, J. H., Swe, a Comprehensive Plasma Instrument for the Wind Spacecraft, *Sp. Sci. Rev.*, *71*, 55-77, 1995.

Olson, J. V., Pi2 pulsations and substorm onsets: A review, *J. Geophys. Res.*, *104*, 17499-17520, 1999.

Østgaard, N., Mende, S. B., Frey, H. U., Sigwarth, J. B., Asnes, A., and Weygand, J. M., Auroral conjugacy studies based on global imaging, *J. Atmos. Solar Terr. Phys.*, *69*, 249-255, 2007.

Parker, E. N., Dynamics of the interplanetary gas and magnetic fields, *Astrophys. J.*, *128*, 664-676, 1958.

Parks, G. K., Mauk, B., Gurgiolo, C., and Lin, C. S., Observations of plasma injection, in *Dynamics of the Magnetosphere*, edited by S.-I. Akasofu, D. Reidel Publishing Co., 371-382, 1980.

Paschmann, G., Haerendel, G., Sckopke, N., Rosenbauer, H., and Hedgecock, P.C., Plasma and magnetic field characteristics of the distant polar cusp near local noon: The entry layer, *J. Geophys. Res.*, *81*, 2883-2899, 1976.

Perreault, P. and Akasofu, S. I., Study of Geomagnetic Storms, *Geophysical Journal of the Royal Astronomical Society*, 54, 547-573, 1978.

Petrinec, S. M. and Russell, C. T., Near-Earth magnetotail shape and size as determined from the magnetopause flaring angle, *J. Geophys. Res.*, 101, 137-152, 1996.

Press, W. H., Teukelosky, S. A., Vetterling, W. T., and Flannery, B. P., Numerical Recipes: The art of scientific computing, 3rd ed., *Cambridge Univ. Press*, Cambridge, UK, 2007.

Prölss, G. W., Physics of the Earth's Space Environment, Springer, 2004.

Pulkkinen, T. I., Partamies, N., McPherron, R. L., Henderson, M., Reeves, G. D., Thomsen, M. F., and Singer, H. J., Comparative statistical analysis of storm time activations and sawtooth events, *J. Geophys. Res.*, 112, 2360, 2007.

Pulkkinen, T. I., Ganushkina, N. Y., Tanskanen, E. I., Kubyshkina, M., Reeves, G. D., Thomsen, M. F., Russell, C. T., Singer, H. J., Slavin, J. A., and Gjerloev, J., Magnetospheric current systems during stormtime sawtooth events, *J. Geophys. Res.*, 111, A11S17, 2006.

Pulkkinen, T. I., Baker, D. N., Pellinen, R. J., Murphree, J. S., and Frank, L. A., Mapping of the Auroral Oval and Individual Arcs during Substorms, *J. Geophys. Res.*, 100, 21987-21994, 1995.

Pytte, T., R. L. McPherron, Hones, Jr., E. W., and West, Jr., H. I., Multiple-satellite studies of magnetospheric substorms: Distinction between polar magnetic substorms and convection-driven negative bays. *J. Geophys. Res.* 83, 663-679, 1978.

Reiff, P. H. and Burch, J. L., Imf By-Dependent Plasma-Flow and Birkeland Currents in the Dayside Magnetosphere .2. a Global-Model for Northward and Southward Imf, *J. Geophys. Res.*, 90, 1595-1609, 1985.

Rosenbauer, H., Grunmwaldt, H., Montgomery, M. D., Paschmann, G., and Sckopke, N., Heos 2 plasma observations in the distant polar magnetosphere: The plasma mantle, *J. Geophys. Res.*, 80, 2723-2737, 1975.

Rostoker, G., Triggering of Expansive Phase Intensifications of Magnetospheric Substorms by Northward Turnings of the Interplanetary Magnetic-Field, *J. Geophys. Res.*, 88, 6981-6993, 1983.

Russell, C. T., How northward turnings of the IMF can lead to substorm expansion onsets, *Geophys. Res. Lett.*, 27, 3257-3259, 2000.

Russell, C. T., The configuration of the magnetosphere. In: E.R. Dyer, Editor, *Critical Problems of Magnetospheric Physics*, Inter-Union Committee on Solar Terrestrial Physics, National Academy of Sciences, Washington, DC, 1-16, 1972.

Samson, J. C., Lyons, L. R., Newell, P. T., Creutzberg, F., and Xu, B., Proton Aurora and Substorm Intensifications, *Geophys. Res. Lett.*, 19, 2167-2170, 1992.

Samson, J. C. and Yeung, K. L., Some Generalizations on the Method of Superposed Epoch Analysis, *Planet. Space Sci.*, 34, 1133-1142, 1986.

Sandholt, P. E., Farrugia, C. J., Oieroset, M., Stauning, P., and Denig, W. F., Auroral activity associated with unsteady magnetospheric erosion: Observations on December 18, 1990, *J. Geophys. Res.*, 103, 2309-2317, 1998.

Sarris, T. and Li, X., Evolution of the dispersionless injection boundary associated with substorms, *Ann. Geophys.*, 23, 877-884, 2005.

Sarris, T. E., Li, X. L., Tsaggas, N., and Paschalidis, N., Modeling energetic particle injections in dynamic pulse fields with varying propagation speeds, *J. Geophys. Res.*, 107, 2002.

Sergeev, V. A., Shukhtina, M. A., Rasinkangas, R., Korth, A., Reeves, G. D., Singer, H. J., Thomsen, M. F., and Vagina, L. I., Event study of deep energetic particle injections during substorm, *J. Geophys. Res.*, *103*, 9217-9234, 1998.

Sergeev, V. A., Pellinen, R. J., and Pulkkinen, T. I., Steady magnetospheric convection: A review of recent results, *Sp. Sci. Rev.*, *75*, 551-604, 1996.

Sergeev, V. A., Dmitrieva, N. P., and Barkova, E. S., Triggering of Substorm Expansion by the Imf Directional Discontinuities - Time-Delay Analysis, *Planet. Space Sci.*, *34*, 1109-1118, 1986.

Sergeev, V. A., On the state of the magnetosphere during prolonged period of southward oriented IMF, *Phys. Solarterr.*, *5*, 39, 1977.

Shukhtina, M. A., Dmitrieva, N. P., Popova, N. G., Sergeev, V. A., Yahnin, A. G., and Despirak, I. V., Observational evidence of the loading-unloading substorm scheme, *Geophys. Res. Lett.*, *32*, L17107, 2005.

Shukhtina, M. A., Dmitrieva, N. P., and Sergeev, V. A., Quantitative magnetotail characteristics of different magnetospheric states, *Ann. Geophys.*, *22*, 1019-1032, 2004.

Siscoe, G. L. and Huang, T. S., Polar-Cap Inflation and Deflation, *J. Geophys. Res.*, *90*, 543-547, 1985.

Slavin, J. A., Tanskanen, E. I., Hesse, M., Owen, C. J., Dunlop, M. W., Imber, S., Lucek, E. A., Balogh, A., and Glassmeier, K. H., Cluster observations of traveling compression regions in the near-tail, *J. Geophys. Res.*, *110*, 2005.

Slavin, J. A., Smith, E. J., Sibeck, D. G., Baker, D. N., Zwickl, R. D., and Akasofu, S. I., An Isee-3 Study of Average and Substorm Conditions in the Distant Magnetotail, *J. Geophys. Res.*, *90*, 875-895, 1985.

Smith, C. W., L'Heureux, J., Ness, N. F., Acuna, M. H., Burlaga, L. F., and Scheifele, J., The ACE magnetic fields experiment, *Sp. Sci. Rev.*, *86*, 613-632, 1998.

Sotirelis, T. and Newell, P. T.: Boundary-oriented electron precipitation model, *J. Geophys. Res.*, *105*, 18655-18673, 2000.

Stone, E. C., Frandsen, A. M., Mewaldt, R. A., Christian, E. R., Margolies, D., Ormes, J. F., and Snow, F., The Advanced Composition Explorer, *Space Science Reviews*, *86*, 1-22, 1998.

Taylor, J. R., Yeoman, T.K., Lester, M., Emery, B.A., and Knipp, D.J., Variations in the polar cap area during intervals of substorm activity on 20–21 March 1990 deduced from AMIE convection maps, *Ann. Geophys.* *14*, 879–887, 1996.

Torr, M. R., Torr, D. G., Zukic, M., Johnson, R. B., Ajello, J., Banks, P., Clark, K., Cole, K., Keffer, C., Parks, G., Tsurutani, B., and Spann, J., A Far-Ultraviolet Imager for the International Solar-Terrestrial Physics Mission, *Sp. Sci. Rev.*, *71*, 329-383, 1995.

Troshichev, O. A., Kotikov, A. L., Bolotinskaya, B. D., and Andrezen, V. G., Influence of the Imf Azimuthal Component on Magnetospheric Substorm Dynamics, *J. Geomagn. Geoelectr.*, *38*, 1075-1088, 1986.

Tu, C. Y., Schwenn, R., Donovan, E., Marsch, E., Wang, J. S., Xia, L. D., Zhang, Y. W., and KuaFu Working Team, Space weather explorer - The KuaFu mission, *Advances in Space Research*, *41*, 190-209, 2008.

Vagina, L. I., Sergeev, V. A., Baker, D. N., and Singer, H. J., Use of mid-latitude magnetic data for modelling and diagnostics of magnetospheric substorms, *Advances in Space Research*, *18*, 229-232, 1995.

Voronkov, I. O., Donovan, E. F., and Samson, J. C., Observations of the phases of the substorm, *J. Geophys. Res.*, *108*, 2003.

Voronkov, I., Donovan, E. F., Jackel, B. J., and Samson, J. C., Large-scale vortex dynamics in the evening and midnight auroral zone: Observations and simulations, *J. Geophys. Res.*, *105*, 18505-18518, 2000.

Walker, R. J., Erickson, K. N., Swanson, R. L., and Winckler, J. R., Substorm-Associated Particle Boundary Motion at Synchronous Orbit, *J. Geophys. Res.*, *81*, 5541-5550, 1976.

Wanliss, J. A. and Showalter, K. M., High-resolution global storm index: Dst versus SYM-H, *J. Geophys. Res.*, *111*, A02202, 2006.

Weimer, D. R. and King, J. H., Improved calculations of interplanetary magnetic field phase front angles and propagation time delays, *J. Geophys. Res.*, *113*, A01105, 2008.

Weimer, D. R., Correction to “Predicting interplanetary magnetic field (IMF) propagation delay times using the minimum variance technique”, *J. Geophys. Res.*, *109*, A12104, 2004.

Weimer, D. R., Ober, D. M., Maynard, N. C., Collier, M. R., McComas, D. J., Ness, N. F., Smith, C. W., and Watermann, J., Predicting interplanetary magnetic field (IMF) propagation delay times using the minimum variance technique, *J. Geophys. Res.*, *108*, 1026, 2003.

Weimer, D. R., Maps of ionospheric field-aligned currents as a function of the interplanetary magnetic field derived from Dynamics Explorer 2 data, *J. Geophys. Res.*, *106*, 12889-12902, 2001.

Weimer, D. R., Substorm Time Constants, *J. Geophys. Res.*, *99*, 11005-11015, 1994.

Wild, J. A., Woodfield, E. E., and Morley, S. K., On the triggering of auroral substorms by northward turnings of the interplanetary magnetic field, *Ann. Geophys.*, *27*, 3559-3570, 2009.

Wild, J. A., Milan, S. E., Owen, C. J., Bosqued, J. M., Lester, M., Wright, D. M., Frey, H., Carlson, C. W., Fazakerley, A. N., and Reme, H., The location of the open-closed magnetic field line boundary in the dawn sector auroral ionosphere, *Ann. Geophys.*, *22*, 3625-3639, 2004.

Wolfe, J. H., Silva, R. W., McKibbin, D. D., and Mason, R. H., Preliminary Observations of a Geomagnetospheric Wake at 1000 Earth Radii, *J. Geophys.*, 72, 4577, 1967.

Yeoman, T. K., Freeman, M. P., Reeves, G. D., Lester, M., and Orr, D., A Comparison of Midlatitude Pi-2 Pulsations and Geostationary Orbit Particle Injections as Substorm Indicators, *J. Geophys. Res.*, 99, 4085-4093, 1994.

Zesta, E., Donovan, E., Lyons, L., Enno, G., Murphree, J. S., and Cogger, L., Two-dimensional structure of auroral poleward boundary intensifications, *J. Geophys. Res.*, 107, 1350, 2002.

Zhou, X. Y. and Tsurutani, B. T., Interplanetary shock triggering of nightside geomagnetic activity: Substorms, pseudobreakups, and quiescent events, *J. Geophys. Res.*, 106, 18957-18967, 2001.